3D unsteady flow in oscillating compressor cascade

Hui Yang

How to cite:

Yang, Hui (2004) 3D unsteady flow in oscillating compressor cascade. Doctoral thesis, Durham University.

3D UNSTEADY FLOW IN OSCILLATING COMPRESSOR CASCADE

Hui Yang
School of Engineering, University of Durham

A dissertation submitted to the University of Durham
for the degree of Doctor of Philosophy

March 2004

Declaration

I declare that no material presented within this dissertation has previously been submitted toward a degree, either at this university or anywhere else

Hui Yang

Acknowledgements

I would especially like to thank my supervisor, Dr. L. He, for his guidance, encouragement and support throughout this research project, and the opportunities he has afforded me.

The financial sponsorship from ALSTOM power UK Ltd. is gratefully acknowledged for providing continual financial support for the four years of this project. I would like to thank Mr. R. Wells, Drs. Y. S. Li, and W. Ning (ALSTOM power) and Dr. D. Bell (ALSTOM Steam Turbines) for their support.

The assistance of the technicians within the School of Engineering and Estates and buildings Department in the construction of the test facility is also acknowledged, Mr. B. Blackburn, Mr. A. G. Swann, Mr. A. Wilson, Mr. I. Glassford, Mr. I. Garret, Mr. R. Mand and Mr. G. Parker are especially mentioned. I would also like to thank Dr. D. Sims-Williams of the School of Engineering for the help regarding applications of the transfer function method.

Colleagues of the CFD group and the thermodynamics Lab have not only provided fun working environment but have been a valuable source of assistance, encouragement and friendship. I would like to mention some of them: Andy, Ben, Grant, Haidong, Olivier, Paul, Stuart, Sue, Vasanthakumar, Xiuquan. Thanks are due to for proof reading this thesis. Haidong and Vasanthakumar provided many helpful suggestions for the computational predictions.

The ultimate acknowledgement is due to my family and parents, for their unending love and support. Without their continuing support none of this would have been possible, especially after my daughter was born in Durham during the time of this research project.

ABSTRACT

An experimental and computational study has been carried out to enhance current understanding of three dimensional (3D) cascade aeroelastic mechanisms. 3D unsteady pressure data produced during executing this project is the first-of-its-kind, which can be directly used for validation of advanced 3D numerical methods for the prediction of aeroelastic problems in turbomachines.

A new, low speed flutter test rig with a linear compressor cascade consisting of seven Controlled-Diffusion Blades has been commissioned. The unsteady aerodynamics of the oscillating cascade is investigated using the Influence Coefficient Method, by which the middle blade is mechanically driven to oscillate in a 3D bending mode. Off-board pressure transducers are utilized to allow detailed measurement of the unsteady blade surface pressures in conjunction with a Tubing Transfer Function (TTF) method to correct tubing distortion errors. The linearity of the unsteady aerodynamic response is confirmed by tests with different oscillation amplitudes, which enables unsteady results of a tuned cascade to be constructed by using the Influence Coefficient Method at various inter-blade phase angles. An examination of the techniques adopted and experimental errors indicates a good level of accuracy and repeatability to be attained in the measurement of unsteady pressure.

A detailed set of steady flow is obtained from the middle three blades, which demonstrates a reasonable blade-to-blade periodicity. At a nominal steady flow condition unsteady pressure measurements were performed at six spanwise sections between 20% and 98% span for three different reduced frequencies. The 2D laminar bubble-type separation around middle chord on the suction surface is identified to have a local effect on the unsteady flow. The measured results illustrate the fully 3D unsteady flow behaviour. Strong spanwise unsteady interaction leads to a non-proportional distribution of unsteady pressure amplitude at different spanwise locations. This questions the assumption that may be used in quasi-3D strip theory. The aerodynamic damping against the whole range of inter-blade phase angle demonstrates the strong blade-to-blade coupling effect on the cascade aeroelastic stability according to inter-blade phase angle. The least stable inter-blade phase angle corresponds to a forward travelling wave mode with one or two nodal diameters (depending on the total number of blades in a real blade row).

The influence of tip-clearance on the aeroelastic response of compressor blades has been experimentally investigated for the first time. The test results with different tip-clearance gaps (1 – 2.3% span) show that the cascade is destabilised for the whole range of inter-blade phase angle as the tip gap is increased. This destabilising effect of tip-clearance is independent on inter-blade phase angle with the maximum influence at the least stable inter-blade phase angle. The destabilised region is seen to extend to almost the whole blade span, which is consistent with the strong spanwise unsteady interaction. The chordwise trend in amplitude of unsteady pressure with increasing tip clearance is observed in the regions where the tip leakage flow has an obvious effect on the corresponding steady loading. The results clearly demonstrate that numerical methods without tip-clearance effect might over predict cascade stability.

A linearised 3D Navier-Stokes method was adopted to compute the 3D unsteady flow around the oscillating cascade. The computational solutions obtained from this method exhibit a consistently high level of agreement with the experimental test data. This clearly demonstrates the ability of the linearised computational method to predict the relevant unsteady aerodynamic phenomenon.

SUBJECT TERMS: blade flutter, 3D unsteady flow, oscillating compressor cascade, aeroelastic stability.

Table of Contents

6. Experimental Unsteady Flow Results and Discussions 109

7. Influence of Blade Tip Clearance 135

8. Computational Methods and Results 158

List of Figures

List of Tables

Nomenclature

A_n	- Complex Fourier coefficients of the undistorted unsteady signal
Am_l	- Local bending amplitude, non-dimensionalised with chord
Am_{tip}	- Bending amplitude at blade tip, non-dimensionalised with chord
Ap_n	- Amplitude of the nth harmonic pressure, *Pa*
B_n	- Complex Fourier coefficients of the distorted unsteady signal
C	- Blade chord length, *m*
Cax	- Blade axial chord length
C_{pitch}	- Calibration coefficient for pitch angle
C_{tot}	- Calibration coefficient for total pressure
C_{yaw}	- Calibration coefficient for yaw angle
Cp	- Blade surface static pressure coefficient, $Cp = \frac{p - p_2}{p_{01} - p_2}$
$C\tilde{p}_{0,tc}$	- Unsteady aerodynamic pressure coefficient acting on the blade 0 in a tuned cascade
$C\tilde{p}_{tc}(0,N)$	- Unsteady aerodynamic pressure coefficient acting on the stationary blade N induced by the oscillation of the reference blade 0
$\lvert Cp_n \rvert$	- Amplitude of the nth harmonic pressure coefficient, $\lvert Cp_n \rvert = \frac{Ap_n}{(p_{01} - p_2)Am_{tip}}$
$C\tilde{p}_{tc}(N,0)$	- Unsteady aerodynamic influence of blade N on blade 0 in a tuned cascade
D	- Blade bending displacement (normal to chord, positive from P.S. to S.S.)
f	- Vibration frequency, *Hz*
h	- Blade span, *m*
k	- Reduced frequency, $k = \frac{\omega C}{V_{ref}}$
p	- Pressure, *Pa*
Re	- Reynolds number
S	- Blade pitch length, *m*
t	- Time, s
T	- Time period
TF_n	- Tubing transfer function
$\tilde{U}$	- Perturbation conservation variables
V_{blade}	- Blade vibration velocity
V_{ref}	- Reference isentropic exit velocity, ms^{-1}, $V_{ref} = \sqrt{\frac{2(p_{01} - p_2)}{\rho}}$
x	- Axial chordwise location, *m*
Y	- Coefficient of total pressure loss

z - Spanwise co-ordinate, *m*

β_1 - Inlet flow angle (*deg.*)

δ - Blade tip-gap

ϕ_n - Phase angle of the n^{th} harmonic pressure response relative to blade vibration (*deg.*)

γ - Stagger angle

ρ - Density

σ - Inter-blade phase angle (IBPA, *deg.*), positive when blade +1 leads blade0 for compressor blades

ω - Angular frequency of blade vibration

ξ_c - Local aerodynamic damping coefficient, $\xi_c = \int_c \frac{-\pi Am_l |Cp_1| \sin\phi_1}{CAm_{tip}} ds$ (*ds is* the chordwise length of surface element)

ξ - Overall aerodynamic damping Coefficient, $\xi = \frac{1}{h}\int_h \xi_c dz$

Superscripts

Pre - Pressure surface

Suc - Suction surface

u - Upper surface

l - Lower surface

Subscripts

0 - Stagnation flow parameter

1 - Inlet parameter; First harmonic

2 - Exit parameter; Second harmonic

Abbreviations

2D - Two Dimensional

3D - Three Dimensional

B0 - Middle reference blade

CDB - Controlled-Diffusion Blade

CFD - Computational Fluid Dynamics

EO - Engine Order

IBPA - Inter-Blade Phase Angle

ICM - Influence Coefficient Method

Pre. Sur. - Pressure Surface

Sur. Sur. - Suction Surface

TipC - Tip-Clearance gap

TTF - Tubing Transfer Function

Chapter 1

Introduction

This chapter introduces the subject area of aeroelasticity related to blade vibration, and the challenging problems of blade flutter and forced response posed to designers of modern turbomachines. In the field of aeroelasticity in turbomachinery, blade flutter is an important problem, which is the major topic of this thesis. In addition to the scope of the work presented here, there is a short preview of what is contained in the following chapters.

1.1 General Background

Aeroelasticity is often defined as the physical science concerned with the interaction between the deformation of an elastic structure in an air-stream and the resulting aerodynamic force. It was described by Collar (1946) as the mutual interaction of aerodynamic, inertial and elastic forces, and the influence of this interaction on the behaviour of structures. Such interaction may tend to become smaller and smaller until a condition of stable equilibrium is reached, or it may tend to diverge and destroy structures. Aeroelastic problems would not exist if structures were perfectly rigid, which only occurs in ideal situations. The flexibility is fundamentally responsible for various types of aeroelastic phenomena in a wide range of engineering applications, such as in aircraft, turbomachines, wind energy converters, pipe flows, and civil engineering structures. In recent years, structures have become more flexible because designers are trying to reach the limits of materials. From this engineering background, it is clear that ignoring aeroelastic problems will lead to structural fatigue, which will result in premature structural failure, so investigating these problems attracts a lot of attention.

Axial-flow turbomachines are particularly susceptible to aeroelastic problems due to their fairly high aspect-ratio blades, which arise from optimisation of high aerodynamic performance and their light weight. The design trend is now to increase thrust-to-weight ratio, stage loading and pressures, to reduce weight and intra-row gaps, which provides conditions that can easily cause aeroelastic problems. Forced response and blade flutter are two basic types of aeroelastic instability in turbomachines. These problems have become limiting factors for increasing aerodynamic performance and engine life-cycle, especially during the development of new machines. Thus the development of accurate prediction tools to avoid these problems becomes the main task and challenge on researchers.

Forced response is induced by upstream or downstream periodic aerodynamic disturbances, which include variations in total pressure, total temperature, and static pressure at inlet and variations in static pressure at exit (Verdon 1993). These variations generally result from inherent sources in an aerodynamic flow path (e.g. wakes passing from upstream rows and static pressure variations on a blade row from upstream and downstream, or inlet/exit flow distortion), and are independent of blade vibration. When the frequency of an unsteady disturbance coincides with that of specific blade mode, resonance usually occurs in higher order vibration mode at high pressure stages and high stress levels may result from a lack of mechanical and/or aerodynamic damping. The consequence of high blade mechanical responses under unsteady disturbances can be serious - especially in high-pressure turbines - where the blades are already under large thermal and centrifugal loadings.

A useful tool for designers to diagram forced response at design condition is Campbell diagram as shown in **Figure 1.1**, which is a plot of blade vibration frequencies against rotor speeds, with the corresponding engine order lines (multiples of the engine rotation frequency) indicating the vibration modes being excited at a particular rotational speed. The forced response problems may be alleviated by reducing the forcing, or by controlling the resultant vibration (e.g. using under platform dampers), or it may be removed entirely by moving coincident frequencies out of the engine running range. It is not easy to move resonance out of the running range as engines operate over a wide range of speeds and aerodynamic conditions. Under start up or shut down conditions, it is impossible to avoid resonance. So it is important to be able to assess the unsteady aerodynamic loading and damping at resonant crossing points, and then evaluate the blade stress levels for fatigue life predictions.

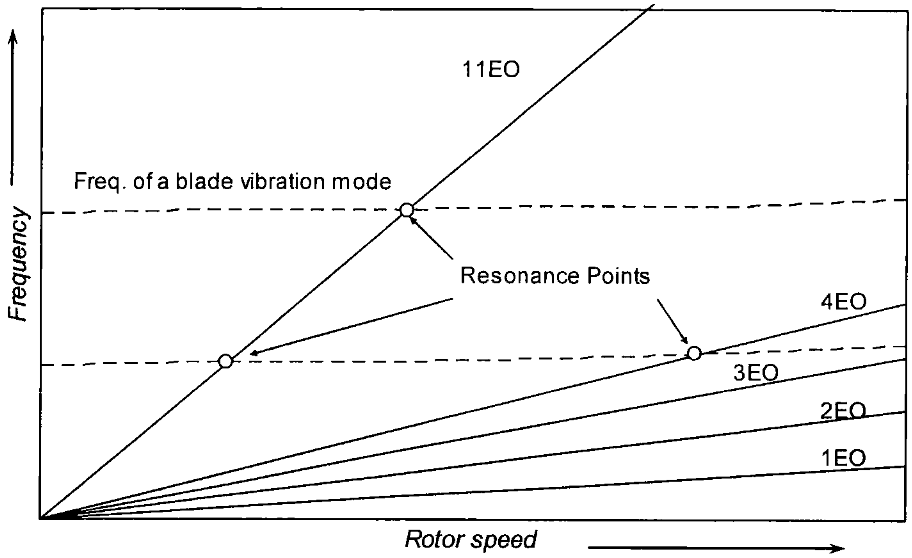

Figure 1.1: Schematic Campbell diagram

Blade flutter is one of the major aeroelastic problems in turbomachines and it is defined as an unstable self-excited vibration of blades, in which unsteady aerodynamic forces only depend on blade vibration. Initially, the unsteady aerodynamic forces are induced by a small amplitude vibration of blades at or near one of their lower structural natural frequencies under certain conditions in a uniform flow field, and then they interact with the blade motion to enhance the initial vibration. The continuous interaction between the flow and the structure and the extent of the resulting unsteadiness in the flow result in blade flutter. Blade flutter is an extremely dangerous condition because the oscillation of blades will grow with time and blades are subjected to fluctuating load, which eventually leads to structural fatigue failure. The most destructive failure caused by blade flutter can usually be attributed to the first bending or the first torsion mode, which can result in loss of an entire blade and then loss of thrust. So the main task of engine designers in dealing with blade flutter is to avoid its onset, namely aeroelastic instability.

Blade flutter often affects fans, low-pressure compressors and low-pressure turbines with high aspect ratio. Comparing with forced response, flutter can occur at non-synchronous engine speeds, which cover over a relatively wide range of engine operational conditions. According to numerous incidents of blade flutter in axial-flow compressors, there are four possible aerodynamic conditions associated with blade flutter shown in the compressor performance map (**Figure 1.2**). The classification has been made according to the corresponding aerodynamic conditions of the aeroelastic instabilities.

The most common type of blade flutter as well as the most serious kind of aeroelastic instability in axial-flow turbomachines is 'stalled flutter'. This is situated close to the surge line of the compressor map, including subsonic/transonic stalled flutter at low and middle rotor speeds and supersonic stalled flutter at high speeds. Usually the flow is likely to be stalled or largely separated on the suction surface of blades, which is thought to be the main cause of stalled flutter. In some instances, the aerodynamic loss behind a rotor did not increase measurably and the stalled flutter boundary has been found near maximum compressor efficiency. This indicates that stalling may not be essential for so-called stalled flutter as presented in Mikolajczak *et al.* (1975) and Stargardter (1977), although it could be the most severe condition. Stalled flutter is commonly seen in fan and front compressor stages (Kielb 1999a). Supersonic unstalled flutter occurs at any pressure ratio, and imposes a limit on the high speed operation of compressors. This is also commonly seen in shrouded fans. The intensive unsteady loading around an oscillating shock is the important feature for flutter induced in transonic and supersonic flow regimes. Choke flutter near the choke line at negative incidence is less common. This type of flutter is often experienced by middle and rear compressor stages. At subsonic flow conditions, it is characterised by separations on the pressure surface of blades, which has many similarities to stalled flutter. At transonic flow conditions, a supersonic region is ended by a weak shock wave, in which oscillating shockwaves also play an important role.

The flutter mechanisms are far more complicated than that described above. Relevant aerodynamic conditions are not clear, so they cannot simply be avoided by changing blade frequencies or blade numbers as with forced response. Inadequate flutter prediction can lead to overly conservative designs which penalize engine performance or conceal problems which require major redesigns leading to increased development costs. For example, the introduction of shrouds located on the part span or tip causes a certain level of uncertainty on structural dynamic analysis and increases weight. So, it is important to understand the underlying physical mechanics of blade flutter because it can lead to effectively active flutter control techniques.

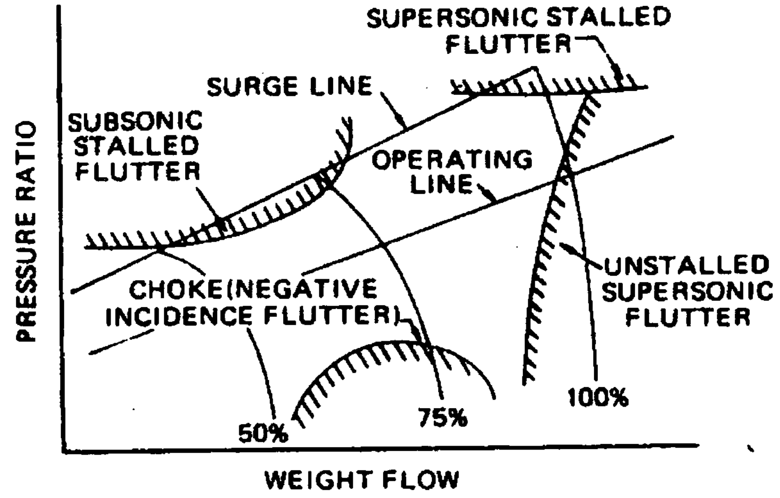

Figure 1.2: Compressor performance map with blade flutter boundaries

To predict the flutter stability, the Energy method (Carta 1967), a kind of uncoupled aeroelastic model, has been widely used with the assumption of uncoupling the fluid motion from that of the structure. When blade flutter occurs, the unsteady aerodynamic forces and moments do positive work on the blades during each vibration cycle and the mechanical and material damping are insufficient to dissipate the work. If the mechanical and material damping which are always positive can be neglected, the flutter stability can be simply determined by the energy transfer between the blade motion and its surrounding flow – the unsteady aerodynamic work. In turbomachinery blade rows, the structure-to-fluid mass ratio is much higher compared with that for aircraft wings. The aerodynamic inertia is much lower than the structural inertia and the aerodynamic stiffness is much lower than the structural stiffness. These result in that the aerodynamic forces have very little effect on the natural frequencies as well as the mode shape of blades. In order to evaluate the amount of unsteady aerodynamic work using the energy method, the structural and aerodynamic quantities need to be measured or calculated separately. They are the mode shape of the blade vibration (structural aspect), and the unsteady aerodynamic forces induced by an oscillating blade in its natural frequency (aerodynamic aspect). The unsteady aerodynamic work is obtained by integrating the unsteady aerodynamic force over the blade in one vibration cycle, which represents a measure of the aeroelastic stability of the blade system. The positive unsteady aerodynamic work indicates the aeroelastic instability, which corresponds with the negative aerodynamic damping. Generally, flutter is accepted as a linear behaviour and the accuracy of the energy method is sufficient for the prediction of the flutter onset. However for transonic unsteady flows, the nonlinear unsteady responses caused by shocks and their motions due to blade vibration are significant to the aeroelastic stability of a system. Coupled structural and aerodynamic methods that include fluid and structure interaction are needed (e.g. Marshall (1997)).

1.2 Unsteady Flow through Vibrating Turbomachinery Blades

In this section, the relevant parameters for blade flutter are described and then some issues in the particular area of unsteady flow around oscillating blades in turbomachines are addressed.

A fairly comprehensive list of parameters that affect the aeroelastic characteristics of blade vibrations has been provided by Srinivasan (1997), see also Fransson (1999a) which range from the blade characteristics, blade geometry, blade row interaction, flow conditions to general parameters. Here only the general parameters - reduced frequency and inter-blade phase angle are presented. Reduced frequency (k) is one of the important parameters for unsteady flow problems. The physical significance of this parameter is how quickly the unsteadiness disturbs compared with how quickly the flow information convects over a reference length. For blade flutter, reduced frequency is defined as

$$k = \frac{\omega C}{V_{ref}} \tag{1.1}$$

Here $\omega = 2\pi f$ is the angular frequency of the unsteadiness, which is caused by blade vibration for blade flutter, f is the physical frequency of blade vibration, C is the blade chord length, V_{ref} is a reference velocity, usually taken to be the flow inlet velocity. When modelling an unsteady flow problem, one must ensure that the reduced frequency is the same as that in the real case. If the reduced frequency is smaller than 0.1, the time length scale of disturbance can be much larger than that for flow particles to be convected over the reference length, and the flow can be regarded as quasi-steady, while for the situation of $k > 0.1$, the unsteady behaviour is dominant. For blade flutter, a typical value of the reduced frequency for the first bending mode is about 0.3, while that for the first torsion is around 1.

The reduced frequency is the most important design parameter for blade flutter and used in the empirical 'design rules' to predict and avoid flutter. In this empirical method, the reduced frequency at design speed is limited to be above certain critical values (e.g. $k > 0.2$ for the first bending and $k > 0.6$ for the first torsion mode) and is not to be exceeded in order to be free from flutter.

The other important parameter for blade flutter is inter-blade phase angle, σ, defined by Lane (1956). Compared with isolated wing flutter, the difference of turbomachinery blade flutter is the interference from adjacent blades in a stage, which includes the structural and aerodynamic coupling. The structural coupling is uniquely different in turbomachines, being strongly affected by the blades' attachments to the hub or to each other. The aerodynamic coupling amongst the blades in a vibrating annular row is extremely complex and depends on many governing parameters, the most important of which is the inter-blade phase angle. Lane (1956) showed that if all blades are identical and equally spaced around the rotor, and that linearity holds, adjacent blades usually vibrate with a constant phase angle difference σ, i.e. the upper blade oscillates with a phase σ lead to the lower blade, where σ is defined as positive for an equivalent forward-travelling wave around the rotor for compressors. Typically, this is called 'tuned cascade mode' or 'travelling wave mode'. The inter-blade phase angle can only take on discrete values. If N_B is the total number of blades in one blade row, then there will be N_B possible values of inter-blade phase angles:

$$\sigma = \frac{2\pi n}{N_B} \qquad (n = 0, 1, 2, \ldots, N_B - 1) \tag{1.2}$$

Here, n is the number of circumferential nodal diameters (the diametric lines of zero displacement) of the vibration mode. Lane (1956) also proved that the critical 'flutter point' could be found at the inter-blade phase angle where the aerodynamic excitation is the largest, usually called the least stable inter-blade phase angle. In order to find out the aeroelastic stability characteristics of a blade row, all possible inter-blade phase angles have to be calculated.

The results of the empirical method offer little to enhance the physical understanding of blade flutter problems. However, with the rapid development of computational techniques, Computational Fluid Dynamics (CFD) has become an acceptable numerical prediction tool. For flutter stability prediction, it is important to predict accurately and efficiently the unsteady aerodynamic responses of oscillating turbomachinery blades. There are two general kinds of numerical methods developed for this particular area. One is nonlinear time-marching solutions operating in the time domain and the other is time-linearised methods operating in the frequency domain. They will be reviewed in Chapter 2. Successful unsteady aerodynamic methods must be capable of predicting important flow features, such as viscous effects and three dimensional (3D) effects.

With the requirement of reducing fuel consumption as well as engine size and weight, future propulsion systems will require compressors with higher pressure ratios and efficiencies than those currently in use. The development of materials technology and stressing techniques allows high rotational speeds to achieve high efficiency for a single stage of blading. This implies that compressor blades frequently meet air flows in transonic regimes for their high performance. In a transonic flow, viscous effects play an important role in establishing the steady flow, e.g. the boundary layer blockage determines the location of passage shockwaves. In addition, the range of shock motion associated with blade vibration strongly depends on the unsteady perturbation of the boundary layer. Even for a subsonic flow, it is well known that the most common and serous blade flutter is stalled flutter, which is associated with oscillations of separated flow. To directly simulate the turbulence is far beyond the computer capability available today. In practice, Reynolds-averaged Navier-Stokes equations are solved for unsteady viscous flows. The Reynolds-averaging indicates the mean turbulent effect averaged over the short turbulent time scales. The extra turbulence Reynolds stresses are modelled directly using the semi-empirical steady flow turbulence models (e.g. the widely used mixing length models). Time-linearised unsteady aerodynamic approaches are widely used in practice due to their high computational efficiency. However, the linear assumption limits their applications in transonic flows and separated flows, where the nonlinear features are obvious. The ability of these numerical methods to accurately predict the viscous effects on both steady and unsteady aerodynamics of oscillating blades is still questionable. Experimental tests with detailed measurements therefore play an essential role in providing the physical understanding and the test data for validation of numerical methods in these particular areas.

The flow through blade rows in axial-flow compressors is generally three dimensional, e.g. hub and tip boundary layer, passage secondary flow, and tip leakage flow, etc. In terms of blade flutter, the modal shape of blade vibration is 3D in space. Hence, the 3D aerodynamic feature of blade flutter becomes very important in understanding and prediction of this problem. However, all published experimental studies with detailed data have been limited to two dimensional (2D) sections with the data typically taken at the midspan of blades. In order to apply 2D theory to the aeroelastic problems of real blade systems one must either use a representative section analysis or else apply strip hypothesis with the assumption that the aerodynamics at one radius is uncoupled aerodynamically at any other radius. The 2D modelling (used strip theory) was indicated computationally to lead to the unreliable prediction of aerodynamic damping by Hall & Lorence (1993), and now 3D CFD methods including time-marching and time-linearised approaches with various assumptions have gone far beyond what the 2D experimental data can offer in terms of validation. While, some measurements have been obtained from instrumented high speed rotating rigs (e.g. Halliwell *et al.* (1984)). These lack sufficient resolution to determine the unsteady aerodynamic responses of blades oscillating in 3D modes. Thus, 3D oscillating cascade test data are needed for CFD developers to understand the physical significance of the real 3D unsteady flow field, to establish the limitations and the range of applicability, and also to indicate the improvements in these analytical models. There have also been attempts to obtain a detailed 3D experimental data on unsteady flows around a single oscillating turbine blade in a profiled channel as documented in Bell (1999) and Queune & He (2001). With regard to validation of 3D unsteady flow methods for blade flutter prediction, the emphasis should be put on the 3D aspects as well as blade-to-blade interaction in order to explain several hitherto unknown phenomena. In this context, it is worthwhile to note that there has not been a published 3D oscillating cascade test case, which can be directly used to validate 3D unsteady aerodynamic methods currently under active development.

In the tip region of compressor blades, the tip clearance cannot be avoided. The mutual interaction of the end-wall boundary layer, the tip leakage flow, the blade passage secondary flow, and the blade-surface boundary layer makes the flow structures very complex there, as shown in **Figure 1.3**. The tip leakage flow is regarded as the multiple tip vortex structure consisting of a tip leakage vortex, a tip separation vortex, and a separation vortex shown in **Figure 1.4** from Kang & Hirsch (1993). It is noted that the flow inside the tip-gap is strongly 3D across almost the entire chord length. The 3D tip leakage flow is now recognized as an important source of loss and is believed to closely relate to the onset of rotating stall in compressors. Due to the relative large vibration amplitude at the tip, the tip section gives a significant contribution towards aerodynamic damping for aeroelastic problems. However, the influence of tip clearance on aeroelastic response (blade aerodynamic damping) of oscillating cascades in a 3D oscillation mode is still unknown, which becomes a barrier for more reliable designs and accurate prediction methods to be developed. In order to gain insights into the effect of tip leakage flow on compressor aeroelastic characteristics and to identify the corresponding unsteady CFD modelling requirement, detailed measurements of unsteady pressure responses of an oscillating cascade at different tip clearances are required.

Aeroelastic experiments normally are conducted in two kinds of models: free flutter and driven flutter. In free flutter, blades are elastically mounted on high speed rotating machines to identify blade flutter margins and aerodynamic stability conditions. While in driven flutter, blades vibrate in a controlled, harmonic vibration mode and the induced unsteady flow field can be investigated and the unsteady pressure/aerodynamic damping can be measured. All blades vibrate at the same amplitude, the same frequency and the constant inter-blade phase angle, which is called the travelling wave mode vibration or a tuned cascade according to Lane's phase angle theorem. In a linear cascade, there is a difficulty to maintain the blade-to-blade periodicity of the unsteady flow when the travelling wave mode vibration is used, in which all blades are driven, due to the effect of wind tunnel walls as documented by Buffum & Fleeter (1993). This difficulty can be avoided by using the Influence Coefficient Method proposed by Hamamura *et al.* (1980) based on a single

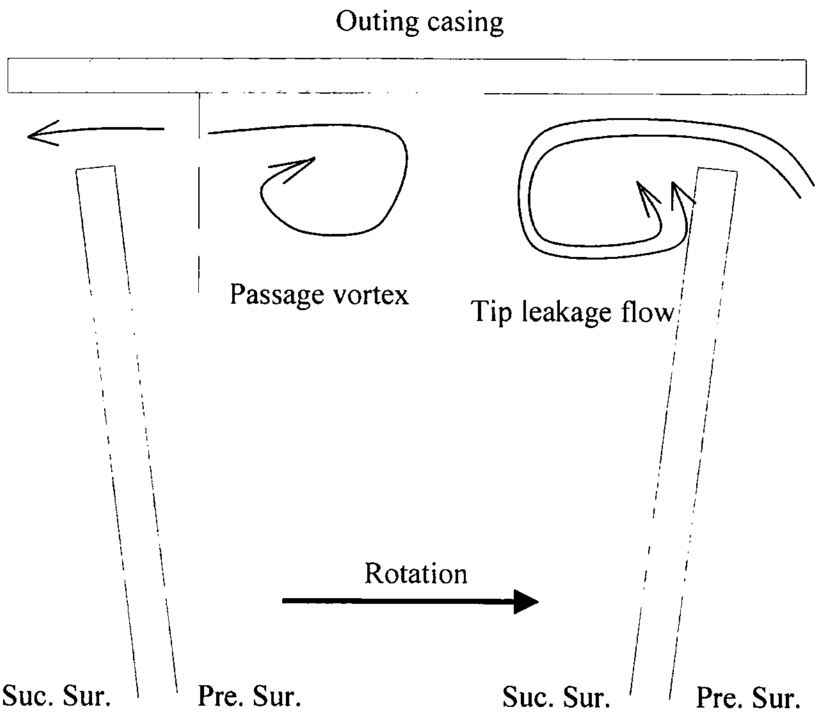

Figure 1.3: Schematic of vortex structures near the tip region of compressor blades

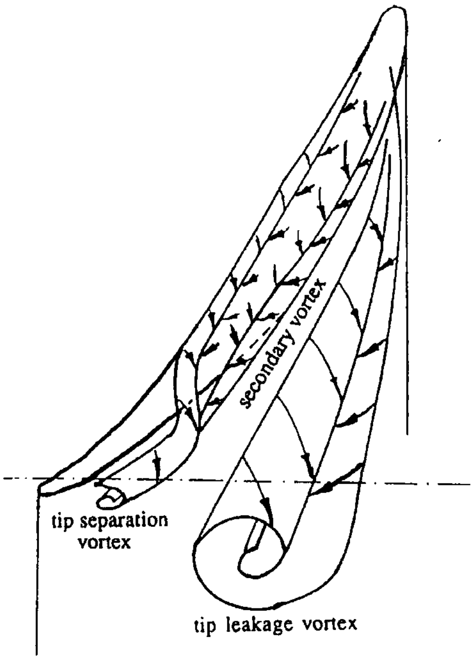

Figure 1.4: Schematic of tip leakage flow from Kang & Hirsh (1993)

driven blade. The unsteady pressure responses induced by the oscillating blade on all blades are measured and are linearly superimposed to get the unsteady aerodynamic response of a tuned cascade at a specific inter-blade phase angle.

1.3 Overview of Project Work

The present work is motivated by the need for enhancing current understanding of blade flutter phenomena with the consideration of 3D effects and blade-to-blade interaction, for providing 3D oscillating cascade test data for validation of numerical prediction methods, and for examining the ability of a 3D time-linearised method to capture the relevant unsteady aerodynamics. In this experimental and computational study, the unsteady flow around a tuned cascade oscillating in a 3D bending mode is investigated in depth using the Influence Coefficient Method. The research project documented in this thesis is broken into four parts.

In the first part of the work (Chapters 3-5), the test facility is described and discussed with special emphasis on the philosophy behind the design. The experimental methods and techniques adopted for the steady and unsteady flow measurements are presented and evaluated.

A low speed flutter test facility with a linear cascade of seven prismatic compressor blades has been purposely commissioned for this investigation, which is described in detail in Chapter 3. To simplify the test facility, the Influence Coefficient Method is used for the superimposition of the unsteady pressures for a tuned cascade with one blade driven in a 3D bending mode. The use of off-board pressure transducers enables detailed measurement of the unsteady blade surface pressures at low cost. The tubing distortion caused by the tubing system, which connects the pressure taping and the pressure transducer, is corrected effectively by the Tubing Transfer Function technique.

In Chapter 4 the experimental procedure is specified and the validity of the experimental technique is examined. An evaluation of experimental errors and repeatability provides further justification of the approach used.

In Chapter 5 the blade-to-blade periodicity of the steady flow is adjusted to a reasonably uniform level to offer a sound aerodynamic baseline for unsteady pressure measurements. The validity of the Influence Coefficient Method for the present case is examined.

In the second part of this project, shown in Chapter 6, a complete set of unsteady pressure measurements is presented and discussed. The aeroelastic stabilities of a tuned cascade for all inter-blade phase angles are examined over a range of reduced frequencies. The unsteady pressure responses of oscillating blades superimposed by the Influence Coefficient Method are investigated comparing with that induced on the oscillating blade. The results, which are provided for six spanwise sections (between 20% and 98% span), clearly show a 3D behaviour of unsteady flow and the significant influence of the inter-blade phase angle on the cascade stability. The influence of the 2D bubble-type separation on the aeroelastic stability of the oscillating cascade is identified. The present results provide a detailed 3D oscillating cascade test case, which can be used for validation of advanced numerical methods and represent the first of their kind.

The third part of this work, presented in Chapter 7, is concerned with the influence of tip leakage flow on the unsteady aerodynamic responses of oscillating compressor cascade. This has a practical implication for compressors. In order to check the importance, the steady and unsteady blade surface pressures are investigated over three settings of tip-clearance gap. The steady flow measurements also provide the aerodynamic background for the unsteady flow measurements. The stability of the cascade is decreased with increasing the tip-gap and the influence of tip clearance on the unsteady aerodynamic responses is seen on the most of blade span. To the author's knowledge, this is the first work to address the influence of tip leakage flow upon the unsteady aerodynamic responses of a 3D oscillating cascade.

The fourth part of this study presented in Chapter 8 deals with the computational phase of the investigation. The principle objective here is to evaluate the ability of the 3D time-linearised method to capture the relevant unsteady aerodynamics exhibited by the experimental data. The computational results and the accompanying discussions are also intended to provide further insight into the behaviour of the unsteady flow due to blade vibration. The first part of Chapter 8 describes the basic computational method, the parameters and conditions for the computational study. Following this, a series of steady and unsteady flow predictions is presented and discussed. Throughout some specific inter-blade phase angles, very good agreement is demonstrated between predicted unsteady pressures and experimental data, although some discrepancies are observed in the regions where the unsteady aerodynamics of a separation bubble is believed to be influential.

The conclusions of the investigation are brought to Chapter 9, where some recommendations for future work are also proposed.

Chapter 2

Review of Previous Work

This chapter describes previous development of understanding and prediction of unsteady flows around oscillating blades in turbomachines, with emphasis on research particularly relevant to the present work in order to highlight the present motivation. The detailed review of aeroelastic problems in turbomachinery through both experimental and numerical investigations can be found in Fleeter & Jay (1987), Sisto (1987), Bendiksen (1990), Verdon (1993), Srinivasan (1997) and He (2003).

2.1 Background

Blade flutter has been a challenging problem to designers of turbomachines in the subject area of aeroelasticity since the 1940s with the first aeroelastic failure of compressor and turbine blades reported by Shannon (1945). Early attempt to predict and avoid blade flutter was empirical 'design rules' based on previous single wing experience with stalled flutter. This empirical method emphasized identification of flutter stability boundaries and susceptible aerodynamic conditions on an existing machine. Flutter boundaries were established for each flow regime by correlating reduced frequency at a specific blade spanwise section with relative Mach number or incidence angle (Mikolajczak 1976). This method is insufficient to provide a physical insight into the unsteady behaviour of a real flow, such as three dimensional effects and viscous effects. Thus, the results of the empirical method are often unreliable for use in the development of new machines. With the development of computational techniques, CFD tools have become useful methods to predict unsteady flows around oscillating blades with the inclusion of real flow features. However, it is not possible to rely entirely on numerical calculations due to assumptions on the behaviour of flow in numerical models. It has been realized that accurate predictions of blade flutter using empirical methods or CFD methods depend on the quality of experimental data to improve the basic physical understanding.

2.2 Experimental Research

Experimental research directed at blade flutter typically has two overall objectives. They are to generate a flutter boundary database to form the empirical correlations and to acquire experimental data to validate analytical models for flutter prediction. Experimental data for unsteady flow around oscillating blades in turbomachines can be obtained in three types of experimental facilities. They are high speed rotating machines (full scale or model), stationary annular cascades and linear cascades. Main contributions/findings and limitations of every experiment associated with each type of facilities will be addressed. It follows underlying experimental methodologies used for investigating blade flutter, together with inherent assumptions made for each type of test models.

2.2.1 High Speed Rotating Machines

High speed rotating machines include full scale (ranging from single stage rig to full engines) and model rigs. The high speed rotating machines are more realistic vehicles and reproduce all basic aerodynamic and mechanical conditions for blade flutter experiments. The true behaviour of oscillating blades can be measured to determine flutter stability margins, and to provide some meaningful data for empirical correlations. The data from this kind of experimental work are also the ultimate benchmark for the examination and validation of computational prediction methods as well as the final test of advanced concepts. Although sophisticated design analysis tools are used, the test validation of new engine designs will still be required. The experimental work can be performed on both free flutter and driven flutter models.

It is known that flutter will occur if the sum of aerodynamic damping and mechanical damping is less zero. If the mechanical damping is negligible, aerodynamic damping indicates flutter stability. The accurate prediction of aerodynamic damping requires the accurate predictions of vibration frequency, mode shape and unsteady aerodynamic loading. In order to verify structural dynamic and unsteady aerodynamic analyses for new designs, direct measurements of blade motion and unsteady aerodynamic loading in flutter are necessary.

Mode shapes were identified successfully in stationary rotors using optical techniques (e.g. Mikolajczak *et al.* (1975)). Holography of a fan blade-disk assembly with part-span shrouds showed the blades vibrated in a second mode (two concentric rings of zero displacement) with three nodal diameters (three diametrical lines of zero displacement). However, the measurements on the static disk assemblies can not be used to verify predictions for shroud contact forces of adjacent blades in a real rotating condition. Stargardter (1977) reported his pioneering work for obtaining mode shapes under actual operating conditions using an optical technique. The reflections of laser beams from mirrors mounted on the suction surface of blades at different spanwise sections were used to gather the mode shape of a rotating fan. When the blades were not fluttering, the laser beam reflected from each mirror went back to a same position on a display screen for every revolution of the rotor, however, when the blades were fluttering, the laser beam went back to a different position for each revolution. Using this optical technique, the vibration frequency and the magnitudes of the deflection distribution of the rotating fan at stalled flutter were recorded successfully and the second mode of vibration was resolved. However, the nodal diameter and inter-blade phase angle were not resolved due to the low speed of recording methods.

Unsteady aerodynamics is the driving mechanism for blade flutter. So unsteady surface pressure data are required for the validation of unsteady aerodynamic analyses. They were obtained in rotating facilities both in free flutter and driven flutter models. For the free flutter model, unsteady pressure data at one blade tip section were measured by Halliwell *et al.* (1984) for a shrouded transonic fan in unstalled supersonic flutter. The results showed that a shockwave played an important role in determining the aeroelastic stability in terms of its position and the unsteady response of the shock. Sanders *et al.* (2003) recorded unsteady aerodynamic loading distributions at stalled flutter regimes in the tip section (90% span) of a shroudless transonic fan blisk (bladed disk assembly). The experimental unsteady pressure results were used as the benchmark data to guide the validation of an unsteady 3D viscous time-marching approach. The influences of tip-clearance and vibration amplitude on unsteady loading predictions and flutter boundary predictions were identified. For the driven flutter model, the Influence Coefficient Method was used in rotating facilities to simplify experimental set-ups. Frey & Fleeter (2001) used this experimental model to obtain unsteady surface pressures of a rotating compressor blade row in torsion mode. The results showed that oscillating amplitude and steady aerodynamic loading had significant effects on the unsteady aerodynamics of oscillating blades. In general, Increasing oscillating amplitude and steady loading resulted in reduced amplitudes of unsteady pressure and larger chordwise phase shifts. The results also indicated that significant higher harmonic, nonlinear effects need to be considered to determine unsteady aerodynamics for flutter and forced response at high amplitudes of oscillation. However, the unsteady pressure data measured at one spanwise section in these rotating facilities lack sufficient information to determine the unsteady aerodynamics of oscillating blades in 3D vibration modes.

There are certain disadvantages of expense and complication to perform tests on high speed rotating facilities. First of all is large amount of energy is needed to run machines. Secondly, it is difficult for detailed instrumentation to pick up blade vibration levels and unsteady aerodynamic responses and only permits sparse instrumentation without alternation of normal flow patterns. Thirdly, the extreme environment provided by these facilities, rotating, gives a challenge to instrument. Due to bonding failures, useful data were only obtained from 5 of 12 mirrors in a rotating fan reported in Stargardter (1977). High response miniature pressure transducers are required for this type of work. Manwaring *et al.* (1997) had experience of pressure transducer failure during testing of a low-aspect ratio transonic fan due to severe centrifugal forces. At high speeds, only 5 of 14 transducers had survived. Finally, detailed calibrations are required to be conducted to minimise the sensitivity of high response pressure transducers to temperature, acceleration and installation, e.g. Manwaring & Wisler (1993) and Manwaring *et al.* (1997). In addition, the requirement for a slip-ring or telemetry system to transmit signals to a stationary frame introduces additional complexity. The detailed survey of unsteady measurement techniques on rotating facilities can be found in Gallus (1987) and Kielb (1999b).

A high speed model rotor can be used as one alternative test vehicle to reduce cost. These facilities have been successfully exploited to acquire unsteady pressure data in the driven flutter model (e.g. Hardin *et al.* (1987), Frey & Fleeter (2001)) and have also qualitatively demonstrated the ability to provide flutter boundaries for a prototype full size fan as shown in Fleeter & Jay (1987).

In general, high speed rotating facilities are not a predictive tool and not applicable in engine development stages. Finally, it should be rememebered that the number of publications and experimental technologies reported in high speed rotating machines is unlikely to be a true reflection of past or present research due to the nature of commercial sensitivity.

2.2.2 Cascade Facilities

Cascade facilities for aeroelastic experiments in turbomachinery simplify structural features of a rotating blade row, which tend to emphasize aerodynamic information related to aeroelastic problems rather than the structural one. However, many specific parameters like mistuning, absolute flow conditions cannot be reproduced exactly in a wind tunnel as in a full-scale machine. Therefore, cascade tests are normally performed to study some basic aeroelastic phenomena by obtaining unsteady aerodynamic pressures and moments acting on vibrating blades. The results are used to study parameter trends to enhance physical understanding and to validate numerical methods, e.g. the well documented test database in Bölcs & Fransson (1986). Generally cascade facilities are divided to annular and linear types. The detailed review on aeroelastic cascade facilities and aerodynamic measurements can be found in Fransson (1999b).

2.2.2.1 Annular Cascades

Annular cascade facilities share most important qualities exhibited by high speed rotating facilities, the very importance of which is infinite. They can establish periodic steady flows automatically around annulus, which is especially important in supersonic inlet flows with 'unique incidence'. They can simulate the flow through a rotating machine more realistically than linear cascade facilities with reduced cost and increase flexibility as compared with rotating rigs. The facilities provide easy instrumentation due to the absence of centrifugal forces and easy data acquisition due to non-rotating blades.

Several researchers have measured unsteady aerodynamic pressures and moments due to blade vibration using annular turbine or compressor cascades in subsonic or transonic flows to reveal flow mechanism causing blade flutter. Kobayashi (1984) investigated unsteady aerodynamic forces in the travelling wave mode in an annular turbine cascade. The cascade flutter occurring in high subsonic flow was demonstrated to disappear as reduced frequency increased. The results showed that the shock wave movement due to blade oscillation contributed largely to the cascade instability in a transonic flow. In his subsequent work (Kobayashi 1989, 1990), more detailed unsteady aerodynamic pressures generated by shock wave movement were measured in a transonic flow. The effect of unsteady aerodynamic forces generated by shock wave movement changed from destabilisation to stabilisation with increasing reduced frequency for a compressor cascade, while for a turbine cascade, inter-blade phase angle controlled the effect of unsteady aerodynamic forces induced by shock wave movement. The stabilising effect of shock wave movement in the turbine cascade at inter-blade phase angle -90° was consistent with the observation in the Fourth standard configuration for the low supersonic exit March number documented in Bölcs & Fransson (1986). Furthermore the unsteady aerodynamic influence coefficients decomposed from travelling wave test data using the Influence Coefficient Method gave some insight into the reasons for the flutter susceptibility of an oscillating cascade in a transonic flow as presented by Fransson (1990). He pointed out that the instability arose due to the unsteady aerodynamic coupling effects between the reference blade and its adjacent suction surface blade, to a lesser extent, the pressure surface neighbour.

To simplify experimental set-ups, the Influence Coefficient Method was also used to obtain the unsteady aerodynamic pressure response for a tuned cascade at a specific inter-blade phase angle, e.g. Ehrlich & Fleeter (1994), Körbächer & Bölcs (1994), Nowinski & Panovsky (1998) and Ehrlich & Fleeter (2000). However, the Influence Coefficient Method is limited by its linear assumption, and its validity is needed to check for the flow concerned. Generally, separated flow, shock wave movement due to blade vibration, and shock-boundary layer interaction are possible sources of nonlinearity. The linearity was experimentally checked for a compressor annular cascade by Körbächer & Bölcs (1994) and for a turbine annular cascade by Nowinski & Panovsky (1998). Körbächer & Bölcs (1994) investigated the unsteady aerodynamics of compressor blades excited in both single blade vibration mode and travelling wave mode to evaluate this technique. The results showed that the superimposition principle was valid for a flow case with a low incidence angle and a high subsonic inlet Mach number with a small supersonic zone on the suction surface but with no shock waves. Nowinski & Panovsky (1998) studied the unsteady aerodynamics of a low-pressure turbine cascade to improve overall understanding of flutter mechanism and to identify key flutter parameters. Several types of unsteady tests were conducted including travelling wave and single blade modes to experimentally evaluate this technique. The travelling wave results demonstrated that the front half of blades played an important role in determining the overall stability of oscillating blades. The adjacent blades gave significant contributions to the cascade stability, which vary significantly by changing mode shape, thus mode shape became the most important flutter parameter for this turbine cascade, reduced frequency was the second important, and to a lesser extent, steady blade loading. For nonlinear separation events, the Influence Coefficient Method was demonstrated its limitation as shown in Ehrlich & Fleeter (2000).

Comparing with linear cascade facilities described below, annular cascade facilities have obvious disadvantages. They are more expensive than linear cascades to build and not easy to instrument for small blades.

2.2.2.2 Linear Cascade Facilities

Linear cascade facilities consist of a number of blades situated in a plane. Such facilities are sometimes also called rectilinear or 2D cascades. Linear cascades have fewer blades comparing with annular cascades, which make it less expensive and allow large blades to be used. The large scale with 2D geometry enables detailed instrumentation for equivalent cost, and also provides a favourable condition for flow visualizations. Lack of centrifugal stress allows static pressure tapings or high response pressure transducers to be located much nearer the leading and trailing edge regions of blades than in a rotating environment. This allows more accurate quantification of both steady and unsteady flow fields obtained.

The other advantage of linear cascades is of simplicity: simple rig design, simple instrumentation, and simple analyses and interpretation of experimental results. This is what makes linear cascades widely used tools for research. The most easily varied parameters are flow speed, incidence, frequency of vibration, chordwise position of the pitching axis (torsion modes) and pressure ratio.

Linear cascade facilities were used to identify aeroelastic stability parameters, e.g. Carta & St. Hilaire (1978; 1980). They investigated the unsteady aerodynamics of an oscillating cascade in the travelling wave mode near stalled flutter including the effects of vibration frequency, inter-blade phase angle and incidence. The results indicated that the unsteady pressure activity was concentrated within the first 10% blade chord and inter-blade phase angle was the most important parameter affecting the aeroelastic stability of the oscillating cascade. The stability of the system was changed directly as altering inter-blade phase angle. The results also showed that unstable conditions were experienced with no indicators of stall. This finding supports the conclusion presented in Mikolajczak *et al.* (1975) that stall is not an essential condition for 'stalled' flutter. The strong effect of inter-blade phase angle on aeroelastic stability was also demonstrated by Buffum & Fleeter (1990) in investigating the unsteady aerodynamics of an oscillating cascade in a transonic flow.

The Influence Coefficient Method was firstly proposed to superimpose the unsteady pressure response for a tuned cascade in a linear cascade by Hanamura *et al.* (1980). This technique was used to measure the induced unsteady pressure responses of blades in a water channel. The results appeared to evaluate the Influence Coefficient Method for a small vibration amplitude in torsion mode. This method was also evaluated experimentally for oscillating biconvex blades in a linear cascade by Buffum & Fleeter (1988) and for sub/transonic flutter of fan blades in a linear cascade by Szechenyi (1987). Buffum & Fleeter (1988) found a good agreement between the data from the Influence Coefficient Method and those from the travelling wave mode for torsion flutter at moderate subsonic Mach numbers. The results have indicated the validity of this method for attached flow for cases with negligible influence of tunnel sidewalls and for unsteady flows that were not in vicinity of acoustic resonance excited by the oscillating blade. In their later investigation, Buffum & Fleeter (1994) pointed out the Influence Coefficient Method was of limited usefulness for compressible flow due to the detrimental effect of wind tunnel acoustic modes and suggested that this problem could be rectified by acoustic treatments. For a transonic flow with strong shock waves, Szechenyi (1987) performed two dimensional unsteady aerodynamic experiments for cases in which the shock wave was attached to the leading edge of blades, and found shock wave oscillation to be the dominant contribution to the aeroelastic instability. However, the experiment with a detached shock wave was not successful because it was too difficult to achieve a blade-to-blade steady periodic condition in the cascade for a high speed flow.

Good blade-to-blade steady flow periodicity is difficult to generate in linear cascades due to the finite extent of cascades and the boundaries introduced by wind tunnel walls especially under transonic operational conditions with shock waves, e.g. Lepicovsky *et al.* (2001). In order to regulate the downstream steady flow periodicity the reflections of shock waves by the tailboards were decreased by using the slotted or perforated ones as documented in Ott *et al.* (1998).

Another area of concern is cascade dynamic periodicity - blade-to-blade variation in unsteady surface pressure. Carta (1983) was the first researcher to investigate the dynamic periodicity of a linear oscillating cascade. Good dynamic periodicity was generally found except for in-phase oscillations, where circumferential gradients in phase angle of unsteady pressure response were found. Carta (1983) gave a plausible explanation of acoustic resonances in the cascade. The influence of the reflection of wind tunnel walls on the dynamic periodicity was presented by Buffum & Fleeter (1993) in investigating the unsteady aerodynamics of a linear oscillating cascade in a subsonic flow. The results showed that the cascade dynamic periodicity was poor for some values of inter-blade phase angle due to cascade produced pressure waves reflected by the wind tunnel walls interfering with the cascade unsteady aerodynamics. The solid tunnel walls were replaced with the porous walls to absorb the acoustic waves. However, for the transonic flow with shock waves as presented in Ott *et al.* (1998), the slotted tailboards created some perturbations for the unsteady pressure measurements and had to be replaced by the solid ones.

Under a typical Reynolds number a separated flow region is often found on blade surfaces in turbomachinery, which influences unsteady pressure distributions. The unsteady behaviour of the bubble-type separated flow was investigated in a compressor cascade by Buffum *et al.* (1998) and in a turbine cascade by He (1998). Buffum *et al.* (1998) recorded the unsteady aerodynamics of a cascade oscillating in a travelling wave torsion mode for both attached and separated flow. Cascade dynamic periodicity was experimentally found to be good for both attached and separated flow conditions. For the large mean incidence angle, separated flows near the leading edge (around 40% chord) on the suction surface have strongly destabilising influences, which increased with reduced frequency for the inter-blade phase angle 180°, while the attached flows have strongly stabilizing influences. The influence of the bubble-type flow separation on the unsteady aerodynamics of turbine blades oscillating in a torsion mode was investigated by He (1998) using the Influence Coefficient Method. A short separation bubble (about 10% - 15% chord) near the trailing edge on the suction surface of turbine blades had a local effect with a destabilizing effect in the separated flow region and a stabilizing effect in the downstream reattachment point.

However, a large leading edge separation bubble (more than 60% chord) on the pressure surface affected the unsteady pressure distribution substantially.

Linear facilities are inhibited by their finite nature. The flow path is not 'closed' in the circumferential direction. The finitude of linear cascades precluded free flutter testing as a means of measuring a rotor flutter boundary in these facilities, as shown in Snyder & Commerford (1974). The results indicated the poor correlation of the supersonic unstalled flutter boundaries of a linear cascade with the high speed rotor.

2.2.3 Low Speed Facilities

It has been recognized that experimental testing of oscillating blades in realistic high speed transonic flow conditions is a very challenging task. There are four aspects associated with this.

1) Difficulty in flow periodicity for transonic flows

The particularly serious problem currently encountered in flutter experiments operating at transonic speeds is the difficulty of establishing a spatially periodic steady (mean) flow and a temporally periodic unsteady flow. For a small inter-blade phase angle, acceptable periodicity is needed over more blades in the travelling wave mode vibration. Ott *et al.* (1998) demonstrated a non-periodic steady transonic flow, in which normal shocks were located on different positions on different blades in a linear cascade. It is easier to establish the periodicity of steady and unsteady flows in low speed flows.

2) Blade pressures exhibit very strong self-induced oscillations in high speed flows

There was the coexistence of self-induced pressure unsteadiness with large magnitudes without driven blade vibration in high speed flows, as indicated in the experimental investigation of Lepicovsky *et al.* (2002) in a transonic fan cascade. The magnitude of the unsteadiness on neighbouring stationary blades strongly depends on inlet Mach number and vibration frequency, whose source is uncertain (likely to be acoustical resonance). For a low speed flow, this problem is not encountered.

3) Difficulties in blade driven system for high speed flows

In order to reach realistic reduced frequencies and simulate transonic aerodynamic flow fields in turbomachines, a high speed inlet velocity requires high vibration frequencies in the order of 300 ~ 1000Hz. It is generally very difficult to realize these high frequencies with measurable amplitude due to the power needed, which is in proportion to the square of angular frequency of blade vibration (Fransson & Borg 1992). The actual blade vibration amplitude and inter-blade phase angle could not always be kept constant in time and were fluctuated around pre-set values because of flow perturbations (e.g. Fleeter *et al.* (1977)). These fluctuations affected the accuracy of unsteady aerodynamic pressure measurements.

For low speed flows, the situation was relaxed, see example Carta & St. Hilaire (1978). It is simple to construct an oscillation mechanism that can control blade vibration at low frequencies and reasonably high amplitudes. For a very low speed, a reasonably high reduced frequency was achieved with a low blade vibration frequency (less 20*Hz*) as shown in Bell (1999) and He (1998).

For a single blade vibration using the Influence Coefficient Method in high speed flows, the validation of the Influence Coefficient Method was a challenging task due to the unsteady pressure disturbances created by wind tunnel acoustic modes, which were excited by the oscillating blade, as demonstrated by Buffum & Fleeter (1994). The combination of the Influence Coefficient Method and low speed flows is at its most favourable in a linear cascade.

4) Measuring techniques for unsteady pressures

The measurement of unsteady flow with high frequency of blade vibration presents further challenges. The induced unsteady blade surface pressure is difficult to obtain due to temporal and spatial resolutions. Uncertainties are expected from the fact that the unsteady pressures are fairly small and the signals have a high noise level. Unsteady pressure data obtained are only 'most probable values'.

Miniaturised high frequency response pressure transducers are usually embedded at discrete locations on blade surfaces to record the induced unsteady pressures. Blade chord and thickness limitations of model blades as well as cost make it impossible to put more pressure transducers on blade surfaces, normally less than 10 at one spanwise section on one blade surface. This number is not sufficient for a good representation of unsteady pressure distribution and hence of aerodynamic damping obtained by integrating the unsteady pressures over blade surfaces. It is recognized that uncertainty in the stability results for high speed flow experiments is greater than that for low speed flow experiments because of the limitation in the number of pressure transducers used to acquire unsteady pressure data. In order to meet the requirement of spatial resolution of the unsteady flow measurements on blade surfaces, various optical measurement techniques were developed, for example pressure sensitive paints (Gregory *et al.* 2002), doppler sensors (Daoud & Naguib 2003), micromachined fabry-perot pressure sensors (Miller *et al.* 2000). However, every method required a complicated optical technique and expensive equipment. This dilemma can be avoided by using off-board pressure transducers. Low frequencies of controlled vibration in low speed flows enable off-board pressure transducers to be used for unsteady pressure measurements. The use of off-board pressure transducers enables more detailed pressure tappings made on the whole blade surface and less pressure transducers used. Off-board pressure transducers have been applied in low speed flutter experiments successfully as shown in Bell (1999), He (1998) and Queune & He (2001). However, the tubing system, which connects off-board pressure transducers and pressure tappings on blade surfaces, introduces the distortion to unsteady pressure signals. This distortion of the tubing system on the unsteady signal in the area of turbomachinery aeroelasticity either largely was neglected because of low frequencies and short tubing lengths (He & Denton 1991) or simply was corrected to directly measure the phase lag and amplitude change for a certain tubing length (Bell & He 2000). For higher flow velocities at more realistic conditions, high physical frequencies are required to reach the realistic reduced frequencies. If off-boarded pressure transducers are applied to measure unsteady pressure signals, they must be distorted by the pressure measurement system and a correction must be carried out for the unsteady data processing. A Tubing Transfer Function approach involving a frequency domain correction was described in (Yang *et al.* 2003) for the unsteady distortion of a pressure measurement system.

Another benefit from low speed facilities is that natural frequencies of blades can be much higher than blade vibration frequencies in the driven flutter model. Hence the natural vibration modes of blades in a low speed cascade will not be excited, when the blades are driven to oscillate. The input of blade displacements to aerodynamic damping calculations is then well defined.

2.2.4 3D Experimental Work in Low Speed Facilities

The previous experimental studies were mostly for 2D unsteady flow problems related to oscillating blades and only a few experimental studies on 3D unsteady flow problems have been carried out ((Bell 1999); (Queune & He 2001)). The unsteady aerodynamic response of a single turbine blade oscillating in a three dimensional bending mode was investigated by Bell (1999). A significant 3D behaviour of unsteady flow around an oscillating turbine blade was indicated by the feature that the amplitude of unsteady pressure at different spanwise sections was not proportional to the local vibration amplitude. The single blade configuration ignored all forms of inter-blade coupling and assumed that each blade flutters just as it would be in the absence of all other blades. Based on the same test rig, Queune & He (2001) investigated the 3D unsteady aerodynamic response of a turbine blade oscillating in a bending mode with high tip separation. The results demonstrated the destabilising effect of the tip separated flow on the aeroelastic stability and a predominant linear behaviour of the unsteady pressure response. In real situations, the flow encountered in compressors is highly 3D and blades oscillate in aerodynamic coupling environment. Until the production of this thesis, there is still no 3D oscillating cascade test data available.

2.2.5 Influence of tip leakage flow on Unsteady Flow around Oscillating Blades

Major efforts have been made to investigate tip leakage flows from both experimental and theoretical points of view. In the context of 3D flows through blade rows in axial compressors, there were many reported researches on the effects of tip leakage flow on aero-thermal performance and flow stability, e.g. Hoying *et al.* (1999), Kang & Hirsch (1993), and Pandya & Lakshminarayana (1983). The tip leakage flow is now recognized as an important source of losses in the endwall region, which comprise a substantial proportion of total losses. In addition to increasing losses, the tip leakage flow alters blade loading in the tip region thereby affecting the flow turning ability of blades and complicating the design of the blade profile. Furthermore, the tip leakage flow was identified as a source of aerodynamic instability in compressors and fans, see the relative works Hoying *et al* (1999) and Mailach *et al.* (2001). The unstable motion of tip clearance vortex forward of the compressor leading edge is believed to be a mechanism leading to the onset of rotating stall in compressors (Hoying *et al.* 1999). For aeroelastic problems, it is realized that tip sections give significant contributions toward overall aerodynamic damping due to the relatively large amplitude of vibration near the blade tip. Investigation of the influence of tip leakage flow on aeroelastic stability of oscillating blades becomes very important.

The effect of tip leakage flow on blade flutter limits of an annular cascade was documented in the sixth cascade standard configuration compiled by Bölcs & Fransson (1986). In this literature, the unsteady aerodynamic characteristics of a steam turbine annular cascade was investigated in both free flutter and driven vibration modes in five flow conditions, where the outlet Mach number varied from subsonic to supersonic. The flutter limits were shown for three different aerodynamic conditions, which were the well-tuned cascade with endplates at the tip of blades to decrease the tip-clearance effect, well-tuned cascade without endplates and mistuned cascade. It was concluded that the mistuning damped the blade vibrations while the tip-clearance excited the blade vibrations. However, the results could not explain how the tip leakage flow changed the aeroelastic stability of the oscillating cascade. The tip-clearance effect on the local unsteady aerodynamic response of an oscillating cascade of flat-plates in a 2D bending mode was firstly investigated by Watanabe & Kaji (1988) experimentally. The Influence Coefficient Method was adopted to superimpose tuned cascade data at arbitrary inter-blade phase angle. The results indicated that the tip leakage flow had a destabilizing effect on the unsteady pressure response at large portion of the blade span while it had a stabilizing effect on the unsteady pressure response very near the blade tip where the tip leakage vortex was formed. While in the study of the unsteady aerodynamics of a single blade oscillating in a 3D bending mode reported by Bell (1999), the aeroelastic stability (the aerodynamic damping) remained unchanged with changing tip-clearance although there were the consistent local variations in the unsteady pressure response at the tip section (90% span). The affected chordwise areas corresponded with the regions where the steady flow loading was influenced by the tip leakage flow. However, the tip-clearance effect on aeroelastic behaviour of 3D oscillating cascades with blade-to-blade interaction is still unknown.

2.3 Computational Methods

In order to predict blade flutter boundaries, calculations of unsteady aerodynamic forces and aerodynamic damping of oscillating blades are of great importance to industry. There are two kinds of methods developed parallel for predicting unsteady flows through oscillating blades in axial-flow turbomachines, which are intended to serve eventually as the aerodynamic component of a flutter or resonant stress design prediction system. The first group is nonlinear time-marching solutions and operates in the time domain. The second group is time-linearised calculations and operates in the frequency domain. Generally, the time-linearised methods are much more efficient than the nonlinear time-marching approaches, while the time-marching approaches should be more applicable to complex flow conditions than the time-linearised approaches with fewer assumptions.

2.3.1 Time Domain Methods

In time-marching approaches, nonlinear unsteady equations are discretised on a computational grid and are integrated in time until all initial transients have decayed and a periodic state is reached. This method offers the advantage that nonlinear flows can be modelled including complicated shock structure, shock motion and viscous effects (flow separation and shock-boundary layer interaction), which makes it suitable for viscous and transonic flows. Thus, engineers can get useful insights into the relative importance of nonlinear and viscous effects on unsteady flows associated with blade vibration in turbomachinery through a validated analysis.

The original unsteady time-marching methods used for predicting unsteady flows around oscillating blades were extended from the established steady flow calculations (e.g. Denton (1983)). Over the last two decades, time domain solutions for this application in turbomachinery were developed from the two dimensional inviscid (Euler) analysis (e.g. (Gerolymos 1988); (He 1990)), three dimensional inviscid analysis (e.g. (Gerolymos 1993); (Chuang & Verdon 1999)), two dimensional viscous (Reynolds-averaged Navier-Stokes) analysis (e.g. (Ayer & Verdon 1998); (Grüber & Carstens 1998); (Abhari & Giles 1997)), to three dimensional viscous analysis (e.g. (Sanders *et al.* 2003)).

Time-marching methods can model flow features with less assumptions. However, this method requires large computing resources because a large number of grid points and small time steps are required for time accuracy and numerical stability. For numerical stability, the time-integration step size used in the explicit integration must be fairly small. The maximum allowable time step is governed by the so-called CFL number. Because of this restriction, the size of the time steps is limited roughly by the size of the smallest mesh in the domain. For viscous flows, the mesh is needed to refine near solid surfaces to resolve viscous effects. As a result, computational time is greatly increased. In developing a time-marching method for engineering applications, computing efficiency is the issue of major concerns, which can be improved by reducing the computation domain (e.g. use single passage domain) and/or releasing the time step limitation. In order to overcome the time step limitation especially for unsteady viscous computations, timewise implicit schemes were adopted although they involve a large amount of computing work for matrix inversion as reported by Ayer & Verdon (1998). For blade flutter problems, blades vibrate at a constant inter-blade phase angle, with the upper blade oscillating a phase angle led to the lower blade. Then, the phase-shifted periodic condition allows computations conducted on a single blade passage domain. There are three methods to deal with phase-shifted periodicity for time-marching methods. The first one is direct store method developed by Erdos & Alzner (1977). The flow variables at the periodic boundaries are stored for one period of disturbance. The stored parameters and the current solutions then correct each other according to the phase-shifted periodicity. Large amounts of data storage can be required, especially for lower frequencies. The second one is space-time transformation method developed by Giles (1988). The treatment of the periodic boundaries is carried out by inclining the time plane in the computational domain along the blade pitchwise direction according to a given inter-blade phase angle. This method doesn't require extra data storages compared with the direct store method. However, there is a limit on the time-inclination angles (which allow inter-blade phase angles) by the characteristics of the governing equations. The third one is generalized Shape Correction proposed by He (1992). In this method the temporal shape of an unsteadiness at the periodic boundaries is defined by the coefficients of a Fourier series in time, which exceptionally allows a single passage solution to deal with the coexist of several unsteady turbomachinery flows with their own phase-shifted periodicities.

In most turbomachinery applications Reynolds' number is sufficiently high for viscous effects to be confined to thin boundary layers adjacent to blades and annulus surfaces. In order to include viscous effects and maintain reasonable computational efficiency, an integral form of boundary layer equations to time-marching Euler equations – inviscid/viscous coupled approach - was firstly adopted by He & Denton (1993). Progress was made by calculating the free stream and the boundary layer regions separately and then matching the two. Later, the simplified thin-layer Navier-Stokes solver was developed by He & Denton (1994) to enhance computational efficiency. Under the thin-layer assumption, only the viscous shear stress terms in the direction tangential to solid surfaces were included in the momentum equations.

2.3.2 Frequency Domain Methods

The alternative way to reach great computational efficiency is the use of time-linearised approaches. In frequency domain methods, the flow is assumed to be decomposed into a mean or steady flow and a small unsteady harmonic perturbation flow. The unsteady perturbation flow is described by linear variable-coefficient equations, which are based on the steady flow solutions. Although limited to small perturbation flows, the computational time required for the solutions of frequency domain methods is much less than that for nonlinear time-marching methods, which is the main reason for their wide applications in turbomachinery aeroelastic analyses in industry.

For predicting unsteady aerodynamics around oscillating blades, frequency domain methods had developed from classical small disturbance linear models, linearised potential equations, 2D linearised Euler equations, to 3D linearised Euler and Navier-Stokes equations.

Classical small disturbance linear models (e.g. Verdon (1973; 1977)) assumed the unsteady flow to be a small perturbation to an unperturbed uniform steady flow. The problem was thus reduced to analyze the unsteady aerodynamics of an oscillating cascade of flat plates operating at zero mean incidence. As a result, the unsteady aerodynamic effects, due to blade geometry and incidence angle (steady loading), were not considered. To overcome the limitations of classic small disturbance linear theory, linearised potential models were developed, e.g. Verdon & Caspar (1980). The steady flow was determined as a solution of full nonlinear potential equations and the unsteady flow was governed by linear time-independent equations with variable coefficients which depend on the underlying steady flow. The linearised potential models were only appropriate when the mean flow was irrotational, subsonic or weakly transonic (Verdon & Caspar 1982, 1984).

In order to deal with rotational, transonic, small disturbance flows, linear Euler equation models were developed, e.g. Hall & Crawley (1989), Lindquist & Giles (1994) and Hall *et al.* (1994). Linear Euler equation models have shown the ability to capture the physics associated with unsteady subsonic and transonic flows in both two and three dimensions with high computational efficiency. For unsteady transonic flows, two numerical techniques were used to model shocks: shock fitting and shock capturing. Shock fitting was demonstrated to model accurately the unsteady motion of shocks without the use of excessively fine grids, but with the limited capacity due to complexity (Hall & Crawley 1989), while shock capturing was shown to be more simple with linear schemes in Lindquist & Giles (1994) and Hall *et al.* (1994). Hall & Lorence (1993) identified the three dimensional feature of unsteady flows due to the blade vibration in turbomachinery by using three dimensional linearised Euler analysis. The results demonstrated that strip theory seriously over-predicted the aerodynamic damping of the vibrating blades.

All of these inviscid analyses are not capable of predicting unsteady flows with viscous effects, e.g. flow separations - an important feature of stalled flutter - and the interaction of shock and blade boundary layer. Direct simulations using nonlinear time-marching techniques are very computationally expensive as mentioned in Section 2.3.1. Thus, two dimensional and three dimensional linearised Navier-Stokes models were developed for analysing blade flutter (for example (Clark & Hall 2000); (Holmes & Lorence 1997)) to save computational cost. Three dimensional time-linearised Navier-Stokes solution was shown to give the good accurate prediction of flutter boundary with more than one order faster than the time-marching Navier-Stokes solution by Chassaing & Gerolymos (2000).

2.3.3. Nonlinear Harmonic Method

In order to meet the requirement of high computational efficiency like conventional time-linearised methods and also can account for nonlinear effects like nonlinear time-marching methods, a novel method in the frequency domain called nonlinear harmonic method was developed by Ning & He (1998) based on a quasi-three dimensional linear Euler method. In this method, the assumption was that the unsteady field was composed of a time-averaged flow, instead of steady flow, plus a small harmonic perturbation. The nonlinear effects were included in a coupled solution between the time-averaged flow and the unsteady perturbation. Due to the unsteadiness, time-averaging generated extra 'unsteady stress' terms in time-averaged equations. The extra terms were evaluated from the solutions of unsteady perturbation equations, while the coefficients of the perturbation equations were evaluated from the solutions of the time-averaged equations. Nonlinearity was included by simultaneously solving the time-averaged and unsteady equations in a strongly coupled manner by integrating in pseudo-time. Their results showed that this method could considerably improve the prediction when the nonlinearity was strong. Later, this nonlinear harmonic method was applied to the 2D viscous Navier-Stokes analysis of unsteady flows in turbomachines by He & Ning (1998). Vansanthakumar *et al.* (2000) extended this method from 2D to 3D for the viscous prediction of unsteady flows around oscillating blades.

2.4 Summary

From above description, the computational prediction methods have been developed for three dimensional viscous unsteady flows around oscillating blades. On the other hand, the experimental test cases are limited to two dimensional and only a very few experimental data exist for the three dimensional single blade oscillation. Thus, none of these three dimensional codes have been thoroughly validated against detailed experimental data for three dimensional features with blade-to-blade effect. Alternatively, they were only validated by comparing the computational results with theoretical analytical results or other CFD code results (e.g. Gerolymos & Vallet (1996)). The absence of three dimensional oscillating cascade test data not only causes a lack of confidence in the results obtained from these numerical methods, but also prevents their development because their shortcomings can not be identified. Three dimensional oscillating cascade data are currently required for enhancing current understanding of the underlying physics of blade flutter and for validating three dimensional CFD codes.

Chapter 3

Low Speed Flutter Test Facility

3.1 Design Philosophy

It is necessary to describe the experimental 'philosophy' before describing the experimental facility in order to ensure a suitable test facility designed. From Chapters 1 & 2, it is clear that the overall objective of this blade flutter experiment is not only to enhance the basic understanding of the physical background of blade flutter, but also to validate the CFD codes, which dictated the set-up of the experimental facility.

The present experimental work includes two parts. The first phase of experiments was designed to investigate the unsteady flow around an oscillating cascade in a 3D bending mode with the intention of validation of numerical methods. The principal objective of the second phase of the experimental work was to investigate the influence of tip leakage flow on the unsteady aerodynamic response of the oscillating cascade.

To design a suitable experimental facility for the basic objectives of the present study, several criteria must be met. The first criterion is that the test results should reflect the characteristics of blade flutter in a real compressor stage. The driven blade flutter test in high speed flows is extremely difficult and costly compared with that low speed flows as discussed in Chapter 2. To validate numerical methods and to enhance the basic understanding of some important 3D unsteady flow physics due to blade vibration, low speed tests can preserve the elementary features of realistic configurations and had proved to be capable of providing high quality data although transonic flow related effects had to be missed.

The second criterion is to ensure reliability of experimental results in terms of accuracy and repeatability. This was achieved in the present experiment by using a large scale working section, operating at a low speed in a simple aero-mechanical environment. The large scale working section can provide a high spatial resolution of measurements, which is essential in obtaining detailed measurement of local unsteady pressures of the 3D oscillating cascade and the detailed information of the influence of tip leakage flow on the unsteady aerodynamic responses of the oscillating cascade. The low speed flow condition enabled a low vibration frequency with a realistic reduced frequency. The low vibration frequency with high natural blade frequencies gave the simple aero-mechanical environment, which prevented unnecessary ambiguities in explaining the test data.

Thirdly, the apparatus should permit flexibility in that a range of test cases should be accommodated in order to check certain significant unsteady flow features. The present test rig was designed with the capability to adjust inlet flow velocity, vibration frequency, incidence and tip-clearance gap.

The fourth criterion is cost-effective, which was realised in this experiment by the build of the test facility and the generation and acquisition of the 3D unsteady pressure data. The Influence Coefficient Method was used to simplify the test rig to superimpose tuned cascade data. The low speed flow condition saved energy to drive the wind tunnel and the low vibration frequency released the difficulty of controlling the blade vibration at high vibration frequency. In addition, off-board pressure transducers were allowed to obtain the unsteady pressures via any static pressure tapping over the whole blade and for all blade positions in the cascade with the easy re-establishment of the low speed flow condition. Furthermore, the low vibration frequency provided a high temporal resolution of the measurements through moderate sampling rates and eased the instrumentation.

The final design of the low speed flutter test facility resulted from the best compromise due to the conflict of some of the design criteria.

3.2 Low Speed Linear Cascade Rig

In this section, the test facility is described in detail including the low speed wind tunnel, the linear compressor cascade, the blade profile used and the three dimensional bending mode, blade instrumentation, and the operational condition. A new test facility purposely built for the current flutter research at Durham University is shown in the photograph of **Figure 3.1**.

Figure 3.1: The test facility

3.2.1 The Low Speed Wind Tunnel

The new low speed wind tunnel was largely based upon existing wind tunnels in the thermo-fluids laboratory of the University. It is an open flow facility with a rectangular test cross section of 0.25x0.8*m*. In the tunnel, a non-uniform discharge from a centrifugal fan (powered by an 11kW motor) is diffused into a large settling chamber, in which the flow has a low velocity, then is driven through a shaped contraction into the working section, and exhausts to atmosphere. The quality of the flow at the working section mainly depends upon the contraction, specifically the shape and the ratio of inlet to outlet area. An established smooth contraction shape of good aerodynamic design was adopted, which is a Vitoshinskii nozzle (Gorlin & Slezinger 1964), with a contraction ratio of 7.5:1. In order to achieve this high contraction ratio with short length of the structure to reduce the sidewall boundary layer of the contraction, it is necessary to contract the tunnel in the vertical as well as the horizontal plane, which requires all four walls to be curved. As it is difficult to manufacture four curved walls, the contraction was divided into four sections, two kinds of small contractions. One is a small contraction with the two vertical walls straight and the two horizontal walls curved, the other is with the two horizontal walls straight and the two vertical walls curved. The two kinds of the small contraction were connected one by one. The cross section of the wind tunnel is shown in **Figure 3.2** and the top view in **Figure 3.3**. There is a screen upstream of the contraction and a section of honeycombs downstream (not shown in the figures) to produce a homogenous flow at the working section. The tunnel is a variable speed facility, which is accurately controlled by a speed controller.

3.2.2 The Working Section

The working section is a linear compressor cascade located in the exhaust of the tunnel. It consists of eight blade passages made up from seven blades plus the wooden frames, the perspex sidewalls and the profiled upper and lower walls, as shown in the photograph of **Figure 3.4** and the schematic in **Figure 3.5**. The various blade positions are shown in **Figure 3.5**. **Table 3.1** shows the linear cascade geometrical parameters.

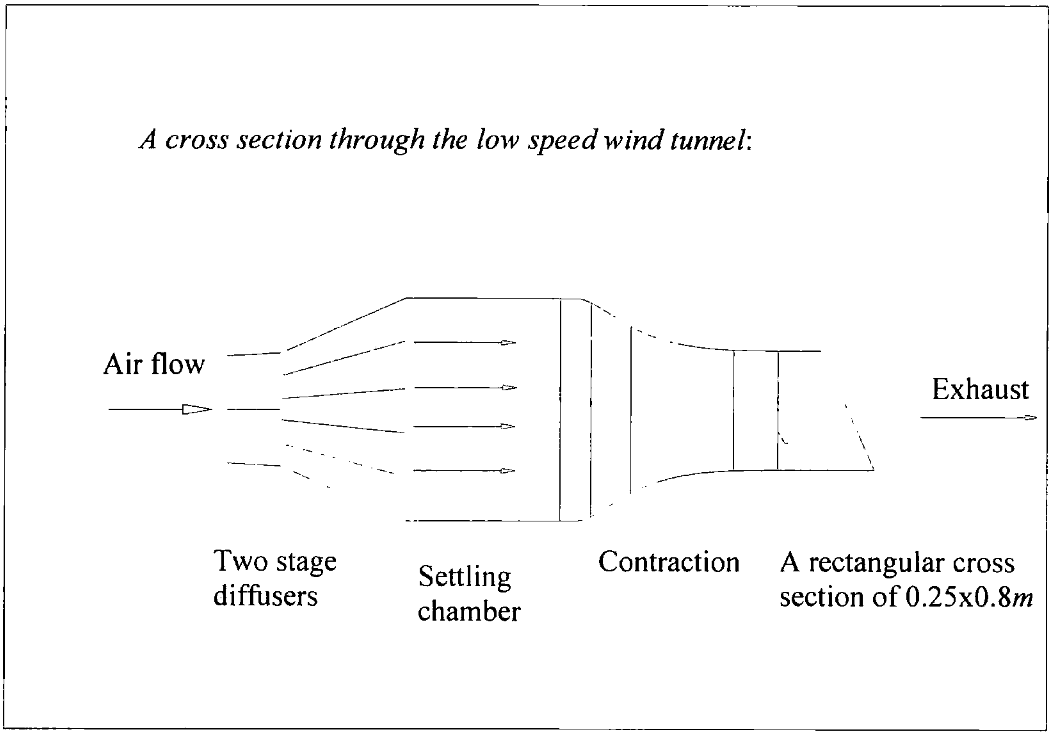

Figure 3.2: The wind tunnel configuration (cross section)

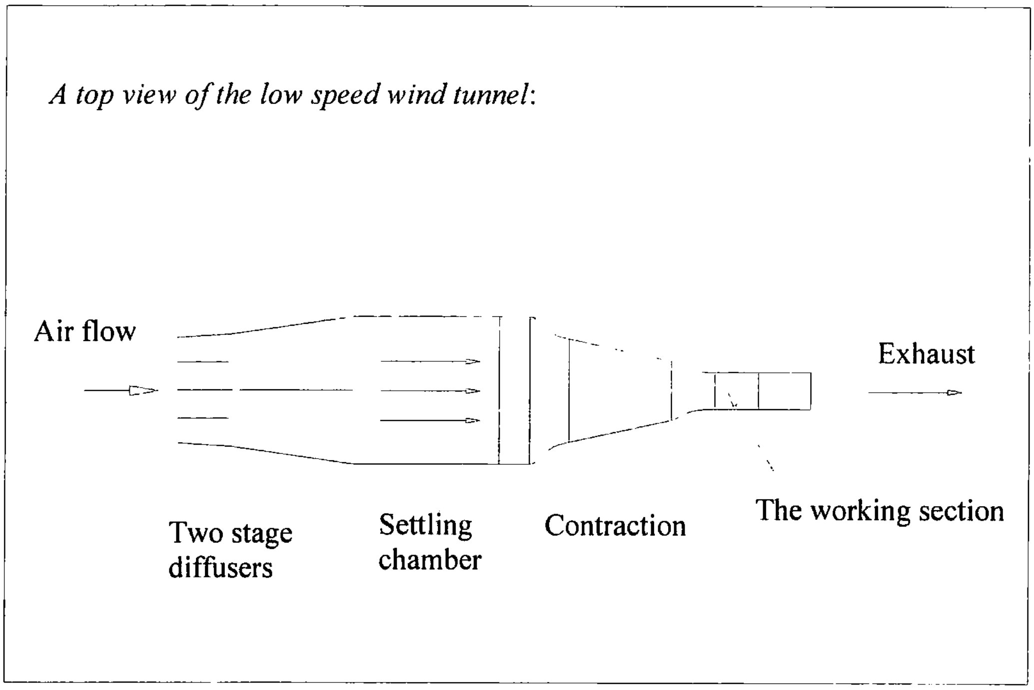

Figure 3.3: The wind tunnel configuration (top view)

Seven blades were inserted through the blade shaped holes in the LHS (Left Hand Side looking from the exit of the working section) perspex sidewall. On the tip of every blade there is a rod, which was inserted through the RHS (Right Hand Side) perspex sidewall. Six stationary blades were fixed by nuts. The middle blade was hinged at the blade hub on the LHS perspex sidewall and was driven at the blade tip to oscillate along a slot cut in the RHS perspex sidewall. The slot was sealed by card, which was fixed on the rod protruding from the blade to reduce the air leakage.

As the middle blade had to oscillate in bending mode for the flutter study it was unavoidable to, compared with the steady flow measurements, introduced gaps between the oscillating blade and the non-oscillating parts, e.g. the small gap between the blade tip and the perspex sidewall, and the comparatively large hole fabricated in the LHS perspex sidewall where the middle blade was hinged. The flow from the

Figure 3.4: The low speed linear compressor cascade

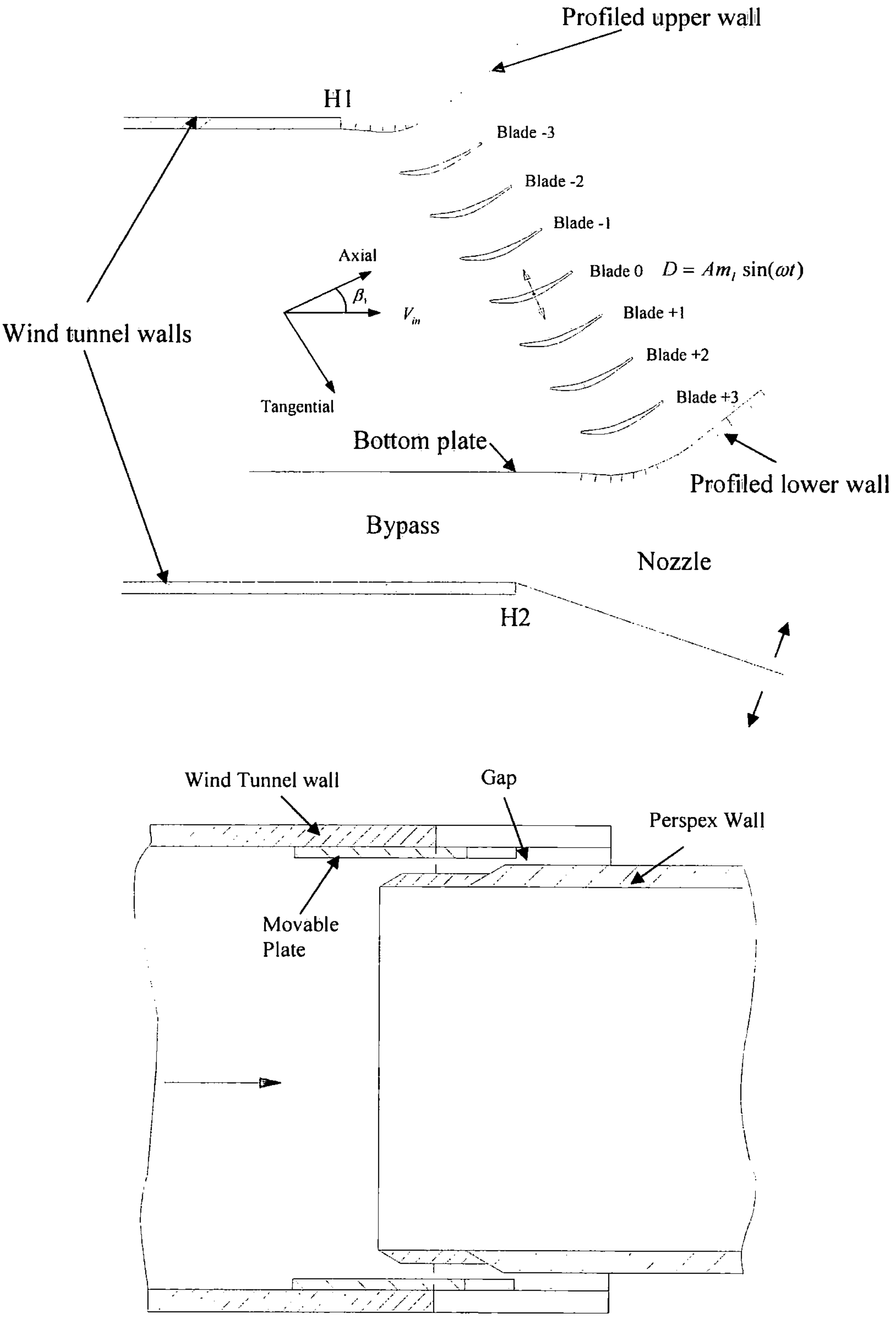

Figure 3.5: Linear cascade geometry (top: cross view; bottom: top view)

The linear cascade geometrical parameters	
Number of aerofoil	7
Pitch length, S	0.09 m
Blade span, h	0.19 m
Stagger angle, γ	14.2°
Bending mode direction	Normal to absolute chord (Positive P. S. → S. S.)
Bending amplitude at tip, Am_{tip}	0.06C
Bending amplitude at hub	0.005C

Table 3.1: Linear cascade geometrical parameters

the pressure surface to the suction surface at the blade tip and the flow through the hole towards the outside of the test facility had to be avoided. In this experiment, a piece of dense sponge was packed in the gap between the vibrating blade tip and the perspex sidewall to prevent the flow leakage. Foam tape covering was used to minimize the effect of the flow leakage through the sidewall hole towards the outside of the test facility in the unsteady pressure measurements, while still ensuring an unrestricted bending motion of the middle blade.

The purpose of the profiled upper and lower walls was to simulate the adjacent blades in the cascade. The Perspex sidewalls of the cascade were designed to extend one chord length upstream and downstream. The wind tunnel sidewall boundary layers were removed by the sidewall gaps started at one chord upstream of the cascade leading edge in order to provide uniform inlet flow conditions. The gaps between the wind tunnel sidewalls and the perspex walls were taped to adjust the blade-to-blade periodicity. Half of each gap was covered with 6*mm* self adhesive tapes. The arrangement provided a linear variation in the open area ratio of the covered part of the gap along the tangential direction, which increased towards the positive tangential direction, as shown in **Figure 3.6.**

The working section was designed so that the required inlet flow angle can be adjusted by rotating the cascade around a horizontal axis (H1 shown in **Figure 3.5)** at the top end while leaving the stagger angle unaltered. Thus the linear cascade was installed at some distance from the lower wall of the wind tunnel, and the height of the exit section of the wind tunnel is much larger than the width with the side ratio of 3.2:1. A bottom plate was hinged with the profiled lower wall of the cascade to adapt the change of the cascade length caused by the rotation of the cascade around the hinge H1, which constructed a bypass. In order to achieve a uniform flow condition at the leading edge section of the bottom plate with its horizontal position, a nozzle with adjustable diffusion ratio was added under the cascade. The uniform flow condition at the tip section of the bottom plate was obtained by adjusting the diffusion ratio of the nozzle and was indicated by the constant static pressures along the vertical direction for each set of the steady and unsteady flow measurements.

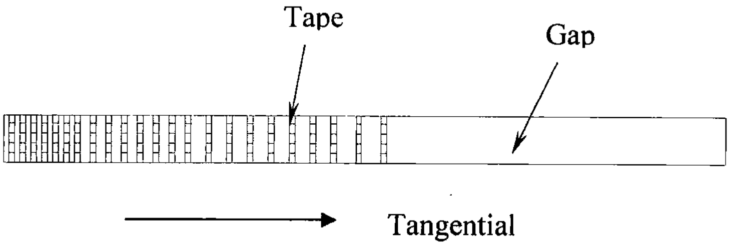

Figure 3.6: The gap covering scheme

3.2.3 Specification of Blade Profile and Oscillation Bending Mode

The blade profile used in this study is a Controlled-Diffusion Blade (CDB), which was designed by Sanger (1983) and extensively investigated in the Naval Postgraduate school, USA (e.g. Sanger & Shreeve (1986); Elazar & Shreeve (1990)) for its steady flow performance in modern compressor blading designs. It was chosen in order to easily compare and check the baseline steady flow results with those in the open literature (e.g. Sanger & Shreeve (1986); Sasaki & Breugelmans (1998)).

The original design has a chord length of 0.127*m*. It was scaled up to 0.150*m* in this experiment to permit detailed instrumentation of the blade surface. The blade coordinates, which were interpolated from the profile shown in Elazar & Shreeve (1990), are given in Appendix. The aerofoil section is shown in **Figure 3.7** and the blade section properties are summarised in **Table 3.2.**

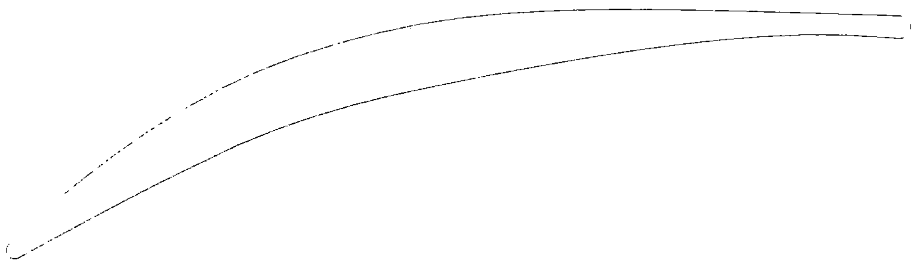

Figure 3.7: Controlled-Diffusion Blade profile

Blade Section Properties	
Aerofoil Type	Controlled-Diffusion Blade
Chord length, C	0.15 *m*
Aspect ratio, h/C	1.27
Maximum thickness	0.07C
Leading edge radius	0.00132 *m*
Trailing edge radius	0.00186 *m*
Solidity, C/S	1.67

Table 3.2: Blade section properties

The blade is untwisted in the spanwise direction for simplicity, unlike those blades found in compressor stages. Straight blades require less data to describe the geometry compared with the twisted one. This eases both the acquisition and presentation of test results, and also reduces computational time and storage required for CFD simulations, while a significant three dimensional effect can be obtained from a 3D bending motion of a straight blade.

The Controlled-Diffusion blades were manufactured from Aluminium on a three-axis numerical controlled machine. The blade profile was described by series of arcs fitted to the blade coordinates. The blade surfaces were hand finished to provide the smooth surfaces. Thus, the real blade profile is slightly different from that shown in Elazer & Shreeve (1990) and the geometrical inlet flow angle of the blade derived from the blade coordinates for the nominal flow condition is 39°.

The middle blade (blade 0) in the linear cascade was hinged at the hub on the LHS perspex sidewall of the working section. A rod extending from the tip of the aerofoil was driven by a single bar mechanical system, which was connected to a D.C. shunt wound motor, as shown in **Figure 3.8**. The speed of the D.C. motor was adjusted by a speed controller. This arrangement provided a linear variation in oscillation amplitude along the blade span to simulate the first bending mode of flutter (shown in **Figure 3.9**), increasing from the blade hub towards the blade tip section. Note that since the blade root hinge had to be positioned outside the test section, there was a small displacement at hub section. The bending amplitude at the blade tip was 6% chord and 0.5% chord at the blade hub. The blade was oscillated in a direction normal to the chord line, positive from the pressure surface to the suction surface, as shown in **Figure 3.8**. This normal-to-chord direction was chosen as it was easy to be set up in the experiment, rather than to simulate the bending direction of a compressor blade in a real rotor.

Although the mechanical oscillation system used did not produce a pure sinusoidal curve, with the length of the crank arm connecting bar being twenty times the amplitude of the blade vibration, the locus of the single bar drive was a close approximation to the sinusoidal curve, shown in **Figure 3.10**. The motion of an oscillating blade was defined by the change in displacement with time $D = Am_l \sin(\omega t)$, where Am_l is the local bending amplitude, and ω is the angular frequency of blade vibration.

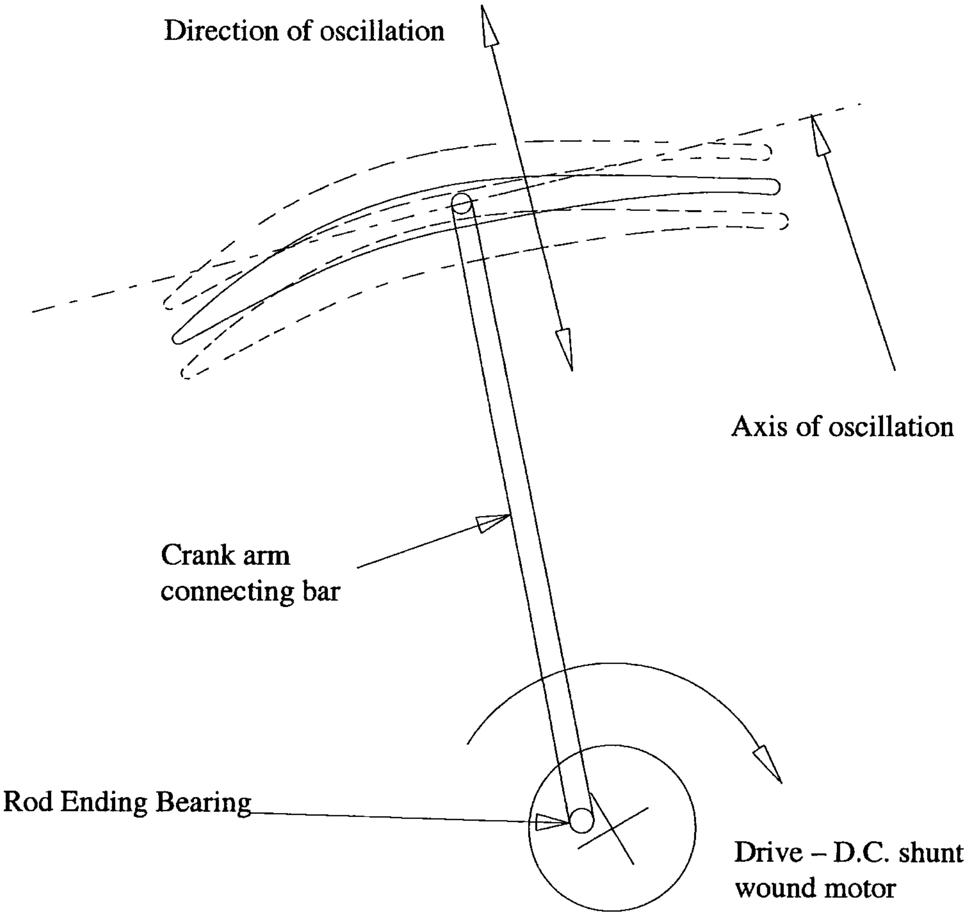

Figure 3.8: Sinusoidal drive mechanism (blade tip section)

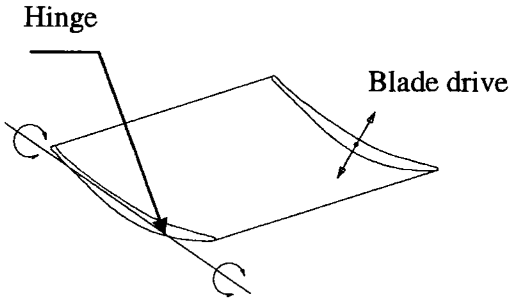

Figure 3.9: The oscillating blade mounting configuration

Blade elastic deformations must be minimised as they produce unknown three dimensional effects. The input to aeroelastic prediction methods is then no longer perfectly known or defined. The blade (made by aluminium) geometry was considered to remain rigid during the bending oscillation. By performing the experiments in this way, the aerodynamic aspects were separated from the structural aspects of the blade flutter, as the natural modes of the blade were of much higher frequencies and hence not excited. For the present experiment the elastic deformation of the blade driven system can also be ignored because the blade vibration frequency was low (less 20*Hz*) and the material of the blade driving system is hardened steel. And as such the distance between the pivot point of the crank arm connecting bar on the top of the D.C. motor and the centre of the motor can be treated as the real vibrating amplitude at the blade tip. This amplitude can be adjusted by changing the radial position of the pivot point of the connecting bar.

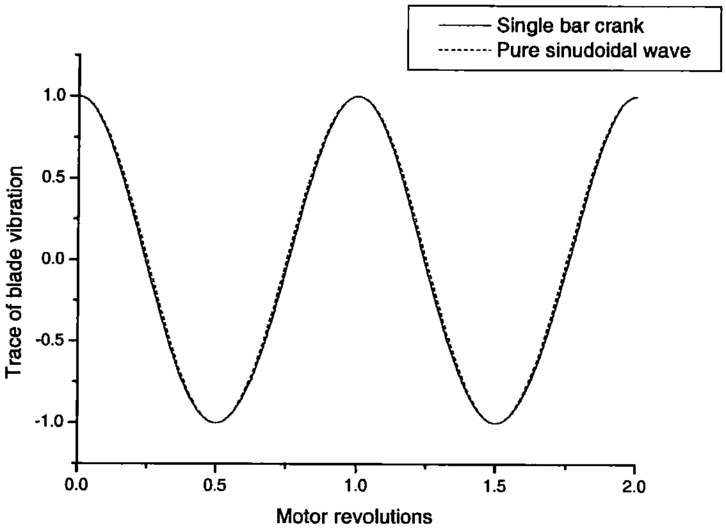

Figure 3.10: Locus of blade displacement delivered by the single bar crank

3.3 Instrumentation of Aerofoil

The oscillating blade and one of stationary blade had fully instrumented. The instrumented stationary blade can take up any of other stationary blade positions in the cascade. The blades had slots machined into the surface to permit the imbedding of 24 brass tubes. Once the brass tubes were bonded in place a filler material was applied to the instrumented surface and the blades were sanded to the original profile. The size of slots machined to install the brass tube relative to the blade thickness was the limiting factor in the placement of the pressure tappings closest to the leading and trailing edges of the blade. At these locations, the positions of the brass tubes on the pressure and suction surfaces were chosen to put alternately, as shown in **Figure 3.11.** At each spanwise section, the pressure tappings are clustered near the leading edge and more on the suction surface than that on the pressure surface to capture the large pressure gradients there. There are 14 tappings on the suction surface and 10 tappings on the pressure surface. These tappings were used for both steady and unsteady pressure measurements. And it was demonstrated that this is sufficient for picking up the steady separation bubble on the suction surface and for a good representation of the unsteady pressure distribution. Their positions are described in **Figure 3.11 and Table 3.3**.

Ideally there would be a transducer at each tapping. Because the thickness of blade is small (the maximum is $10mm$), along the blade span six static tappings of internal diameter $0.3mm$ are located on one brass tube at six different span sections: 20% (near blade hub), 50%, 70%, 90%, 95% and 98% (near blade tip) span. One exit of a brass tube was blocked and the other was connected to a transducer by plastic tubing, approximately $0.2m$ long, along which the unsteady pressure signal travelled. Care was taken to ensure only one tapping was open and the others were blocked on a single brass tube during the measurements. Any air leakage from another tapping would have compromised the accuracy of the experimental results. In practice, the five span sections of the pressure tappings were covered with very thin self-adhesive tapes to allow only one section of the pressure tappings open. The brass tube was connected to a controlled pressure source to check *only* one tapping opened by a test, in which the pressure of air applied to the brass tube *only* sensed to the open or close of the test pressure tapping.

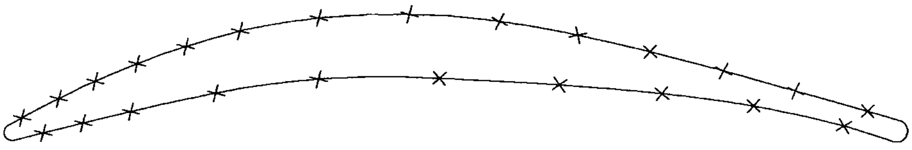

(Tappings located at six spanwise sections: 20%, 50%, 70%, 90%, 95% and 98% span)

Figure 3.11: Location of blade surface pressure tappings

Suction Surface		Pressure Surface	
Tapping	Position	Tapping	Position
S1	0.017C	P1	0.043C
S2	0.060C	P2	0.086C
S3	0.100C	P3	0.140C
S4	0.147C	P4	0.233C
S5	0.200C	P5	0.346C
S6	0.260C	P6	0.480C
S7	0.347C	P7	0.613C
S8	0.447C	P8	0.726C
S9	0.547C	P9	0.826C
S10	0.633C	P10	0.926C
S11	0.713C		
S12	0.793C		
S13	0.873C		
S14	0.953C		

Table 3.3: Distribution of blade surface pressure tappings

3.4 Nominal Operational Conditions

The nominal operational conditions realized in all test cases with measured inlet flow angle are showed in **Table 3.4**, which resulted from the considerations discussed in Section 3.1.

The Reynolds number was relatively low in this experiment, where the viscous behaviour of the flow could be influential.

The reference velocity was taken to be the isentropic exit velocity in defining the reduced frequency (see equation 1.1) in this experiment. Its definition is:

$$V_{ref} = \sqrt{\frac{2(p_{01} - p_2)}{\rho}} \tag{3.1}$$

The present test facility was purposely designed for the operation at the low speed with the isentropic exit velocity of $19.5ms^{-1}$ to avoid the measuring difficulties and the high cost of building facilities to perform tests at transonic speeds.

Ideally, the linear cascade should simulate a compressor row as closely as possible to enable the investigation of the influence of the various parameters on blade flutter. According to the overall objectives of the present experiment, the most important unsteady parameter is reduced frequency. Increasing the value of the reduced frequency can be achieved either by increasing the vibration frequency or reducing the flow velocity. In this experiment, the realistic reduced frequency was determined uniquely by changing the vibration frequency f, while the reference velocity V_{ref} (isentropic exit velocity) was held constant throughout the test. Steady flow conditions are of great interest but tests with different incidence angles had not been carried out.

The steady flow measurements were conducted at the operational conditions shown in **Table 3.4** and the unsteady pressure measurements at a nominal zero tip-gap were performed at a range of reduced frequencies at the constant steady flow conditions.

The influence of the tip-clearance on the aeroelastic stability of the oscillating cascade was investigated with three settings of tip-clearance gap at reduced frequency of 0.4 at the same constant steady flow conditions.

Operational conditions	
Measured inlet flow angle, β_1	37.5^0
isentropic exit velocity, V_{ref}, ms^{-1}	19.5
Reynolds number, Re *(Based on blade chord and isentropic exit velocity)*	195000
Reduced frequency range, k	0.2, 0.4, 0.6
Nominal vibration frequencies, f, Hz	4.14, 8.28, 12.4
Nominal frequencies at ambient conditions of 1 atm. and $20^0 C$	

Table 3.4: Summary of operational conditions

Chapter 4

Experimental Methods and Techniques

This chapter describes the instrumentation, data acquisition and data processing procedures used for the steady and unsteady flow measurements including the definition of every parameter recorded and an estimation of the errors of possible sources. In addition, the experimental methods used for the unsteady pressure measurements and the unsteady data reduction are presented.

4.1 Steady Flow Measurements

Regular steady equipment was used for the steady flow measurements including the inclined manometer bank for measuring blade surface static pressures, and two three-hole probes for measuring the inlet flow angle and the inlet total pressure loss. The definition of the calibration coefficients of three-hole probes is expressed and the calibration charts for yaw and pitch angles are presented.

The type of pneumatic probe employed for the measurement of inlet flow condition is a fixed direction, three-hole, 45° probe with space between tubes filled. Two probes were used to traverse the inlet measurement plane of the cascade, which was located at half chord length upstream of the cascade leading edge. One probe has previously been calibrated in a calibration tunnel at a representative Reynolds number of 2.6×10^3 (based on probe diameter) over a range of $\pm20°$ yaw angle, at 2° intervals, the other probe calibrated at the same Reynolds number over a range of $\pm18°$ pitch angle, at 2° intervals. The definitions for the calibration coefficients for yaw angle, pitch angle and total pressure are given below:

$$C_{yaw} = \frac{p_{top} - p_{bottom}}{p_{center} - p_{av}}; \qquad C_{pitch} = \frac{p_{right} - p_{left}}{p_{center} - p_{av}}; \qquad C_{tot} = \frac{p_{center} - p_0}{p_{center} - p_{av}};$$

$$p_{av} = \frac{p_{bottom} + p_{top}}{2} \quad for\ C_{yaw}; \qquad p_{av} = \frac{p_{right} + p_{left}}{2} \quad for\ C_{pitch} \tag{4.1}$$

The negative deviation flow angle in yaw shows the flow offset to the negative tangential direction from the set geometrical inlet flow angle, and the negative deviation flow angle in pitch indicates the flow offset to the negative radial direction, as shown in **Figure 4.1.** The tubes at the probe heads measuring pressures p_{top} and p_{right} are exaggeratedly demonstrated in **Figure 4.1** when the two probes were used to measure the deviation flow angles in yaw and pitch directions.

The calibration chart of the three-hole probe for yaw angle is shown in **Figure 4.2,** for pitch angle shown in **Figure 4.3**. The smooth and continuous calibration curves for yaw angle and total pressure, and for pitch angle and total pressure were considered satisfactory for the purpose of the present investigation with the resolution of flow angles within the accuracy of 1° by the interpolation on the calibration charts.

During the steady flow measurements in the low speed flutter test facility, the pressures from the three-hole probes were recorded by the inclined manometer bank. The deviation flow angle in yaw (± Δyaw) and in pitch (± Δpitch), and the total pressures were obtained through simple bilinear interpolation on the calibration charts. The measured inlet flow angle is the sum of the set geometrical inlet flow angle and the measured deviation flow angle in yaw.

The definition of the local total pressure loss coefficient is:

$$Y = \frac{p_{01} - p_0}{p_{01} - p_2} \tag{4.2}$$

here, p_0 is the total pressure recorded at half chord length upstream of the leading edge of cascade, p_{01} is the inlet total pressure measured at a midspan position and one chord length upstream of the leading edge of cascade by using a Pitot-static tube.

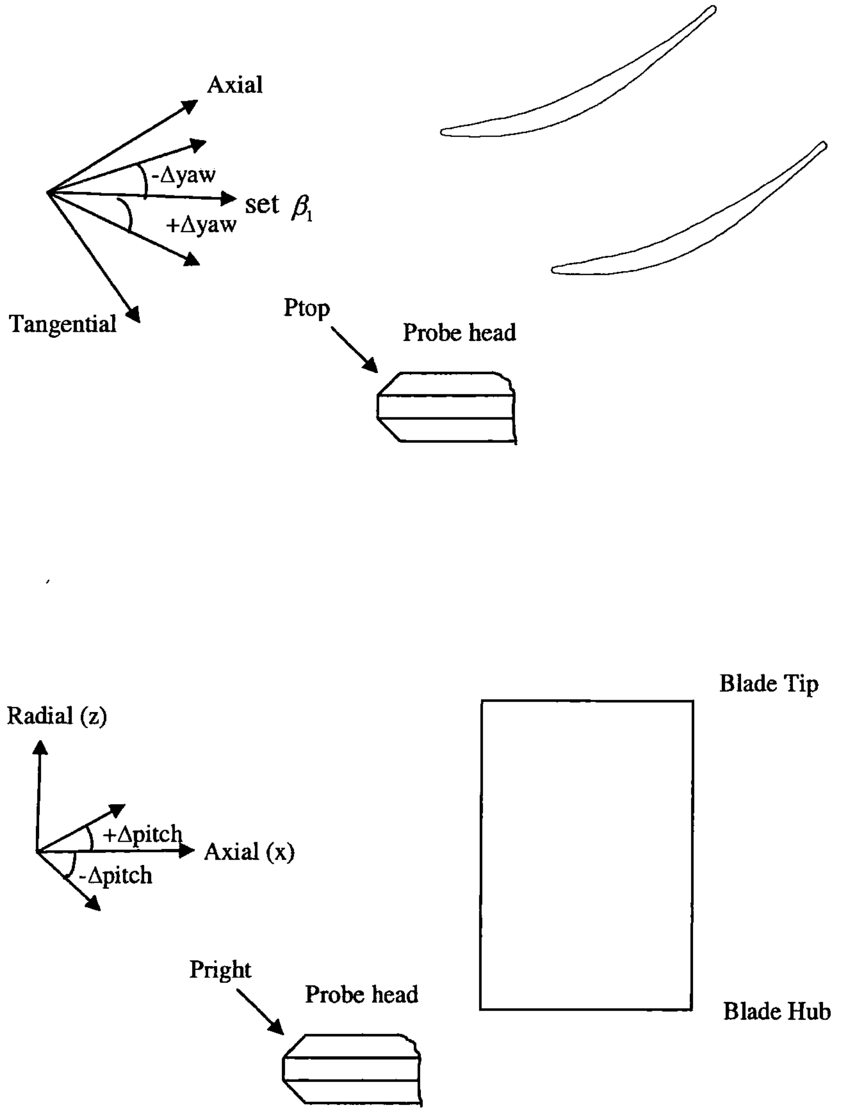

Figure 4.1: Definition of deviation flow angle in yaw and pitch directions

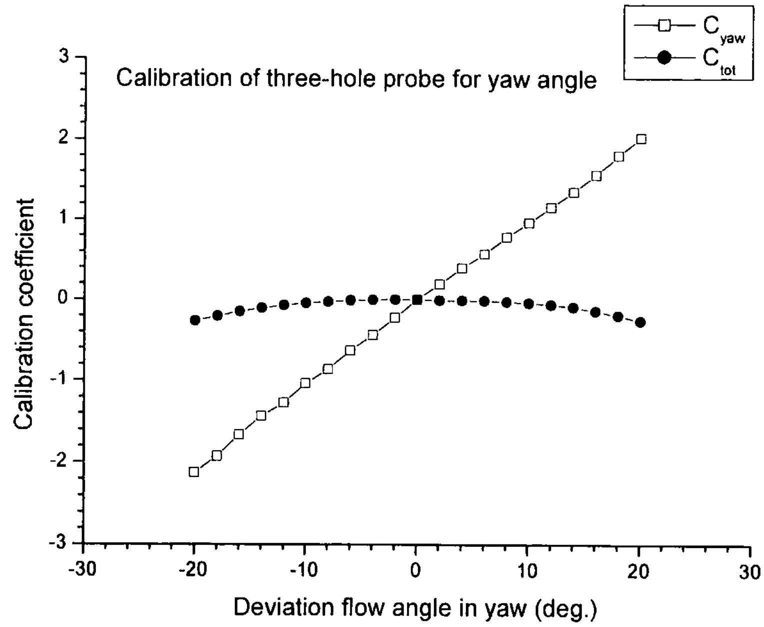

Figure 4.2: Three-hole probe calibration chart for yaw angle and total pressure

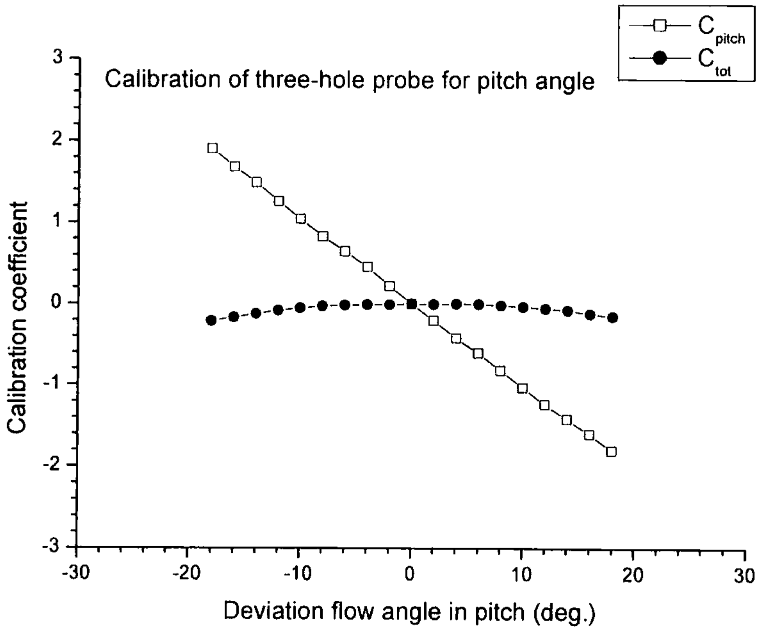

Figure 4.3: Three-hole probe calibration chart for pitch angle and total pressure

4.2 Unsteady Flow Measurements

In this section, firstly, the technique used in the unsteady pressure measurements is presented mainly focusing on the validation of the Tubing Transfer Function for the correction of the unsteady pressure signals. Secondly, the data-logging procedures and the data reduction are described. In addition, the repeatability of the unsteady pressure measurements is demonstrated and the possible error sources are pointed out. Finally, the experimental model of the Influence Coefficient Method is described.

4.2.1 Off-board Pressure Transducer & Correction of Unsteady Pressure Signal – Tubing Transfer Function Method

The experimental data are expected to have small certain errors resulting from the measurements and the data reduction. Thus, to improve accuracy, the calibrations were performed and the special techniques were used.

4.2.1.1 Off-board Pressure Transducer

Five temperature compensated, signal conditioned pressure transducers (type: Sensym 42C01D, 0-1*psi* range, sensitivity: 5*V*/*psi*) were used to record the unsteady pressure signals from five of the static tappings on the oscillating blade or the instrumented stationary blade at any one time. The same type of transducers was used in the previous experiments ((He 1998); (Bell 1999); (Queune & He 2001)).

There are 144 pressure tappings located on each of the two instrumented blades. The unsteady pressure measurements were performed on the middle five blades. There were 150 measurements required to obtain a full set of data. **Figure 4.4** shows the response of a pressure transducer over the unsteady pressure ranges of interest for the same pressure transducer by two sets of calibration tests performed at different days (over a two weeks period). Due to temperature compensation and a regular voltage supply (8.00volts ± 0.01volts), the response of the pressure transducer reveals the highly linear and constant behaviour over this pressure range.

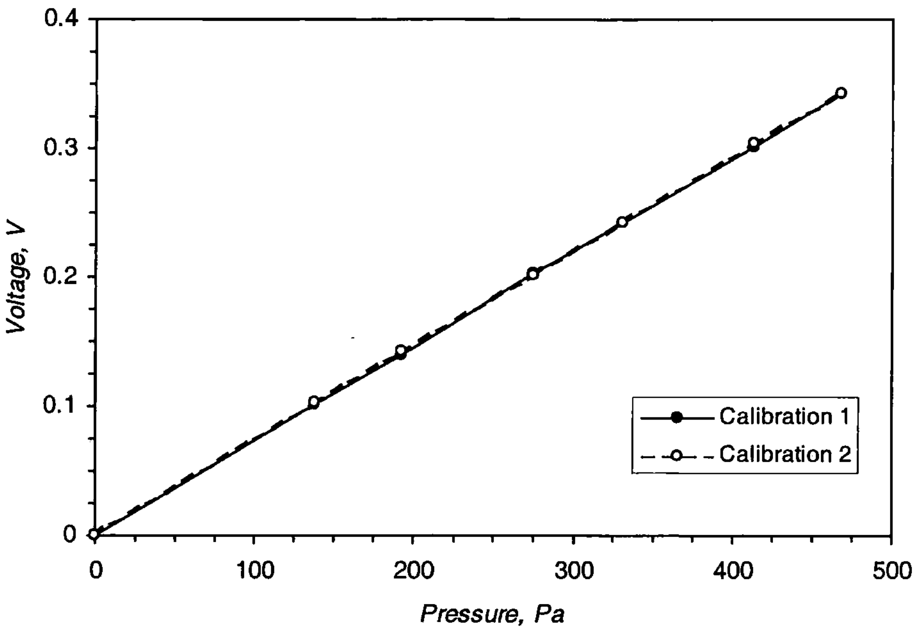

Figure 4.4: Pressure transducer response

Although the variation in the gradient of the pressure response was slight, a calibration was made to verify the linearity and the offset of the transducer output before each set of the unsteady pressure measurements in this experiment. A two-point calibration procedure was performed to prevent the errors being induced by this variation as well as any deviation in the linear response of each channel of the data-logging card. In this calibration procedure, an arbitrary pressure was loaded on each transducer and a manometer simultaneously. The data-logging card recorded the voltage offset of each transducer and the pressure transducers measured the arbitrary pressure, which also was indicated on the manometer. These two measurements allowed the linear response of each transducer to be accurately defined for each set of the measurements. Unsteady calibration of the pressure transducers is not necessary since the oscillation frequency (~ 20*Hz*) used is very much lower than the specified frequency response of this kind of transducers (10K*Hz*).

4.2.1.2 Tubing Distortion Effects

For the unsteady aerodynamic experiment using off-board pressure transducers, the blade can be instrumented with detailed static pressure tappings, which are connected to off-board pressure transducers by plastic tubing. This approach makes economical use of pressure transducers. The tubing system introduces a distortion of unsteady pressure signals. The signals can be amplified by resonance effects and attenuated by viscous effects. The time of the unsteady signals reaching the transducer is delayed, which is essential if multiple simultaneous signals are to be compared. The issue of the correction of the signal distortions needs to be addressed.

In following, Tubing Transfer Function approach involving a frequency domain correction is described, the typical measured transfer function is presented and its effectiveness is demonstrated.

4.2.1.3. Tubing Transfer Function Method

The tubing transfer function method described in this thesis was based on a technique originally employed for wall pressure measurements in wind engineering by Irwin *et al.* (1979). This technique was subsequently applied to multi-hole probe measurements for vehicle unsteady aerodynamics by Sims-Williams (2001).

An unsteady pressure signal $p_A(t)$ propagates from a pressure tapping to the sensing surface of a transducer via a tubing length between them as shown in **Figure 4.5**. The unsteady signal $p_B(t)$ measured by the transducer can be amplified by resonance effects at particular frequencies and attenuated by viscous effects at higher frequencies. The time-lag for the pressure signal to reach the transducer will result in an increasing phase shift at higher frequencies. This frequency-dependent tubing response can be characterized by a transfer function. Once the transfer function of a given tubing system is known then it is possible to correct for the tubing distortion, which depends on the whole system between the pressure tapping and the sensitive surface of the transducer, including the tubing length, the tubing internal diameter, and the transducer internal volume.

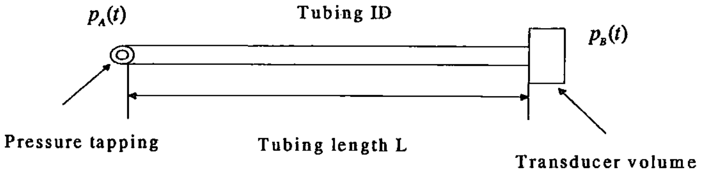

Figure 4.5: Tubing system

This technique requires that the system obeys the linear superposition so that unsteady signals can be decomposed to multiple frequency components.

The unsteady part of the pressure $p_A(t)$ at the pressure tapping is written as a Fourier series:

$$p_A(t) = \sum_{n=-\infty}^{+\infty} A_n e^{in\omega t} \tag{4.3}$$

The unsteady pressure $p_B(t)$ at the pressure transducer can be described as:

$$p_B(t) = \sum_{n=-\infty}^{+\infty} B_n e^{in\omega t} \tag{4.4}$$

Then the complex tubing system transfer function is expressed as equation 4.5.

$$TF_n = B_n / A_n \tag{4.5}$$

where, A_n are the complex Fourier coefficients of the unsteady pressure measured at the pressure tapping, and B_n are the complex Fourier coefficients of the unsteady pressure measured by the pressure transducer.

To utilize this approach, the tubing transfer function of a pressure measuring system must be known first, which can be obtained experimentally.

To correct the distorted unsteady signal, it is logged in the time domain and transformed into its Fourier coefficients in the frequency domain by the Fast Fourier Transform (FFT), which is corrected digitally using the known transfer function of the tubing system:

$$A'_n = B_n / TF_n \tag{4.6}$$

Finally, the corrected pressure $p'_B(t)$ is constructed through the corrected A'_n, i.e.

$$p'_B(t) = \sum_{n=-\infty}^{+\infty} A'_n e^{in\omega t} \tag{4.7}$$

4.2.1.4 Apparatus for Measurement of TTF

In the present experiment, the tubing transfer function was obtained experimentally. A block diagram of the apparatus used in the measurements of TTF of a static pressure tapping and the plastic tubing is presented in **Figure 4.6.**

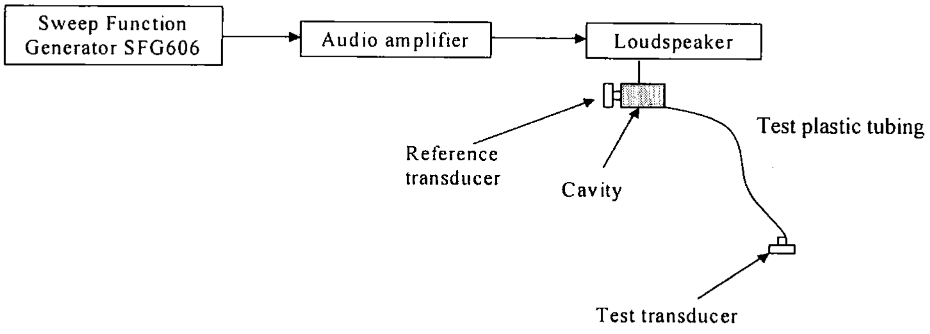

Figure 4.6: Correction apparatus

A swept sine wave was generated which covered the range of frequencies concerned and this was fed to an audio amplifier and a loudspeaker. For the present experiment, the frequency range used was from 0.1*Hz* to 50 *Hz* with a sweep period 0.75 *second* when logging sets of 2048 samples at 800*Hz*. The loudspeaker produced the pressure fluctuations with approximately the same waveforms as the input voltage. The loudspeaker was connected to a small cavity via a short rubber tube to isolate the mechanical vibration. A reference pressure transducer was directly connected to the small cavity and was used to record the pressure inside the cavity. A static pressure tapping used in the unsteady pressure measurements (0.3*mm* diameter for this experiment) was also connected to the cavity. A length of the plastic tubing was used to connect the static pressure tapping with another pressure transducer as would be done for the unsteady pressure measurements.

The tubing system included the transducer's volume, the connector, the plastic tubing and the brass tube, as used in the present experiment. The definition used to calculate the measured complex transfer function is:

$$TF_n = \frac{1}{M}\sum_{j=1}^{M}[(B_n)_j/(A_n)_j] \tag{4.8}$$

The complex Fourier coefficients A_n and B_n were defined in Section 4.2.1.3. M is the number of measured data sets used to average TF_n. In order to obtain a smooth transfer function desired for correcting the unsteady pressure signals, M can be greater than 20. A Hanning window function was used to reduce the effect of the finite data length, which has been found to improve the quality of the results.

4.2.1.5 Examples of TTF and its Effectiveness

Figure 4.7 shows a typical example of the measured tubing transfer function for the tubing length used in the measurement of the unsteady pressures in this experiment. A slight amplification can be seen over the frequency range of interest, indicating a resonant peak at a higher frequency. The phase distortion is more significant due to the importance of the relative phase of unsteady pressures and the vibration of the blade.

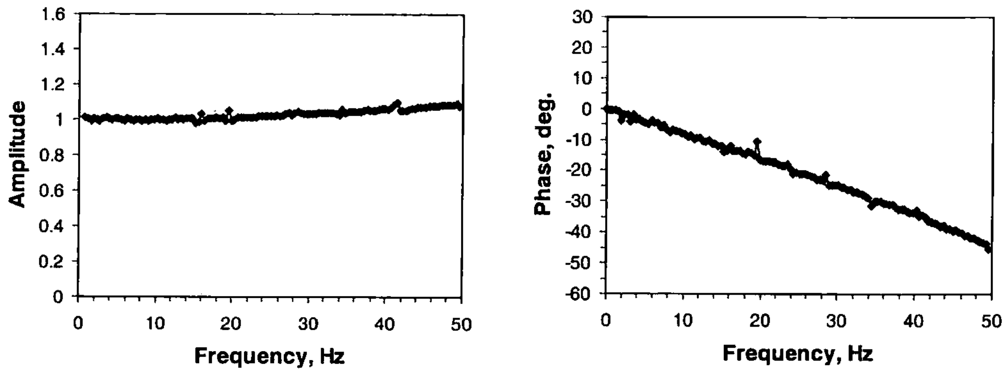

Figure 4.7: Transfer Function of the measurement system for the unsteady pressure measurements (brass tube, 0.18*m* x 0.001*m* plastic tubing, connector)

For the present case, the calibration tests were performed to correct the amplitude and phase distortions of the first and second Fourier coefficients of the unsteady pressures at their frequencies through the known tubing transfer function.

The effectiveness of this technique is demonstrated clearly in the comparison shown in **Figure 4.8.** The tubing system with 1.5*m* plastic tubing was subjected to a 9*Hz* sine wave - the middle value of the vibration frequency range used in the unsteady pressure measurements – using the transfer function measurement apparatus. Significant phase lag and amplification relative to the reference signal are obvious in the uncorrected signal. The previously measured transfer function was then used to infer the original signal and this is labelled "corrected" in **Figure 4.8**. This can be seen to closely match the original reference signal. This tubing correction method is more generally applicable than the previous treatments by He & Denton (1991) and Bell & He (2000). The distortion of the unsteady signal was generally either neglected because of low frequencies and short tubing lengths (He & Denton (1991)) or simply was corrected for phase lag and amplitude attenuation for a certain tubing length (Bell & He (2000)). However, it should be commented that in the present low speed test set-up, the typical tubing length is about 0.18*m*, so that the effects are not as significant as that shown in this figure.

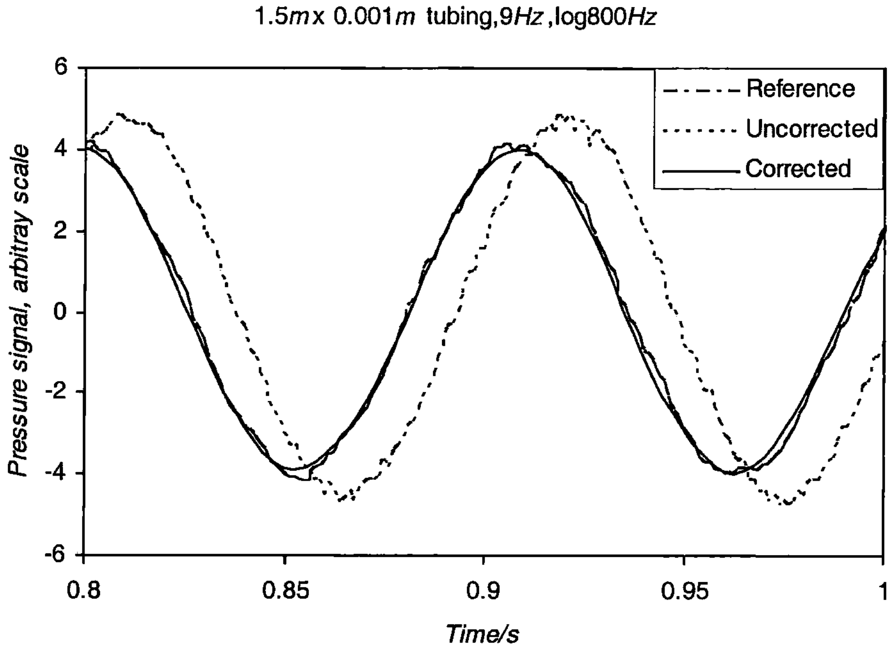

Figure 4.8: Effect of tubing transfer function with 1.5*m* tubing length

4.2.2 Data-Logging Procedures

This section describes the hardware for the acquisition of the unsteady pressures, the sampling scheme, the errors of the data-logging procedure, the method to reduce errors (e.g. the ensemble-average method), and the software used for the data-logging procedures.

The schematic representation of the principal hardware components employed in the unsteady pressure acquisition system is shown in **Figure 4.9**. These hardware components were constructed for the acquisition of the synchronized unsteady pressure signals.

In this system, a one-per-revolution pulse from an optical encoder mounted to the end of a D.C. shut wound motor was served as a trigger and was monitored by the digital I/O port of an Amplicon PC30G data-logging card. It triggered the data gathering at a fixed phase of the blade vibration and the unsteady signals were logged over a specified number of oscillations. This also was a trigger input to a digital tachometer, which acted as an accessible record of the vibration frequency for each set of the unsteady pressure measurements. The blade vibration frequency was prescribed to match the test reduced frequency and Reynolds number, which was set and adjusted by the speed controller of the D.C. motor according to the reading of the digital tachometer. The reading gave the number of revolutions per minute with an error of ± 1% in the measurement of the specified vibration frequency.

Unsteady voltage outputs from the five pressure transducers were discretised and acquired on a PC by the data-logging card. The techniques used to measure the unsteady surface pressure signals are similar to the set-up of Bell & He (2000).

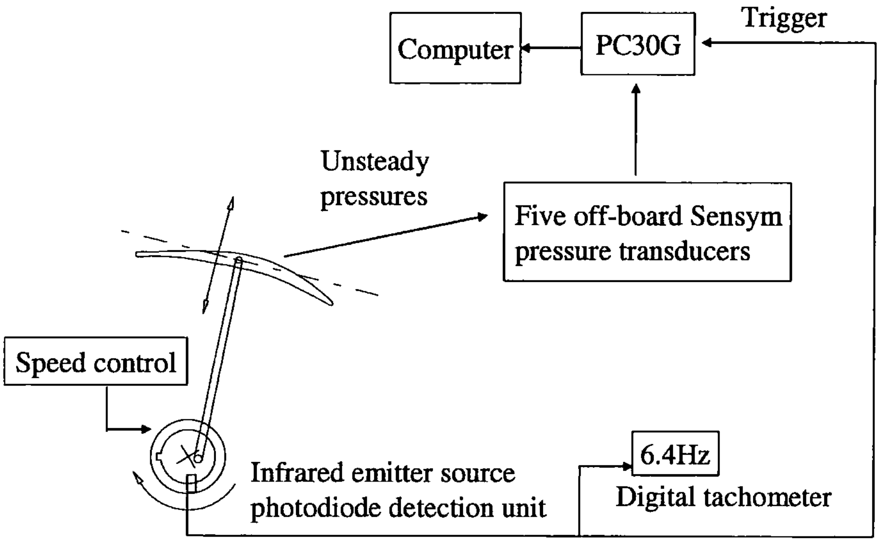

Figure 4.9: Schematic of the data-logging hardware for unsteady pressure measurements

The analogue-to-digital converter (ADC) onboard PC30G accepted the analogue voltage inputs from the pressure transducers. There are four ranges of the input voltage for the ADC channels: 0 to $5V$, 0 to $10V$, $-5V$ to $+5V$ and $-10V$ to $+10V$. As with all tests, the measurement will be most accurate if it is possible to keep the input range as low as possible with matching the output range of the pressure transducer. The range of 0 to $5V$ is equivalent to the output range of the pressure transducer of 1 to $6V$ and was used.

After recording the analogue voltage inputs from the pressure transducers, the ADC converted them into 12 bit digital codes, which provided 4096 equally distributed quantisation levels for the input range of 0 to $5V$. The maximum error of half a quantisation level introduced by the sampling procedure indicated the accuracy of $\pm 0.8Pa$ of the pressure transducer response shown in **Figure 4.4**.

The sampling of data channels on the PC30G data-logging card was performed sequentially with the time between sampling the consecutive channels defined by the overall sampling rate, which is the sampling rate multiplied by the number of channels being sampled. This meant that the sampling of channel one was initiated by the trigger signal with the sampling of other channels initiated slightly later and the fifth transducer triggered last. To minimise this error, a burst mode sampling was used, which enables all the selected channels in one burst to be sampled successively at the throughput sampling rate of the data-logging card with the specified sampling rate for every channel. For the PC30G card with 100K*Hz* throughput sampling rate, the phase error introduced by the sampling procedure was within the range of 0 to 0.1728°, which can be ignored. The signals from the transducers were sampled at the overall sampling rate of 10K*Hz*, which allows sampling five pressure transducers with the frequency up to 2K*Hz* for every transducer. This sampling frequency equated to 150 samples per cycle at the highest oscillation frequency. According to the Sampling theorem (Lynn & Fuerst 1989), the minimum of 150 samples is sufficient to capture the frequency components up to 75th harmonic without the aliasing error. The high sampling rate was used to increase accuracy in the evaluation of the Fourier coefficients of the low order harmonic components comparing with a data set with a relatively few sampling points.

The unsteady tests with the vibrating blade were done in the controlled vibration model. The vibration frequency, amplitude and the phase point logging the unsteady signals were kept constant over time. Thus, the blade vibration serves as a well known and well defined disturbance and the unsteady pressures are regarded as the responses to this disturbance. Ideally the signal obtained from the pressure transducer should be a pure harmonic wave. However, the pressure responses were usually distorted by any random error, which included the errors from discretisation, turbulence and electrical noise. For the known vibration frequency of the controlled vibration, the unsteady signal was repetitive and the signal-averaging can extract the periodic information from the raw unsteady pressure data. The unsteady signals were acquired over a number of periods, and each acquisition was added to the last, the sum then was divided by the number of acquisitions N_{enb}, as shown in equation 4.9. The corresponding points in the successive waveforms were then averaged, the periodic parts adding coherently and the non-periodic parts incoherently. Since the non-periodic parts tended to be random with mean of zero, the contribution of the random parts was reduced.

$$p(n,t) = \frac{1}{N_{enb}} \sum_{N=1}^{N_{enb}} p(n, t + T(N)) \quad (n = 1, 2, \ldots, n_p) \tag{4.9}$$

where n_p is the number of sampling points in one period of oscillation for each transducer, which was usually taken to be greater than 150. T is the time period.

During the first series of measurements it was found that 50 period ensemble-averaged signals (i.e. $N_{enb} = 50$) were sufficient to reduce the effects of time-unresolved unsteadiness and gave a well-defined periodic signal. **Figure 4.10** presents the raw unsteady pressure traces recorded on the suction surface of the oscillating blade at the reduced frequency of 0.4, which indicate the high frequency random components. They were all 'filtered' out after 50 times ensemble-averaging as shown in **Figure 4.11**. The smooth and clear unsteady periodic signals shown in this figure demonstrate the high level temporal resolution achieved both in the raw and the final ensemble-averaged unsteady pressure response, despite the low amplitude of the unsteady pressures generated at the low speed operational conditions. The smooth and clear unsteady periodic signals provide the qualitative and quantitative justification of the procedure adopted for the unsteady data acquisition.

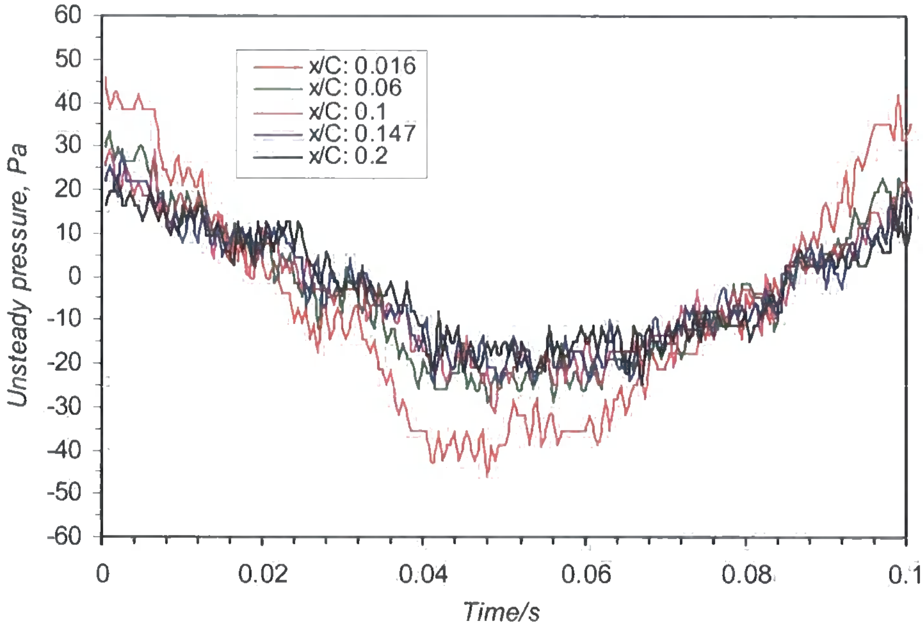

Figure 4.10: Raw unsteady signals at 70% span on blade 0 ($k = 0.4$)

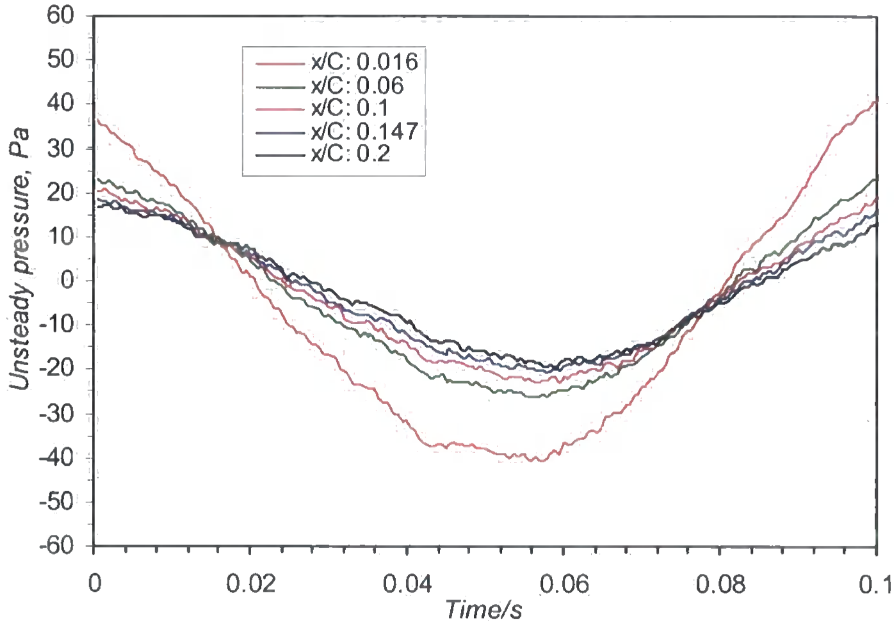

Figure 4.11: Ensemble-averaged unsteady signals at 70% span on blade 0 ($k = 0.4$, *50 periods*)

In addition to the ensemble-averaging technique, the effects of noise interference and pick-up were limited by wire shielding throughout the data acquisition hardware.

The procedures described in this section were controlled by C programme, which was modified from the software written by Bell (1999) to interface with the new data-logging card. The programme performed several functions including the setting of the flow conditions to match the prescribed test conditions, the calibration of the pressure transducers, the setting of sampling rates, the acquisition of the synchronised raw unsteady pressures and the process of ensemble-averaging. The programme also was modified to provide a visual display of the measurements at each stage of the acquisition procedure, which allowed errors and erroneous measurements to be readily identified.

After the unsteady digitized pressures were recorded, the results were analysed off-line to determine the fundamental aerodynamic characteristics of the unsteady flow phenomena.

4.2.3 Experimental Method – Influence Coefficient Method (ICM)

In order to achieve a true 'travelling wave mode' in a tuned cascade as described in Chapter 1 , all the blades of the cascade would have to vibrate at exactly the same frequency and amplitude with any given constant inter-blade phase angle. In practice, it is difficult to control the vibration amplitude and inter-blade phase angle accurately for all blades, and the vibration drive system is complicated. In addition, the results yielding do not allow an assessment of the relative importance of each blade in the cascade to the generation of the unsteady pressure response of a tuned cascade.

The Influence Coefficient Method proposed by Hanamura *et al.* (1980) provides an effective way to obtain a tuned cascade data by oscillating only one blade. This method also has the potential to reduce the data contamination by not oscillating the blades next to the wind tunnel walls, which avoids the complicated wall reflection problems seen in Buffum & Fleeter (1993).

According to the description of Fransson (1999c) and He (1998), this method can be explained as follows. For a finite blade cascade with '2N+1' blades executing identical amplitude harmonic oscillations with a constant inter-blade phase angle σ in a travelling wave mode, the blades are numbered from '-N' to '+N'. The reference blade is defined as blade 0, with the blade +1 immediately to the suction side, the blade -1 immediately to the pressure side, and so on to define the entire cascade. The unsteady pressures, which occur on the reference blade in the tuned cascade with a specific inter-blade phase angle, are generated by a combination of the contributions made by the individual vibrating blade N in the tuned cascade. These contributions can be represented by the unsteady aerodynamic influences. **Figure 4.12** shows a tuned cascade of only seven blades and the unsteady aerodynamic influences on the blade 0 from all blades in this cascade.

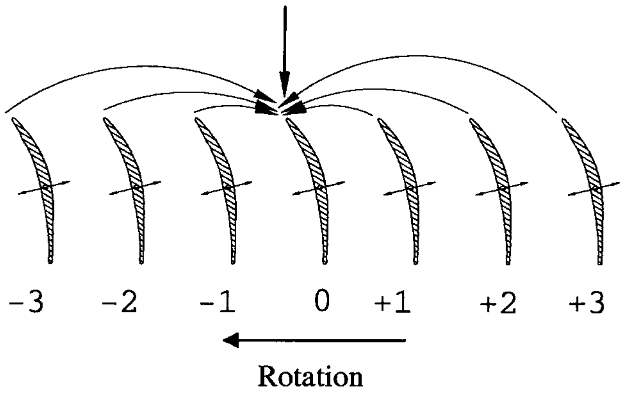

Figure 4.12: Unsteady aerodynamic influences on one particular blade from all blades in a tuned cascade

Under the assumption of linearity, the non-dimensional unsteady pressure, called the unsteady pressure coefficient, on the blade 0 in a tuned cascade with an inter-blade phase angle σ is expressed as in the complex form to separate the time related term out:

$$\tilde{Cp}_{0,tc} \cdot e^{i\omega t} = \sum_{N=-3}^{+3} \tilde{Cp}_{tc}(N,0) \cdot e^{iN\sigma} . e^{i\omega t} \tag{4.10}$$

And thus

$$\widetilde{Cp}_{0,tc} = \sum_{N=-3}^{+3} \widetilde{Cp}_{tc}(N,0)e^{iN\sigma} \tag{4.11}$$

$\widetilde{Cp}_{0,tc}$ is the unsteady aerodynamic pressure coefficient acting on the blade 0 in a tuned cascade, and $\widetilde{Cp}_{tc}(N,0)$ is the unsteady aerodynamic influence coefficient of the blade N on the blade 0 in a tuned cascade. The inter-blade phase angle σ is defined as positive when the blade +1 leads the blade 0, which corresponds to a forward travelling wave mode for compressors.

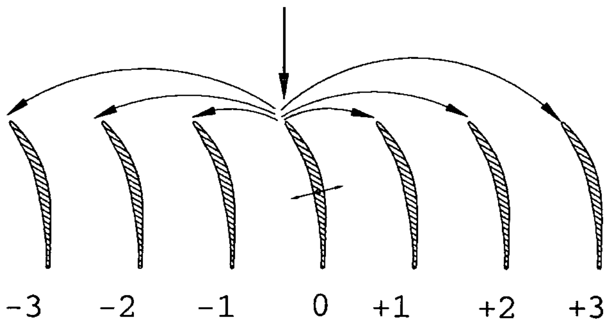

Figure 4.13: Unsteady aerodynamic influences acted on all blades in a cascade from one particular oscillating blade

The unsteady aerodynamic response $\widetilde{Cp}_{0,tc}$ can be obtained using an alternative method shown in **Figure 4.13**. In the linear cascade, only the reference blade 0 is oscillated, the others are stationary. The unsteady influence coefficients from the oscillating blade on itself and its neighbouring blades are directly measured. Under the linear assumption, these measured unsteady aerodynamic influence coefficients can be superimposed to determine the unsteady aerodynamics equivalent to the case where all blades in the cascade oscillate with a constant inter-blade phase angle at the same vibration frequency and amplitude.

The unsteady pressure coefficient $\widetilde{Cp}_{0,tc}$ for the equivalent tuned cascade is equal to:

$$\widetilde{Cp}_{0,tc} = \sum_{N=-3}^{+3} \widetilde{Cp}_{ic}(0,N)e^{-iN\sigma} \tag{4.12}$$

$\widetilde{Cp}_{ic}(0,N)$ is the unsteady aerodynamic influence coefficient acting on every blade in the cascade induced by the oscillation of the reference blade 0.

From a purely analytical point of view, this technique is based on the principle of the linear superimposition of an infinite number of blades. However, in real cases $\widetilde{Cp}_{ic}(0,N)$ becomes small quickly when N becomes large, and only several terms are needed to the construction of the equivalent tuned cascade data $\widetilde{Cp}_{0,tc}$.

Some further points are made regarding the advantages and disadvantages of the Influence Coefficient Method. The unsteady aerodynamic influence induced by the vibrating blade on itself, is independent of the inter-blade phase angle and is called the "direct term", while the unsteady aerodynamic coefficient $\widetilde{Cp}_{0,tc}$ including the contributions from each blade is called the "coupling term", which varies with the inter-blade phase angle. For a given cascade geometry, reduced frequency, and inlet flow condition, the Influence Coefficient Method allows that the direct and coupling terms to be measured and assessed separately. The various influence coefficients from all blades give the physical insight of the relative importance of each blade in a cascade to the generation of aeroelastic stability of oscillating blades. The practical consequence of the superimposition principle is that only one blade must be vibrated and only two blades need to be instrumented in order to measure the unsteady aerodynamic influence coefficients on all blade positions in the linear cascade. This technique considerably simplifies the experimental set-up. It should be noted that inter-blade phase angle is not an experimental parameter but merely appears in the post-processing calculations. Thus, the Influence Coefficient Method can be most easily used to predict the cascade aeroelastic stability for any inter-blade phase angle.

For validity of the Influence Coefficient Method, two aspects are essentially required. One is the convergence check to ensure that the limited number of blades measured in a cascade is sufficient. This can be shown by the decay rate of the unsteady pressure response on those blades far from the reference blade. The other is the validity of the linear assumption of this method for the unsteady flow behaviour concerned. The validation of this technique can be achieved ideally by comparing the oscillating cascade data determined from the influence coefficients with the corresponding data for a cascade in which all blades oscillate at a specific inter-blade phase angle. Alternatively, the examination can be conducted by checking the effect of the blade vibration amplitude on the unsteady pressure response.

The previous experimental work as reviewed in Chapter 2 indicated that the Influence Coefficient Method can be used for blade flutter problems as far as the flutter inceptions are concerned, which is the most important to designers. The design aim is that all tendencies towards flutter must be avoided, and no self-excitation appears at a small vibration amplitude. For the flutter problem with small vibration amplitudes, a linear approach is valid.

4.2.4 Data Reduction and Presentation

The procedures for analysing the experimental data to obtain the Fourier components of unsteady pressure, and to calculate the aerodynamic damping for a tuned cascade are described in the section.

4.2.4.1. Fourier Decomposition to Unsteady Pressure – the First Harmonic Component

The data reduction was based upon the standard techniques previously adopted in the similar studies (e.g. Carta & St. Hilaire (1978); He (1998); Bell (1999)). After the unsteady surface pressure was ensemble-averaged to eliminate the random pressure fluctuations, the ensemble-averaged unsteady pressure was decomposed into its Fourier harmonic components, as described in equation 4.13.

$$\begin{aligned} p(x,z,t) &= a_0 + \sum_n p_n \\ &= a_0 + \sum_n (a_n \cos(n\omega t) + b_n \sin(n\omega t)) \qquad (n = 1, 2, 3, \ldots) \\ &= a_0 + \sum_n Ap_n \sin(n\omega t + \phi_n) \end{aligned}$$

$$\phi_n = ArcTan(a_n / b_n) \tag{4.13}$$

Where Ap_n is the amplitude of the nth harmonic component of the induced unsteady pressure, and ϕ_n is the phase angle lead of the nth harmonic component with respect to the blade motion.

The non-dimensional unsteady pressure is expressed in terms of the unsteady pressure coefficient as defined in equation 4.14.

$$|Cp_n| = \frac{Ap_n}{(p_{01} - p_2)Am_{tip}} \tag{4.14}$$

Where, Am_{tip} is the blade bending amplitude at the blade tip. It is noted that the bending amplitude at the blade tip is introduced, rather than the local bending amplitude in order to directly compare the amplitude of unsteady pressure response at any spanwise section to highlight the 3D effects.

The amplitude and phase of every harmonic component of the unsteady pressure can be corrected by the calibration procedure described in Section 4.2.1 for the phase shift and the amplitude distortion of the unsteady signal.

4.2.4.2. Aerodynamic Damping

A three dimensional aerodynamic damping parameter ξ , has been established to describe a global definition of the oscillating cascade stability, which is based on the aerodynamic work done by the flow field on the oscillating blade over one cycle of blade motion.

The displacement (D) of arbitrary point at any instant of time for the present sinusoidal blade vibration is given:

$$D = Am_l \sin(\omega t) \tag{4.15}$$

Am_l is the local bending amplitude. The blade vibration velocity is:

$$V_{blade} = Am_l \omega \cos(\omega t) \tag{4.16}$$

The unsteady force induced by this blade vibration movement at that point is in sinusoidal forms with phase angles ϕ_n relative to the blade vibration displacement from equation 4.13:

$$\sum_n p_n = \sum_{n=1}^{N} (Ap_n \sin(n\omega t + \phi_n)) \tag{4.17}$$

The rate at which the aerodynamic force does work input to the blade per cycle is defined as:

$$\begin{aligned} W_{period} &= \int_T (\sum_n p_n . V_{blade}) dt \\ &= \int_T (\sum_{n=1}^{N} (Ap_n \sin(n\omega t + \phi_n))) \cdot Am_l \omega \cos(\omega t) dt \end{aligned} \tag{4.18}$$

The equation reduces to equation 4.19 because only the first harmonic component contributes to the net energy transfer between the blade oscillation and the surrounding flow field for a pure sinusoidal movement.

$$W_{period} = \pi Am_l Ap_1 \sin(\phi_1) \tag{4.19}$$

where Ap_1 is the amplitude of the first harmonic component of the induced unsteady pressure and ϕ_1 is the phase angle lead of the first harmonic component with respect to the blade motion. For a given inter-blade phase angle, the 1st harmonic component of the unsteady pressures on the oscillating blade in a tuned cascade was obtained using the Influence Coefficient Method described in Section 4.2.3 as a sum of 1st harmonic unsteady pressures Ap_1 from blade -2 to blade +2 in the present cascade.

To integrate equation 4.19 along the chordwise direction, the unit span work done at a given spanwise section can be obtained.

$$W_{span} = \int_c \pi Am_l Ap_1 \sin(\phi_1) ds \tag{4.20}$$

Where ds is the chordwise length of surface elements.

The local aerodynamic damping is normalized by the blade vibration amplitude at the tip, the isentropic exit dynamic head and the blade chord, which is expressed in equation 4.21.

$$\begin{aligned}\xi_c &= \frac{-W_{span}}{C \cdot Am_{tip} \cdot Am_{tip} \cdot (p_{01} - p_2)} = \int_c \frac{-\pi Am_l \,|\, Cp_1 \,|\, \sin(\phi_1) ds}{C \cdot Am_{tip}} \\ &= \left(\int_c \frac{-\pi Am_l \,|\, Cp_1 \,|\, \sin(\phi_1) ds}{C \cdot Am_{tip}}\right)^{pre} - \left(\int_c \frac{-\pi Am_l \,|\, Cp_1 \,|\, \sin(\phi_1) ds}{C \cdot Am_{tip}}\right)^{suc} \\ &= \left(\int_c \frac{\pi Am_l \,|\, Cp_1 \,|\, \sin(\phi_1) ds}{C \cdot Am_{tip}}\right)^{suc} - \left(\int_c \frac{\pi Am_l \,|\, Cp_1 \,|\, \sin(\phi_1) ds}{C \cdot Am_{tip}}\right)^{pre}\end{aligned} \tag{4.21}$$

The sign convention used, defines that a positive work corresponds to a negative aerodynamic damping. A positive coefficient of aerodynamic damping indicates a stable condition when the net work input to blade vibration is negative.

The overall aerodynamic damping is obtained by integrating the local aerodynamic damping along the blade span *h*, which indicates the aeroelastic stability of oscillating blades during the three dimensional blade vibration.

$$\xi = \frac{1}{h}\int_{h} \xi_c dz \tag{4.22}$$

The aerodynamic damping under different test cases was compared to check the aeroelastic stability of the oscillating cascade over a range of inter-blade phase angles.

4.2.5 Repeatability of Unsteady Flow Measurements

The use of off-board pressure transducers requires a series of tests to obtain the unsteady aerodynamic responses of five blades in the linear cascade. Hence, there is an additional need to ensure a good repeatability of the measurements.

Forty sets of the unsteady pressure measurements were performed at reduced frequency of 0.3 to examine the repeatability. The five tapping points were chosen from the midspan of the oscillating blade. The unsteady pressure signals were obtained by the experimental procedures described above, ensemble-averaged over 50 times and corrected by the measured Tubing Transfer Function for the phase shift and amplitude distortion of the unsteady pressure signals. **Figures 4.14 - 15** show the results in the form of the deviation from the mean in phase (ϕ_1) and the deviation from the mean in amplitude of the 1st harmonic pressure response from the five tapping points. The range of the deviation in amplitude normalized by the mean value is within ± 0.05. The deviations in phase angle fall within the range of ± 3°. The corresponding standard deviation is 0.028 in $|Cp_1|$ and 1.16° in phase angle. The deviations can be attributed to random errors, and are negligibly small. Thus the results indicate a good repeatability.

For a detailed comparison between experimental data and numerical predictions, it is important to know to what extent theoretical assumptions approximate an experiment.

In general, experimental errors cannot be avoided because of difficulties in accurately measuring unsteady flow phenomena. Thus, it is extremely important to identify the source of experimental errors, to minimize and get a detailed error analysis for experimental data obtained. For an accurate physical interpretation of computational results, the information about the accuracy and uncertainties in experimental data is also necessary to validate computational results.

The main error sources of the present unsteady experiment came from two sources. One was the measuring equipment and the reliability of calibration (the pressure transducers, and the rest of the measuring chain), the other was the experimental model. In this chapter, the first source was discussed fully. The expected experimental errors are small. The performed tests are shown to be repeatable and reliable. The second source was evaluated and will be presented in the following chapter.

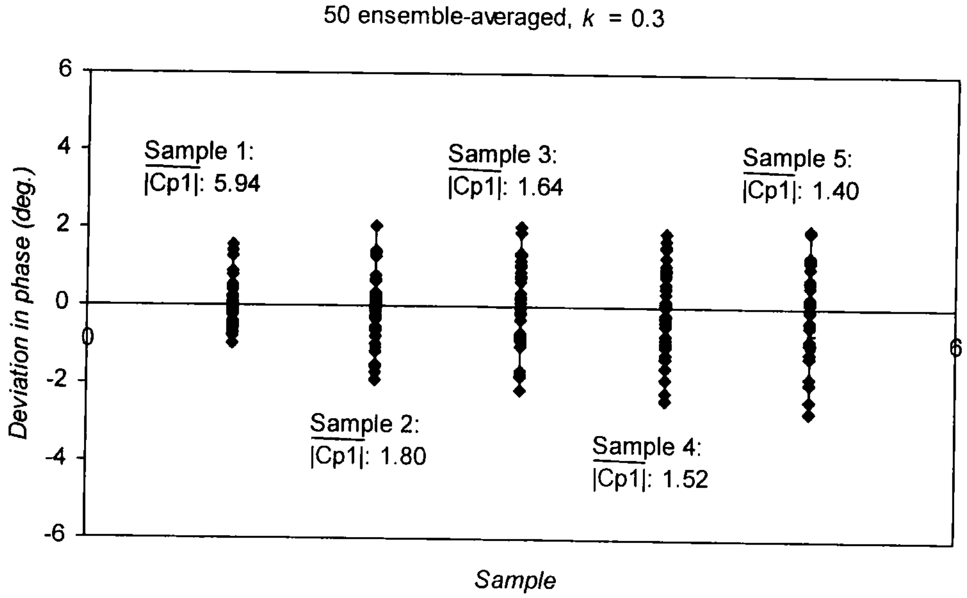

Figure 4.14: Deviation in phase of the first harmonic pressure coefficient

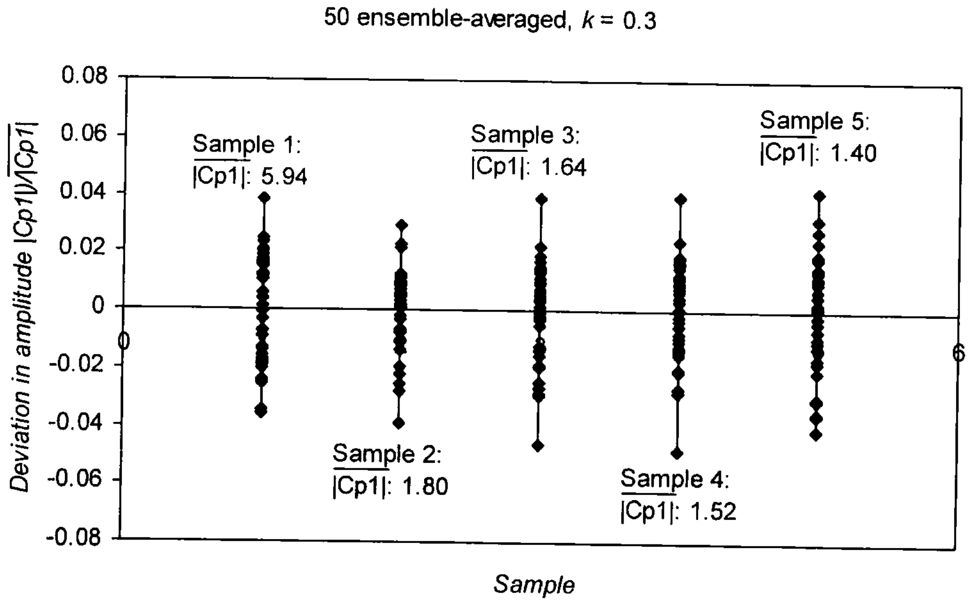

Figure 4.15: Deviation in amplitude normalized by mean value

Chapter 5

Experimental Method Validation

In this chapter the steady flow results are presented for a nominal aerodynamic loading (around 0° incidence) based on improving the blade-to-blade steady flow periodicity. The basic steady flow characteristics including the 2D steady separation bubble and the 3D end wall flow patterns, and the inlet flow conditions are examined. Following this, the validity of the experimental model - the Influence Coefficient Method – used for the construction of unsteady pressure response of oscillating blades in a tuned cascade is addressed.

5.1 Steady Flow Results

The objectives of the steady flow measurements are twofold. One is to provide the aerodynamic background for the unsteady flow measurements, i.e. to capture any steady flow phenomenon which may affect the unsteady aerodynamic response of the oscillating cascade (including the 2D separation bubble and the endwall vortical flow structures). The other is to provide the inlet flow conditions for the validation of numerical methods.

The steady aerodynamic data of interest are the inlet flow field and the detailed cascade characteristics including the inlet flow direction, the inlet total pressure loss and the blade surface static pressure distribution, which were acquired with the standard steady state instrumentation. The inlet flow conditions were recorded by traversing two three-hole probes in the spanwise and tangential (blade-to-blade) directions along the inlet measurement plane located at half chord length upstream of the leading edge of the cascade. The blade-to-blade probe surveys were conducted over four adjacent blade passages about the middle reference blade. Three tangential positions were measured in every blade passage. The blade surface static pressures were obtained from all tappings between 20% and 98% span, using the tilted manometer bank. The data obtained at 98% span are only shown for the trend reference because some tappings at 98% span on the two instrumented blades were blocked during the manufacture (six tappings on the suction surface and five tappings on the pressure surface of the reference blade, and one on the suction surface of the instrumented stationary blade). Since the experimental model of the Influence Coefficient Method was used to obtain the unsteady pressure response of a tuned cascade, the blade-to-blade steady flow periodicity was very important, which is discussed before the inlet flow conditions are presented.

5.1.1 Blade-to-Blade Periodicity

For a linear cascade to be a valid simulation of a tubomachinery blade row and a suitable facility for unsteady pressure measurements based on the Influence Coefficient Method, the cascade must exhibit a good blade-to-blade periodicity for the steady flow field. Prior to the unsteady pressure measurements, an effort was made at the test rig setting to verify and improve the blade-to-blade periodicity. Four configurations of the working section were investigated in order to improve the periodicity. A CFD code was used to provide a baseline to understand the behaviour of the original facility. The distribution of the surface static pressures on the middle three blades gave a rigorous assessment of periodicity. In particular, the blade-to-blade periodicity for the middle three blades is important for the present cascade because the main unsteady aerodynamic influences, as will be seen in Section 5.2, come from the middle three blades.

The working section described in detail in Section 3.2.2 was a linear cascade, which was hinged about the axis on the top end with the wind tunnel in order to adjust the inlet flow angle. The moveable plate was fixed on the wood frame of the cascade and rotated with the cascade together to extend the sidewall of the wind tunnel. There was a gap on each side between the perspex sidewall of the cascade and the moveable plate to generate a 'clean' flow field to the cascade.

5.1.1.1 Original Design of Working Section

The original design of the working section is shown in **Figure 5.1**. The moveable plate was extended downstream to the outlet of the wind tunnel. The width of the gap between the perspex sidewall of the cascade and the moveable plate was 3*mm*. The bottom plate separated the flow into two parts: the main flow and the bypass flow as shown in **Figure 3.5.** The blade-to-blade periodicity was adjusted by the bottom plate.

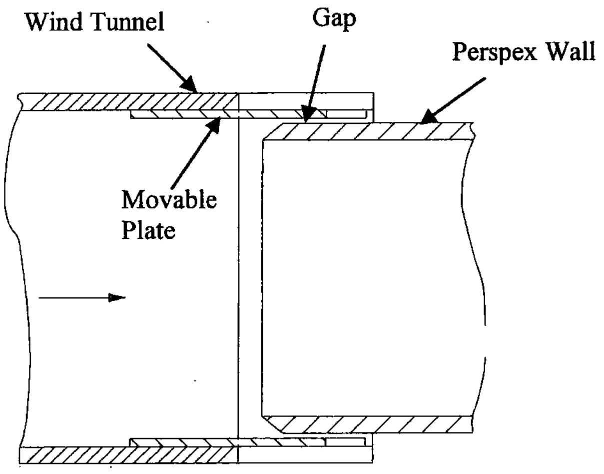

Figure 5.1: The original design of the working section (top view)

The blade-to-blade variations are shown in **Figure 5.2** in the form of the blade surface pressure coefficient Cp measured at 50% span on the middle three blades with the proper adjustment of the bottom plate. The original definition of Cp is

$$Cp = \frac{p - p_1}{p_{01} - p_1} \tag{5.1}$$

Here, p_1 is the inlet static pressure and p_{01} is the inlet total pressure, both were measured using a Pitot-static tube with its tip located at one chord length upstream of the leading edge of the cascade, p is the measured blade surface pressure.

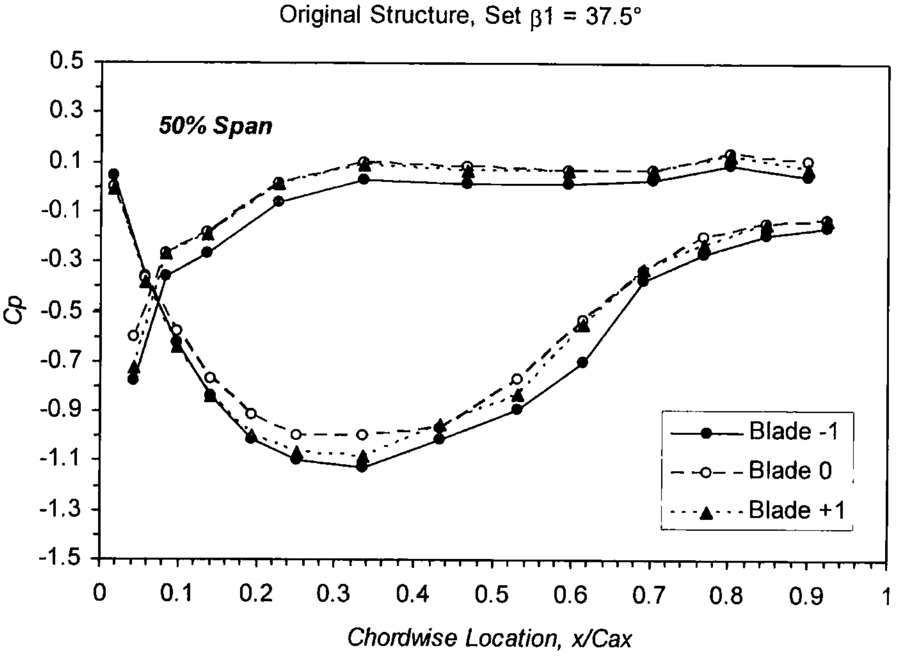

Figure 5.2: Surface static pressure distribution on the middle three blades for original structure

Figure 5.2 indicates a non-periodic loading along the tangential direction of the cascade. Compared with the steady flow results presented in **Figure 5.3** from Sanger & Shreeve (1986), the shape of the surface static pressure distribution is similar to that measured at the inlet flow angle of 28° in this literature and the whole pressure distribution was shifted to the lower values along the vertical axis. These indicate the inlet flow to the cascade was not horizontal as designed, and the measured value of p_1 was higher than that should be, which was caused by the blockage at the inlet of the working section due to the existence of the movable plate (**Figure 5.1**).

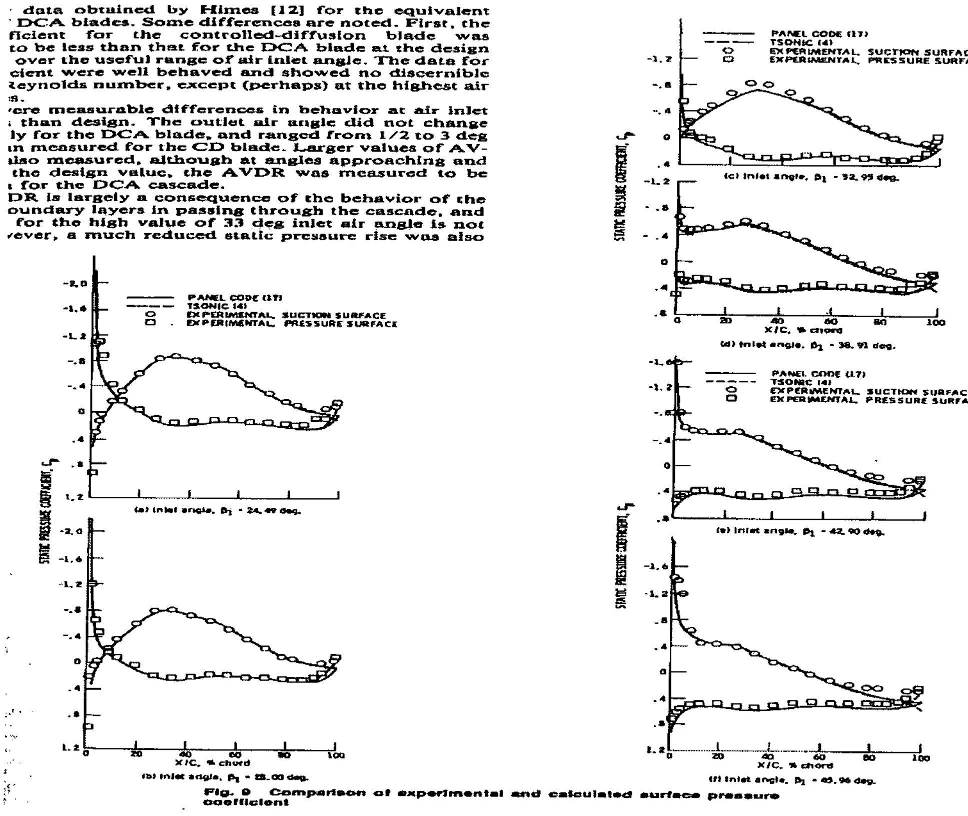

data obtuined by Himes [12] for the equivalent
DCA blades. Some differences are noted. First, the
ficient for the controlled-diffusion blade was
to be less than that for the DCA blade at the design
over the useful range of air inlet angle. The data for
cient were well behaved and showed no discernible
eynolds number, except (perhaps) at the highest air
s.
ere measurable differences in behavior at air inlet
than design. The outlet air angle did not change
ly for the DCA blade, and ranged from 1/2 to 3 deg
n measured for the CD blade. Larger values of AV-
lso measured, although at angles approaching and
the design value, the AVDR was measured to be
for the DCA cascade.
DR is largely a consequence of the behavior of the
oundary layers in passing through the cascade, and
for the high value of 33 deg inlet air angle is not
ever, a much reduced static pressure rise was also

Fig. 9 Comparison of experimental and calculated surface pressure coefficient

Figure 5.3: Surface static pressure distributions at six inlet flow angles from Sanger & Shreeve (1986)

5.1.1.2 Four Modifications to Working Section

The initial attempts to improve the cascade periodicity used the experimental measurements to study the effect of the blockage caused by the moveable plate at the inlet. Four modifications are presented in **Figure 5.4.** Structure 1(S1) is to cut slots along the tangential direction in the two moveable plates, structure 2 (S2) is to cut off part of the moveable plates out of the frame of the cascade, structure 3 (S3) is to cut off all moveable plates out of the frame of the cascade and structure 4 (S4) is to extend the perspex wall upstream till one chord length to the leading edge of the cascade.

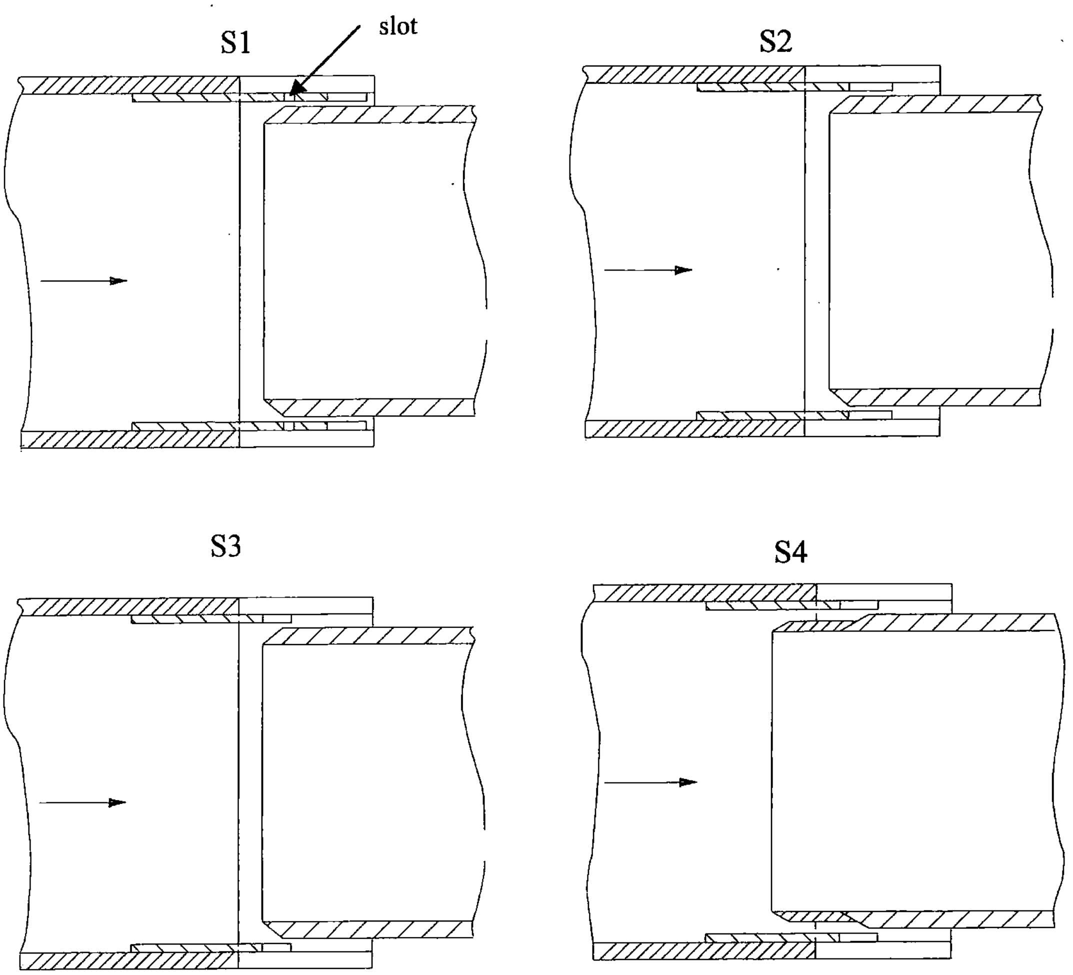

Figure 5.4: Four modifications to the working section

The surface pressure distributions for the corresponding structures (S1, S2, S3 and S4) are presented in **Figures 5.5 - 5.8** with the proper adjustment of the bottom plate respectively. The solid line is the inviscid CFD calculation.

The definition of *Cp* expressed in equation 5.2 was used in **Figures 5.5 - 5.8** due to the inconstant values of the inlet static pressure p_1 measured at one chord upstream of the leading edge of the cascade. The inlet static pressure was changed by the different blockages of the movable plate shown in **Figure 5.4**.

$$Cp = \frac{p - p_{01}}{(p_{01} - p_2) * R^2} + 1 \tag{5.2}$$

where p_2 is the ambient pressure which the cascade exit is subject to, and R is the blade area ratio of the exit to the inlet (A2/A1 = 1.172 for this Controlled-Diffusion Blade).

For all these modifications, with the good agreement of the measured and the predicted surface static pressure distribution, the difference between the experimentally set and the numerically set inlet flow angle is in the range of 6° - 9°, which indicates the inlet flow was deviated in yaw direction. The blade-to-blade variations show that the periodicity was not significantly improved.

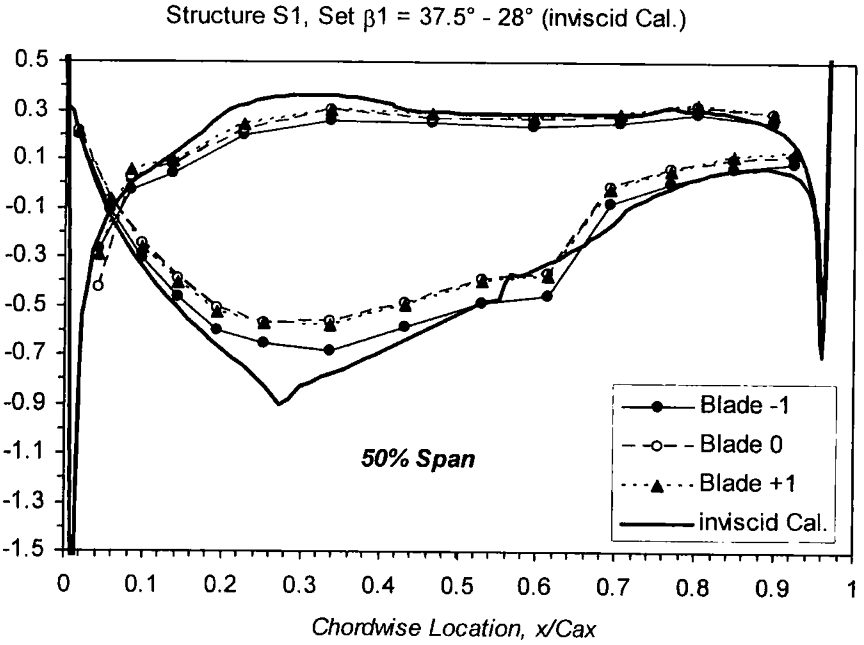

Figure 5.5: Surface static pressure distribution for structure S1

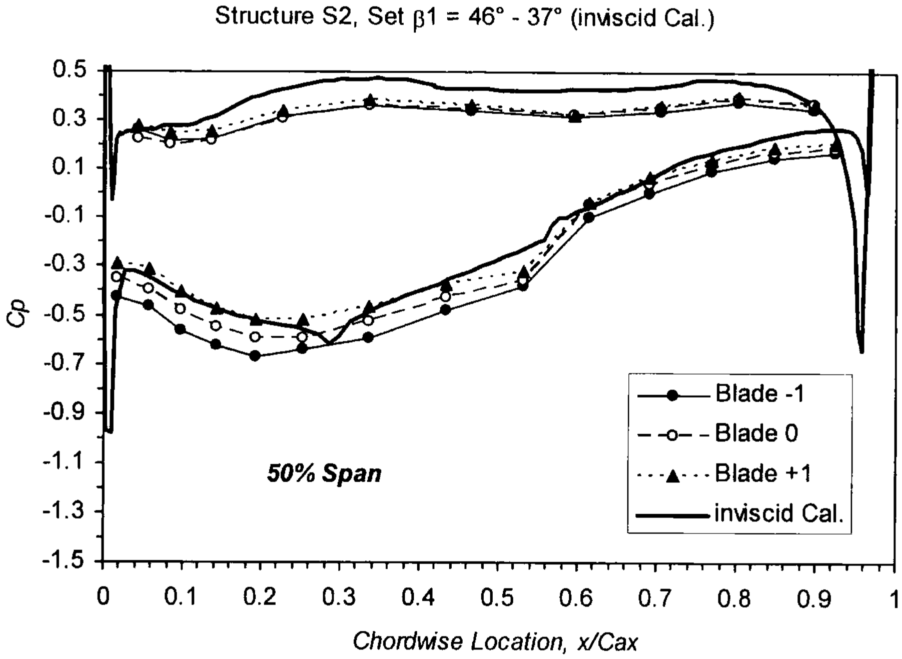

Figure 5.6: Surface static pressure distribution for structure S2

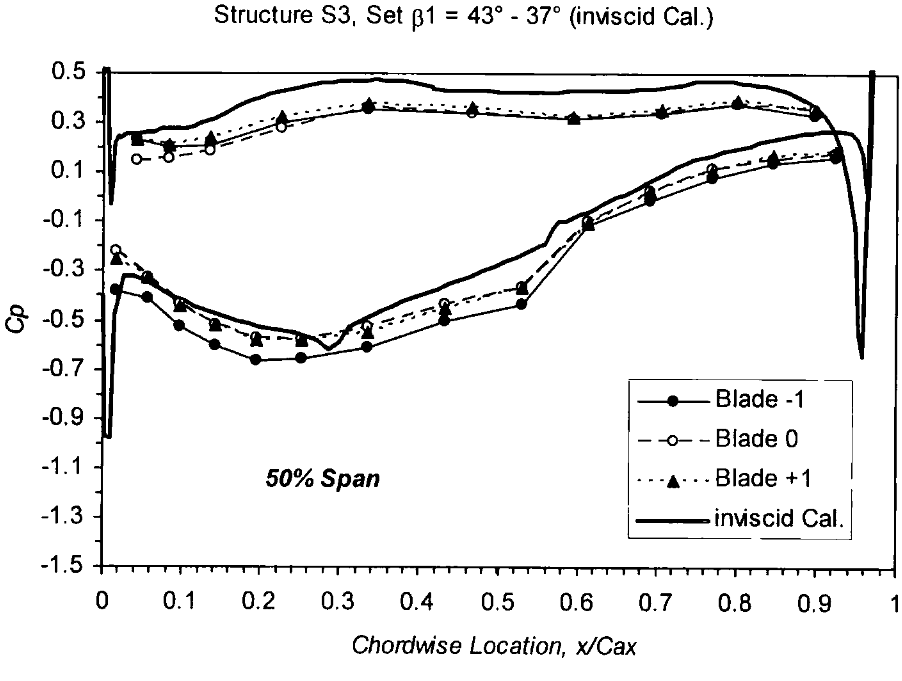

Figure 5.7: Surface static pressure distribution for structure S3

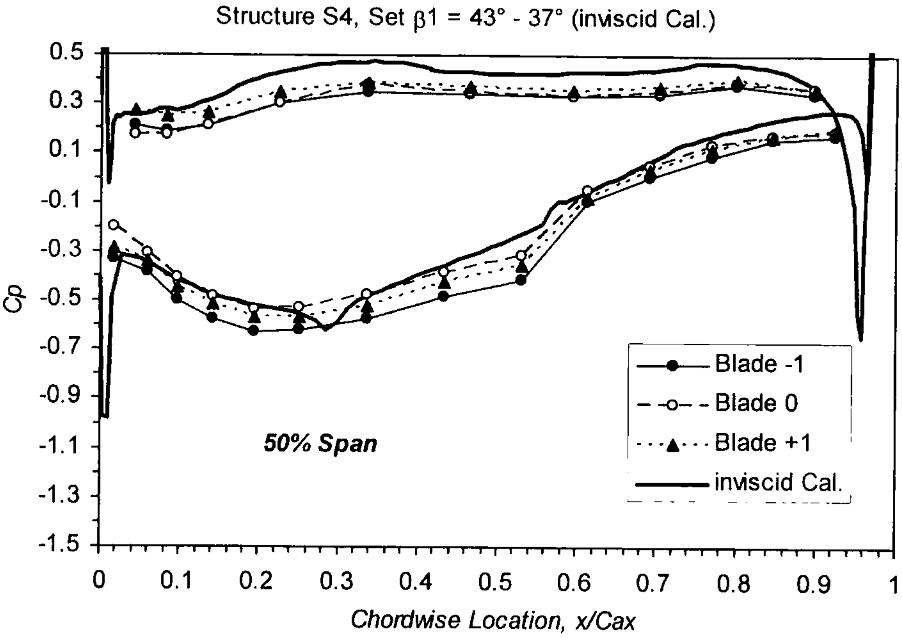

Figure 5.8: Surface static pressure distribution for structure S4

5.1.1.3 Final Modification

With an appreciation of the deviation flow angle in yaw, the final modification was made in order to avoid the main flow disturbed by the inclined position of the bottom plate. That was to keep the bottom plate horizontal and to add a small nozzle to diffuse the bypass flow, which gave the same diffusion ratio as that of the linear cascade, and thus to keep the inlet flow along the leading edge of the bottom plate uniform, as shown in **Figure 3.5**.

The final attempt to improve the cascade periodicity was to study the effect of the side bleeding from the gaps. After a certain trial and error adjustment of the side bleeding, a good blade-to-blade periodicity has been achieved with the deviation of the surface static surface pressures on the middle three blades within a 5% range at all span locations. The surface static pressure coefficient is defined finally in equation 5.3 and used for the rest of the thesis.

$$Cp = \frac{p - p_2}{p_{01} - p_2} \tag{5.3}$$

Here, p is the surface static pressure and p_{01} is the inlet total pressure measured at the midspan position one chord length upstream of the leading edge of the cascade using the Pitot-static tube.

Figures 5.9 - 5.13 show the surface static pressure distribution at the five span locations (20% (near the blade hub), 50%, 70%, 90%, and 95% span) respectively on the middle three blades. The main differences show up on the suction surface near the leading edge as well as in the near end wall region, as expected. Overall, the periodicity of the middle three blades is reasonably good at each span section, which forms a sound aerodynamic baseline for the unsteady flow measurements in the present experiment by using the Influence Coefficient Method.

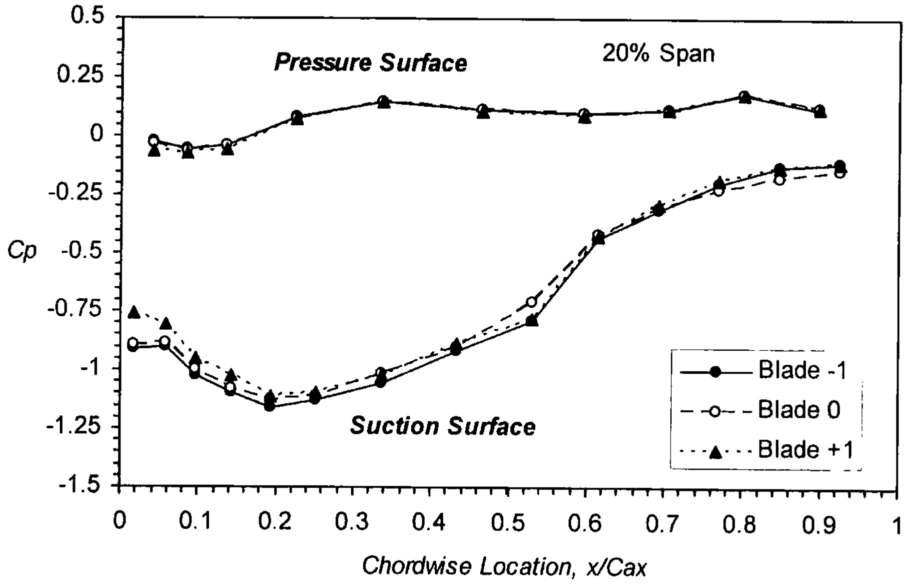

Figure 5.9: Surface static pressure distribution at 20% span

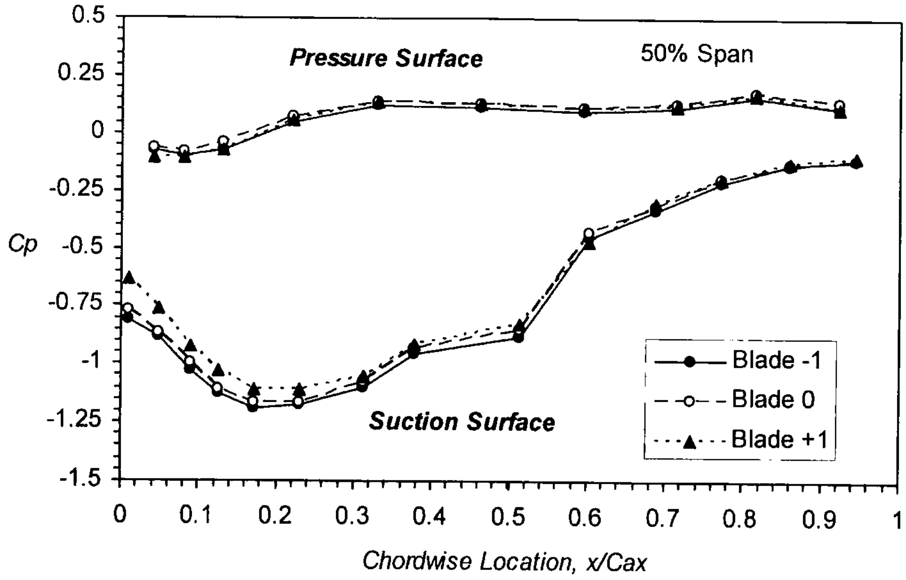

Figure 5.10: Surface static pressure distribution at 50% span

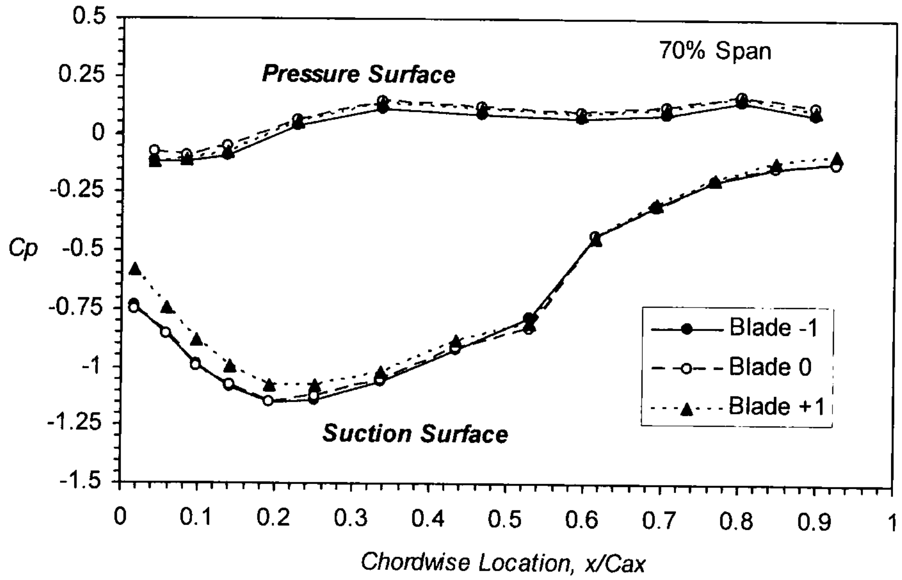

Figure 5.11: Surface static pressure distribution at 70% span

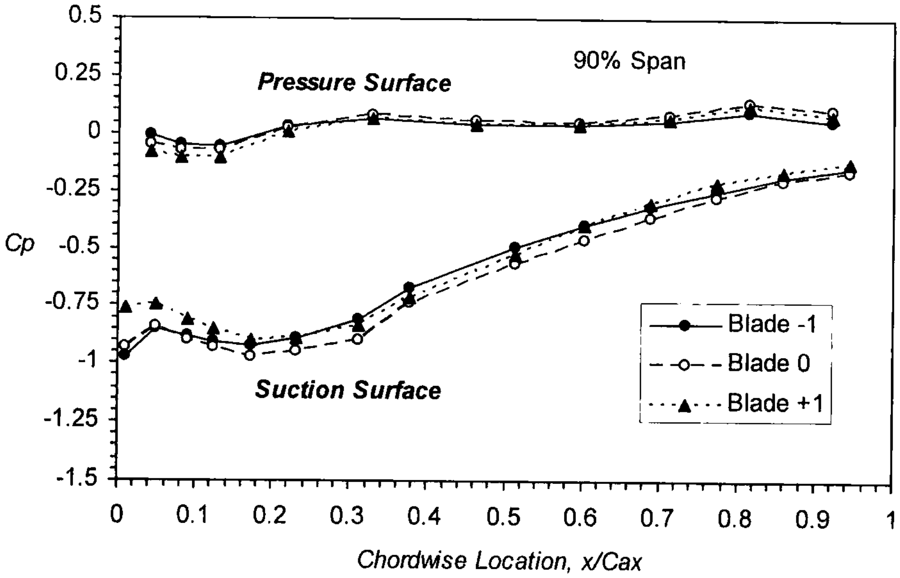

Figure 5.12: Surface static pressure distribution at 90% span

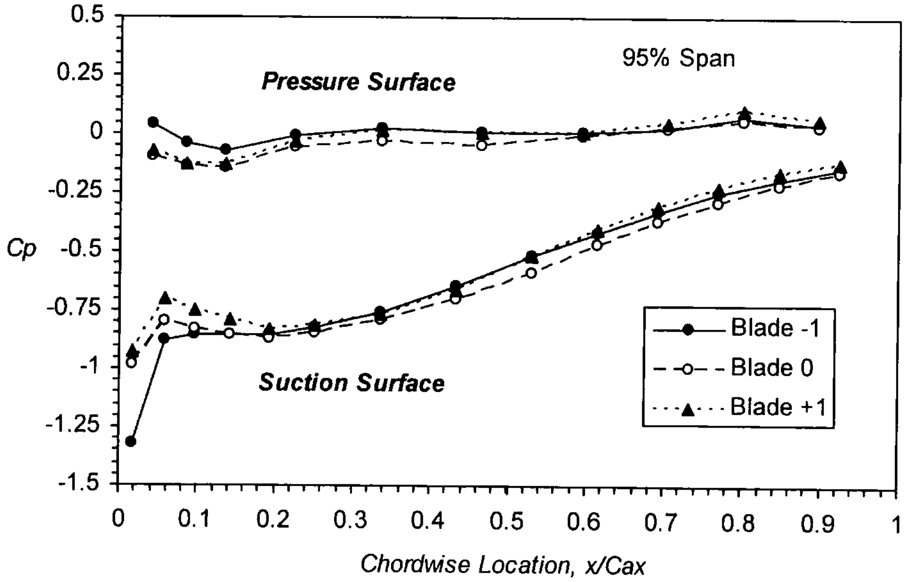

Figure 5.13: Surface static pressure distribution at 95% span

5.1.2 Main Steady Flow Characteristics

To quantify the main steady flow characteristics at the nominal flow condition including a 2D steady separation bubble and the end wall flow unloading, surface static pressure distributions at the six span sections on the middle three blades are presented in **Figures 5.14 - 5.16**.

It is noted that there are lower pressures at 54% chord between 20% and 70% span on the suction surface of blade -1 and blade +1, between midspan and 70% on the suction surface of blade 0, which are identified as the bubble-type laminar flow separation and are confirmed by the unsteady pressure results presented in Sections 6.1 and 6.2.2.

The 2D laminar separation was located in the region downstream of the suction peak. The separation zone was found to diminish near the end wall regions. The interchangeable instrumented blade was used to measure the surface static pressures at position blade -1 and blade +1, and thus the end wall configuration of the two positions was same. In order to cover the air leakage induced by the blade vibration mechanical system (blade 0 was hinged at hub outside the test section), the end wall geometry of the middle reference blade at the hub was different from that of its adjacent blades. Hence, the influence of the end wall vortex, which was caused by the endwall boundary layer and the flow deflection in the blade passage, on the 2D separation bubble of the middle blade was a little different from that of its adjacent blades, which extended further along the spanwise direction on the middle blade. Thus, the 2D separation bubble at 20% span on the middle blade was not clear than that on its immediately adjacent blades. Although there are no tappings located at 30% span, the 2D separation bubble can be at least identified from 30% to 70% span because the steady flow field is largely symmetrical about the midspan without the influence of blade tip-clearance. It should be commented that the Reynolds number of the present case was relatively low (Re = 195000). At higher and more realistic Reynolds numbers in compressors, there was the same type of laminar separation bubble, though the chordwise location was moved more upstream (Sanger & Shreeve 1986) for the same blade geometry.

Figures 5.14 to 5.16 indicate the uniform steady loading over the majority of the middle three blade surfaces, between 20% and 70% span except the first point on the suction surface. In the end wall region (from 90% span), there are evident deviations in the static pressure distribution over the suction surface of the three blades, and slight deviations over the pressure surface. These deviations resulted from the blockage, which was caused by the blade passage vortex as reported in Sasaki & Breugelmans (1998)'s work with high loading at the midspan and less loading at the end wall.

Overall, there is the reasonable uniform steady loading at each span section on the middle three blades, which forms a reasonably sound basis for the unsteady pressure measurements, which were thus performed at the nominal steady flow conditions.

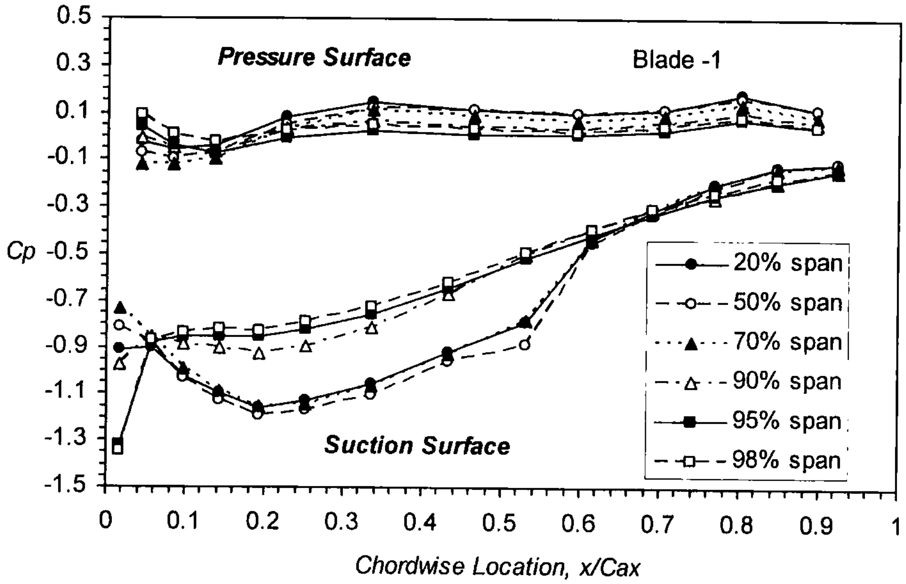

Figure 5.14: Surface static pressure distribution on blade -1

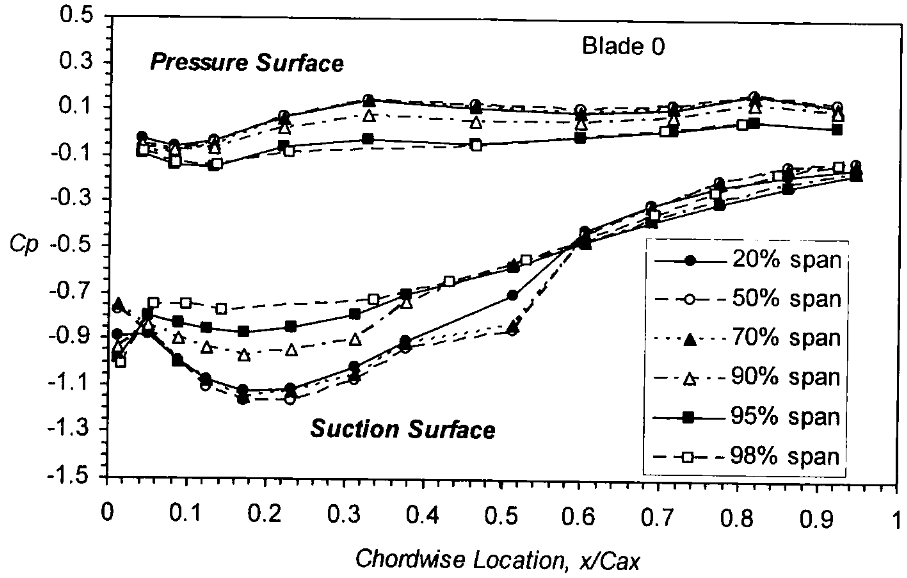

Figure 5.15: Surface static pressure distribution on blade 0

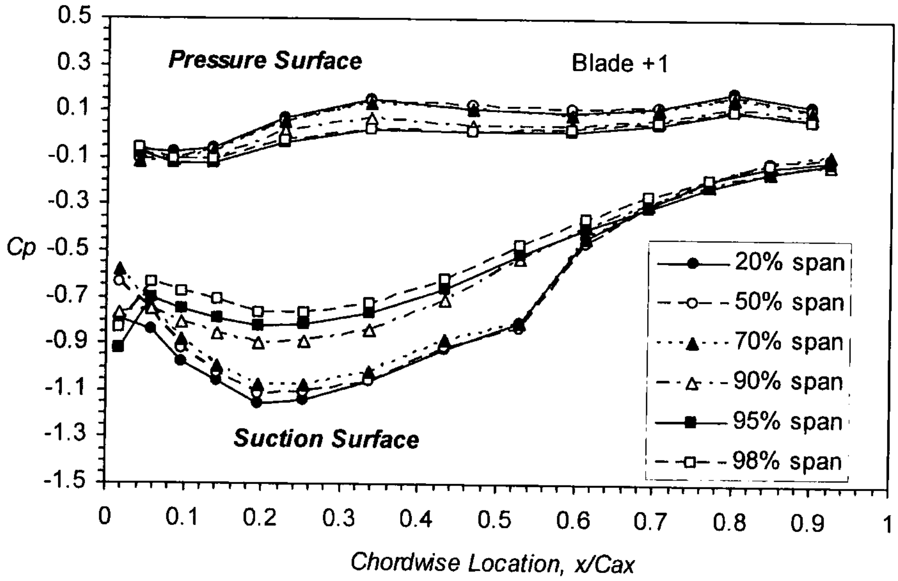

Figure 5.16: Surface static pressure distribution on blade +1

5.1.3 Inlet Flow Conditions

5.1.3.1 Measured Inlet Flow Angles along Tangential Direction of Cascade

The definitions of the inlet flow angle β_1, and the deviation flow angles in pitch and yaw were indicated in **Figure 4.1.**

Figure 5.17 shows the passage-averaged deviation flow angle in yaw and pitch at each spanwise location. The deviation flow angles in pitch are in 1° band between 20% and 80% span. They are symmetrical about the middle span except for that at 10% span, and these deviations increase as the perspex sidewall is approached, while it is not evident in the deviation flow angles in yaw. The variations of the deviation flow angle in yaw are less than 1° between 10% and 90% span.

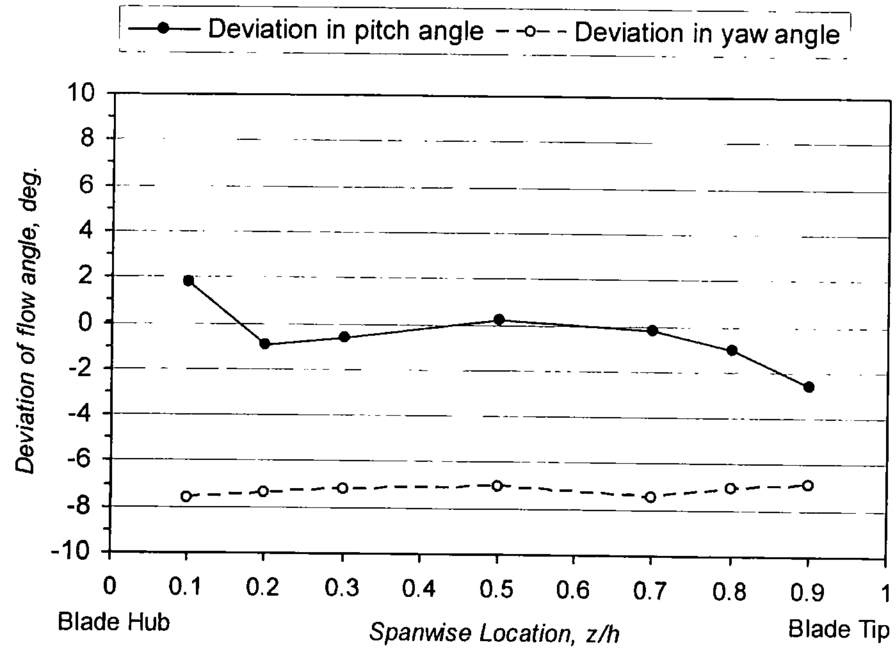

Figure 5.17: The passage-averaged deviation flow angle in pitch and yaw along the blade span

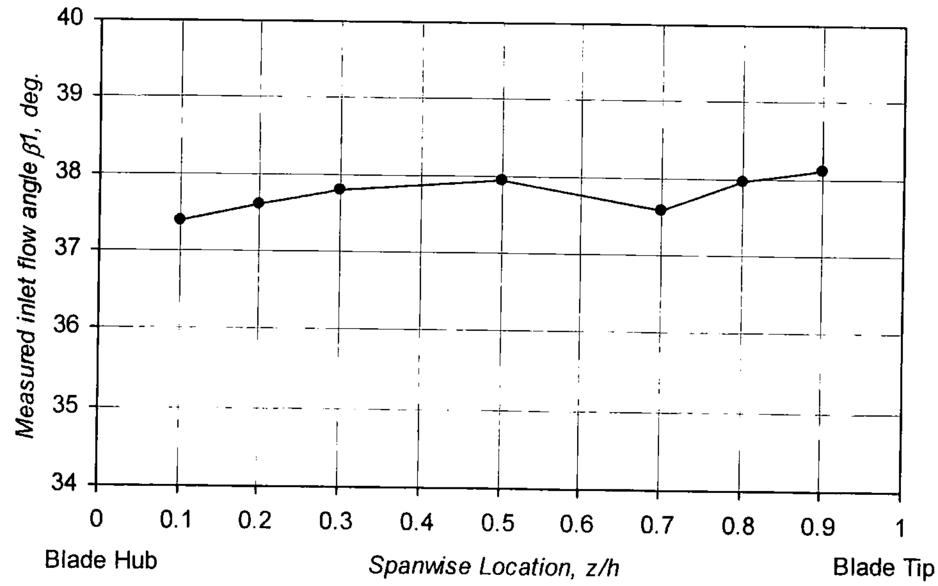

Figure 5.18: Passage-averaged inlet flow angle along the spanwise section

Figure 5.18 presents the passage-averaged inlet flow angle along the spanwise location, which was measured relative to the horizontal direction and is equal to the sum of the geometrical inlet flow angle and the measured deviation flow angle in yaw. The steady and unsteady flows were investigated for the measured inlet flow angle.

5.1.3.2 Inlet Total Pressure Loss

The disadvantage of three-hole probes is that they only determine flow angles in one plane, however, the kind of three-hole probe used showed that all three pressures were effectively insensitive to the plane (in which the three holes were located in) within the range ± 12° (Bryer & Pankhurst 1971). Thus, the average total pressure loss at each spanwise position can be obtained according to the total pressure corrections only in the yaw angle measurements.

The passage-averaged inlet total pressure loss distribution from the midspan to the blade tip is shown in **Figure 5.19** with the setting of zero blade tip-gap. The higher total pressure losses near the endwall were due to the endwall inlet boundary layer, starting to grow about one chord upstream of the blade leading edge. Neglecting the tip-clearance effect on the upstream flow, the cascade can be assumed symmetrical about the midspan and so is the total pressure loss distribution.

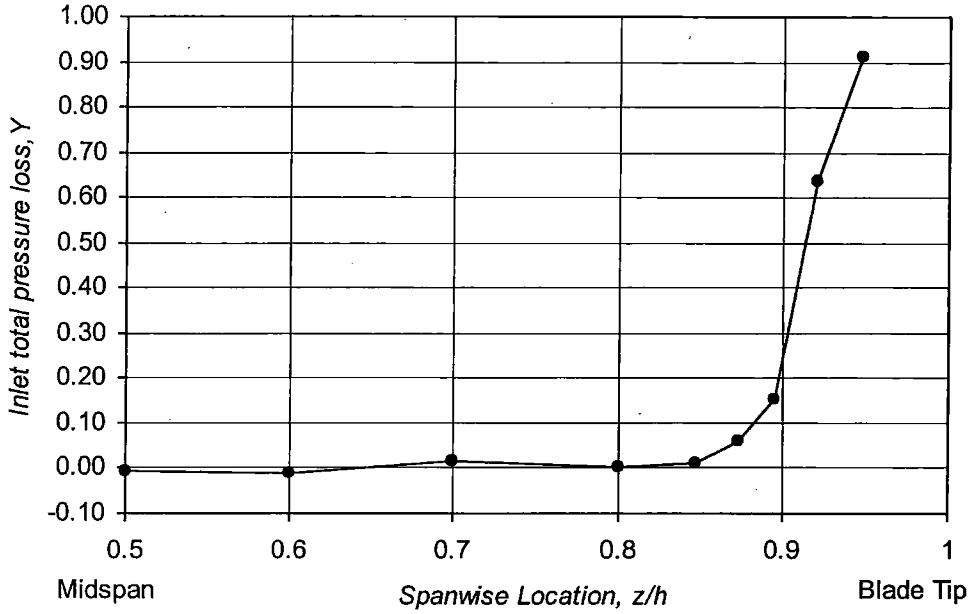

Figure 5.19: Inlet total pressure loss at a nominal aerodynamic loading with zero blade tip-gap

5.2. Validation of Influence Coefficient Method

For validation of the Influence Coefficient Method in the present experiment, two aspects are essentially required. One is a sufficient decay of the unsteady pressure responses on those blades far from the oscillating blade to ensure that only a small number of blades need to be measured. Another is the linearity of the unsteady aerodynamic response of the oscillating cascade.

The decay of the aerodynamic influence coefficients is demonstrated in **Figures 5.20 and 5.21**, which show the first harmonic pressure coefficient at midspan on the blade -2 to the blade +2 at $k = 0.4$ due to the oscillation of the reference blade. The unsteady aerodynamic responses on the suction surface (**Figure 5.20**) converged quite quickly with increasing distance from the oscillating blade. The responses on the pressure surfaces (**Figure 5.21**) converged even faster. There was greater unsteady response on the blade 0 than that on its adjacent blades shown in **Figures 5.20 and 5.21** with the maximum value at the blade leading edge. The same level of the aerodynamic influences on the suction surface of the blade –1 and on both surfaces of the blade +1 was produced, but the affected chordwise location was different. The blade -1 was affected largely at 30% chord on the suction surface and the blade +1 was influenced strongly at the leading edges of both blade surfaces. This resulted from the fact that the corresponding flow area had predominant change at 30% chord on the blade -1, whereas the leading edge on the blade +1 when the reference blade vibrated. The responses on the blades "±2" were of much smaller and insignificant magnitudes. The overall aerodynamic damping components contributed from the middle five blades to a tuned cascade at IBPA 0° also confirms the same trend (**Figure 5.22**). It is seen that, the reference blade itself gave the main stable contribution to the overall aerodynamic damping, and the adjacent blades gave obviously decreased contributions with increasing the distance from the reference blade. The influence on the upper blades (Blade +2, Blade +1) had a reduced effect on the overall aerodynamic damping at IBPA 0°. The primary reason is that the aerodynamic influence on the blades +1 and +2 was largely from the aft portion of the reference blade. In contrast, the aerodynamic influence on the blades –1 and –2 located below the reference blade was largely from the leading edge region of the reference blade, where the unsteady aerodynamic pressures were large. So, the blades -1 and -2 had more unsteady aerodynamic influences than the blades +1 and +2.

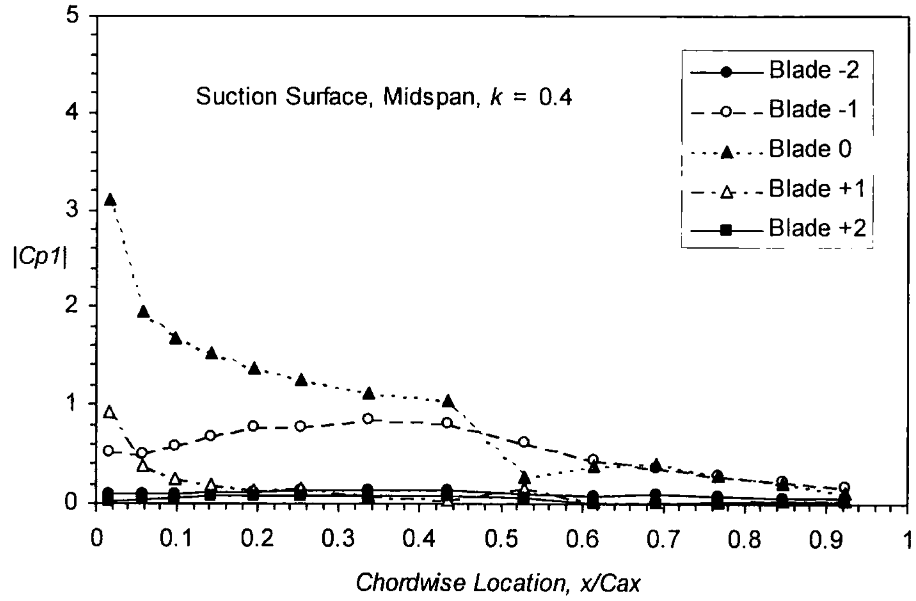

Figure 5.20: Unsteady pressures due to the oscillation of blade 0 at midspan at *k* = 0.4 on the suction surface of the middle five blades

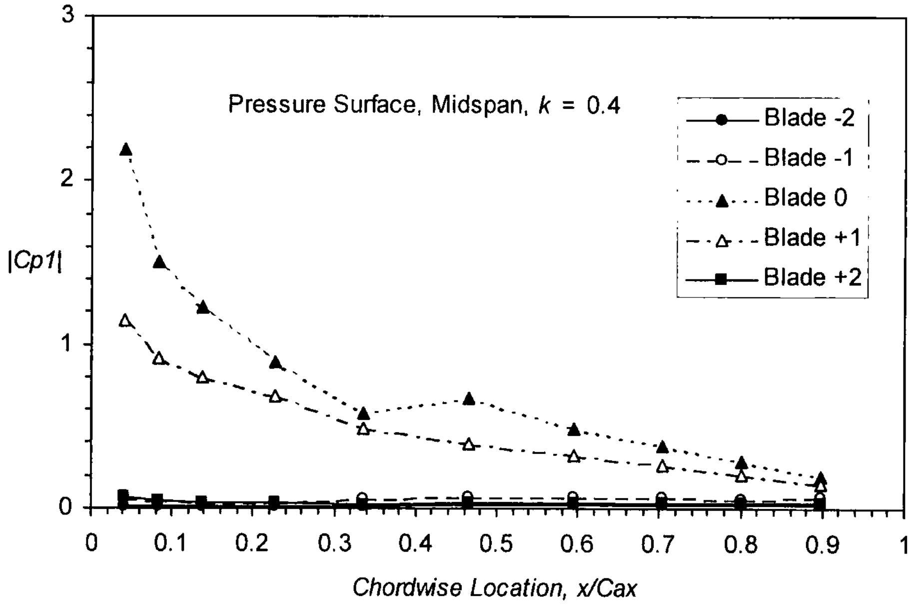

Figure 5.21: Unsteady pressures due to the oscillation of blade 0 at midspan at *k* = 0.4 on the pressure surface of the middle five blades

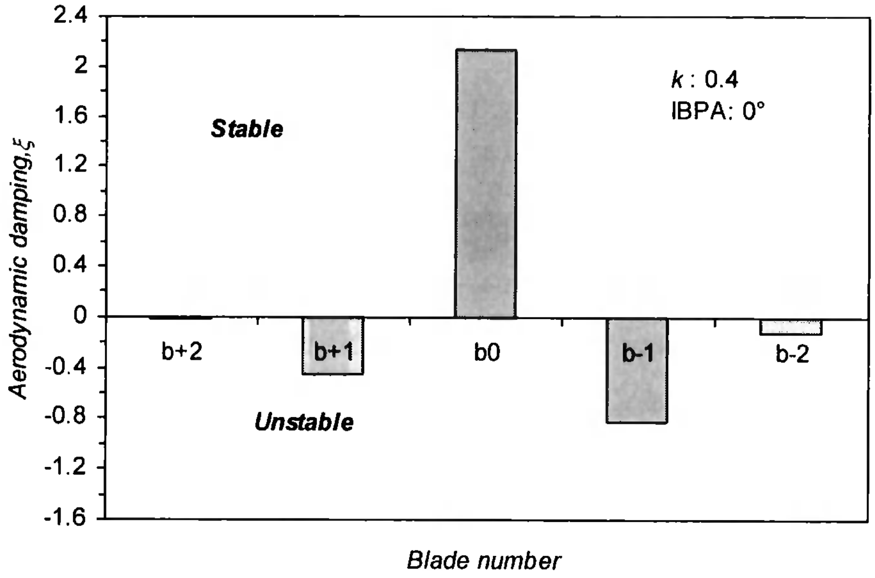

Figure 5.22: Aero-damping components contributed from the middle five blades (IBPA 0° and $k = 0.4$)

The linear assumption is not only fundamental for the validation of the Influence Coefficient Method, but also of general interest to the unsteady aerodynamic modelling. For the present test cascade, there were a 2D laminar separation bubble on the suction surface, and a large area of passage vortex near the end wall whose influence reached around 20% - 30% span from the endwall. Therefore, the linearity issue was required to be experimentally checked.

The unsteady aerodynamic responses obtained at two blade vibration (bending) amplitudes and the relative amplitude of the second harmonic pressure coefficient were used to check the linearity. Two bending vibration amplitudes (6% and 3.3% of blade chord) were provided by fixing the crank arm connecting bar on the different radial positions from the centre of the D.C. motor as shown in **Figure 3.8**.

Figure 5.23 compares the amplitude of the first harmonic pressure coefficient at 20%, 50%, 90% and 95% span on the reference blade at the two bending amplitudes, and **Figure 5.24** for the phase angle. The amplitude of unsteady pressure normalized by the corresponding blade vibration amplitude is almost identical for both cases. The phase angle also shows good agreement for both of the blade surfaces.

Regarding the relative amplitude of the 2nd harmonic pressure coefficient at five different spans on the reference blade as shown in **Figure 5.25**, a quite large relative amplitude of the 2nd harmonic is indicated at the trailing edges on both surfaces. In these regions the amplitude of unsteady pressure is small and the signal-to-noise ratio is small. The large relative amplitude of the 2nd harmonic in this region is not the indicator of non-linearity. A large peak in the relative amplitude of the 2nd harmonic is seen in the separation bubble region at 20%, 50% and 70% span on the suction surface, which is an unsteady feature of the separation bubble. In **Figure 5.26,** it is noted that the reattachment point at 54% chord had less stable condition comparing with the neighbouring points. Its destabilizing contribution to the overall aerodynamic damping was small. This local effect of the separation bubble on the unsteady flow was also demonstrated by He (1998). As a result, the separation bubble's contribution to the aerodynamic damping shows no apparently global effect. A smaller peak in the relative amplitude of the 2nd harmonic is observed around 30% chord at 50% and 70% span on the pressure surface, where there was a change of the steady flow gradient (as indicated in **Figure 5.15**) and the 1st harmonic pressure was also relatively low.

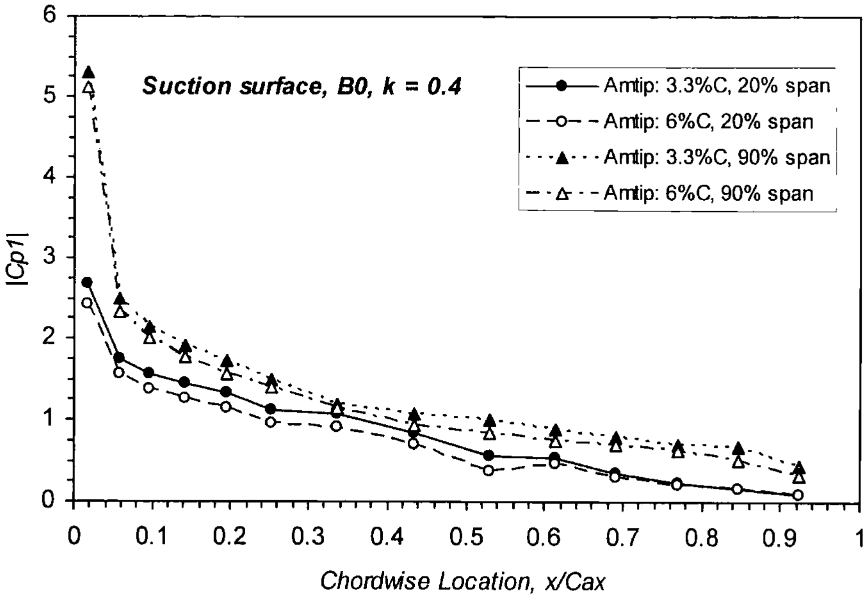

(*i*). **Suction surface 20% and 90% span**

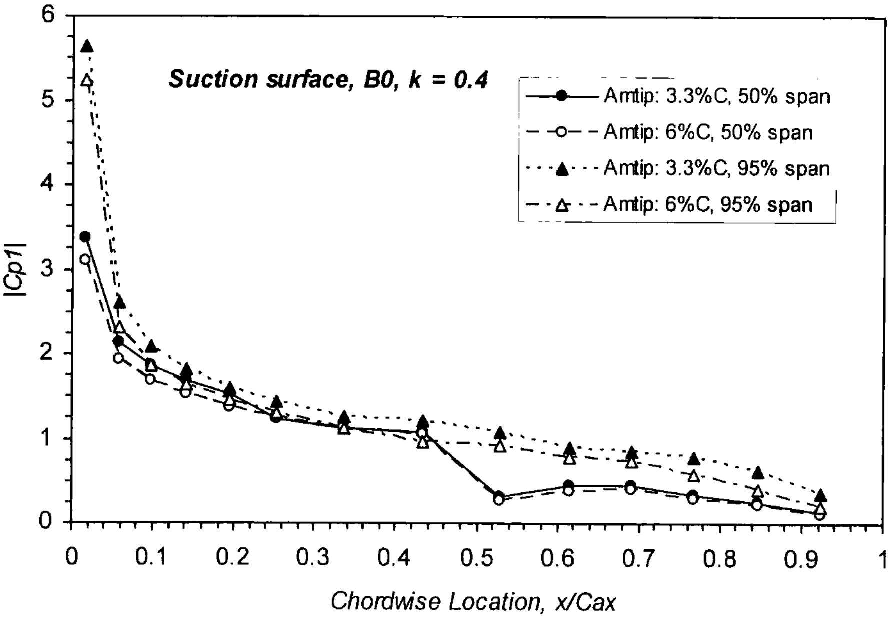

(*ii*). **Suction surface 50% and 95% span**

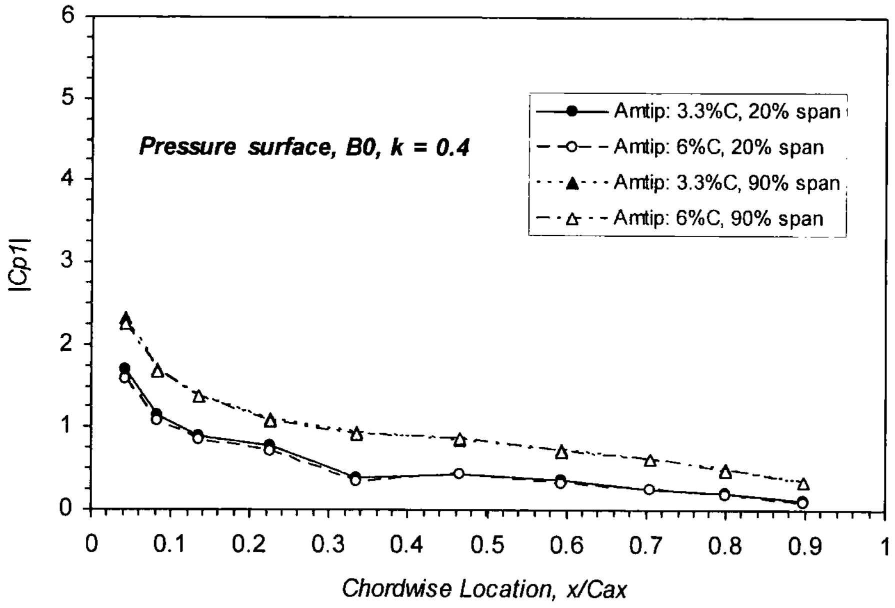

(*iii*). **Pressure surface 20% and 90% span**

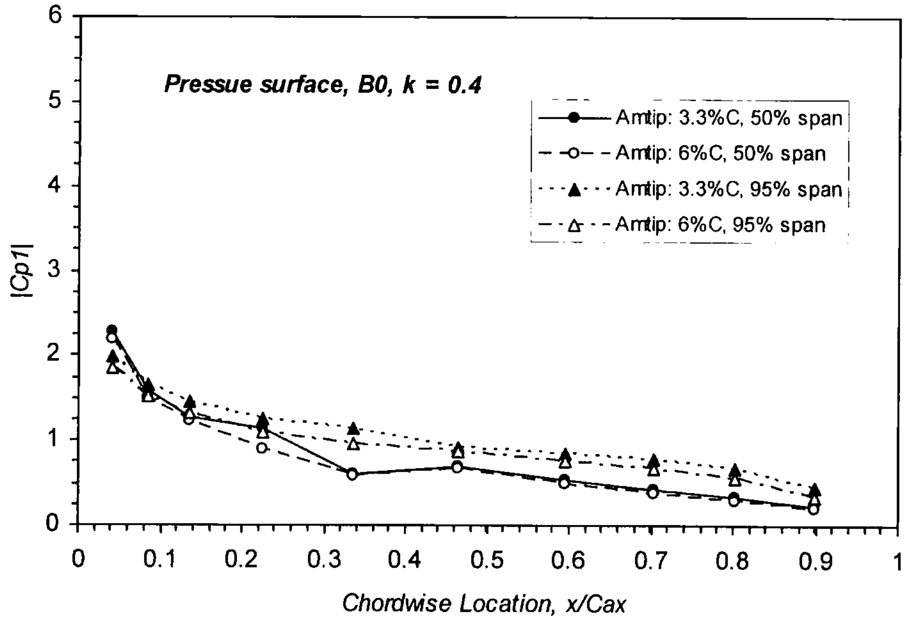

(*iv*). **Pressure surface 50% and 95% span**

Figure 5.23: Amplitude of the first harmonic pressure coefficient on the oscillating blade (at 20%, 50%, 90% and 95% span) at two oscillating amplitudes

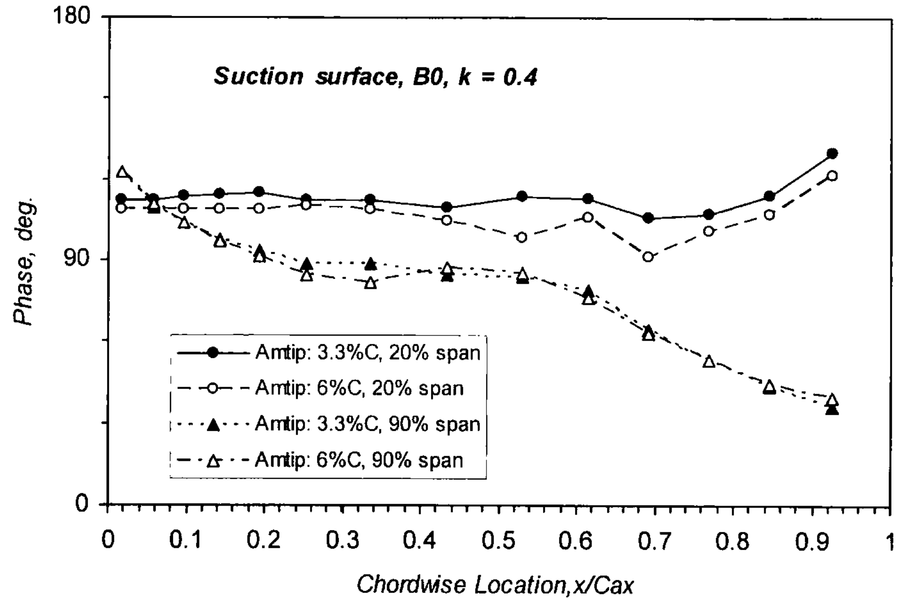

(*i*). Suction surface 20% and 90% span

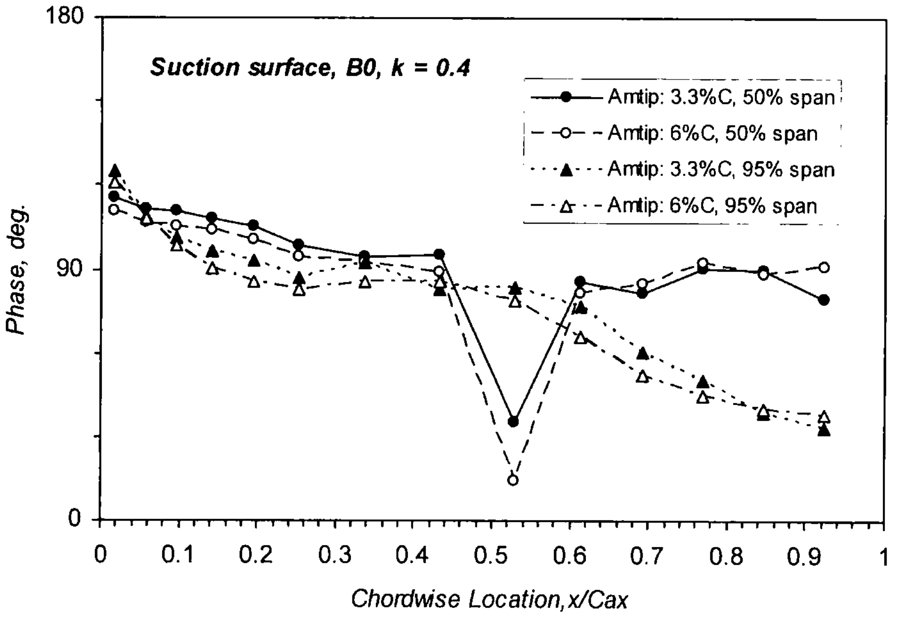

(*ii*). Suction surface 50% and 95% span

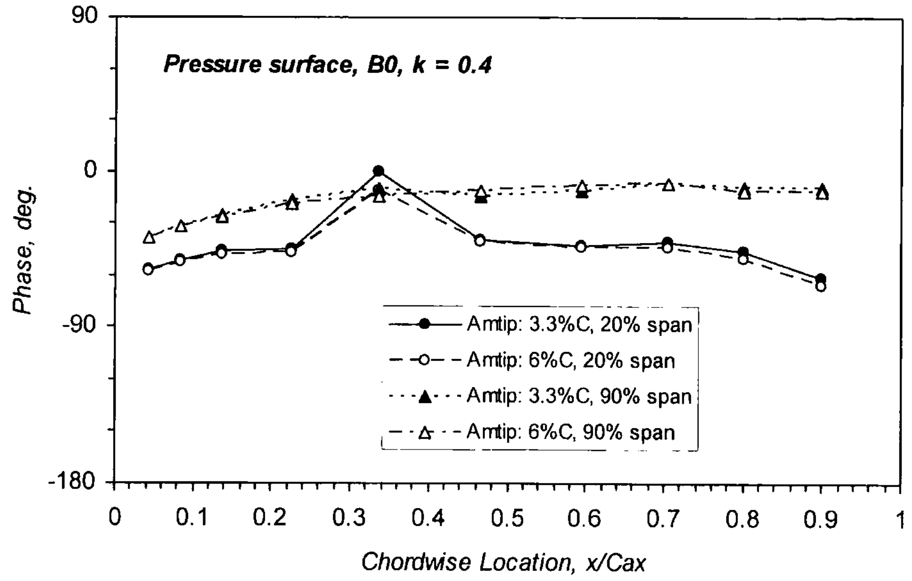

(*iii*). Pressure surface 20% and 90% span

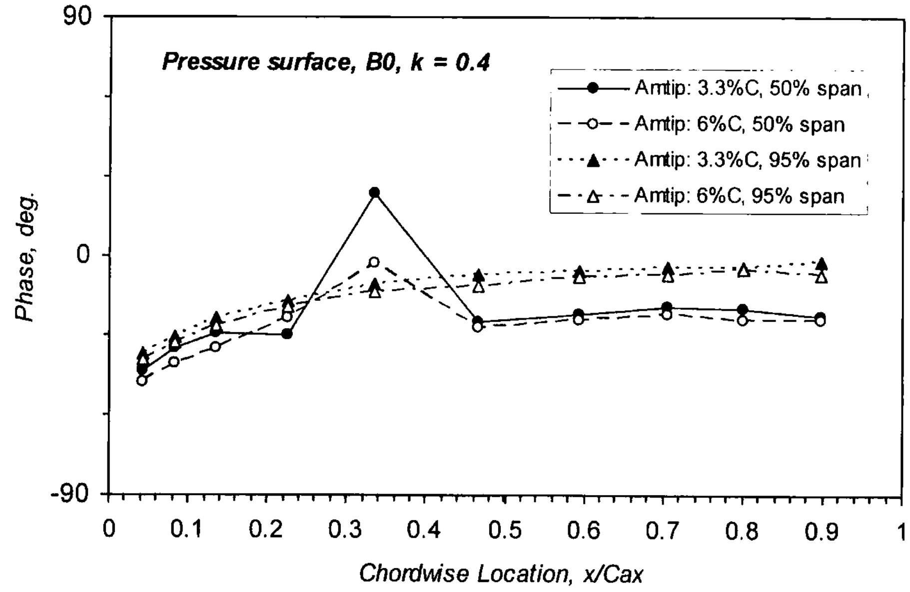

(*iv*). Pressure surface 50% and 95% span

Figure 5.24: Phase of the first harmonic pressure coefficient on the oscillating blade (at 20%, 50%, 90% and 95% span) at two oscillating amplitudes

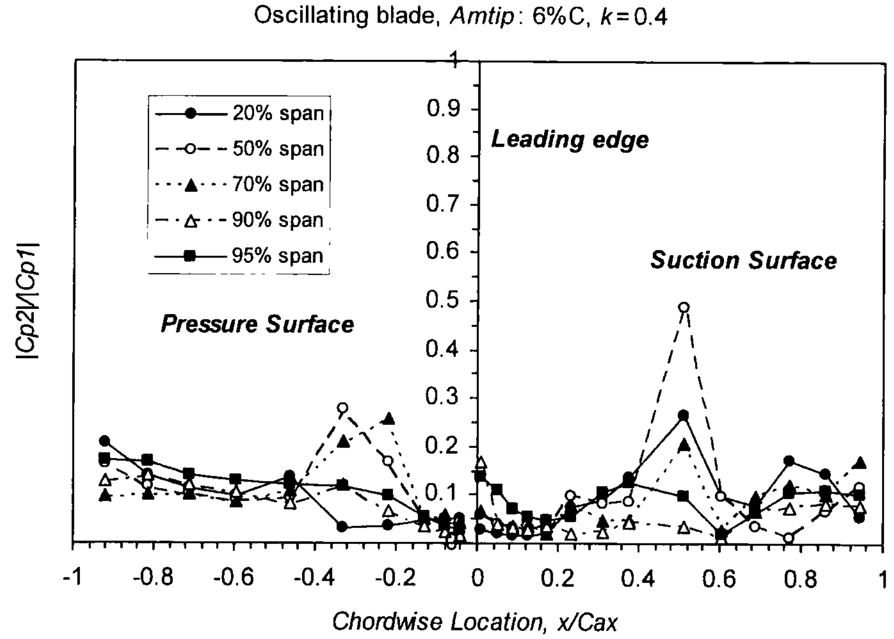

Figure 5.25: Relative amplitude of the second harmonic pressure coefficient

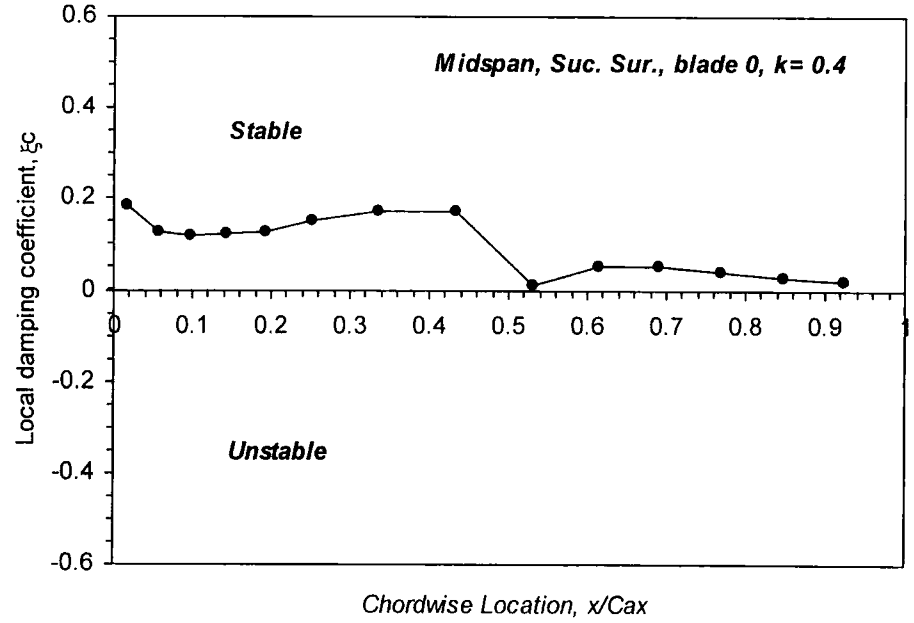

Figure 5.26: Chordwise local damping coefficient on the suction surface of blade0 at $k = 0.4$

The relative amplitude of the 2nd harmonic pressure coefficient at the tip span sections (90% and 95% span) is the same level as that at other spans. This indicates the passage endwall vortex has no nonlinear effect on the unsteady aerodynamic response of the oscillating blade although there was some unloading near the blade tip (up to 90% span) shown in **Figure 5.15.** The same conclusion can be drawn from the linear variation in the local aerodynamic damping coefficient along the blade span on the blade 0 at k = 0.4, as presented in **Figure 5.27,** which demonstrates a stable aeroelastic condition at all spanwise sections. The local aerodynamic damping follows the linear behaviour from 20% to 90% span, and the value at 95% span is slightly smaller than that obtained from the linear damping line extended from 20% span. This clearly supports the above conclusion that the passage endwall vortex has no effect on the unsteady aerodynamic response near the endwall.

Overall, the experimental results indicate the predominantly linear behaviour of the unsteady flow due to the blade vibration. Thus, the Influence Coefficient Method should be applicable to the present case.

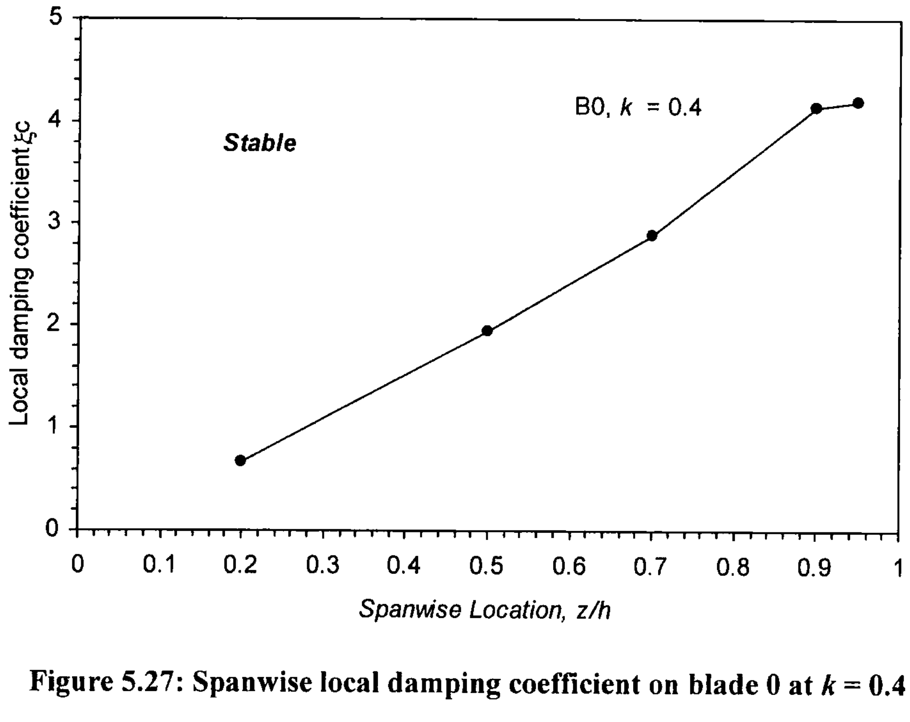

Figure 5.27: Spanwise local damping coefficient on blade 0 at k = 0.4

Chapter 6

Experimental Unsteady Flow Results and Discussions

In this chapter a detailed set of the unsteady pressure measurements at the nominal zero tip clearance is presented. The unsteady aerodynamic characteristics of the bubble-type separation, the 3D features of the unsteady aerodynamic response, and the influence of inter-blade phase angle on the unsteady aerodynamic response are demonstrated.

The unsteady pressure measurements were conducted with the middle blade vibrating in a 3D bending mode (Am_{tip}: 6% chord unless otherwise stated) at three different values of reduced frequency (k = 0.2, 0.4, & 0.6), and at an operating Reynolds number of 195000. The specification of the other operational conditions was provided in **Table 3.4**. At each setting of reduced frequency, the unsteady pressures on the oscillating blade which determine the self-induced unsteady aerodynamics, and the unsteady pressures on the stationary blades induced by the oscillating blade were measured with the instrumented stationary blade in relative positions n = -2, -1, +1 and +2. The unsteady pressure measurements were acquired at five spanwise sections between 20% and 98% span with six pressure transducers located outside the test-rig. The unsteady pressure data was digitized and ensemble-averaged in computer. The data recorded at 98% span was only used to indicate the trend and not used for data analysis due to the blocked tappings. Fourier series were used to determine the amplitude and phase angle of the harmonic components. Then, the unsteady signals were corrected for the tubing distortions by the measured Tubing Transfer Function. The discussion and presentation of the unsteady flow results are mainly concerned with the first harmonic pressure response, which determines the aeroelastic stability, and the overall aerodynamic damping, which indicates the aeroelastic stability. A particular attention is given here to the predominant 3D nature of the unsteady flow behaviour and the influence of the inter-blade phase angle on the unsteady aerodynamics by comparing the unsteady pressure response of the oscillating blade with that of a tuned cascade for a specific inter-blade phase angle obtained using the Influence Coefficient Method.

6.1 Raw Unsteady Pressure Time Traces

The ensemble-averaged unsteady pressure time traces for all tappings at 70% span on both surfaces of the reference blade are presented in **Figure 6.1**. The lowest curve in each plot is the blade motion, and the remaining curves are the unsteady pressure readings from the suction surface (upper plot) and the pressure surface (lower plot). Note that the leading edge trace has been shifted to the top, and the trailing edge trace shifted to the bottom of each plot for clarity, so that only their relative values should be referred to. The unsteady pressure signal at the leading edge on the suction surface (S1) is nearly the maximum value at time $\omega t = 0°$ of the blade vibration and decreases in time, and the signal at the leading on the pressure surface (P1) is nearly the minimum value at time $\omega t = 0°$ and increases in time. This feature may suggest that the unsteady pressure generation is significantly driven by a local incidence effect induced by the motion of the blade, instead of the passage area change. This can be illustrated in **Figure 6.2**. The induced unsteady pressure is a maximum at the leading edge on the suction surface and a minimum at the leading edge on the pressure surface at the maximum negative local incidence caused by the maximum upward velocity at time $\omega t = 0°$ of the blade vibration. While for the change of the passage area, the unsteady pressure induced on the oscillating blade is a maximum at the leading edge on the suction surface and a minimum at the leading edge on the pressure surface at time $\omega t = 90°$ when the passage gap between the oscillating blade and the upper adjacent blade is a minimum. This quasi-steady explanation is also supported by the unsteady pressures recorded on the middle reference blade shown in Section 6.2.

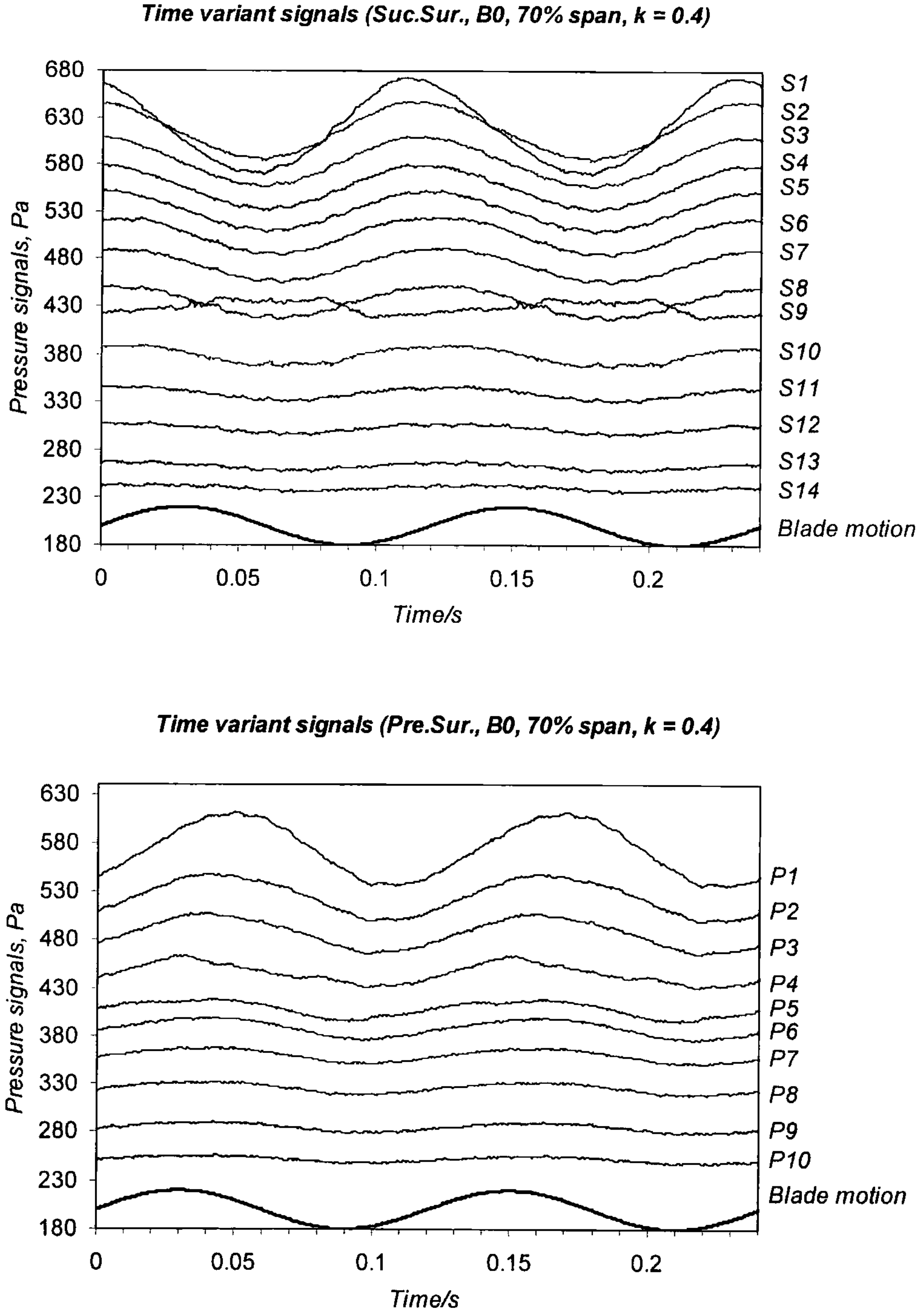

Time variant signals (Suc.Sur., B0, 70% span, k = 0.4)

Time variant signals (Pre.Sur., B0, 70% span, k = 0.4)

Figure 6.1: Ensemble-averaged unsteady signals at 70% span of Blade 0, k = 0.4 (*50 periods*)

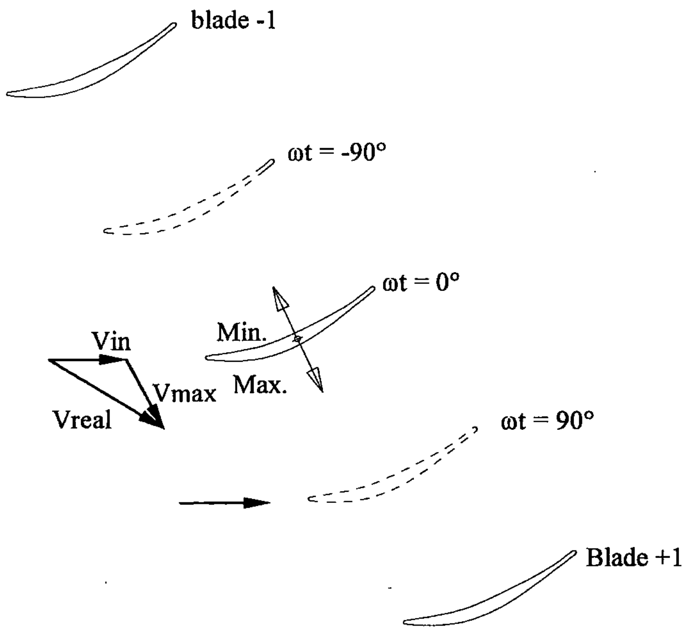

Figure 6.2: Local incidence effect on the oscillating blade (tangential scale exaggerated for clarity)

The time variant signals indicate that the unsteady pressure response over the suction surface is slightly led by the leading edge, while the unsteady pressure response is slightly led by the trailing edge over the pressure surface. This shows that a pressure wave propagates downstream from the leading edge over the suction surface and upstream from the trailing edge over the pressure surface.

It is noted that the non-sinusoidal variation observed at tapping S9 on the suction surface corresponds to the suction surface separation bubble, as mentioned in Section 5.1.2 and will be further discussed later.

6.2 Unsteady Aerodynamic Response on the Oscillating Blade - 'direct term'

As expressed in equation 4.12, the middle term of $\widetilde{Cp}_{ic}(0,0)$ is the unsteady aerodynamic pressure coefficient induced by the vibrating blade on itself, which is independent of the inter-blade phase angle and called the "direct term", while the unsteady pressure coefficient $\widetilde{Cp}_{0,tc}$ including the contributions from each blade is called the "coupling term", which varies with the inter-blade phase angle. Also equation 4.19 showed that only the 1st harmonic component of unsteady pressure contributes to the net energy transfer between the blade oscillation and the surrounding flow field for a pure sinusoidal movement. In this section, the 1st harmonic component of the direct term is presented and that of the coupling term is shown in Section 6.4. The varied experimental parameter was the reduced frequency. The amplitude and phase angle of the 1st harmonic pressure response on the oscillating blade at a range of reduced frequency (0.2, 0.4 & 0.6) are presented in **Figures 6.3 - 6.8**, which is the function of the chord location with reduced frequency. There are two figures provided for each reduced frequency, the first describing the variation in the normalized amplitude of the 1st harmonic pressure coefficient ($|Cp_1|$) over both blade surfaces and the second the variation in phase angle (ϕ_1) relative to the blade motion. According to equation 4.21, the stability of the system characterised by the aerodynamics leading the bending motion of the blade depends on the sign of ϕ_1. Thus the phase angle range of $0 < \phi_1 < 180°$ corresponds to a positive aerodynamic damping on the suction surface and a negative aerodynamic damping on the pressure surface, whereas the phase angle range of $180° < \phi_1 < 360°$ or $-180° < \phi_1 < 0°$ indicates a negative damping on the suction surface and a positive damping on the pressure surface.

6.2.1 General Observations

Upon inspection of the set of the 1st harmonic pressure coefficient on the oscillating blade, a consistent trend of the results with few exceptions is observed according to the chordwise position, spanwise location and reduced frequency. The chordwise trend of the unsteady pressure response indicates the influence of incidence, the aerodynamic loading over the blade on the unsteady pressure generation. The spanwise trend supplies the information on the three-dimensionality of the unsteady flow field.

To demonstrate the main unsteady flow characteristics, the 1st harmonic pressure coefficient on the oscillating blade at a reduced frequency of 0.2 is considered first. The amplitude and phase angle are presented in **Figures 6.3 and 6.4.** The amplitude of unsteady pressure is generally higher on the suction surface (**Figure 6.3**), with a maximum at the leading edge. The peak value depends on the spanwise location with the lower peak nearer the blade hub. Downstream of the peak amplitude of unsteady pressure on the suction surface, the amplitude decreases quickly to near zero recorded at 92% axial chord location, which corresponds with the pressure tapping located nearest the trailing edge. The same trend is evident in the amplitude over the pressure surface, but the amplitude reaches a much smaller peak near the leading edge and the amplitude gradient is less steep. The amplitude of the first harmonic pressure coefficient along the chord length increases with the increase of reduced frequency and has a consistent trend shown in **Figures 6.5 and 6.7**. The concentration of unsteady pressure activity in the forward 30% chord on both surfaces supports that the unsteady pressure generation is largely driven by the local incidence effect, which was also indicated by the raw time traces of the unsteady pressure response shown in Section 6.1.

The amplitude of unsteady pressure is lower in the leading edge region at 90% and 95% of the span on the pressure surface than that should be according to the trend along the three lower spans (**Figure 6.3**), whose area along the chordwise location is reduced with increasing reduced frequency (**Figures 6.5 and 6.7**). This feature is not obvious on the suction surface for the whole range of reduced frequency and may be caused by the unavoidable tip leakage flow due to the blade vibration. This explanation is supported by the investigation on the influence of the tip leakage flow on the aeroelastic stability of the oscillating cascade presented in Chapter 7.

The chordwise variation in phase angle over the suction surface at the reduced frequency of 0.2 (**Figure 6.4**) indicate that the unsteady pressure response is led by the leading edge. At the two higher reduced frequencies, the unsteady pressure response over the suction surface is led by the leading edge near the blade tip and gradually becomes uniformly distributed towards the blade hub shown in **Figures 6.6**

and 6.8. The phase angle on the pressure surface at *k* = 0.2 (**Figure 6.4**) is nearly constant along the chordwise location with the exceptions at 34% chord at the three lower spans. The trend of the phase angle at *k* = 0.4 and *k* = 0.6 is the same as that at *k* = 0.2 over the whole pressure surface (**Figures 6.6 and 6.8**). The chordwise variation in phase angle over the pressure surface demonstrates the unsteady pressure response is slightly led by the trailing edge for all reduced frequencies concerned.

The phase angle of the 1st harmonic pressure coefficient indicates a stable aeroelastic condition except for the abrupt phase angle at 54% chord at 50% and 70% span on the suction surface and the deviations at 34% chord at 20%, 50% and 70% span on the pressure surface for the three reduced frequencies. The phase on the pressure surface indicates a more stable aeroelastic condition with the increase of reduced frequency.

6.2.2 2D laminar Separation Bubble on the Suction Surface

From the blade surface static pressure distributions as shown in **Figure 5.15**, a 2D laminar separation bubble was identified on the suction surface at 50% and 70% of the span.

The existence of the separation bubble on the suction surface can also be identified from the abrupt phase shift as shown in **Figures 6.4, 6.6, and 6.8** for the range of reduced frequency. There is about 180° phase shift at 54% chord at 50% and 70% of the span on the suction surface compared with the points above and below this location, which is a typical unsteady feature of the 2D laminar separation bubble as documented by He (1998). His experimental work supported by a quasi-steady calculation pointed out that there is an abrupt unsteady phase change of 180° around the reattachment point of a laminar separation bubble. The existence of the separation bubble is also featured by the abrupt amplitude of unsteady pressure presented in **Figures 6.5 and 6.7**, which is not clear on the suction surface at *k* = 0.2 (**Figure 6.3**) due to the relatively small amplitude. The largely 2D separation bubble (range from 30% to 70% span) disappears in the end wall regions as a result of the strong influence of the local 3D secondary flow vortex structure.

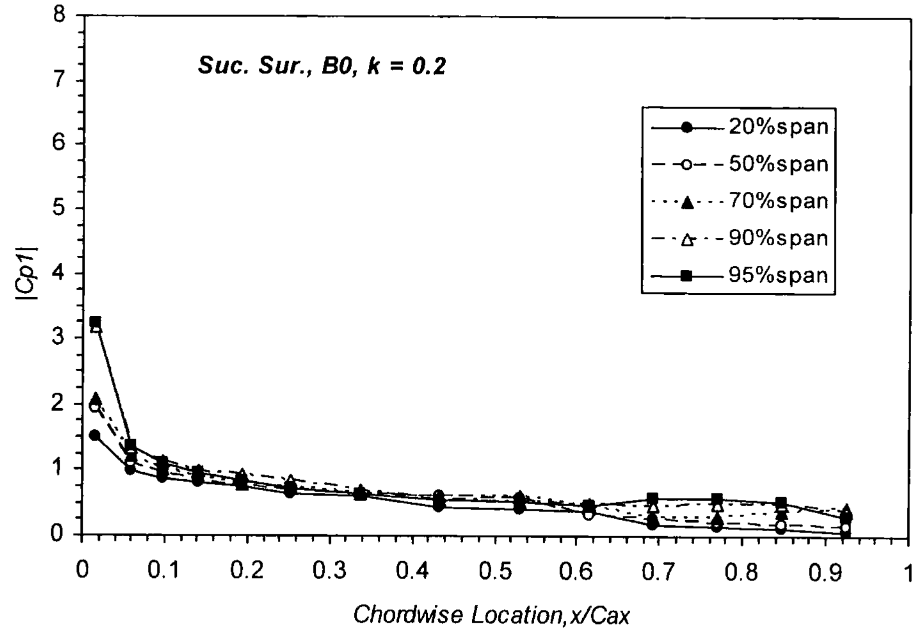

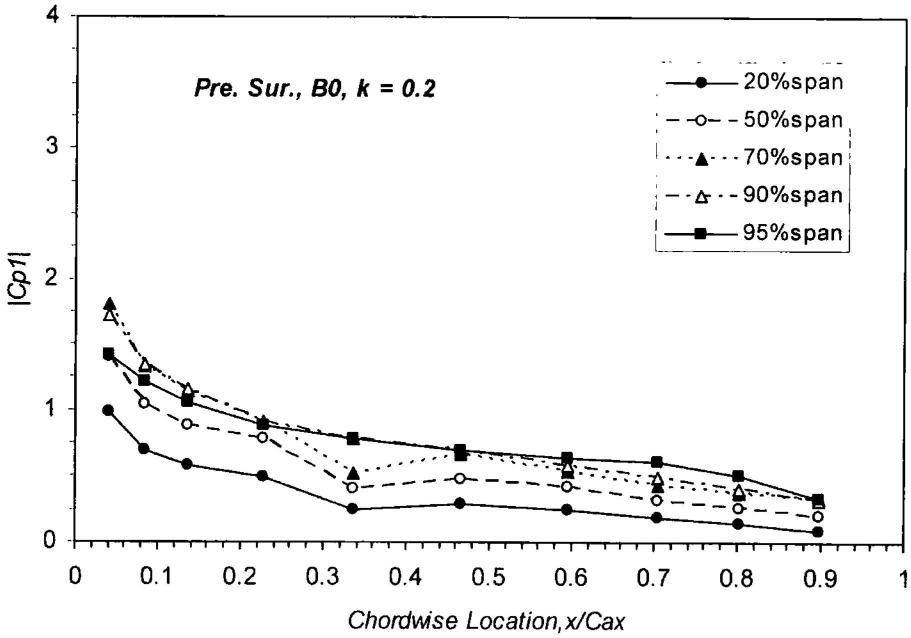

Figure 6.3: Amplitude of the first harmonic pressure coefficient on blade 0 at $k = 0.2$

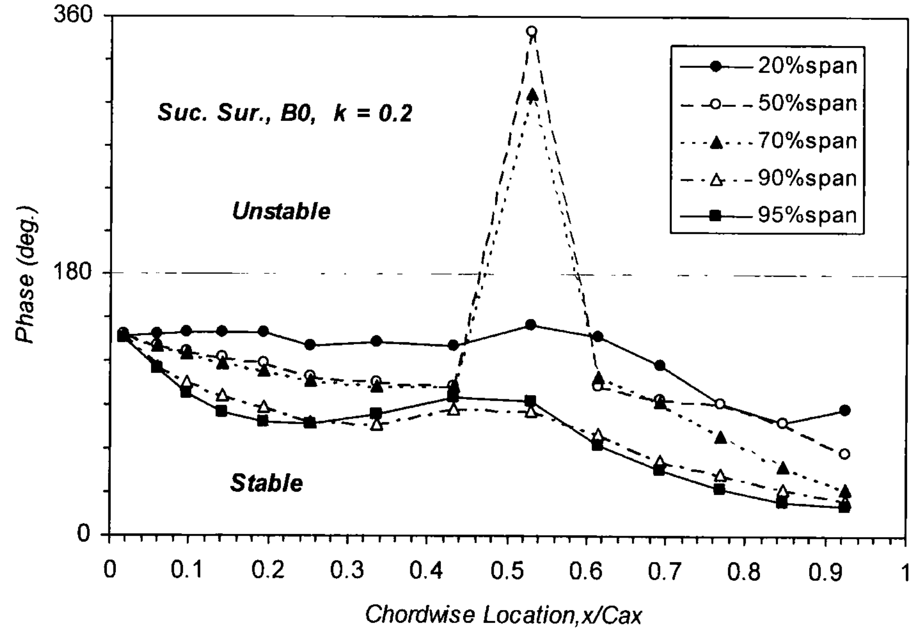

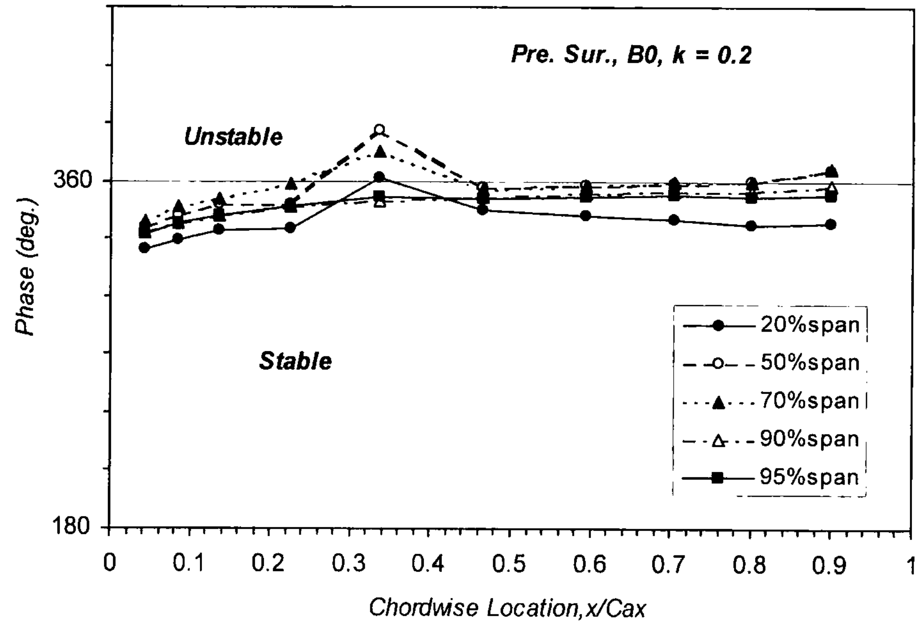

Figure 6.4: Phase of the first harmonic pressure coefficient on blade 0 at $k = 0.2$

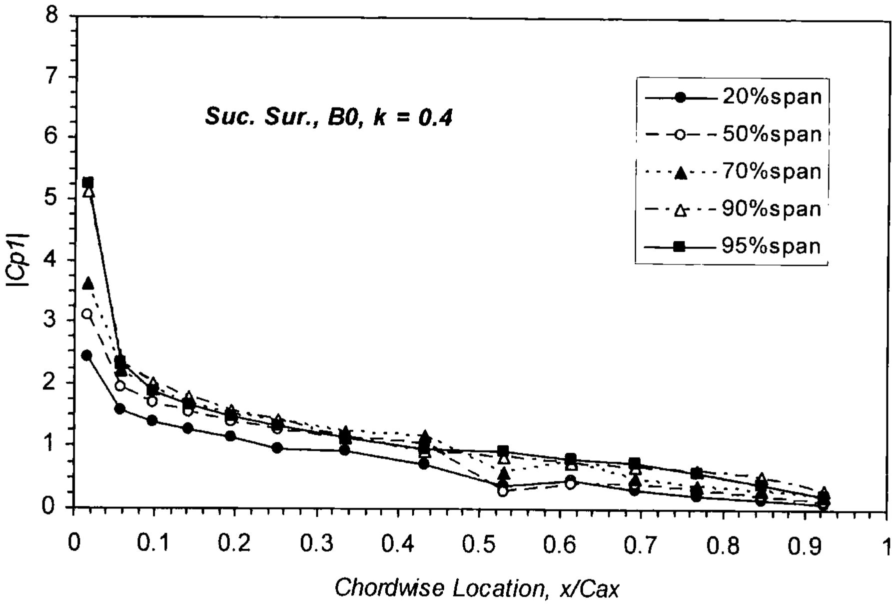

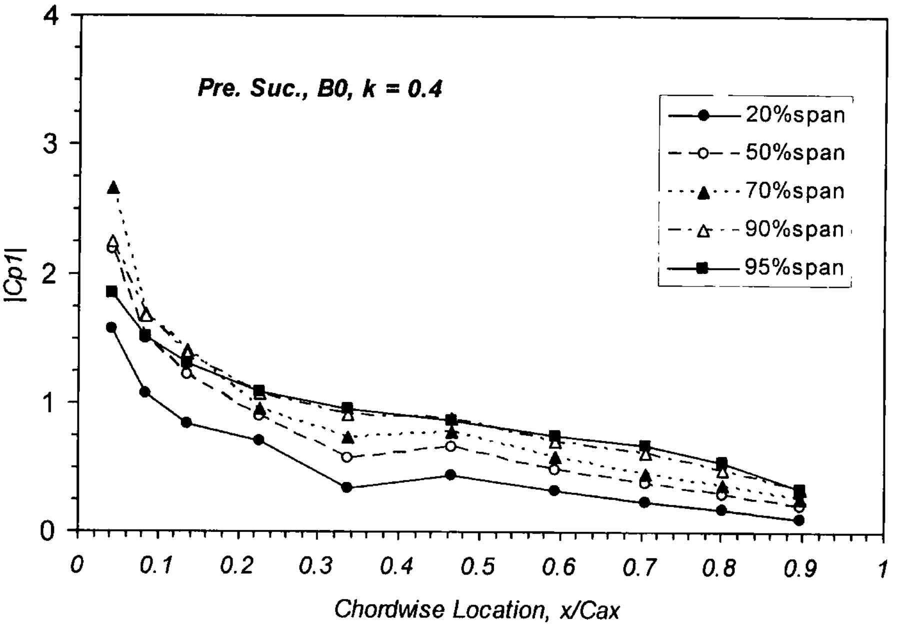

Figure 6.5: Amplitude of the first harmonic pressure coefficient on blade 0 at k = 0.4

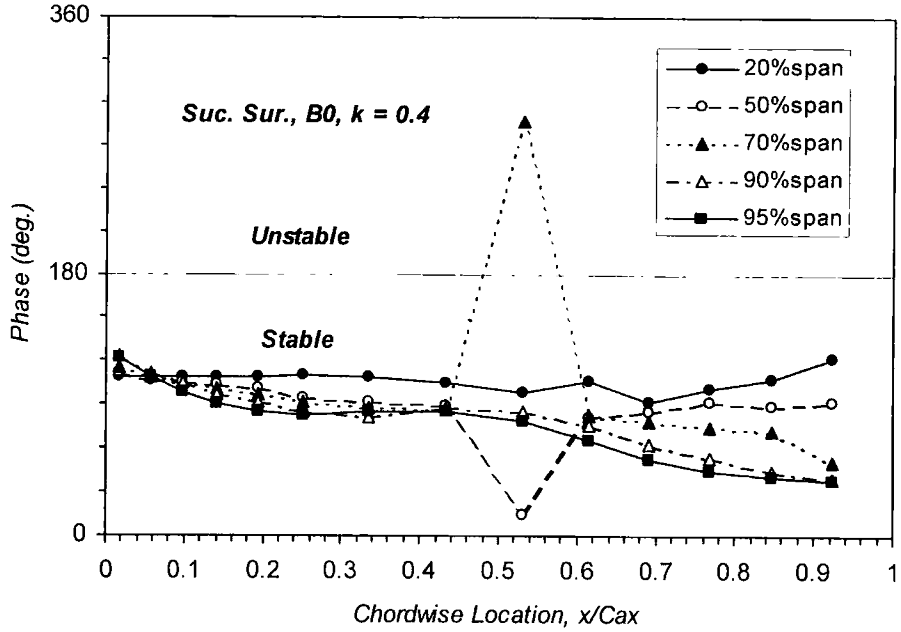

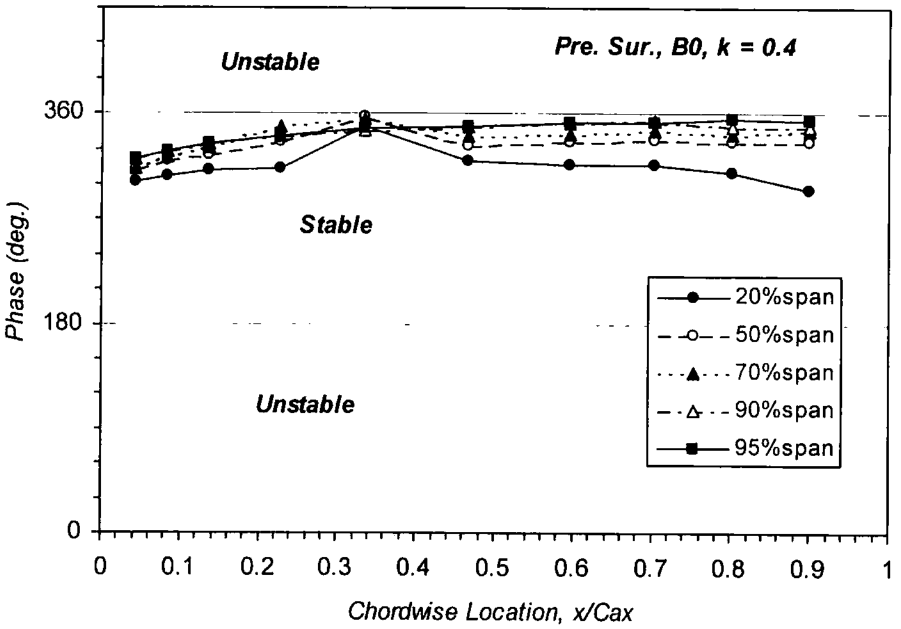

Figure 6.6: Phase of the first harmonic pressure coefficient on blade 0 at $k = 0.4$

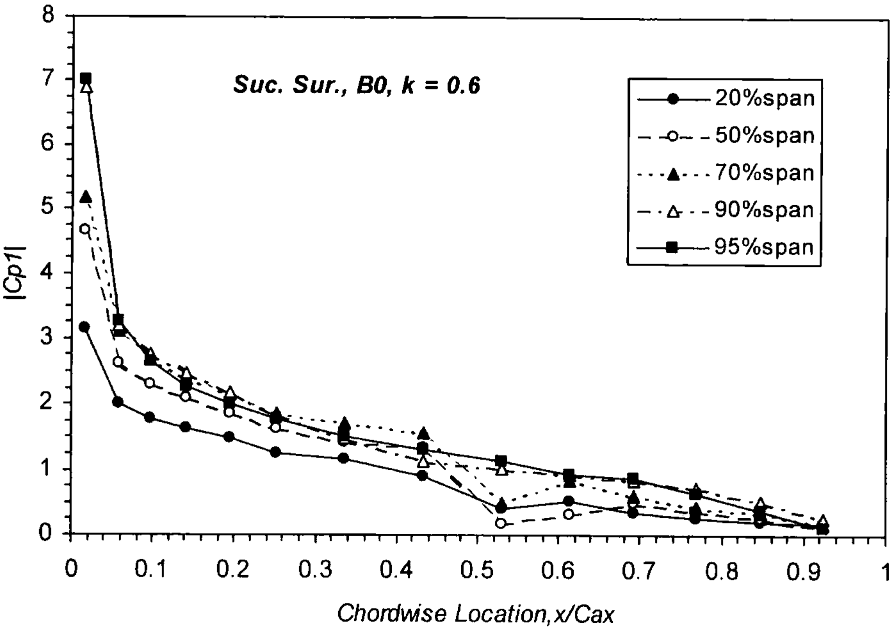

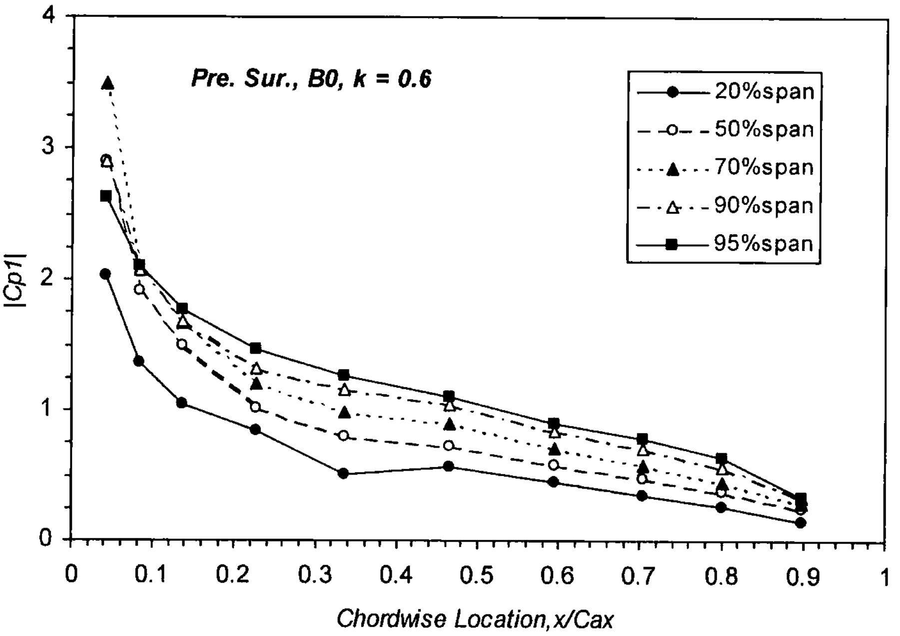

Figure 6.7: Amplitude of the first harmonic pressure coefficient on blade 0 at *k* = 0.6

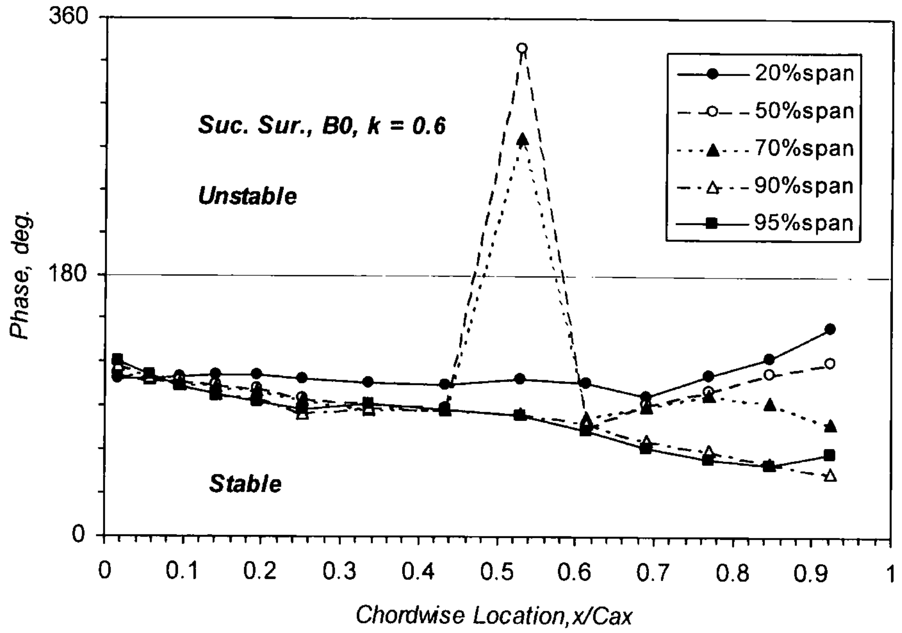

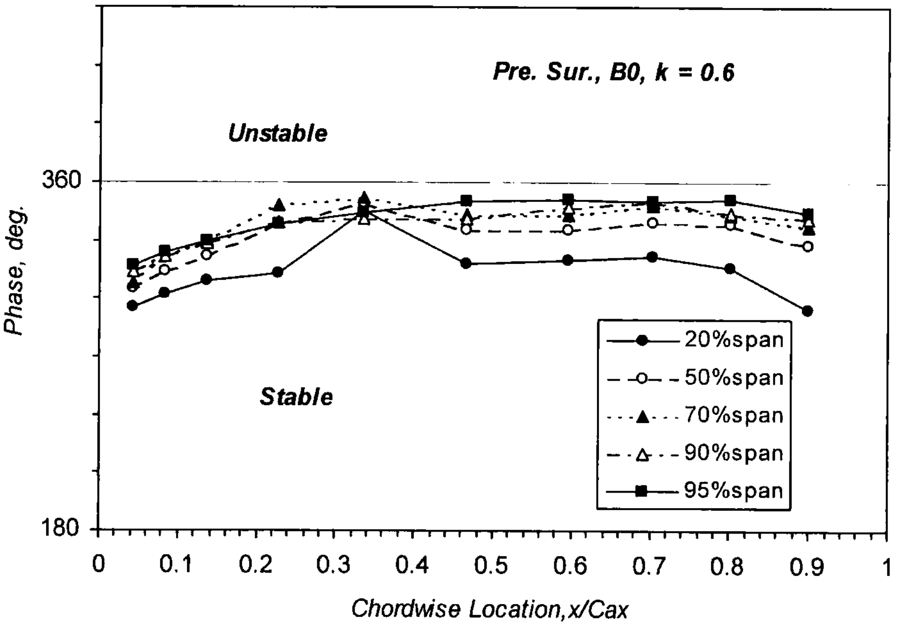

Figure 6.8: Phase of the first harmonic pressure coefficient on blade 0 at $k = 0.6$

6.2.3 3D Features of the Unsteady Response According to the Spanwise Variation

As shown in **Figures 6.3, 6.5 and 6.7** at all values of reduced frequency, the amplitude along the blade span obtained on both surfaces is almost identical at any given chordwise location between 20% and 95% span, except for that at the leading edges. At the leading edge, there is a marked and fairly consistent increase in the amplitude of the 1^{st} harmonic pressure coefficient along the blade span. The increasing rate of the amplitude of the 1^{st} harmonic pressure coefficient along the span is lower than the corresponding increase in bending amplitude. Even in the most extreme case (the leading edge on the suction surface at the reduced frequency of 0.2 as shown in **Figure 6.3**), the amplitude at 95% span is just two times greater than that obtained at 20% span, whilst the local bending amplitude differs by five times. This indicates that the variation in amplitude of the 1^{st} harmonic pressure coefficient at different span locations is non-proportional to the local bending amplitude and the unsteady pressure wave has an instantaneous radial interaction. This fully 3D nature certainly challenges the validity of the conventional quasi-3D strip-theory used in the prediction of unsteady flows of this kind. A similar feature has been identified computationally by Hall and Lorence (1993) for linear and annular cascades using a three dimensional linearised Euler solver, and experimentally by Bell (1999) for a single oscillating turbine blade.

The spanwise variation in phase angle of the first harmonic pressure coefficient, shown in **Figures 6.4, 6.6 and 6.8**, provides further evidence of the three dimensional behaviour of the unsteady flow, which indicates that the unsteady pressure response is led by the blade hub on the suction surface while that is led by the blade tip on the pressure surface. With increasing reduced frequency the spanwise variation in phase angle is more obvious in the region from 60% chord to the trailing edge on the suction surface as shown in **Figures 6.6 and 6.8**, which corresponds to the strong diffusion area on the suction surface and the viscous effect becomes more predominant.

6.2.4 Influence of Reduced Frequency on the Unsteady Pressure Response of the Oscillating Blade

To clarify the effect of reduced frequency, the amplitude and phase of the first harmonic pressure coefficient at 50% span on the oscillating blade are presented in **Figures 6.9 and 6.10** for the range of reduced frequency (k = 0.2, 0.4 & 0.6). As mentioned before the unsteady pressure response was obtained for the same flow conditions but at different vibration frequencies.

Increasing reduced frequency has a noticeable influence on amplitude of unsteady pressure but the phase angle remains practically constant especially for the two higher reduced frequencies.

The trend in amplitude of unsteady pressure along the chordwise location remains unchanged whereas the amplitude at the front half of the chord on both surfaces markedly increases with the increase in reduced frequency as shown in **Figure 6.9**. The level of increase in amplitude of unsteady pressure is reduced toward the trailing edge. The amplitude of unsteady pressure at the trailing edge for the range of reduced frequency is nearly the same on both surfaces. The increased amplitude of unsteady pressure with reduced frequency indicates the increase of the local incidence effect, induced by the blade motion, as the blade vibration frequency increases. Increasing reduced frequency also reduces the amplitude of unsteady pressure at the reattaching point (54% chord) at $k = 0.4$ and $k = 0.6$.

Figure 6.10 demonstrates almost identical phase angle on both surfaces at $k = 0.4$ and $k = 0.6$ except for 54% chord and the region from 85% chord to the trailing edge. The trend of the phase at $k = 0.2$ is the same as that at $k = 0.4$ and $k = 0.6$ over the front 70% chord on the suction surface and over the whole pressure surface, and the phase values at $k = 0.2$ are higher than those at $k = 0.4$ and $k = 0.6$.

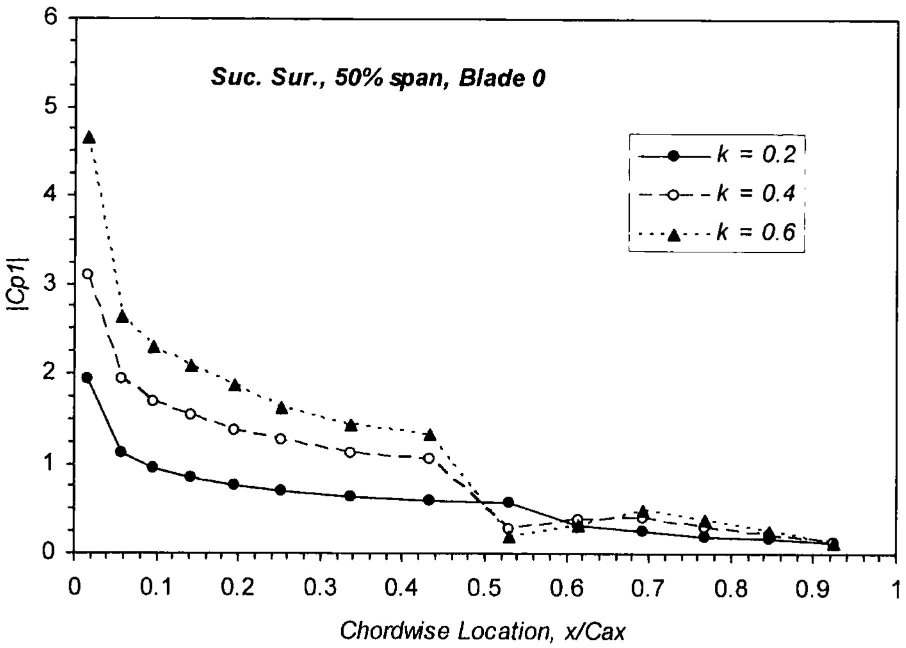

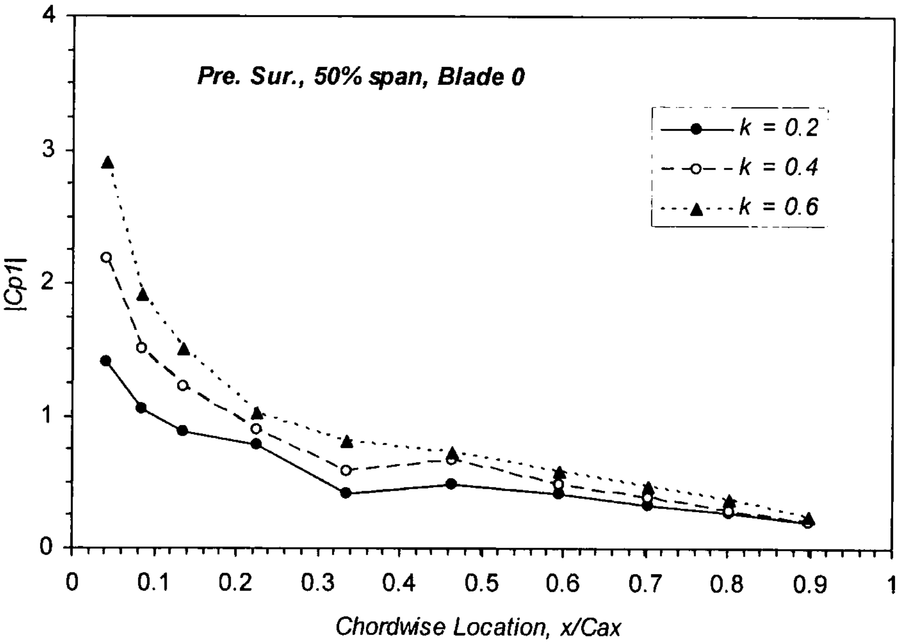

Figure 6.9: Influence of reduced frequency on the amplitude of the first harmonic pressure response

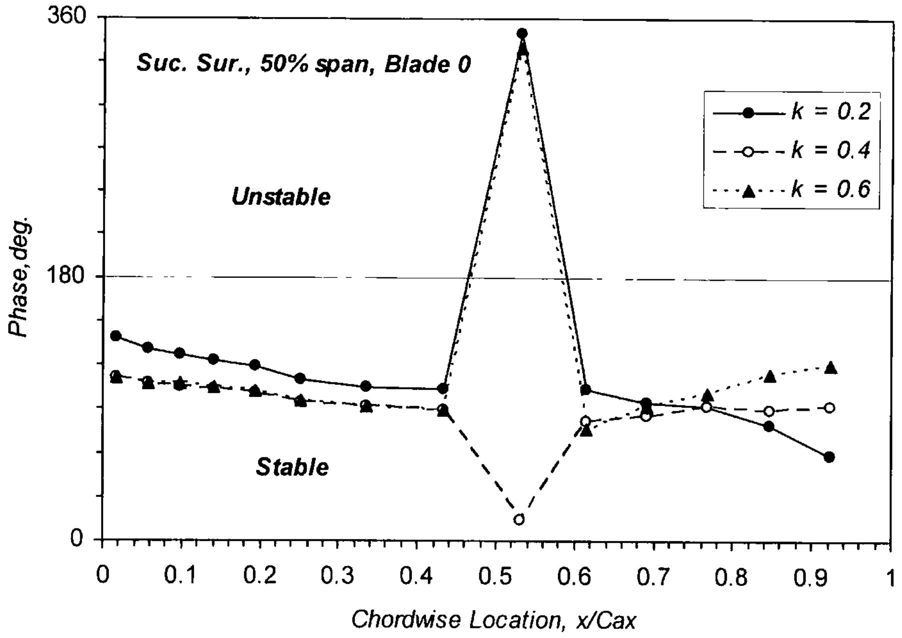

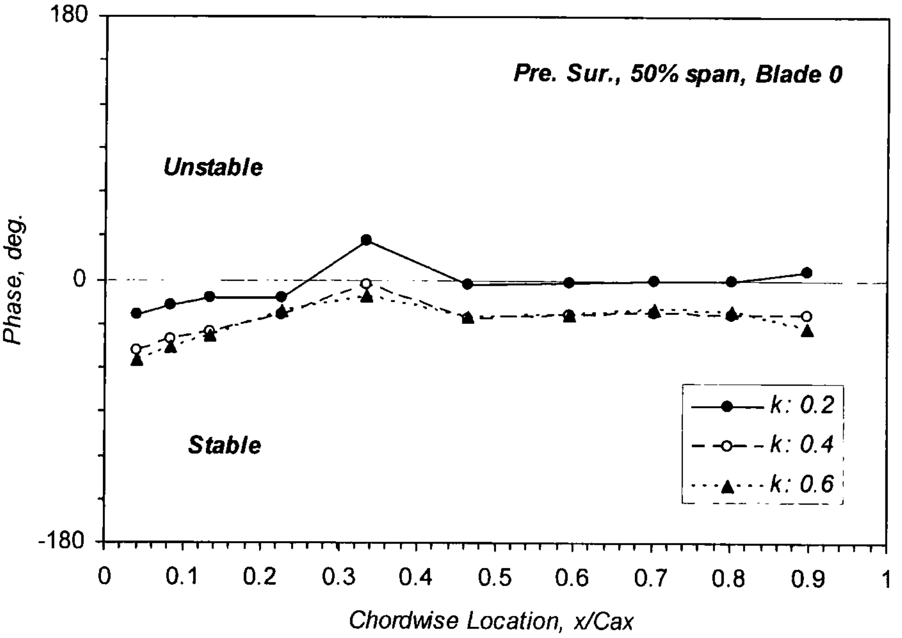

Figure 6.10: Influence of reduced frequency on the phase of the first harmonic pressure response

6.3 Overall Aerodynamic Damping

The overall aerodynamic damping was produced from integrating the unsteady pressure distributions (superimposed by the Influence Coefficient Method) over the blade surface, which is a direct measure of the energy transferred from the flow field to the oscillating blade per cycle of the blade motion and quantifies the aeroelastic stability.

To indicate the aeroelastic conditions of the oscillating cascade with inter-blade phase angle (IBPA) and reduced frequency, **Figure 6.11** plots the overall aerodynamic damping as a function of IBPA at the range of reduced frequency tested. The inter-blade phase angle is ranged from -180° to 180° in steps of 20°. Positive inter-blade phase angle is defined as such that blade N+1 leads blade N referring to **Figure 4.12** and corresponds to a pressure wave moving in the direction of rotor rotation.

The distributions of unsteady pressure were closed at the leading and the trailing edges of the blade by assuming a constant level of $|Cp_1|$ with that measured at the end points.

The damping-IBPA diagram clearly demonstrates a sinusoidal trend. At the reduced frequency of 0.4, it is seen that the aerodynamic damping increases with σ over the range $30° < \sigma < 180°$ and $-180° < \sigma < -150°$ with the maximum value at $-150°$, and decreases for $-150° < \sigma < 30°$ with the minimum value at 30° (Note that $\sigma = +180°$ and $\sigma = -180°$ are actually the same point and that damping trends over σ through this common point are continuous). The aerodynamic damping is symmetric with regard to IBPA 30°. This indicates that this cascade provides the maximum aerodynamic damping of the bending mode for out-of-phase blade oscillations and the minimum aerodynamic damping when the blades oscillate in-phase.

The cascade is indicated as being aeroelastically stable by the positive values of the overall aerodynamic damping over the entire range of inter-blade phase angles at the three reduced frequencies. The aero-damping curves on the damping–IBPA diagram seem to follow a trend that as the vibration frequency decreases, the sinusoidal damping curve moves downward as well as rightward as indicated by the dash line. The least stable IBPA is 30° at $k = 0.4$ and 40° at $k = 0.2$, corresponding to a forward travelling wave mode with one or two nodal diameters (depending on the total number of blades in a real blade row). The trend suggests that at a lower vibration frequency, the least stable forward travelling wave mode should have a larger number of nodal diameters. On the other hand, the number of nodal diameters at the minimum damping point will decrease at a higher frequency. Following this trend, it might be possible that for a given high vibration frequency, the minimum aero-damping, which may well be positive, even occurs at a negative inter-blade phase angle, corresponding to a backward travelling wave mode. The experimental results are consistent with industrial design experience, i.e., that increasing the reduced frequency generally increases the overall aerodynamic damping.

The further examination of the 1^{st} harmonic pressure coefficient at the three reduced frequencies, as shown in **Figures 6.9 - 6.10,** reveals that the expected trend of the increased aerodynamic damping with reduced frequency mainly results from a marked increase in amplitude of unsteady pressure in the first half of blade chord on both surfaces. The increased level of aerodynamic damping is higher between $k = 0.2$ and $k = 0.4$ than that between $k = 0.4$ and $k = 0.6$ for each inter-blade phase angle. This indicates that the phase shift on both surfaces at the low reduced frequency of 0.2 also gives the contribution to the decreased aeroelastic stability with decreasing oscillation frequency.

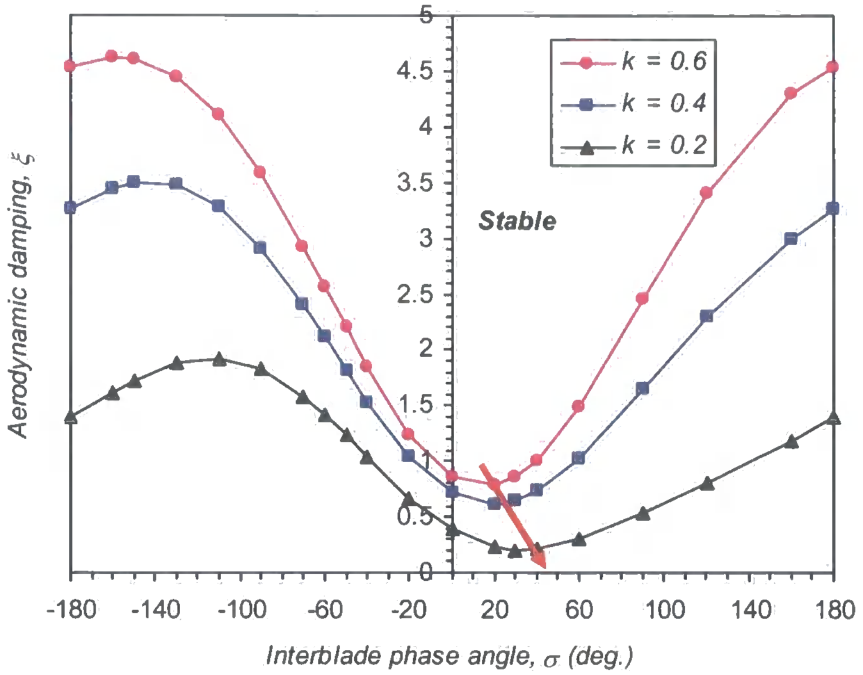

Figure 6.11: Overall aerodynamic damping at three reduced frequencies

6.4 Unsteady response of a tuned cascade for IBPA -150° and IBPA 30° - 'coupling term'

The aerodynamic damping gave some insight into parameter dependence (i.e. IBPA and k), but could not reveal the unsteady aerodynamic behaviour leading to this dependence. The unsteady pressure distributions over the blade go a step further and give some understanding of the unsteady aerodynamics behind this behaviour. Since only the minimum stability is of concern in a practical sense, the least stable IBPA 30° at $k = 0.4$ is chosen to inspect the influence of IBPA on the unsteady pressure response with comparing to that for the most stable IBPA -150°. The blade-to-blade aerodynamic coupling effects appear as vector additions to the single blade effect, which either increase or reduce aeroelastic stability according to the inter-blade phase angle. The amplitude and phase of the 1st harmonic pressure coefficient constructed over the blade surface are plotted in **Figures 6.12 to 6.15** for the two inter-blade phase angles. Comparisons between the unsteady pressure response at IBPA –150°, IBPA 30° and the oscillating blade will be used to isolate the effect of the inter-blade phase angle on the unsteady aerodynamics.

There is a pronounced effect of IBPA on the amplitude of unsteady pressure along the chordwise location on both surfaces. The chordwise trend in amplitude of unsteady pressure on both surfaces is the same for the two IBPAs as that on the oscillating blade (**Figure 6.5**). The 3D features of the unsteady aerodynamic response are not changed by the coupling influence from other blades although the effect of IBPA can enhance or reduce its extension. A change in inter-blade phase angle from IBPA 30° to IBPA –150° causes a significant increase in amplitude of unsteady pressure over the front half of the blade (near the leading edge) for all spanwise locations. Thus the slope is steeper for IBPA-150° (**Figures 6.12 and 6.13**). The spanwise variation in amplitude of unsteady pressure is reduced after 60% chord on the suction surface at IBPA –150° and is increased at IBPA 30°. The same case is on the pressure surface to a smaller extent.

The inter-blade phase angle has a significant influence on the cascade stability by changing the phase angle shown in **Figures 6.14 and 6.15**. As mentioned before, the phase leading the blade motion over the suction surface and lagging the motion over the pressure surface indicates an aeroelastically stable condition. In **Figure 6.14** for IBPA -150° the phase angle shows a stable condition on the suction surface except for the position at 54% chord at 70% span due to the presence of the separation bubble. This is also the case for IBPA 30° with the unstable additions at 54% and 60% chord at 50% span. The feature of 2D separation bubble at 54% chord on the suction surface is obvious for the two IBPAs. The destabilizing effect of 2D separation bubble at IBPA 30° is changed to the stabilizing one at IBPA -150° at 50% span by inter-blade phase angle. The chordwise phase gradient on the suction surface at IBPA 30° is larger than that for the isolated blade with less stable trend and the gradient decreased at IBPA –150° with the stable trend. The spanwise variation in phase angle after 60% chord on the suction surface is reduced compared with that on the oscillating blade (**Figure 6.6**) for the two IBPAs.

This also holds true for the phases on the pressure surface as shown in **Figure 6.15**. The positive gradient of phase angle on the pressure surface increases from IBPA –150°, isolated blade to IBPA 30°, which indicates that the oscillating blade (**Figure 6.6**) has a more stable condition than that for IBPA 30° and less stable condition than that for IBPA –150°. The phase angle of the pressure surface indicates a destabilizing contribution to the aerodynamic damping after 15% chord for IBPA 30°. In contrast to this, at IBPA -150°, the phase distribution indicates a stabilizing contribution over the entire pressure surface. There is a small abrupt phase change at 34% chord on the pressure surface over all blade spans for the two IBPAs with an unstable condition at IBPA 30°.

Overall, the results indicate a strong cascade effect on the unsteady aerodynamic response influenced largely by the changes in inter-blade phase angle. The aerodynamic stability or instability of a tuned cascade is primarily governed by the changes in amplitude of unsteady pressure on the front half chord on both surfaces and in phase angle of unsteady pressure on the pressure surface with inter-blade phase angle. This indicates that the leading edge phenomena with respect to the stability or instability of a single oscillating blade are enhanced when the blade is in a cascade.

The experimental data documented in this chapter provide the first 3D oscillating cascade test case for aeroelastic predictions in turbomachines.

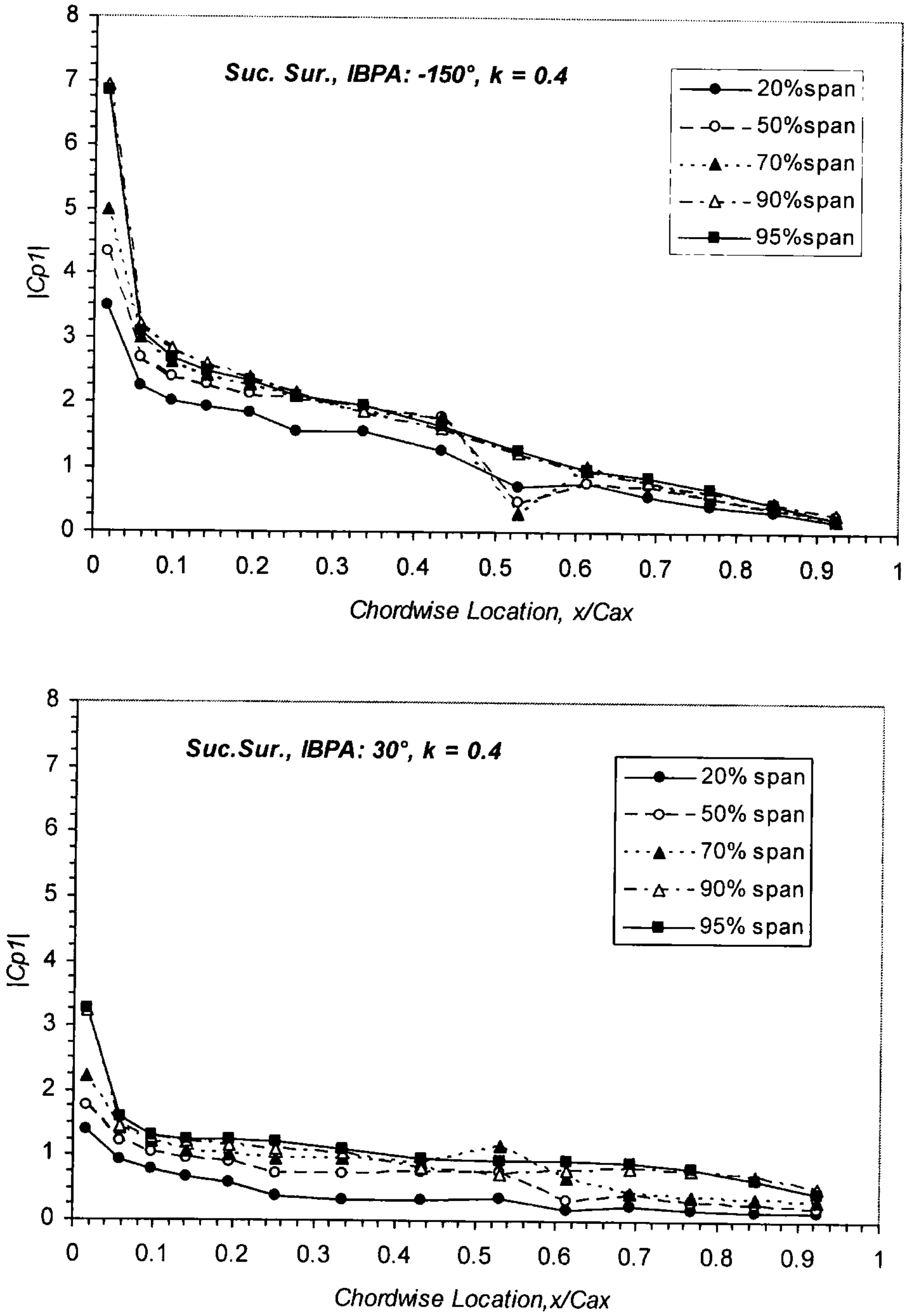

Figure 6.12: Effect of IBPA on the amplitude of first harmonic pressure coefficient on the suction surface

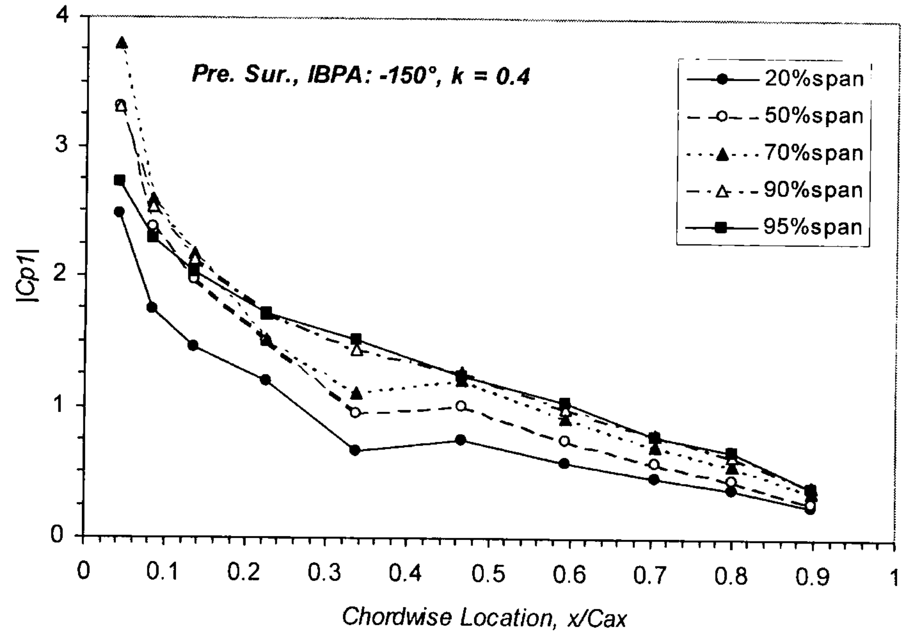

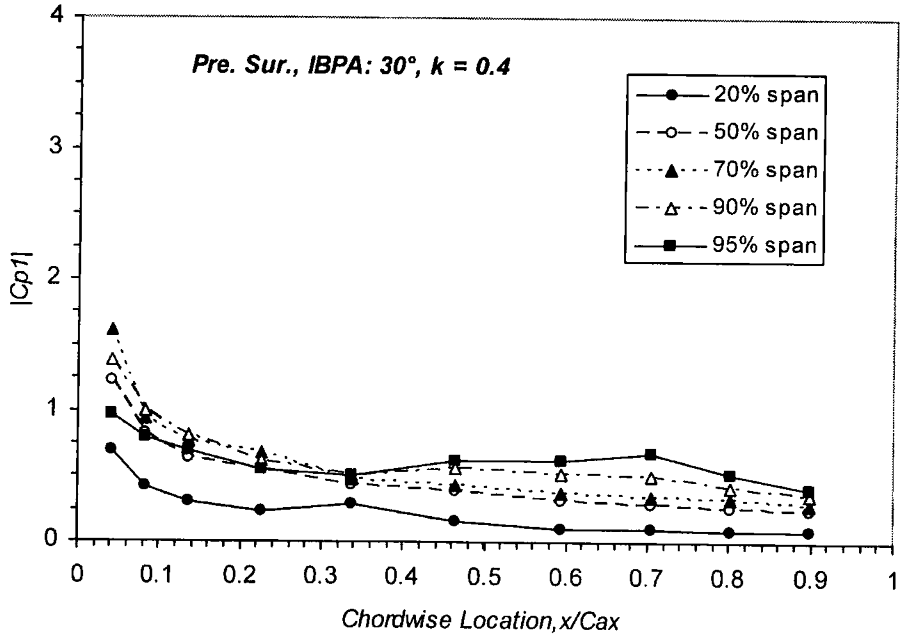

Figure 6.13: Effect of IBPA on the amplitude of first harmonic pressure coefficient on the pressure surface

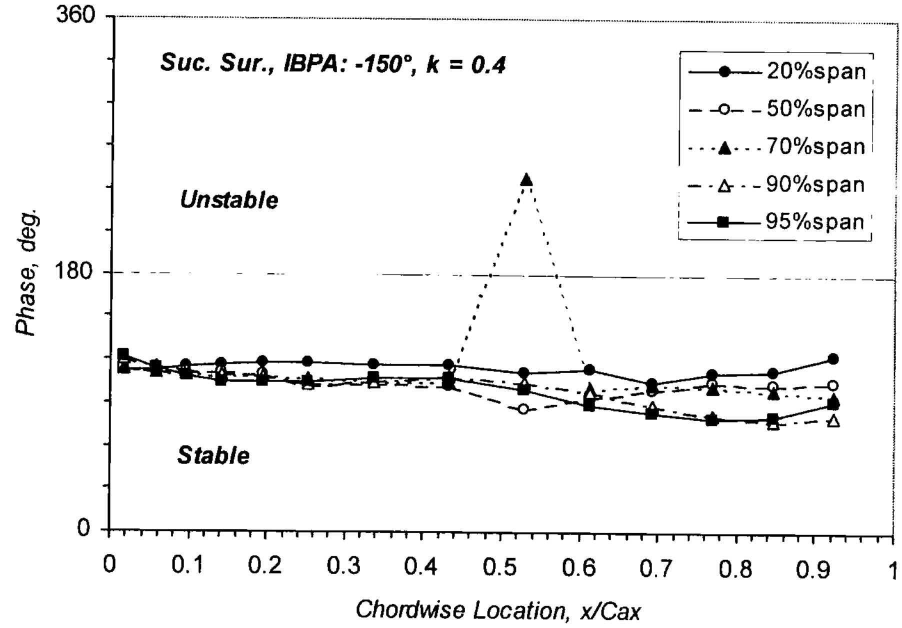

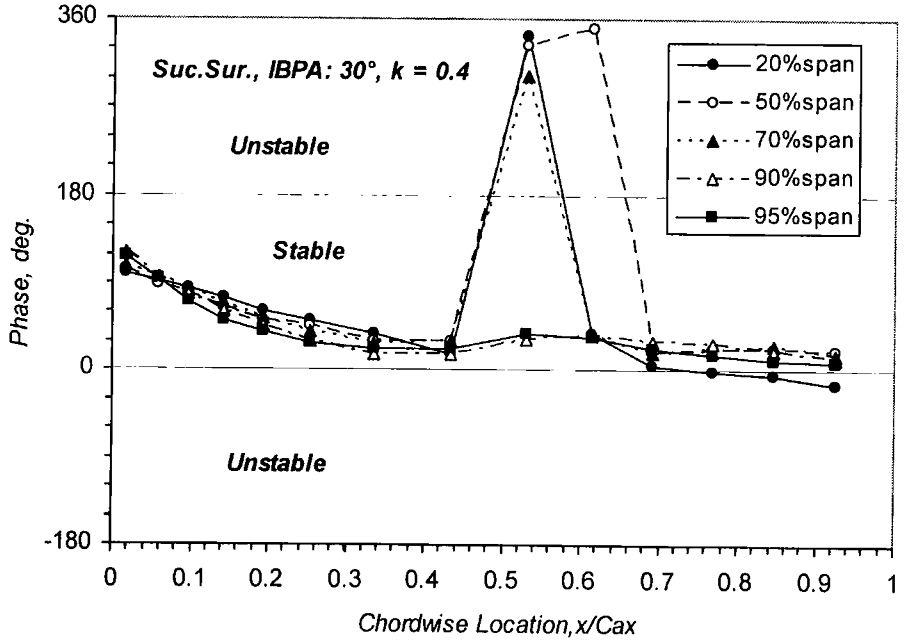

Figure 6.14: Effect of IBPA on the phase of first harmonic pressure coefficient on the suction surface

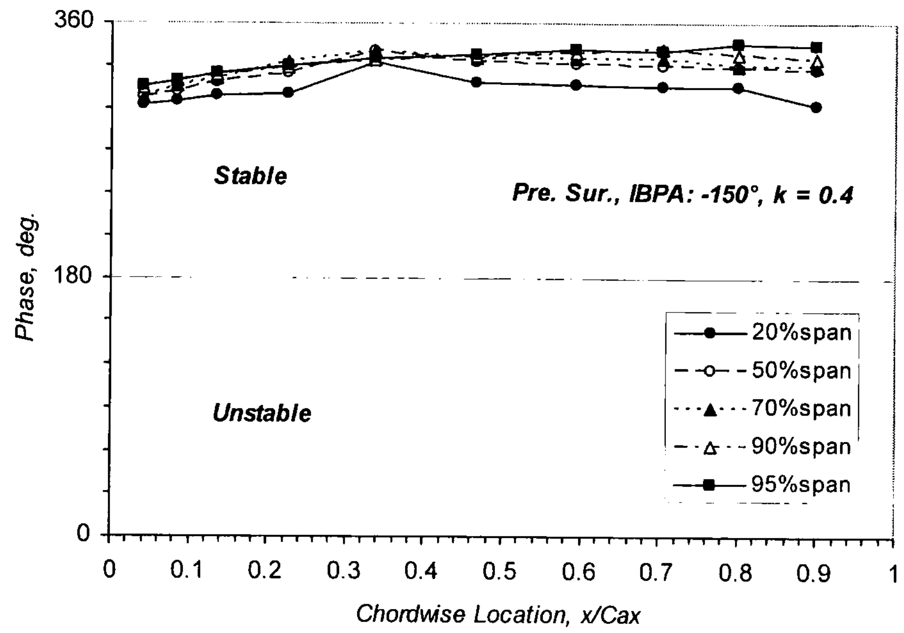

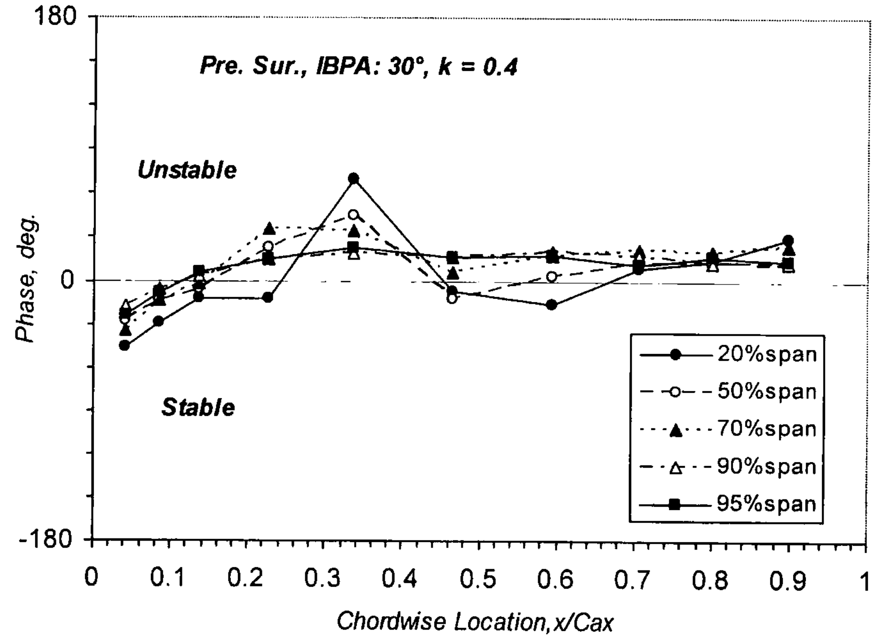

Figure 6.15: Effect of IBPA on the phase of first harmonic pressure coefficient on the pressure Surface

Chapter 7

Influence of Blade Tip Clearance

In this chapter, the experimental results on the influence of blade tip-clearance on the unsteady aerodynamic response of a tuned cascade are presented and discussed. Firstly, the steady flow measurements with two settings of tip-clearance gap are provided to form the aerodynamic baseline states for the unsteady pressure measurements. Following this, the unsteady pressure responses at two settings of tip-clearance are documented.

7.1 The Setting up of Experiment

The investigation of the blade tip-clearance has been carried out on two settings, tip-gap at 1% and 2.3% of the span. The free-stream flow conditions previously shown in **Table 3.4** were applied. The selection of these two gaps was based on the typical blade tip gaps in real turbomachines. The tip-gap δ given in **Table 7.1** was specified with an uncertainty of $\pm\ 0.1mm$. The tip-gap of each stationary blade could be changed by moving the blade relative to the perspex endwall in the spanwise direction, and the reference blade was hinged at the blade hub so that it could be adjusted to vary the clearance gap at the tip by moving the spanwise location of the hub hinge as shown in **Figure 7.1**. Using this method to change the tip-clearance would cause a slightly shorter blade height than that with zero tip-clearance, and the spanwise locations of the pressure tappings with tip-clearance are lower than those with zero tip-gap, e.g. the tapping at 98% span without tip-gap is actually located at 97.95% span with the tip-gap of 2.3% span. This small difference can be neglected. In order to avoid confusion, the spanwise locations of the pressure tappings with tip-gap are assumed the same as those with zero tip-gap. At each setting of tip-clearance, the static and unsteady pressures on the blade surface were measured at six spanwise sections over the middle five blades at the reduced frequency of 0.4.

$\delta\,(m)$	δ/C	δ/h
0.0019	0.013	0.01
0.0043	0.029	0.023

Table 7.1: Summary of tip-gap setting

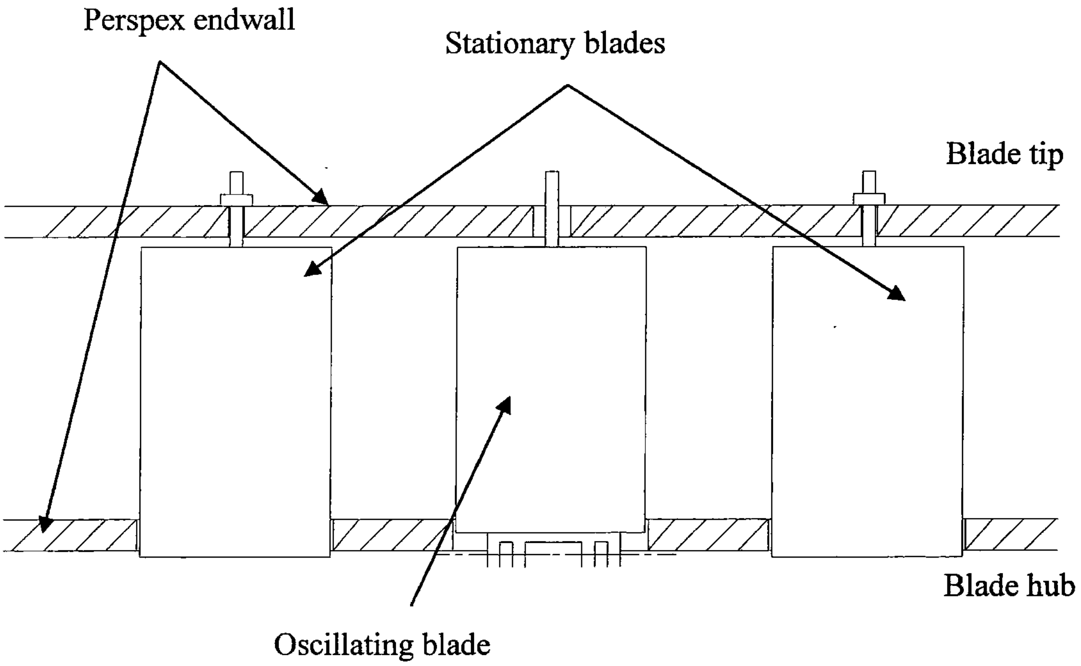

Figure 7.1: Schematic of the setting of the blade tip-gap

7.2 Steady Flow Results

The purpose of the steady flow measurements is to provide an aerodynamic baseline flow for the unsteady pressure measurements and to identify the features of the tip leakage flow that may influence the unsteady aerodynamic response of the oscillating compressor cascade.

The steady flow data with the two settings of tip-clearance are compared to that with zero tip-gap (previously presented in Chapter 6) to identify the influence of tip leakage flow on the steady flow loading. At the setting of zero tip-gap, the gap between the oscillating blade and the sidewall to accommodate the blade motion was covered by a piece of dense sponge, while there was effectively no gap between the stationary blades and the sidewall. **Figure 7.2** shows the static pressure distribution at 70% span of the oscillating blade at the three settings of tip-gap. The good agreement shows that the influence of the tip-clearance on the steady flow loading is fairly small from 70% span inwards. The surface static pressure distributions at the three spans near the blade tip (90%, 95% and 98% span) are presented in **Figures 7.3 - 7.5** for the three settings of tip-gap. Measurable variation in blade loading relative to zero tip-gap with increasing the tip-clearance is observed from 90% to 98% span. Apart from the endwall unloading caused by the passage vortex, another unloading effect is identified due to the tip-clearance. The extreme situation is located at 98% span with the maximum tip-clearance (2.3% span) as shown in **Figure 7.5.** The unloading can be observed between the leading edge and 25% chord at 98% span on the suction surface. Then a small reloading takes place at 25%-54% chord although the data at 20% and 34% chord are absent due to the blocked tappings at 98% span. The unloading strength and the affected chord length are reduced with decreasing tip-gap. The pattern of unloading near the leading edge following the reloading area can also be noticed at 90% and 95% span to a smaller extent (**Figures 7.3 -7.4**). A similar trend in blade loading has been reported by Kang & Hirsch (1993) in investigating tip leakage flows in a linear compressor cascade. They gave an explanation of the loading effects: the pressure near the tip increases on the suction surface near the leading edge due to the interaction of the main flow with the flow passing through the tip-gap from the pressure side, where the tip leakage vortex originates, and the reloading area results from the low-pressure core of the tip leakage vortex. This behaviour has also been mentioned by Storer & Cumpsty (1991) in their investigation of a tip clearance cascade.

Compared with that on the suction surface, the steady loading on the pressure surface is only slightly affected at 98% span by the tip-clearance (**Figure 7.5**). There is an obvious loading increase at 46% chord at 98% span. The strength is reduced with decreasing the tip-clearance. This also holds true at 95% span (**Figure 7.4**). In contrast, the steady loading on the pressure surface is largely unaffected at 90% span (**Figure 7.3**). This sensitivity of the loading on the pressure surface to the tip leakage flow was also demonstrated in Kang & Hirsch (1993).

Overall, the significant changes in blade loading due to increasing tip clearance are identified near the blade tip region (90% span outwards). The experimental facility provides a suitable vehicle for investigating the effect of tip leakage flow on the steady flow, which provides a sound aerodynamic background for investigating the influence of tip leakage flow on the unsteady aerodynamic response of the oscillating compressor cascade.

7.3 Unsteady Flow at Two Different Tip Clearances

The unsteady pressure responses of a tuned cascade obtained by the Influence Coefficient Method at two settings of tip-clearance are presented here with the validation of linearity at each set of tip-clearance. The unsteady pressure measurement procedures and the data reduction previously described in Chapter 4 were used, which allow the influence of tip leakage flow on the local unsteady aerodynamic response to be readily identified.

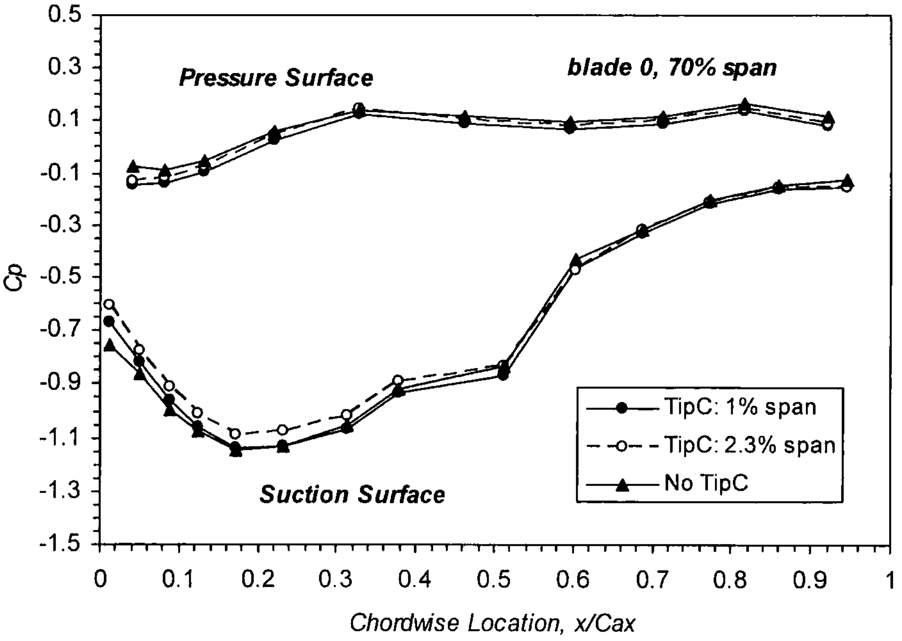

Figure 7.2: Variation in blade static pressure distribution with three settings of tip clearances at 70% span

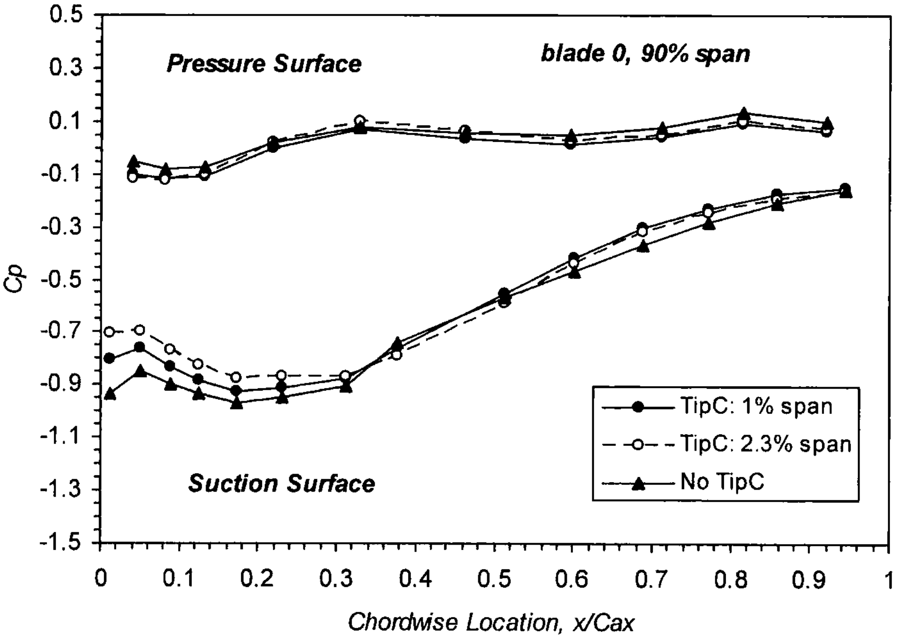

Figure 7.3: Variation in blade static pressure distribution with three settings of tip clearances at 90% span

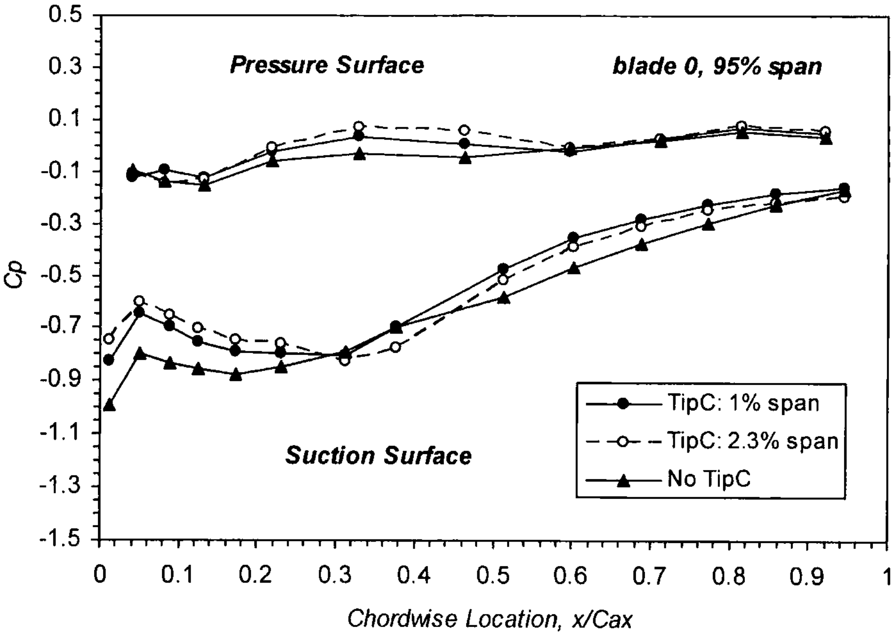

Figure 7.4: Variation in blade static pressure distribution with three settings of tip clearances at 95% span

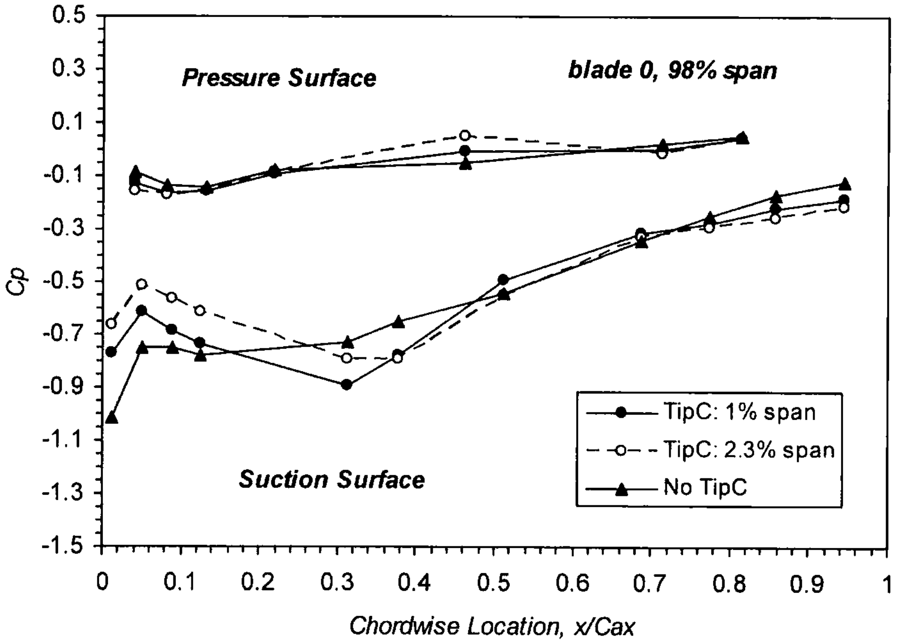

Figure 7.5: Variation in blade static pressure distribution with three settings of tip clearances at 98% span

7.3.1. Validation of Linearity of Unsteady Aerodynamics with Tip Clearance

Before the tip-clearance effect on the unsteady aerodynamic response of the oscillating compressor cascade is examined, the linearity of the unsteady aerodynamics for the two sets of tip clearance is required to be evaluated for the validity of the Influence Coefficient Method for these cases. The linearity is again examined by considering the effect of the oscillation amplitude on the unsteady pressure response and the relative amplitude of the second harmonic pressure coefficient at the two sets of tip clearance.

Figure 7.6 compares the amplitude of the first harmonic pressure coefficient at two different bending amplitudes (Am_{tip}: 6% chord and 3.3% chord) at 90% and 95% span on the oscillating blade with 1% span tip-clearance, and **Figure 7.7** for the phase angle. The amplitude of unsteady pressure normalised by the corresponding vibration amplitude is almost identical at two different blade vibration amplitudes at 90% and 95% span. The phase angle also shows a good agreement for the whole pressure surface and the majority of the suction surface with slight exceptions in the strong diffusion region (after 70% chord). The case is also held true for 2.3% span tip-clearance as shown in **Figures 7.8 and 7.9**.

Figure 7.10 demonstrates the relative amplitude of the second harmonic pressure coefficient at two tip sections (90% and 95% span) on the oscillating blade with 1% span tip-clearance, and **Figure 7.11** for that with 2.3% span tip-clearance. The linear behaviour is shown in the two figures with the small relative amplitude of the second harmonic. To inspect the details, the large relative amplitude of the second harmonic is indicated around the middle chord on the suction surface with the tip-clearance of 2.3% span as shown in **Figure 7.11**, which would be associated with the development of the tip leakage vortex.

Overall, the experimental results indicate the predominantly linear behaviour of the unsteady flow in response to blade vibration at two sets of tip clearance. Hence, the Influence Coefficient Method should be applicable to these cases.

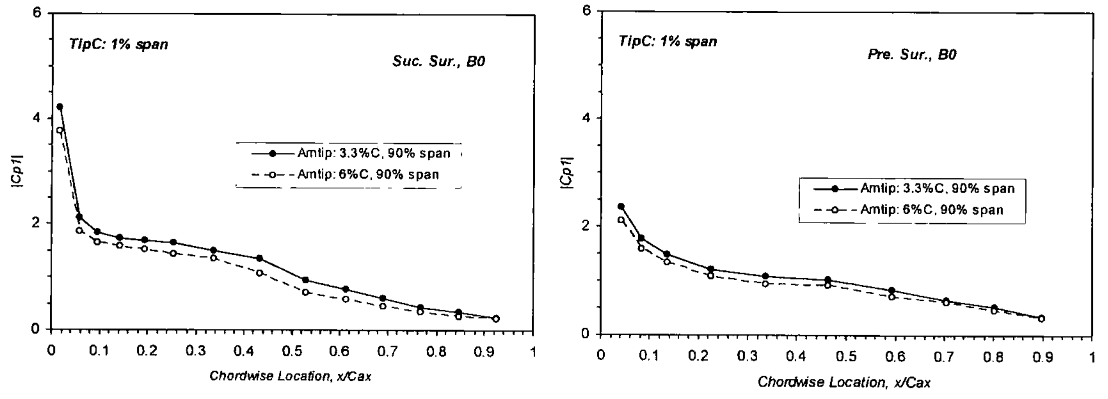

(*i*) 90% span

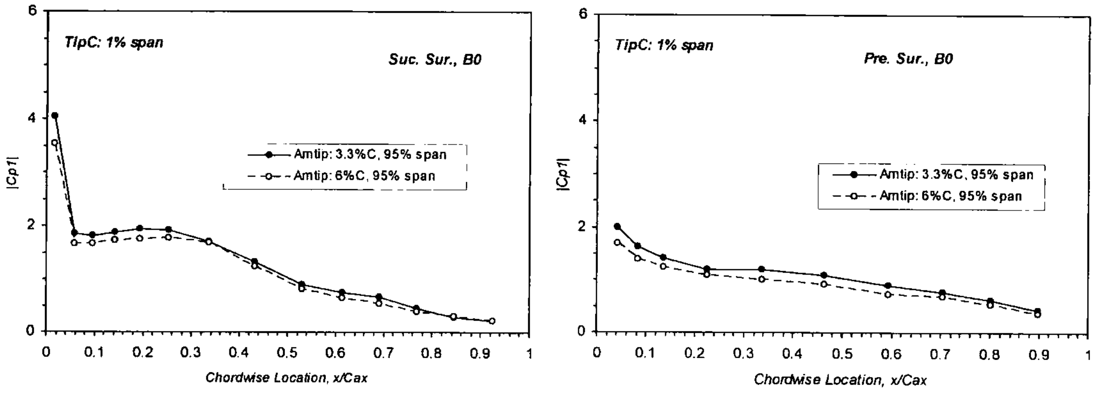

(*ii*) 95% span

Figure 7.6: Amplitude of the first harmonic pressure coefficient on the oscillating blade (at 90% and 95% span) at two oscillating amplitudes with 1% span tip clearance

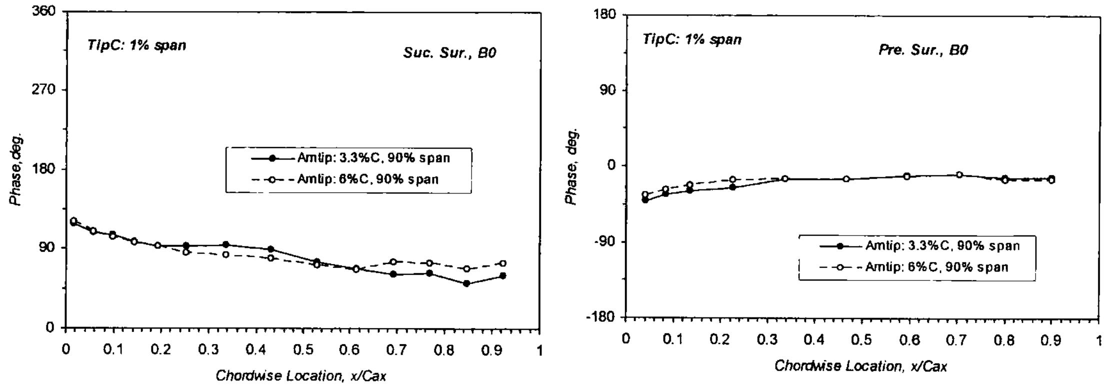

(*i*) 90% span

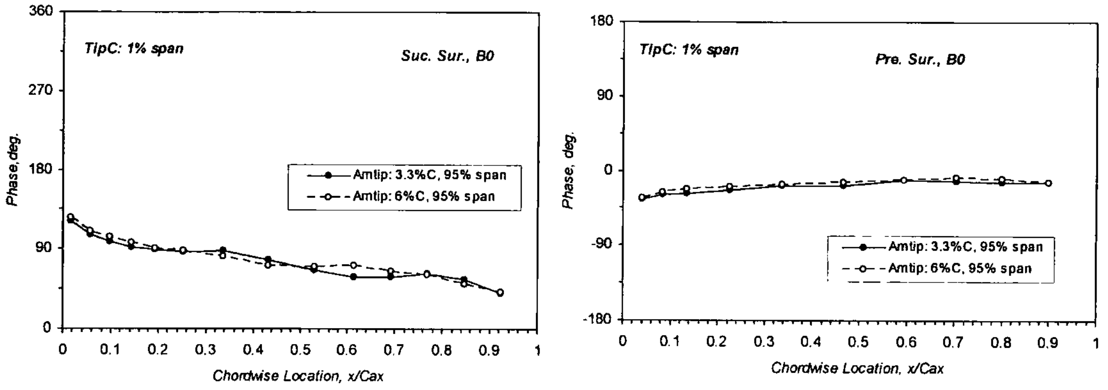

(*ii*) 95% span

Figure 7.7: Phase of the first harmonic pressure coefficient on the oscillating blade (at 90% and 95% span) at two oscillating amplitudes with 1% span tip clearance

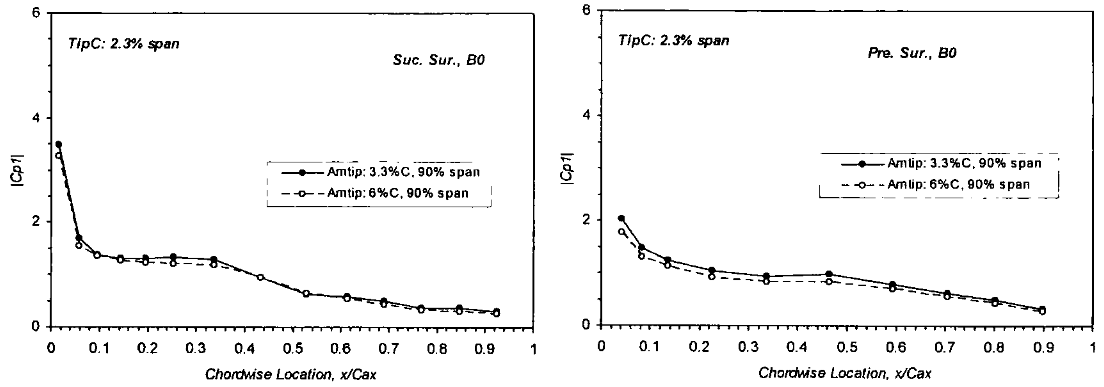

(*i*) 90% span

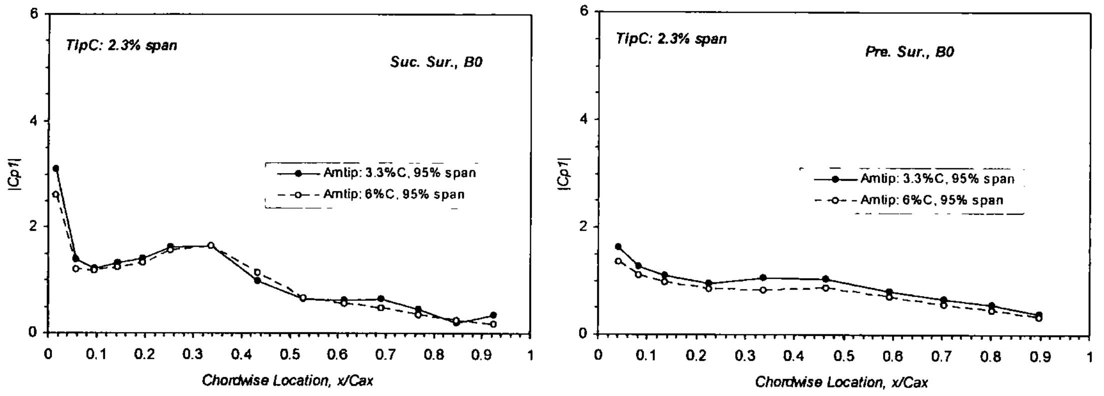

(*ii*) 95% span

Figure 7.8: Amplitude of the first harmonic pressure coefficient on the oscillating blade (at 90% and 95% span) at two oscillating amplitudes with 2.3% span tip clearance

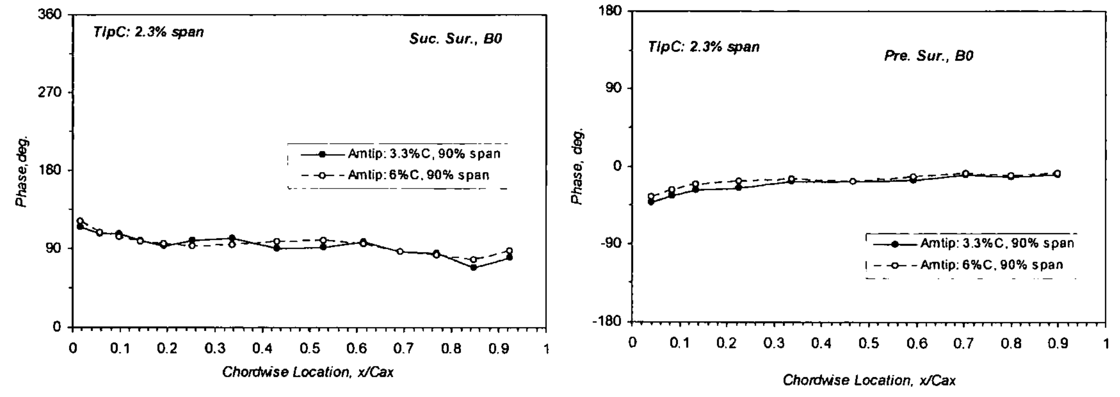

(*i*) 90% span

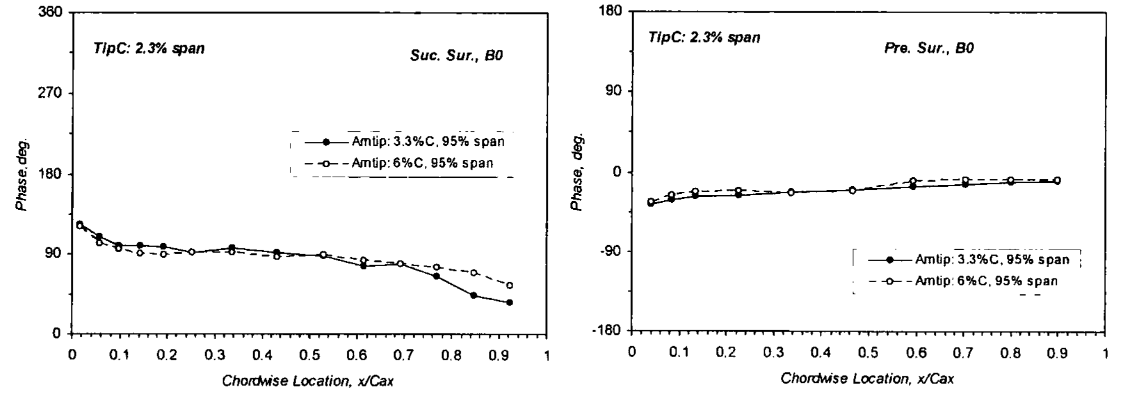

(*ii*) 95% span

Figure 7.9: Phase of the first harmonic pressure coefficient on the oscillating blade (at 90% and 95% span) at two oscillating amplitudes with 2.3% span tip clearance

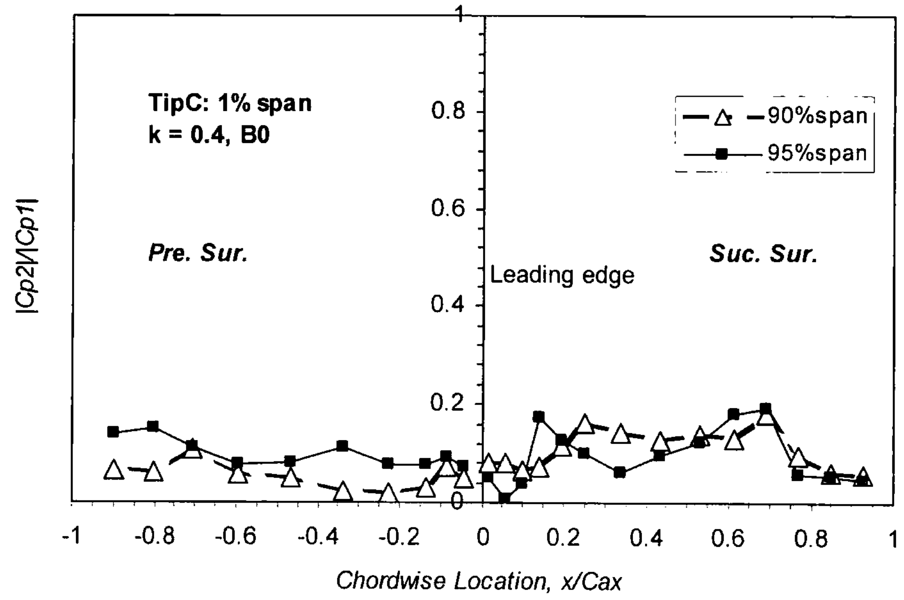

Figure 7.10: Relative amplitude of the second harmonic pressure coefficient with 1% span tip-clearance

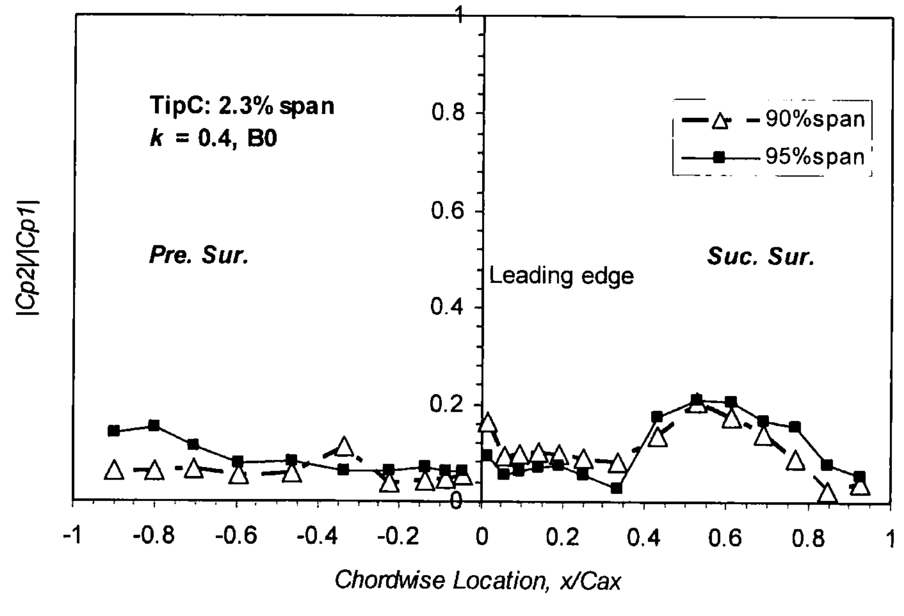

Figure 7.11: Relative amplitude of the second harmonic pressure coefficient with 2.3% span tip-clearance

7.2.2 Unsteady Responses at Two Different Tip Clearances

The tip-clearance effect on the aeroelastic stability of the oscillating cascade is examined by comparing the unsteady aerodynamic responses at two settings of tip-clearance (1% span and 2.3% span) to that at zero tip-clearance.

It is the advantage of the Influence Coefficient Method to investigate the overall aerodynamic damping for all inter-blade phase angles through one set of the unsteady aerodynamic influence coefficients from each tip-gap. **Figure 7.12** plots the overall aerodynamic damping against inter-blade phase angle (IBPA from -180° to 180°) for each tip-gap setting at k = 0.4. The figure shows that the tip leakage flow has destabilizing effect on the cascade stability over the whole range of inter-blade phase angle, whose strength is increased with increasing tip-clearance. This destabilizing effect is qualitatively independent of inter-blade phase angle. The maximum and minimum damping conditions affected by the different tip leakage flows would also change slightly the corresponding inter-blade phase angles. The minimum damping indicates the least unstable condition of the linear oscillating cascade. It can be seen that the maximum destabilizing influence of tip-gap is at IBPA 30° with the tip-clearance of 2.3% span, at which the minimum damping has been reduced by around 27% compared with that at the nominal zero tip-gap condition at the same frequency. The strength of the tip-gap destabilizing effect can be compared with that of reduced frequency effect when the reduced frequency was halved from 0.4 to 0.2 and the minimum aero-damping was reduced (**Figure 6.11**).

The least stable condition of system is always of interest to designers. In order to inspect the influence of tip-gap on the unsteady aerodynamic response of a tuned cascade in detail at the minimum damping (IBPA 30°), the amplitude and phase angle of the first harmonic pressure coefficient recorded at the three tip spans (90%, 95% and 98% span) are presented in **Figures 7.13 - 7.18** at the two settings of tip-gap, compared with those at the zero tip-gap.

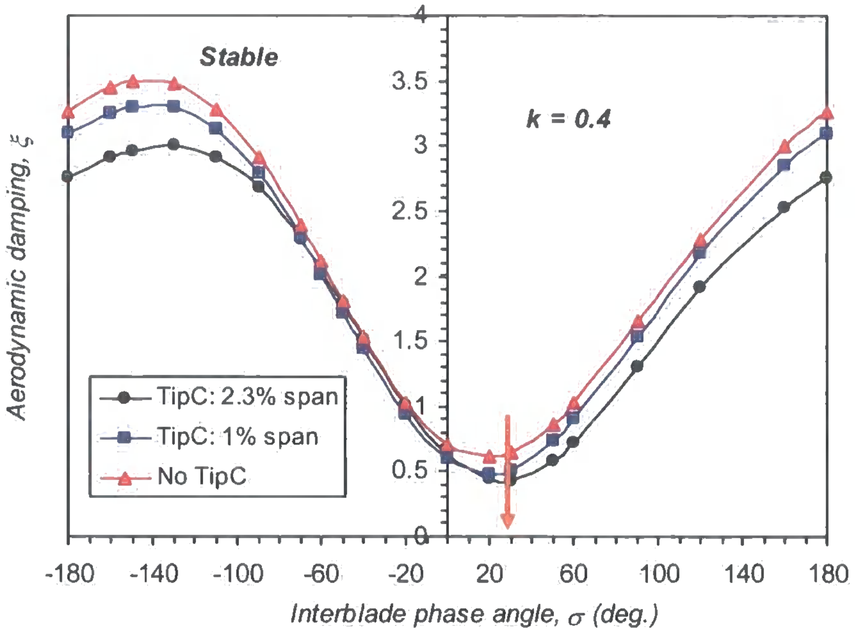

Figure 7.12: Overall aerodynamic damping for three tip-gap settings (k = 0.4)

There is a pronounced effect of tip-clearance on amplitude of unsteady pressure at 95% span on the suction surface as shown in **Figure 7.15**. The amplitude consistently decreases in the leading edge region on the suction surface with tip-gap. The influenced chordwise region extends with the increase of tip-gap and decreases toward the blade tip as shown in **Figure 7.17**. The strength of decreasing amplitude of unsteady pressure is enhanced toward the blade tip and reduced toward 90% span (**Figure 7.13**). The decreased amplitude of unsteady pressure with increasing tip-gap on the suction surface corresponds to the frontal unloading area in the steady flow as shown in **Figures 7.3 - 7.5**, similar to that reported by Bell (1999) for a single oscillating turbine blade. The frontal region with decreased pressure amplitude (up to 25%C) at 95% span with 2.3% span tip-gap is followed by a region with increased amplitude (25% - 45%C) comparing with that with zero tip-gap (**Figure 7.15**). The regions of the increasing amplitude are increased for both settings of tip-clearance when the blade tip is approached (**Figure 7.17**). It is noted that the region of increased unsteady amplitude corresponds to the development of the tip leakage vortex – the reloading around 40% chord on the suction surface with the strength and influenced chordwise area increased towards the blade tip (**Figures 7.3 - 7.5**) -

although the steady reloading area along the chord is smaller than that of increased unsteady amplitude for the two sets of tip-clearance at 90% and 95% span (**Figures 7.3 - 7.4**). This indicates that the unsteady aerodynamics in the blade tip region is influenced by tip leakage flow to much larger extent than the steady flow field, a similar observation was also made by Sanders *et al.* (2003) for a transonic rotor.

Regarding the phase angle at 95% span (**Figure 7.16**), two points should also be noted. Firstly the phase angle in the region 40%-70% chord on the suction surface decreases noticeably and hence the local aerodynamic damping becomes less stable as the tip-gap increases. Secondly the phase in the rear part on the pressure surface (40%C - 100%C) increases and thus the area becomes more destabilized with the increase in tip-gap. These patterns of the influence of tip-gap on the phase angle at 95% span also govern the trend of phase angle at 90% span (**Figure 7.14**) and 98% span (**Figure 7.18**) with the affected area along the chord changed more or less.

To illustrate the influence of tip-gap on the unsteady aerodynamic response along the blade span at the minimum damping condition (IBPA 30°), **Figure 7.19** presents the spanwise distribution of the local aerodynamic damping at the largest tip-gap compared with that at the nominal zero tip-gap for the two IBPAs corresponding to the aerodynamic damping extrema. This figure demonstrates the stable aeroelastic conditions at all spanwise locations for all cases. Note that the influence of tip-gap is not localized in the tip region due to the unsteady 3D effect (radial instantaneous interaction), although it is more announced near the blade tip. At the least stable IBPA 30°, the local aerodynamic damping in the region of 90% ~ 95% span is decreased by around 45% when the tip-gap is increased from zero to 2 % span.

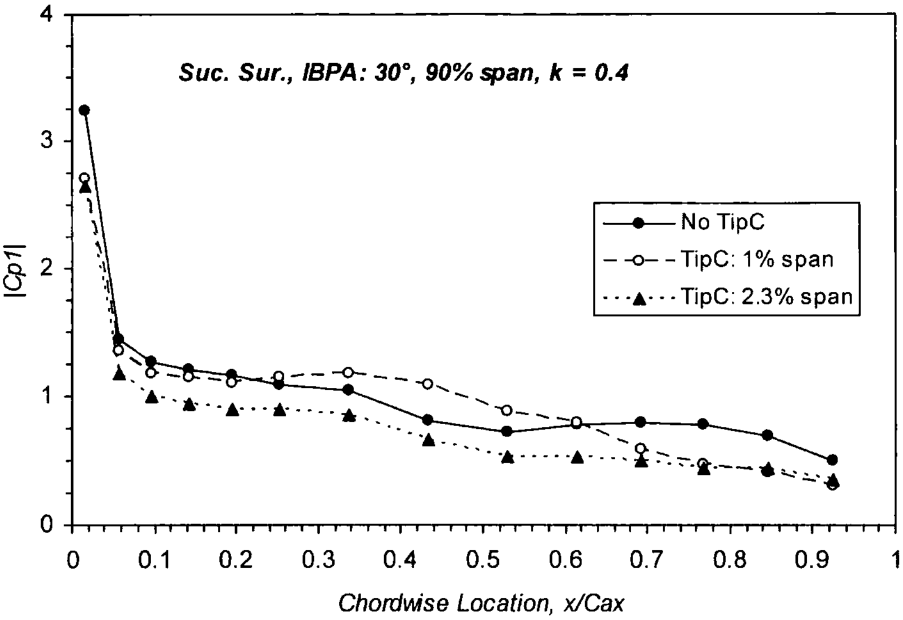

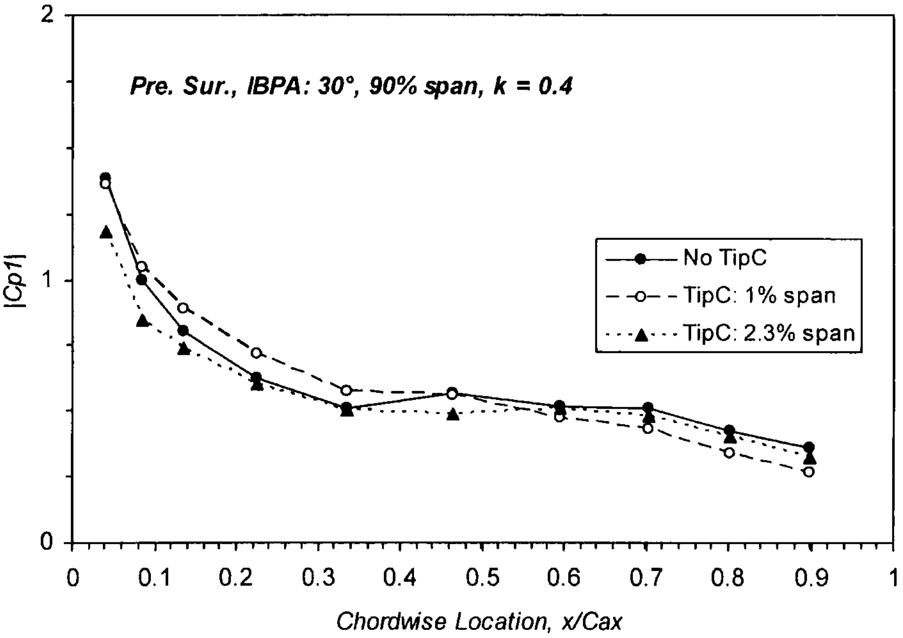

Figure 7.13: Amplitude of the first harmonic pressure response at 90% span (IBPA= 30° and $k = 0.4$)

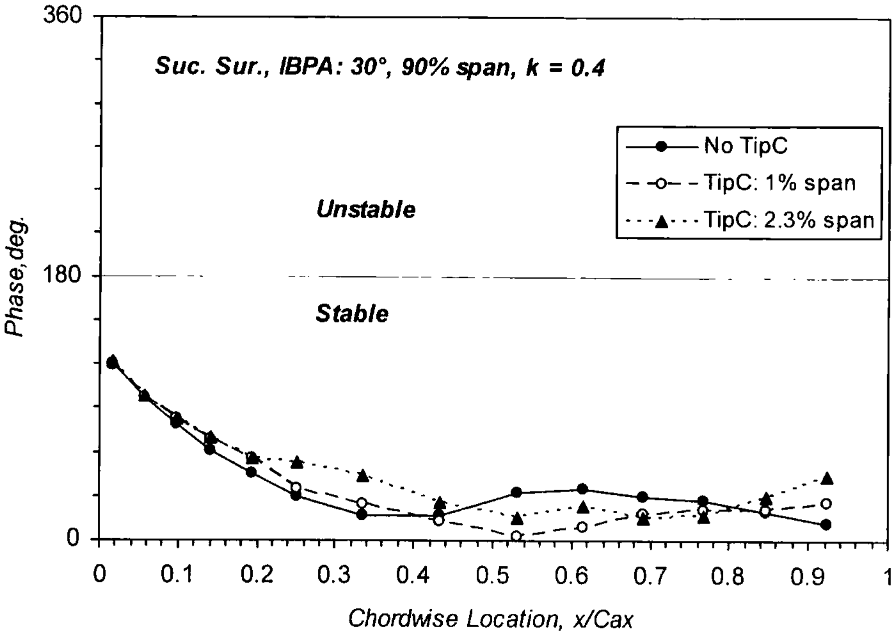

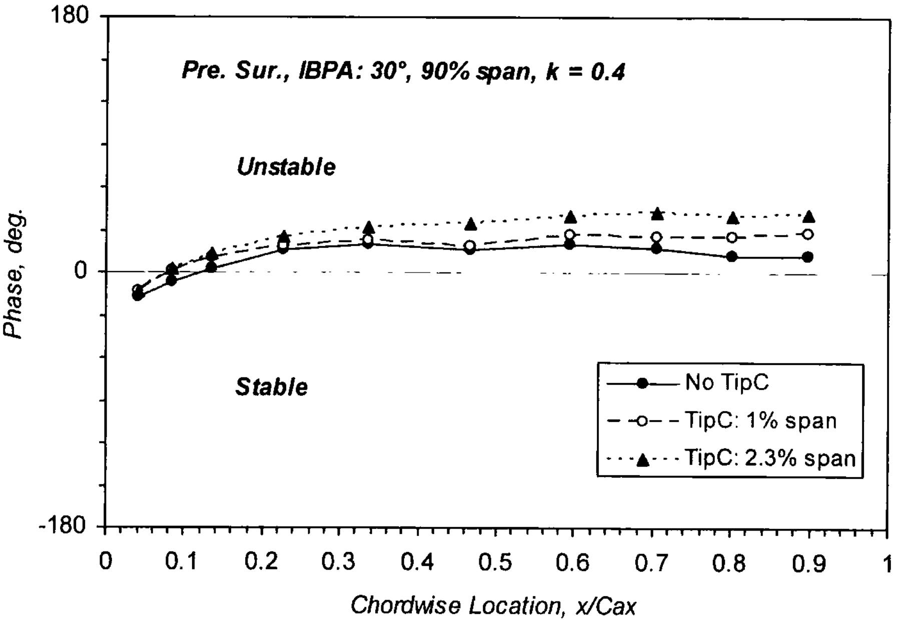

Figure 7.14: Phase angle of the first harmonic pressure response at 90% span (IBPA = 30° and $k = 0.4$)

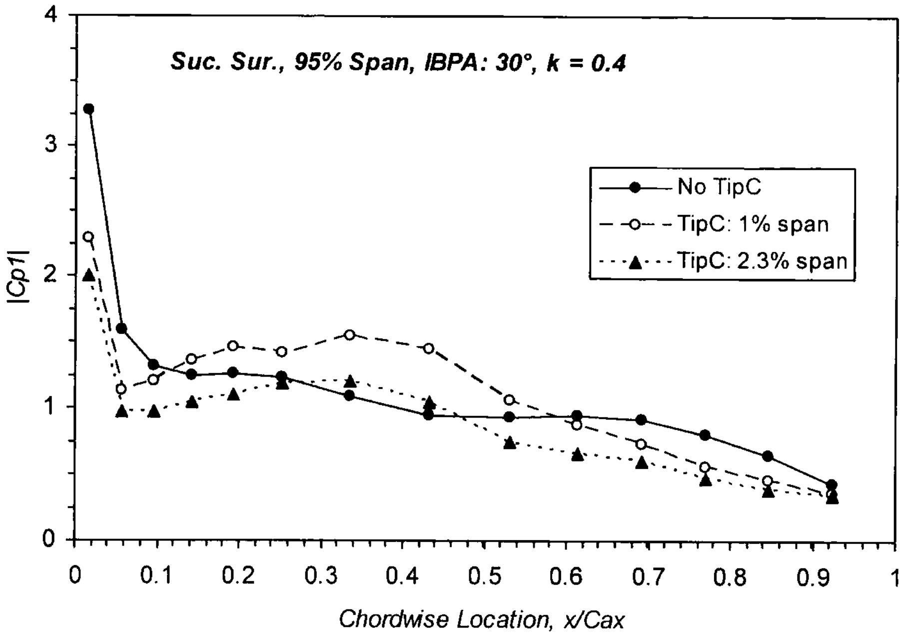

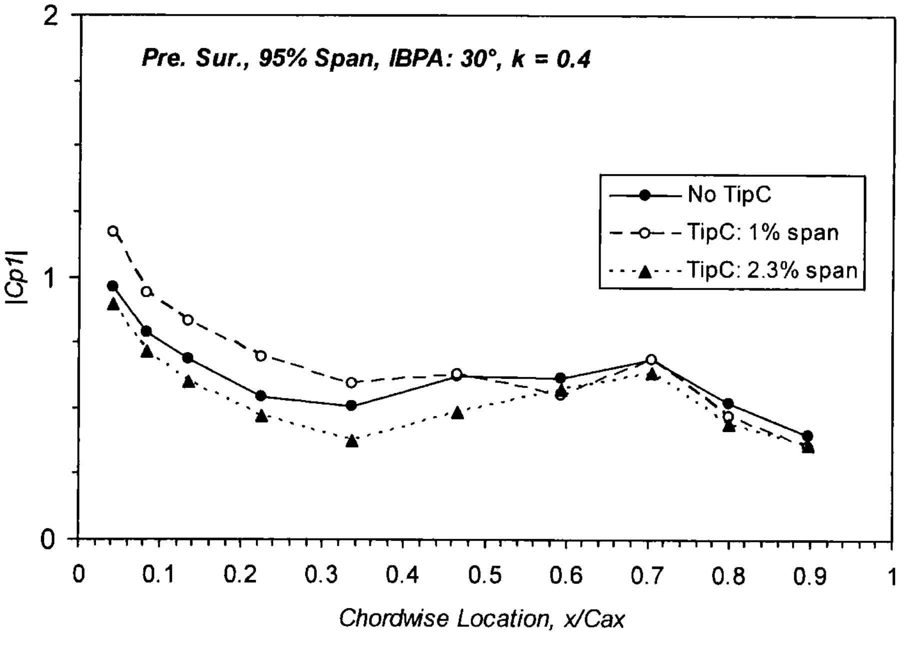

Figure 7.15: Amplitude of the first harmonic pressure response at 95% span (IBPA = 30° and $k = 0.4$)

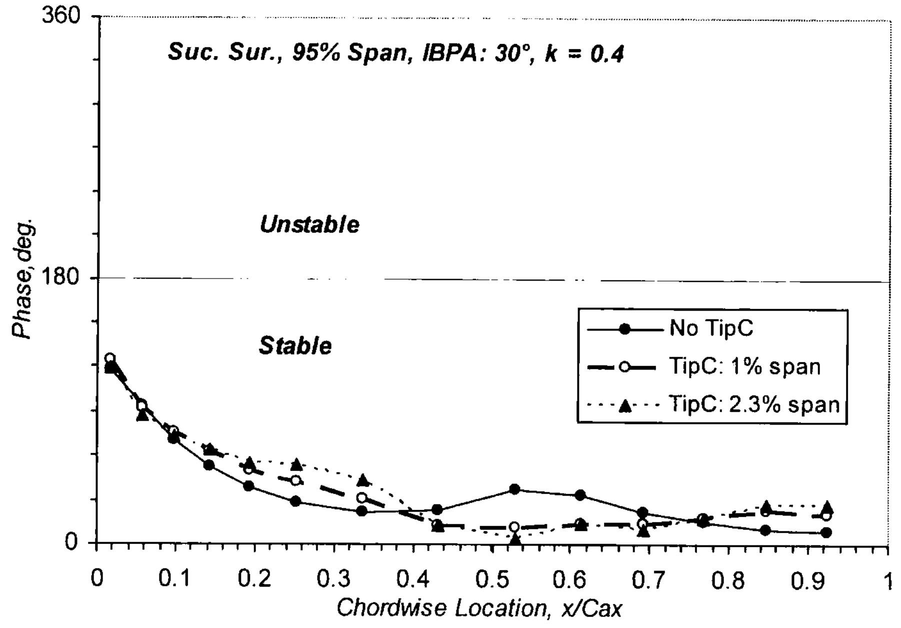

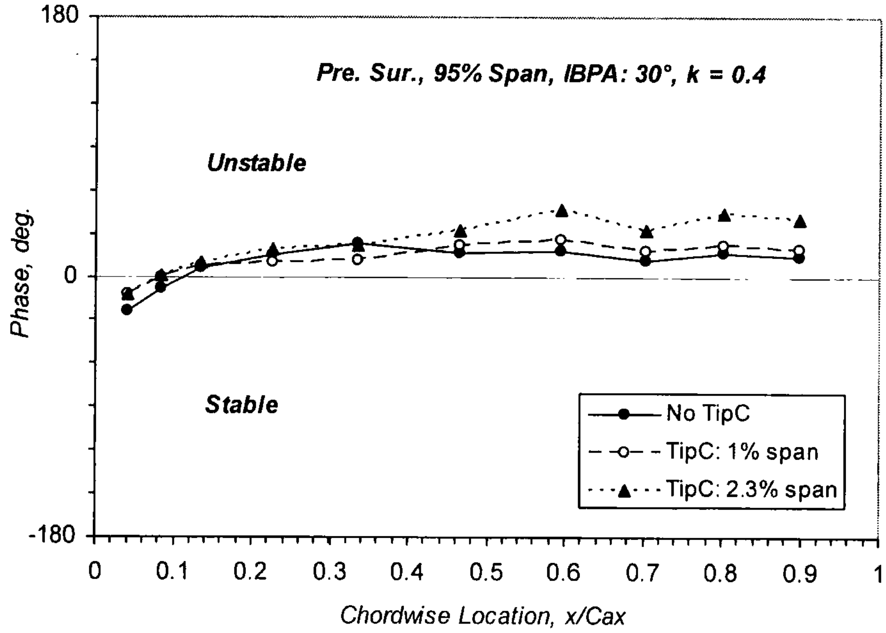

Figure 7.16: Phase angle of the first harmonic pressure response at 95% span (IBPA = 30° and $k = 0.4$)

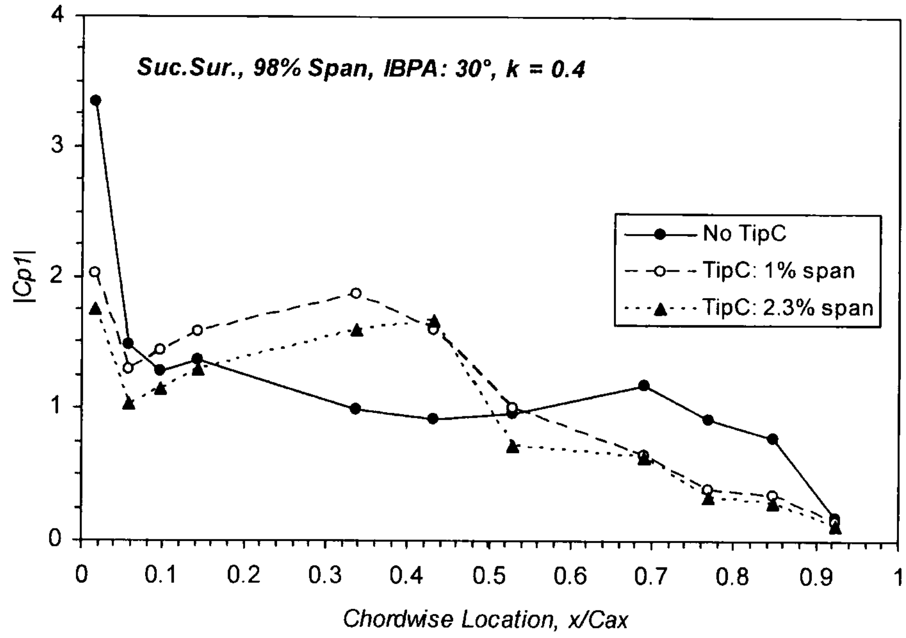

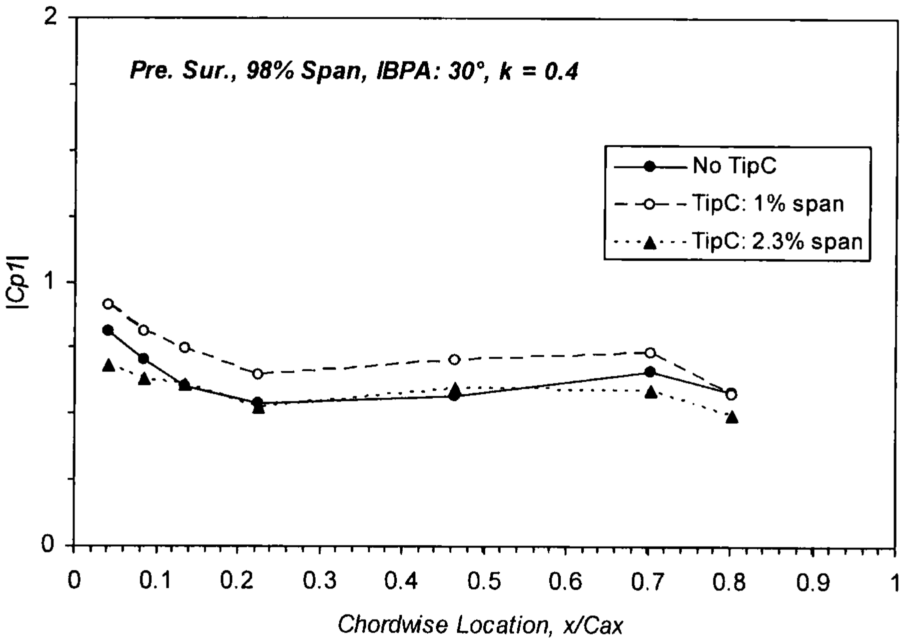

Figure 7.17: Amplitude of the first harmonic pressure response at 98% span (IBPA= 30° and k = 0.4)

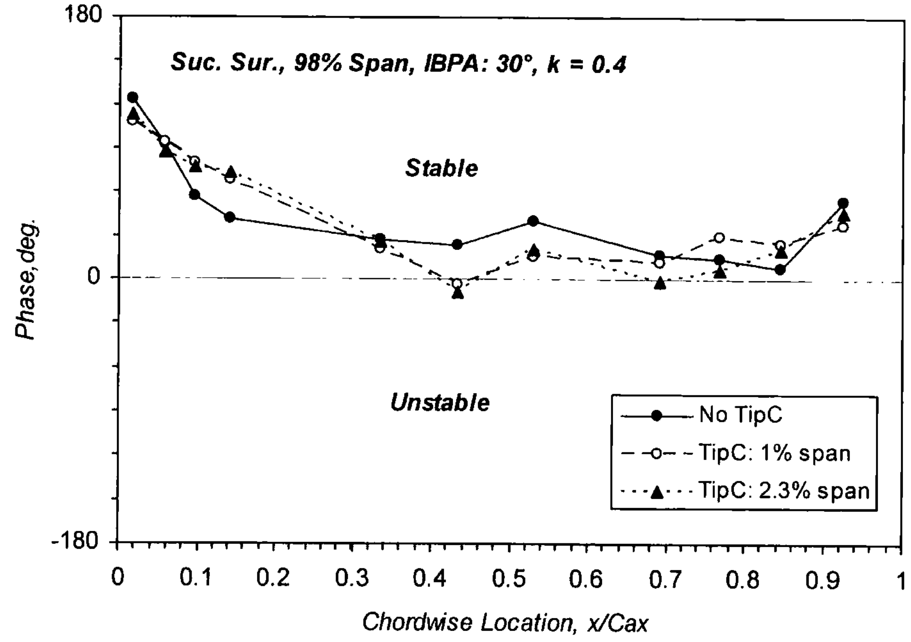

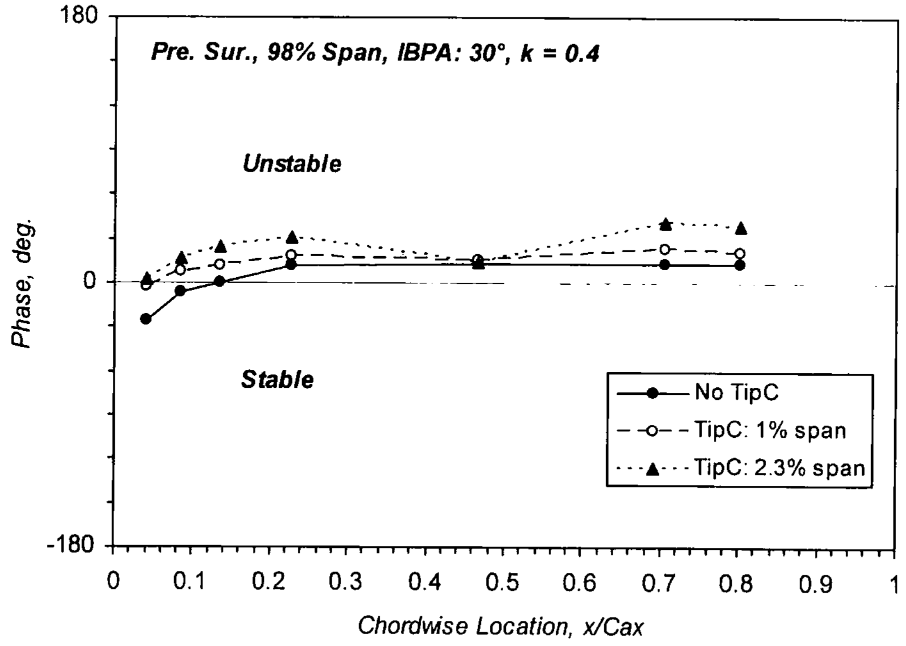

Figure 7.18: Phase angle of the first harmonic pressure response at 98% span (IBPA = 30° and $k = 0.4$)

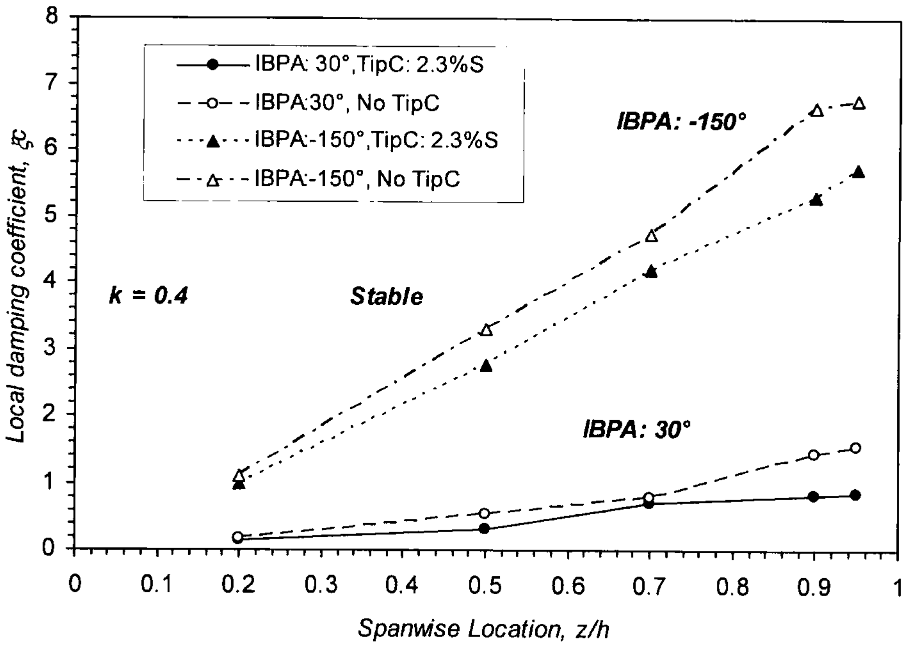

Figure 7.19: Spanwise local aero-damping coefficients with and without tip-gap (IBPA = 30° and -150° at $k = 0.4$)

Based on the observations above, the destabilising effect of tip-clearance on the aeroelastic response (the overall aerodynamic damping) at the least stable condition (IBPA 30°) as shown in **Figure 7.12** mainly results from the changes in amplitude of unsteady pressure on the suction surface and in phase angle on the both surfaces, and in terms of the blade spanwise section the blade tip sections give the main contributions to the greatly reduced aeroelastic stability of the oscillating cascade with the increase in tip-gap.

7.4. Summary

The steady flow measurements and the unsteady pressure aerodynamic responses at three tip spans for two sets of tip-gap had been presented comparing with those at the nominal zero tip-gap. The tip leakage flow was shown to have a destabilizing effect on the oscillating cascade for all inter-blade phase angles with the most significant influence at the least stable condition. Detailed unsteady pressure results showed that the region with reduced aerodynamic damping coincides with the localized region when the tip leakage flow had an impact on the steady flow. The destabilising tip-gap effect covers the most of blade span with the pronounced influence near the blade tip. This observed tip-gap destabilising effect would imply that a computational method without tip-clearance modelling might lead to an over-stable prediction of the onset of blade flutter.

For the influence of tip leakage flow on aeroelastic responses in real circumstances, two issues should be commented here. Firstly, in the present rigid body configuration, the oscillation amplitude varies linearly along the blade span, whilst practical flexible blades in 1st flap/bending mode will have relatively larger deflection near the blade tip (and hence larger local modal damping work). Hence, a larger influence of tip-gap on overall aerodynamic damping for real flexible blades might be expected than that observed in the present experiment. Secondly, a normal tip section tends to be much thinner than the blade section used in this investigation, which induces higher pressure gradients to driven tip leakage flow. Therefore the more significant influence of tip leakage flow, on both steady and unsteady blade loading, might be expected than that observed in this experiment.

It is recognised that the test facility does not allow the effect of rotation (relative to the tip section) and the influence of outer casing curvature on the tip leakage flow, which affect the inferred vortex structures of the tip leakage flow.

The investigation presented in this chapter provides the first test case on the influence of tip leakage flow on the unsteady aerodynamics of the oscillating cascade in a 3D bending mode.

Chapter 8

Computational Methods and Results

In this chapter, the computational phase of the present work is concerned, which was performed using a 3D time-linearised Navier-Stokes method. The principal objective is to assess the capability of this method to predict the relevant 3D unsteady aerodynamic phenomena exhibited by the oscillating compressor cascade experimental data. The results and accompanying discussions are also intended to help to gain further understanding of the behaviour of the unsteady flow previously discussed in Chapter 6. In the beginning, the computational method is briefly described. Then the numerical solutions of the experimental test cases are presented and discussed.

8.1 The Computational Model

Time-linearised approaches have been widely used in turbomachinery aeroelastic analyses because of their high computational efficiency. A 3D time-linearised unsteady Navier-Stokes method was used in the present study. In this method, unsteadiness can be assumed as a small harmonic perturbation to the steady flow. For blade flutter problems, the unsteady fluctuation in the flow only arises from the blade vibration. The moving grid is used to accommodate the movement of the mesh due to the blade motion. The original nonlinear unsteady Navier-Stokes equations can be divided into the steady and the linear unsteady equations by linearization with neglecting non-linear second order terms. The linear unsteady equations are only space dependent for a harmonic perturbation, in which the coefficients are obtained from the solution of the steady flow equations. In this time-linearised method, solving an unsteady flow problem is now effectively equivalent to solve two steady flow problems. A pseudo-time time-marching technique originally proposed by Ni & Sisto (1976) is used to time-march the steady equations and the linear unsteady equations. These equations are spatially discretised on a simple "H-type" mesh using a cell-centred finite volume scheme, and temporally integrated by a 4-step Runge-Kutta scheme. To enhance the convergence, the three levels of the multiple-grid acceleration are employed. To ensure the numerical stability, the second and fourth order adaptive smoothing is adopted to suppress the numerical oscillations. A single passage computational domain is adopted with phase-shifted periodic condition at the upper and lower boundaries to simulate all blades oscillating with the same frequency and a given inter-blade phase angle in a tuned cascade. The detailed description of the three dimensional time-linearised method for the Navier-Stokes equations can be found in Vasanthakumar (2003). The CFD code was provided by Prof. He, which incorporates the time-marching, the time-linearised and the nonlinear harmonic methods for 3D unsteady flows in turbomachinery applications.

8.2 Parameters and Conditions for the Computational Study

For blade flutter problems, adjacent blades usually vibrate with a constant inter-blade phase angle σ. The flow variables at the upper boundary will have the same phase shift relative to those at the lower boundary as shown in **Figure 8.1**. The phase-shifted periodic condition must be implemented at the upper and the lower boundaries as follows if a single passage solution domain is used:

$$\tilde{U}^{u} = \tilde{U}^{l} e^{i\sigma} \qquad (8\text{-}1)$$

Where, $\tilde{U}^{u}$ and $\tilde{U}^{l}$ are the perturbation conservation variables on the upper and lower boundaries, respectively. For time-linearised harmonic methods solving the linear unsteady equations in frequency domain, the implement of the phase-shifted periodicity on a single passage solution domain is very straightforward.

In the current study, all the computations were conducted on a single passage domain. In addition to the periodic boundary condition, there are three others: inlet, outlet, and solid wall. At an inlet, total pressure, total temperature and inlet flow angle for a subsonic flow are prescribed. For the present computations, an inlet flow angle of 37° was set referring to the experimental value. The inlet total pressure condition was specified according to the measured inlet total pressure. The total temperature was assumed to be constant. At the exit, a reflecting fixed constant static pressure condition was specified, which corresponds with the exhaust to atmosphere in the experimental test configuration. The density-based compressible flow computational scheme is unsuited to the flow at a very low speed, thus the exit static pressure was prescribed to increase the isentropic exit velocity to 66 *m/s*. This increase in exit velocity was required to ensure that the flow have a sufficiently low speed to resemble the test case while the present solver can still handle the solution. On the blade surface, there were no numerical fluxes across the boundaries during the viscous flow calculations. While for the energy equation, work terms done by pressure due to the surface movement must be included.

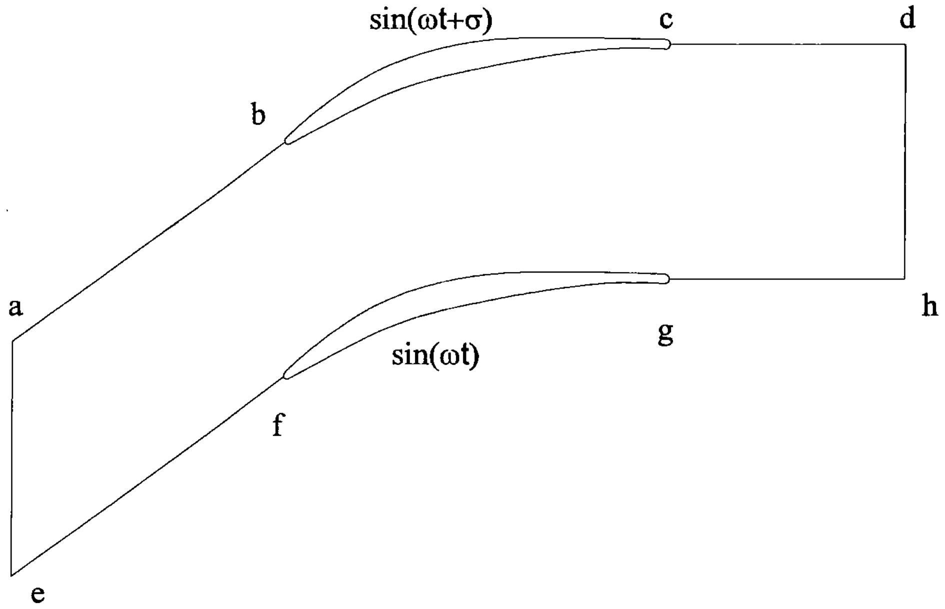

Figure 8.1: Single passage computational domain for blade flutter

The unsteady flows due to a bending motion of the blade in a direction perpendicular to the chord line were computed. The reduced frequency was set based on the isentropic exit velocity, which is consistent with the experimental setting. The vibration amplitude at the blade tip was 6% of the chord. The blade in the experimental setup was hinged well below the blade hub. Hence, the vibration amplitude at the hub was non-zero, but 0.5% of the chord. The experimental test configuration had a small tip-gap covered by a piece of dense sponge to accommodate the blade motion. However, this setting of tip-gap in the experimental configuration was simulated as no tip-gap in the computational domain. The experimental cascade is finite in extent while the numerical calculation modelled an infinite cascade with assuming a very large diameter (100*m*) of a blade row. So that the effect of the top and bottom walls of the linear cascade was not simulated in the prediction.

The side view and blade-to-blade view (two single computational domains were merged to construct the blade profile for clarity) of the computational mesh are shown in **Figure 8.2.** The computational domain is to extend one axial chord length upstream of the blade leading edge and one axial chord length downstream of the trailing edge, which corresponds with the exhaust to atmosphere. The mesh consists of 135 nodes distributed in the axial direction, 41 nodes in the circumferential direction and 51 nodes in the radial direction. In the near blade surface regions, the mesh was refined to resolve the viscous effects.

8.3. Numerical Results and Discussions

The numerical results of the steady flow and the unsteady flow at the reduced frequency of 0.4 are presented here, which were obtained on the conditions described above.

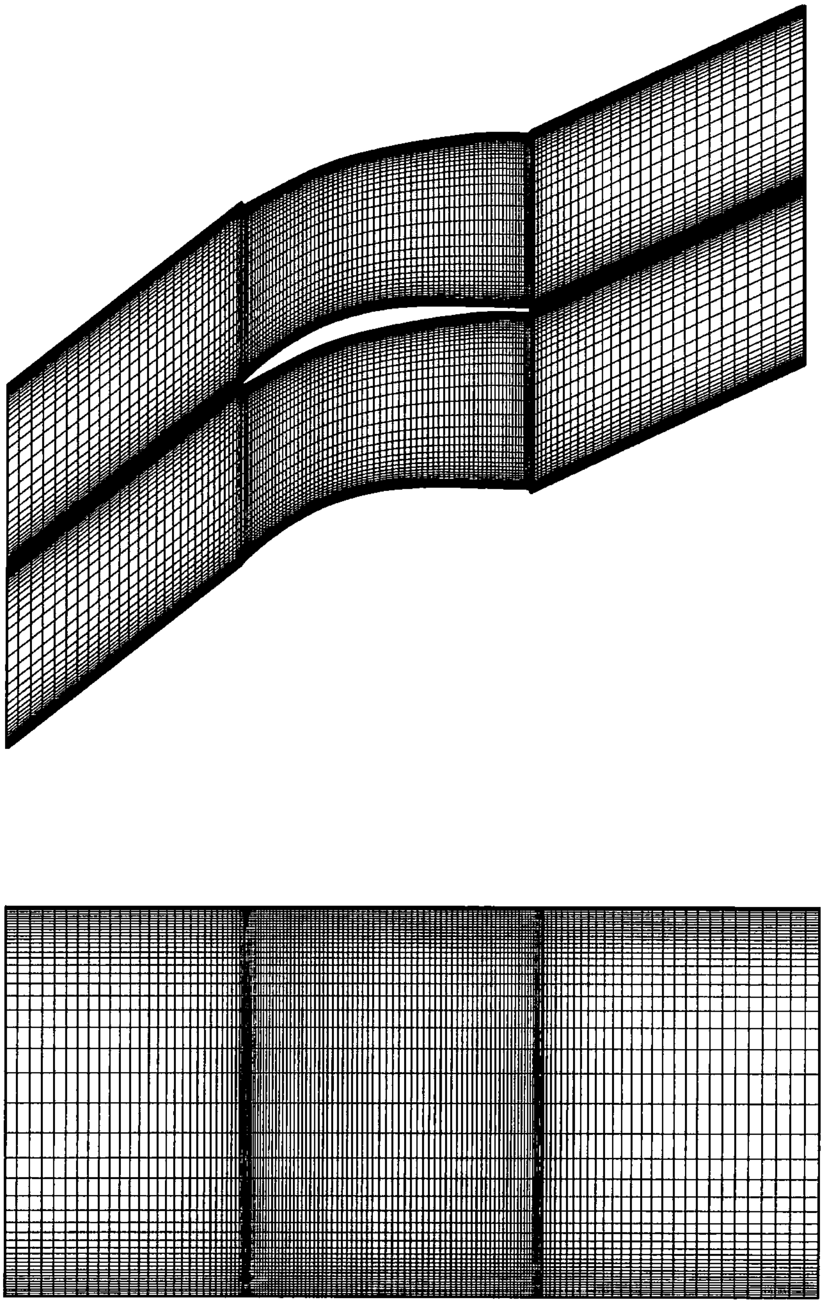

Figure 8.2: The computational mesh: blade-to-blade view (above) and side view (bellow)

8.3.1. Steady Flow Results

The proper modelling of the steady flow field is especially important for the time-linear unsteady methods as the one used here, where the steady flow is used as the base flow around which the linearisation is performed. The experimentally determined inlet flow angle is 37.5°. According to the existence of the experimental errors, there is a need to correct slightly the inlet flow angle to obtain the steady flow solution more closely in agreement with the experimental data.

Figure 8.3 is the predicted static pressure coefficient along the chord at 50% span comparing with the experimental data at the inlet flow angle 37°, 38° and 39° respectively. The solid line represents the steady flow code prediction and the solid triangles represent the experimental results. Increasing inlet flow angle has obvious influence on the surface static pressure on the suction surface, while its effect on the pressure surface is very small. The best match of the prediction to the experimental data is obtained at the inlet flow angle of 37°.

The steady flow predicted at the inlet flow angle 37° is compared with the experimental data in **Figure 8.4** for the five spanwise sections (20%, 50%, 70%, 90% and 95% span). The overall agreement with the experimental data is quite satisfactory at all five spanwise sections with some deviations. It is noted that the computational results are not able to capture the 2D laminar separation bubble on the suction surface at 50% and 70% span indicated by the experimental data because a fully turbulent solution can not predict a laminar separation-bubble due to the absence of the appropriate transition model. The end wall unloading near the blade tip shown at 90% and 95% span is not predicted by this solver, which is associated with the endwall passage vortex. The computed steady pressure distributions show some "wiggles" in the leading and trailing edge regions as well as around 30% chord on the suction surface for all spanwise locations. This is believed to be resulted from the non-smoothing of the blade geometry. The leading and trailing edge meshes are refined using O-type mesh as shown in **Figure 8.6** comparing with that using H-type mesh shown in **Figure 8.5,** and hence the shorter spikes of the predicted steady pressures at the leading and trailing edges were obtained comparing with those shown in **Figure**

8.5. This suggests a lack resolution of the present structured H-type mesh around the blade leading edge and trailing edge. The improved surface static pressure distribution on the suction surface shown in **Figure 8.7** was obtained by smoothing the blade profile in the "wiggles" area comparing with the prediction shown in **Figure 8.5**.

Apart from these deviations, the satisfactory prediction of the steady flow forms a good basis for the unsteady flow calculations.

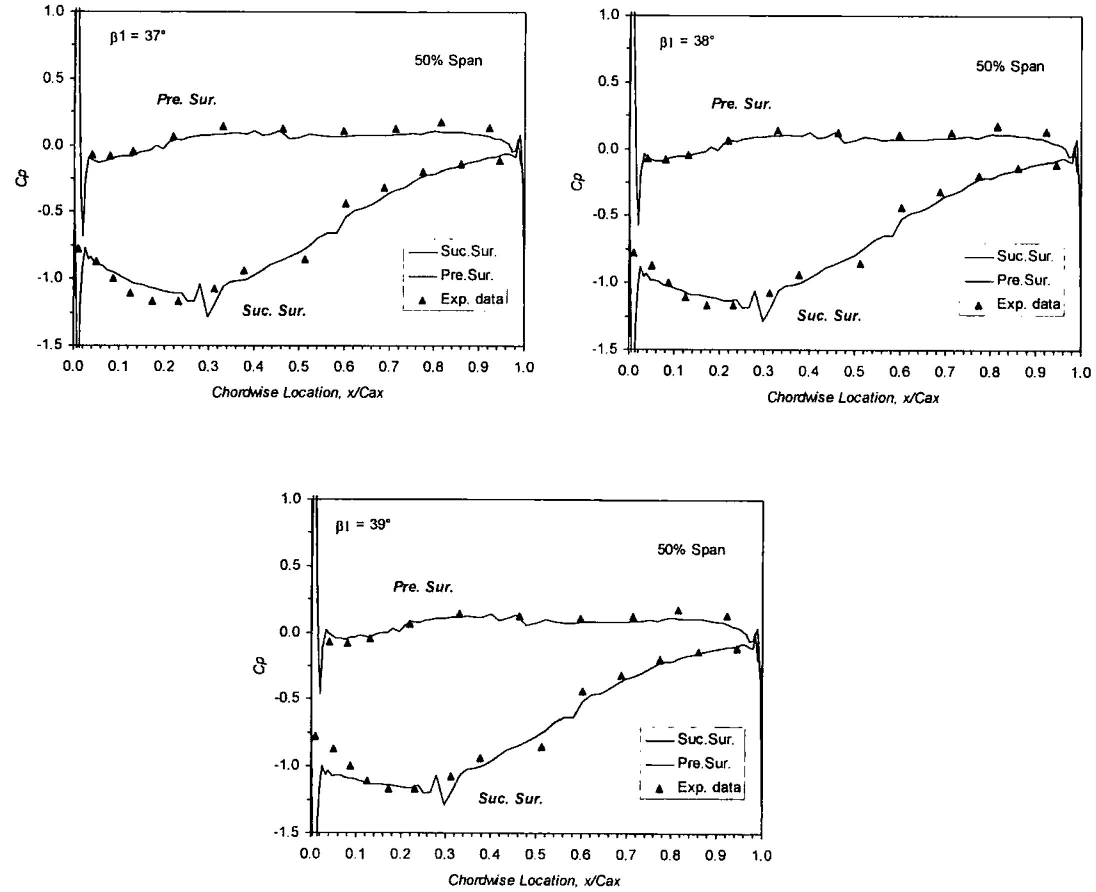

Figure 8.3: The comparison of static pressure distribution for three inlet flow angles at midspan

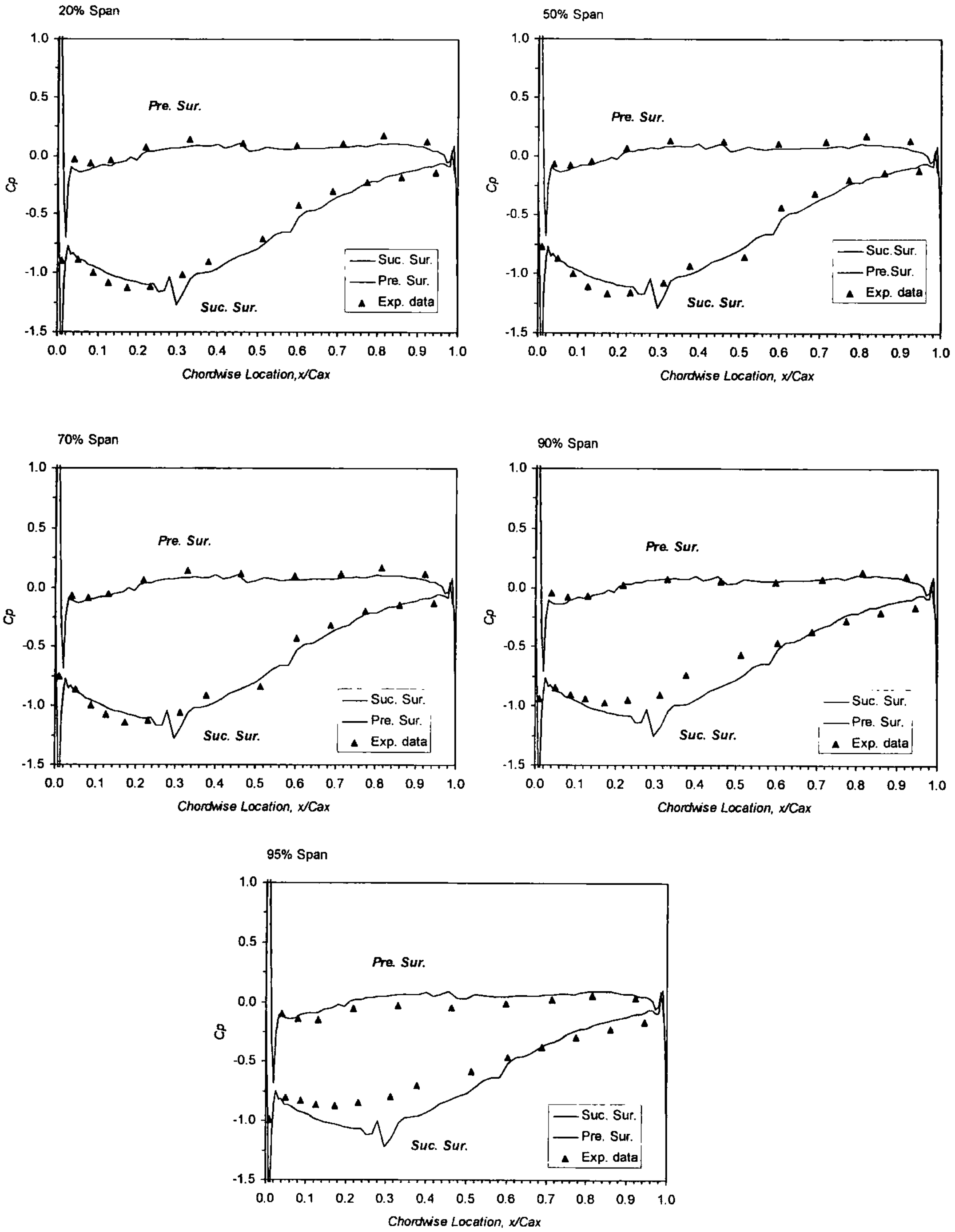

Figure 8.4: Predicted and measured blade surface pressure distribution at 20%, 50%, 70%, 90% and 95% span

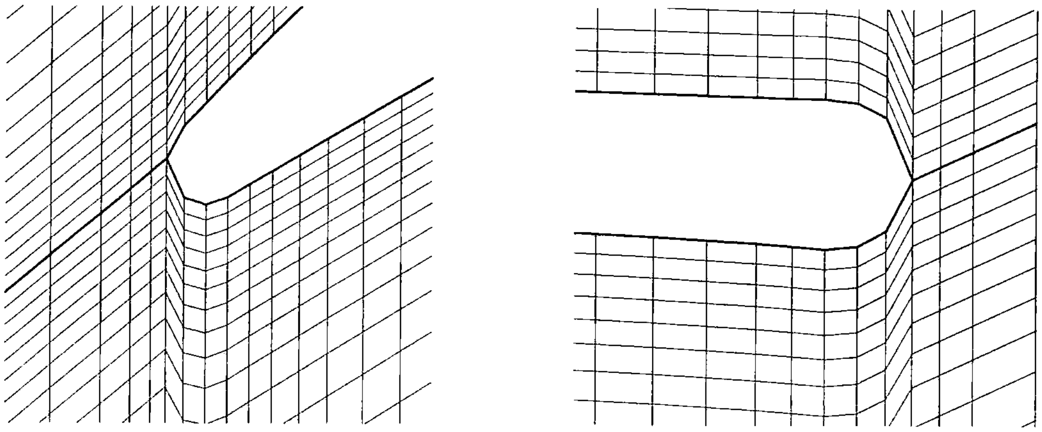

Leading edge mesh

Trailing edge mesh

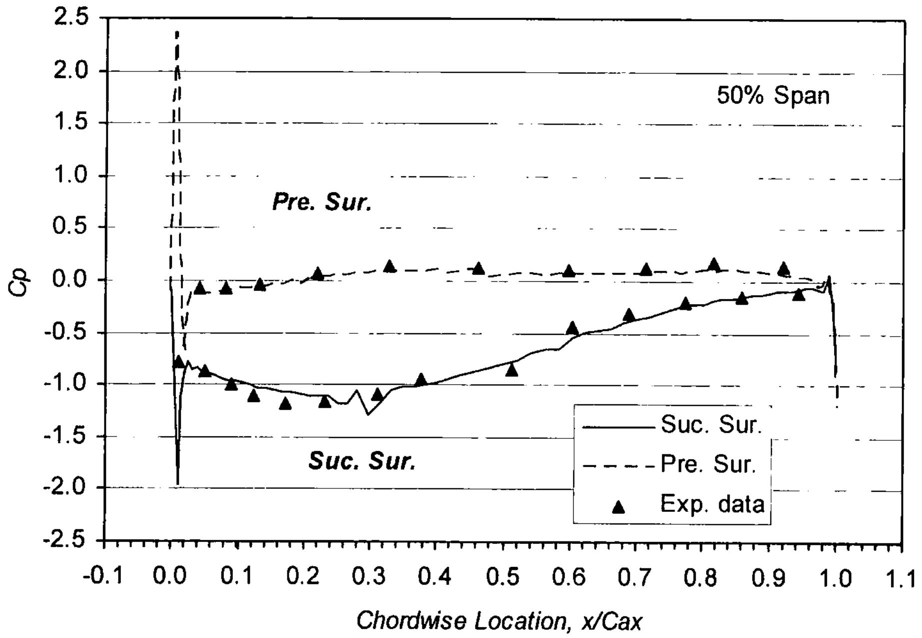

Figure 8.5: Static pressure distribution at 50% span using H-type mesh

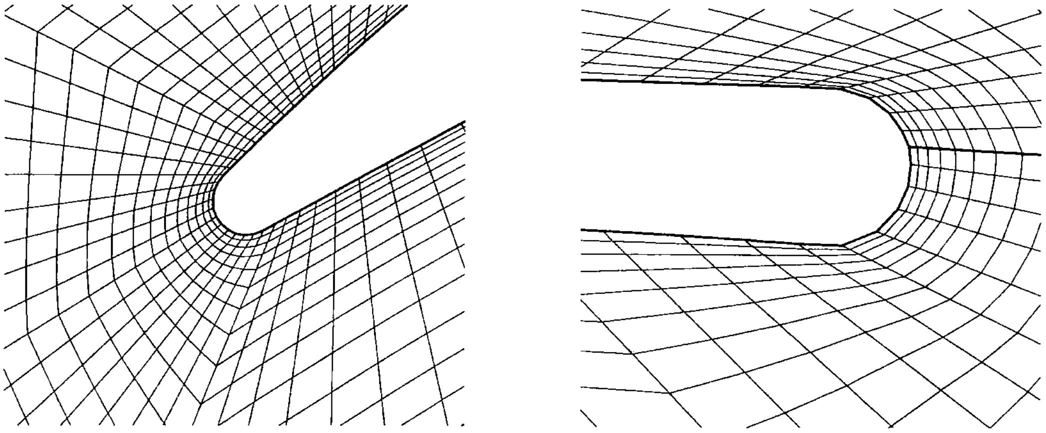

Leading edge mesh

Trailing edge mesh

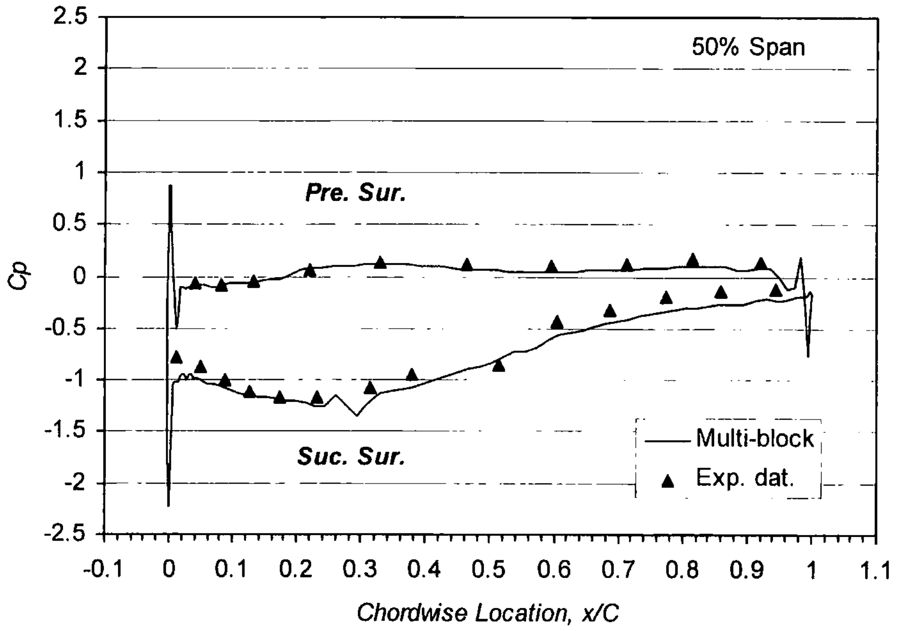

Figure 8.6: Static pressure distribution at 50% span using O-type mesh

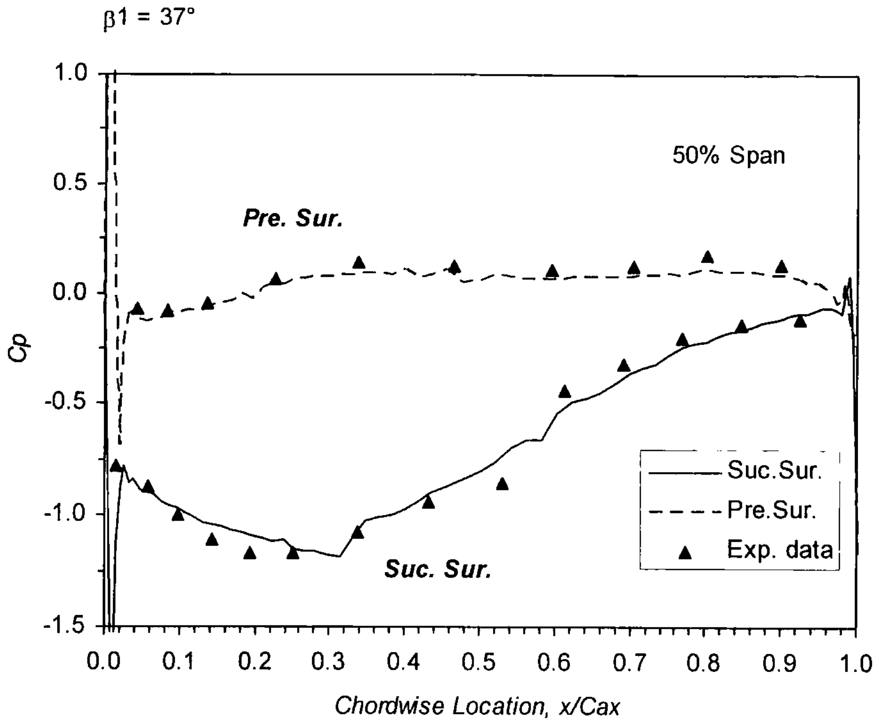

Figure 8.7: Static pressure distribution at 50% span with smoother surface

8.3.2. Unsteady Flow Calculations

The unsteady flow computations were performed using a single blade passage regardless of inter-blade phase angles. Comparisons of the linear analysis with the experiment results are made on the basis of the calculated aeroelastic stability and the first harmonic component of unsteady pressure.

The predicted overall aerodynamic damping at the reduced frequency of 0.4 at six values of inter-blade phase angle, together with the experimental data, is presented in **Figure 8.8.** The aerodynamic damping defined in Section 4.2.4.2 is based on exit dynamic head, blade chord, blade span and vibration amplitude at the blade tip.

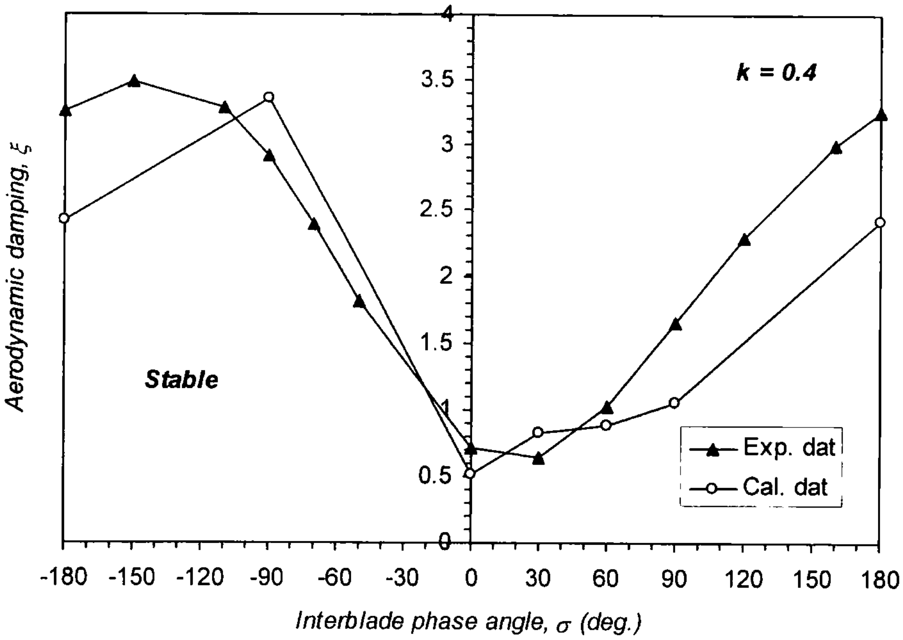

Figure 8.8: Predicted aerodynamic damping comparing with experimental data against IBPA at $k = 0.4$

The damping prediction more closely follows the trend of the experimental data at most IBPAs except the IBPA 30° at the minimum aerodynamic damping. The higher value predicted at IBPA 30° indicates a more stable condition. Predicted damping values at 90° and 180° IBPA are lower than those actually measured, indicating a more unstable condition. Based on the investigation of the tip-clearance effect on the aeroelastic stability of the oscillating cascade documented in Chapter 7, numerical simulations ignoring the tip-clearance effect will cause over stable prediction for all inter-blade phase angles with the maximum influence at the minimum aerodynamic damping condition. Thus, this suggests that modelling the influence of tip-clearance is needed for the aeroelastic stability although the present test rig was set up with very small tip-gap to accommodate the blade vibration. **Figure 8.9** shows the time steps indicating the convergence of the unsteady flow calculations at different IBPAs. The convergence was obtained at different IBPAs when the absolute value of the relative error of the predicted aerodynamic damping (Derror) is less than 10%. Its definition is expressed in equation 8.2.

$$Derror = \frac{Damping_{current} - Damping_{previous}}{Damping_{previous}} \tag{8.2}$$

where $Damping_{current}$ is the calculated aerodynamic damping at the current time step and $Damping_{current}$ is the predicted value of aerodynamic damping at the previous time step.

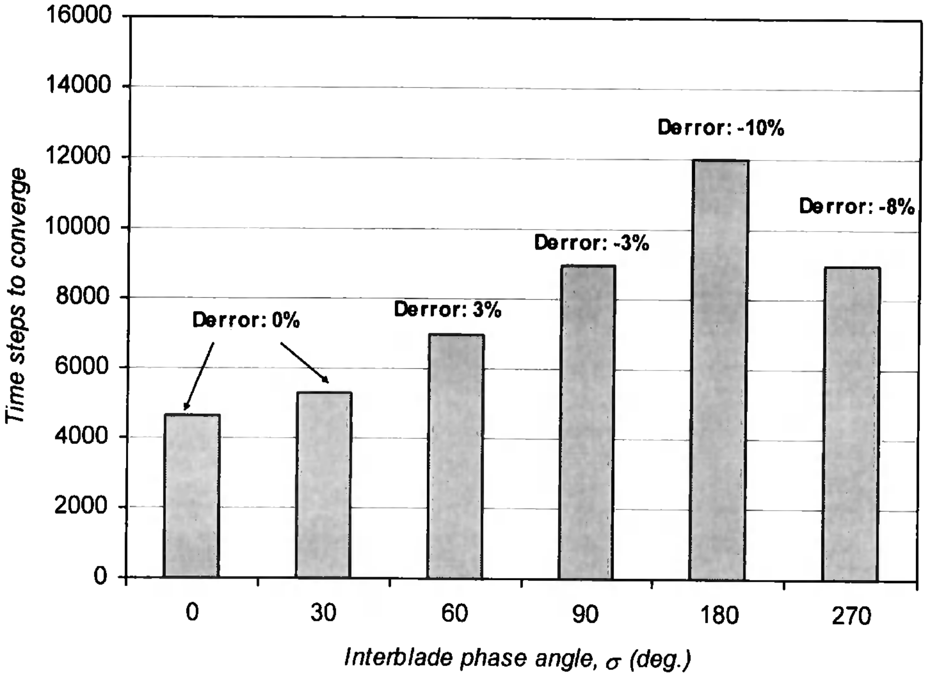

Figure 8.9: Time steps of unsteady flow calculations to converge

The number of the time steps of unsteady flow calculation to converge at different IBPAs is different with the quickest convergence at IBPA 0° and the slowest convergence at IBPA 180° for the present simulation. The variation in convergence time of unsteady flow calculation at different IBPAs only comes from the different periodic boundary conditions due to different inter-blade phase angles as shown in **Figure 8.1**, which means the pressure perturbations decay quickly at some inter-blade phase angles and slowly at other inter-blade phase angles due to the different periodic boundaries in the tuned cascade model, while this situation can not be modelled in the present experiment configuration using the Influence Coefficient Method. Thus, this seems to suggest that the difference between the boundary conditions in the simulation and the experiment gives the contribution to the deviation in the prediction of the overall aerodynamic damping.

The linear harmonic predictions of the amplitude and phase of the first harmonic pressure coefficient are presented at the five span sections comparing to the experimental data in **Figures 8.10 - 8.14** for IBPA 90°, and **Figures 8.15 - 8.19** for IBPA 180°. The reduced frequency is 0.4.

The calculated amplitude and phase of unsteady pressure generally exhibit good correlation with the experimental data for IBPA 90° as shown in **Figures 8.10 - 8.14**. The overall shape of the unsteady pressure amplitude distribution is closely reproduced by these computational results. While the overall agreement is rather satisfying, some details are worth a closer inspection. The one area where the present code does not match the experimental data very well is in the leading edge region, where the predictions show a steeper pressure gradient. The calculation under-predicts the amplitude for the front 30% chord on both of blade surfaces till 70% span section, which corresponds to the regions at these span sections that the present code over-predicts the static pressures on the suction surface shown in **Figure 8.4**. Toward the blade tip, there is a peak in amplitude at 30% chord on the suction surface, which is more obvious at 95% span with the increase of the local blade amplitude. This is associated with the differing change in blade passage along the blade span when blades vibrate and is not clear in the unsteady pressure amplitude obtained by the experiment, which demonstrates a predominant incidence effect. There is a better agreement between the amplitude data and the linear predictions for the aft half chord on both surfaces for the lower three span sections as shown in **Figures 8.10 - 8.12** except for 54% chord on the suction surface at 70% span due to the separation bubble, which also corresponds to the regions at these span sections that the predicted static pressures agree well with the experimental data as shown in **Figure 8.4**.

The measured phase data and predictions exhibit a general trend agreement on the majority of the suction surface and the whole pressure surface. The predicted phase angles offset to lower values on both surfaces. The large differences in phase angle of unsteady pressure over the suction surface are observed. Differences between the experimental data and the predictions are most prominent in the 2D laminar separation region where the deviations in the steady flow also influence the unsteady flow predictions. The abrupt phase change for the 2D separation bubble on the suction surface at 50% and 70% span is not predicted by this solver (**Figures 8.11 and 8.12**). The differences in phase angle on the pressure surface are much smaller than that on the suction surface.

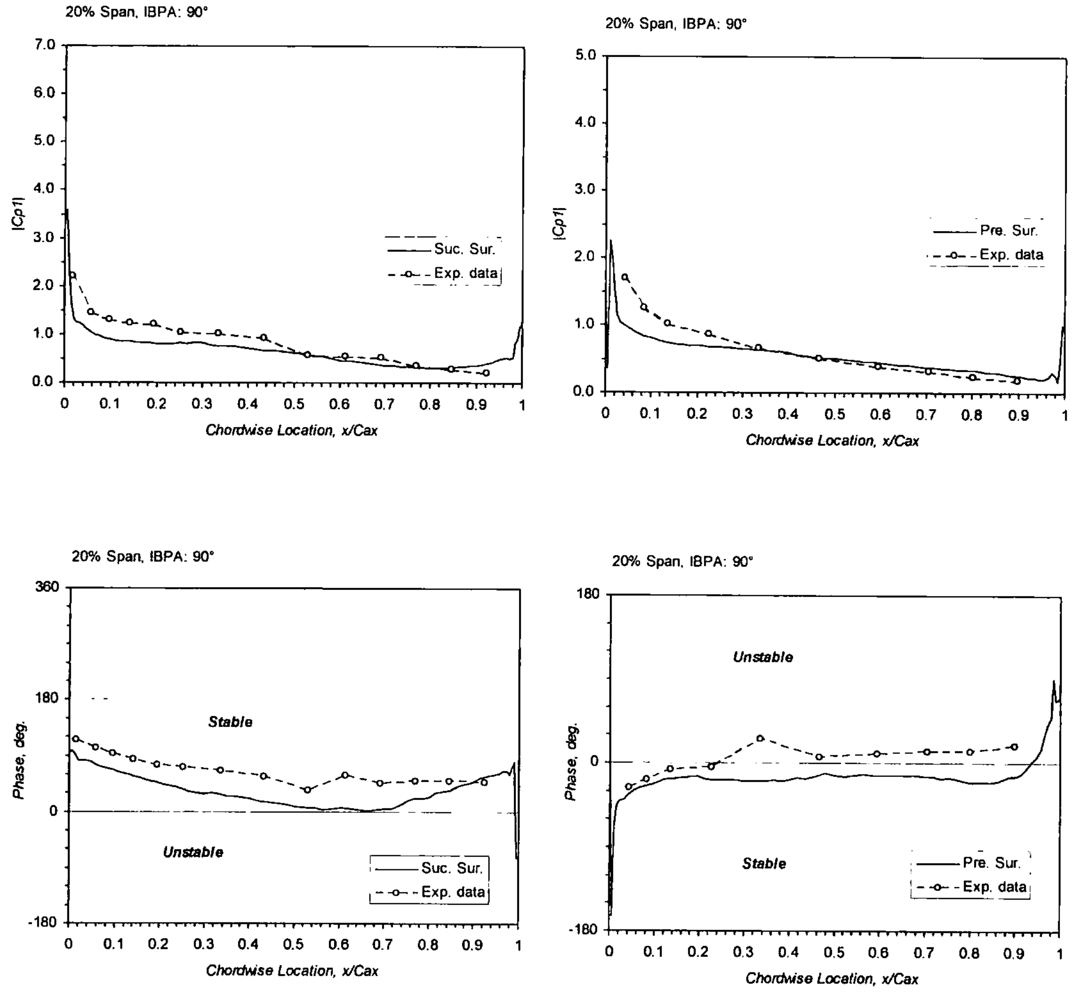

Figure 8.10: Predicted and measured amplitude and phase of the first harmonic pressure coefficient at 20% span for IBPA 90°

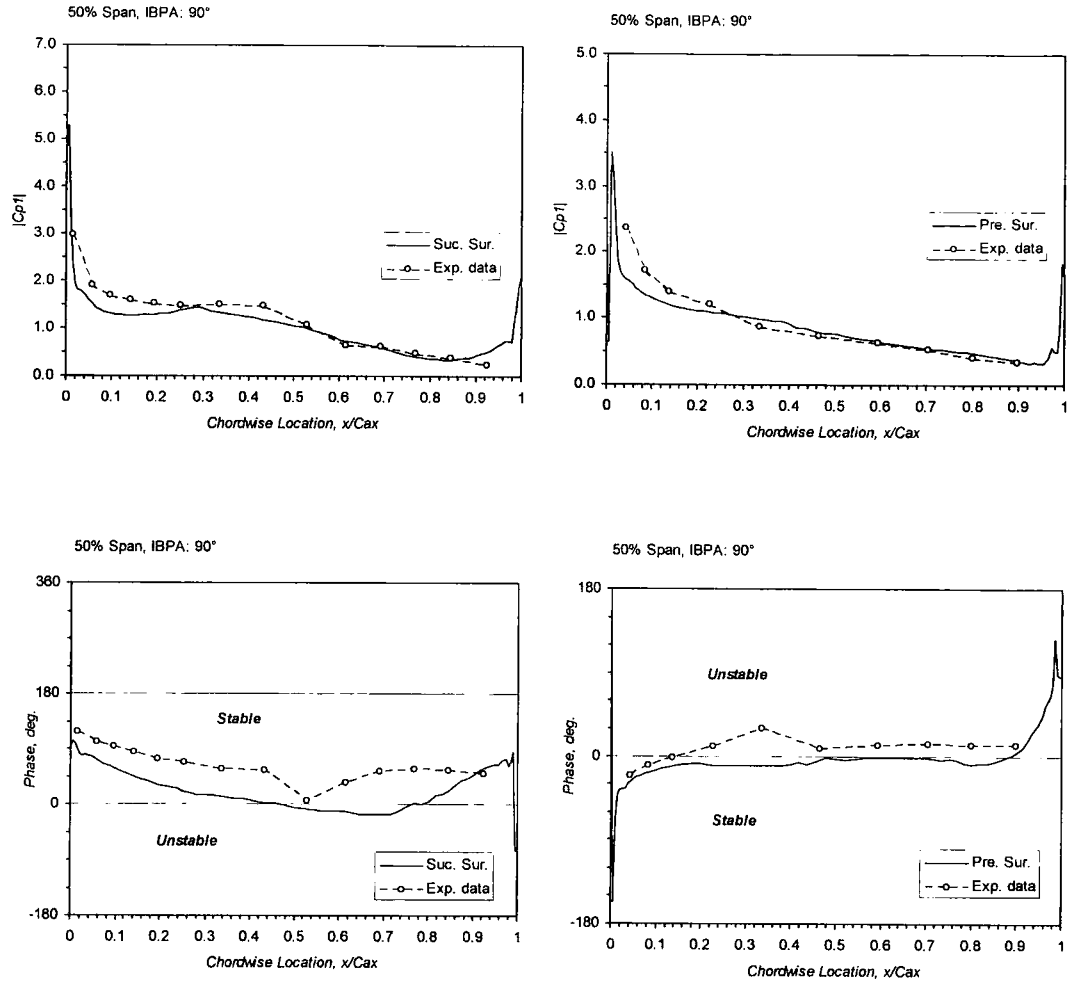

Figure 8.11: Predicted and measured amplitude and phase of the first harmonic pressure coefficient at 50% span for IBPA 90°

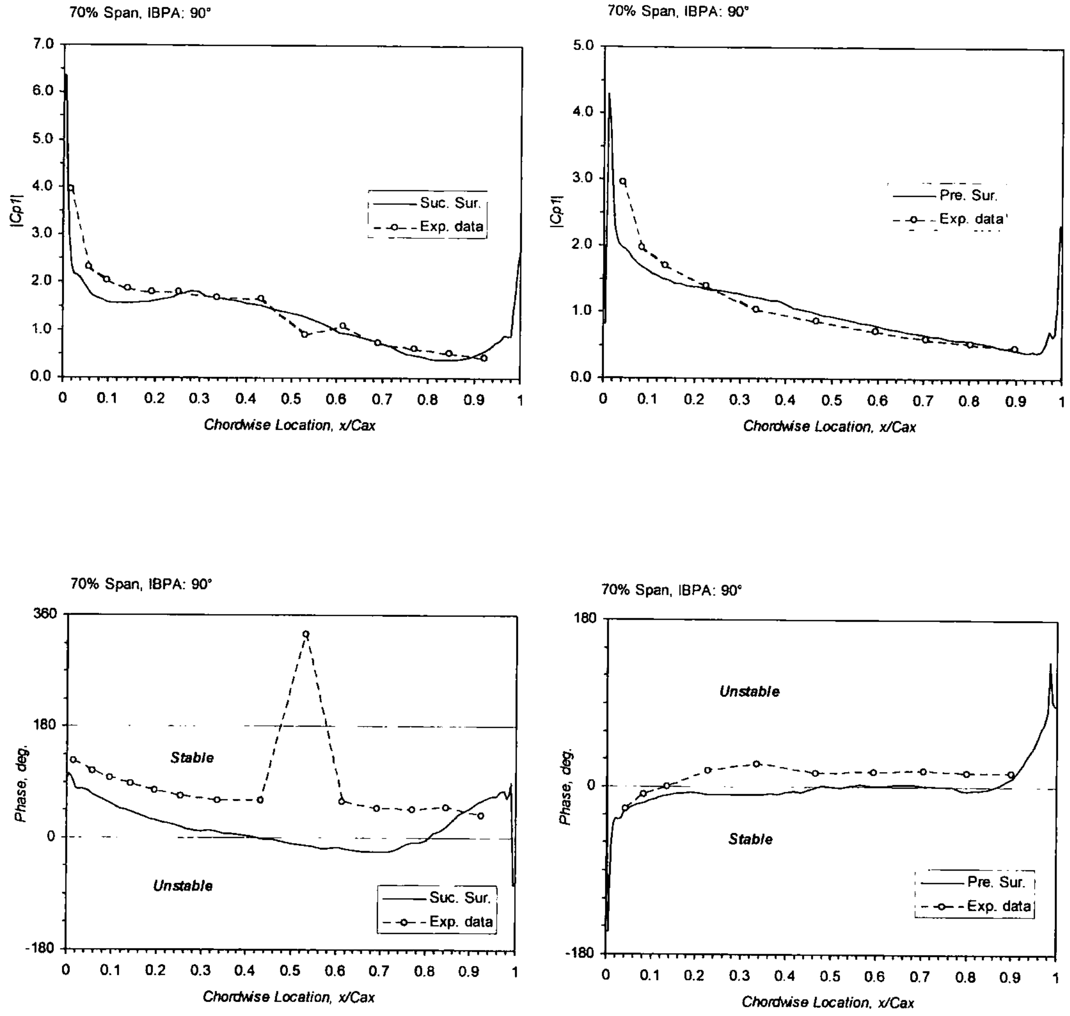

Figure 8.12: Predicted and measured amplitude and phase of the first harmonic pressure coefficient at 70% span for IBPA 90°

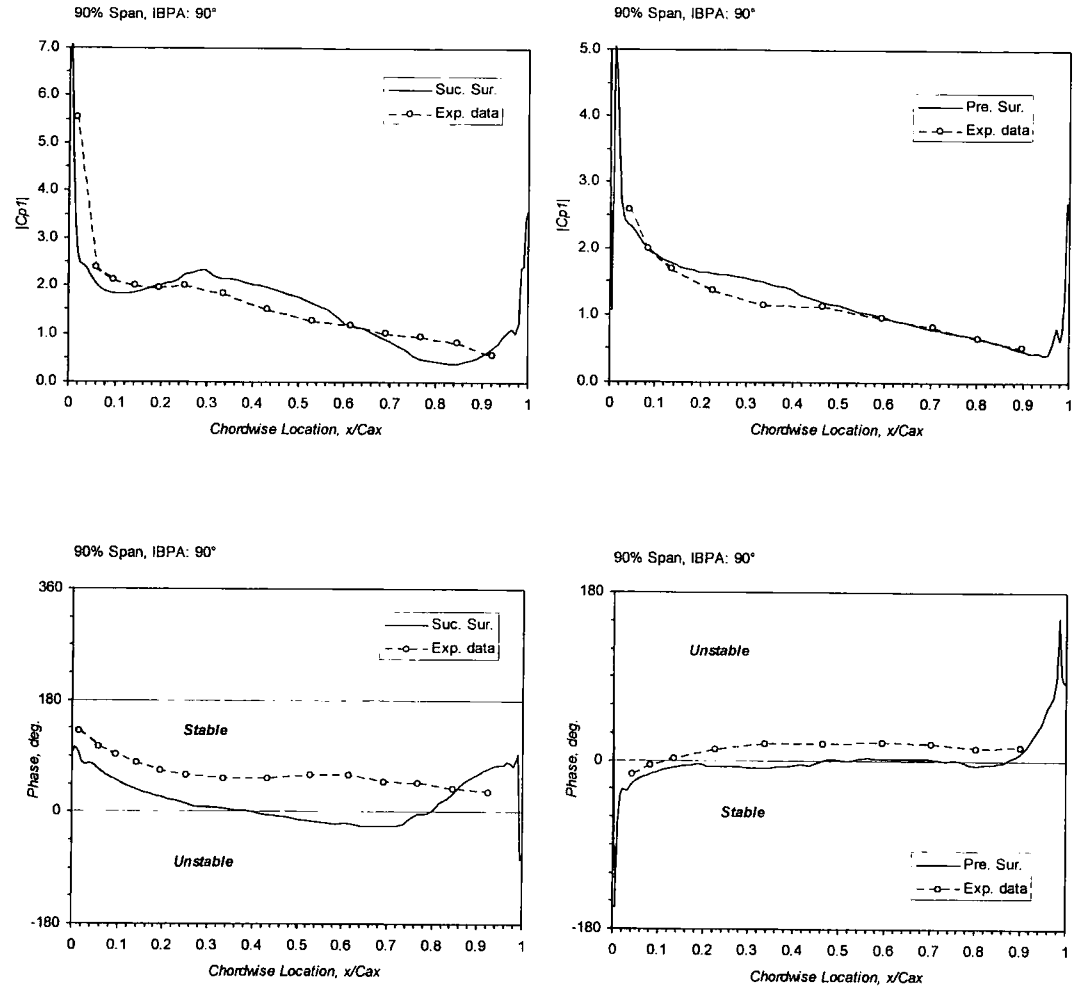

Figure 8.13: Predicted and measured amplitude and phase of the first harmonic pressure coefficient at 90% span for IBPA 90°

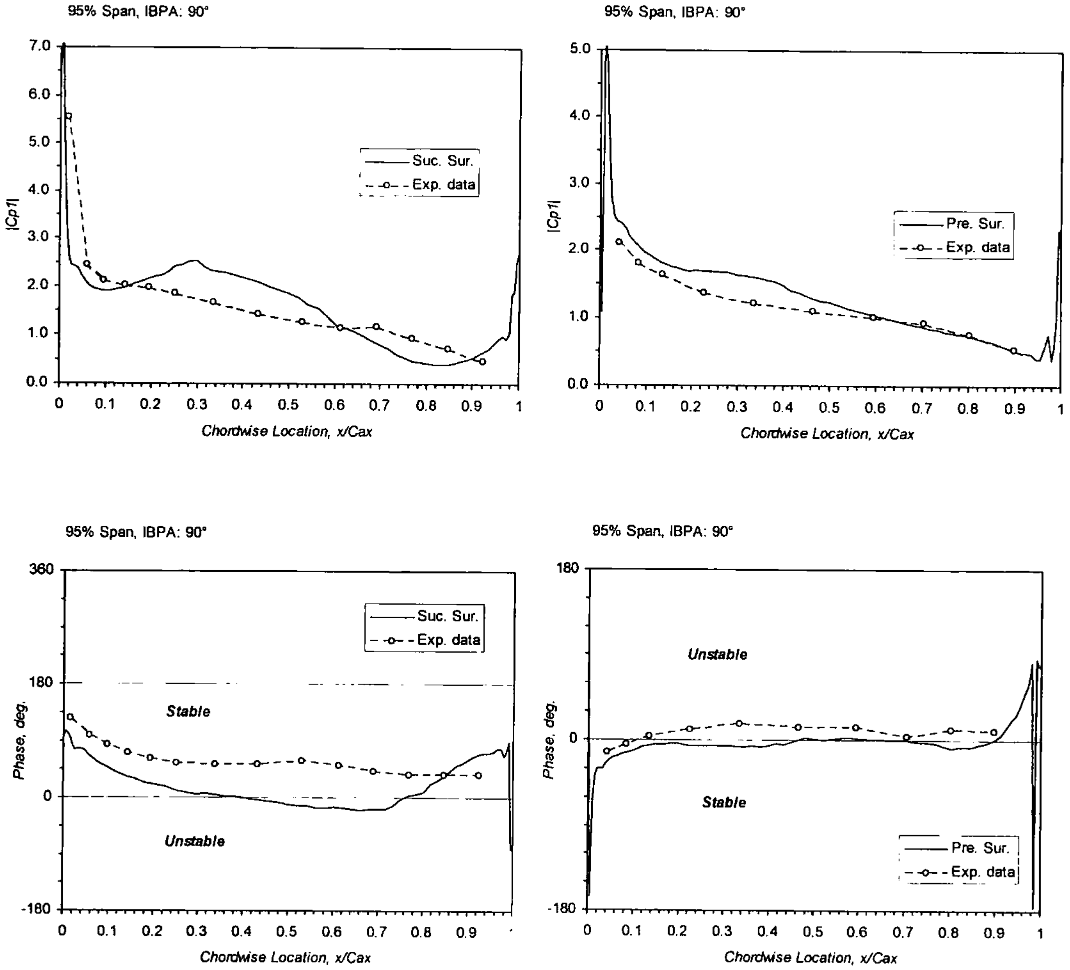

Figure 8.14: Predicted and measured amplitude and phase of the first harmonic pressure coefficient at 95% span for IBPA 90°

The comparisons of the predictions with the experimental data at the five spanwise sections for IBPA 180° are presented in **Figures 8.15 – 8.19**. The trend of the amplitude and phase angle of unsteady pressure was predicted very well at all span sections. The predicted unsteady amplitude is lower up to 70% span on the suction surface comparing to the experimental data, and the prediction is unable to capture the abrupt amplitude change around 54% chord which associates with the separation bubble at 50% and 70% span as demonstrated by the experimental data. The unsteady amplitude values are low calculated up to 30% chord on the pressure surface till 70% span while the amplitude is high predicted from 50% span around 30% chord whose chord length is increased towards the blade tip. The predicted values of the amplitude and phase angle of unsteady pressure agree with the experimental data better on the pressure surface than those on the suction surface, as that demonstrated for IBPA 90°. There is relatively better correlation between the predictions and the experimental results in amplitude of unsteady pressure on the suction surface at 90% and 95% span, and in phase angle on the pressure surface for all span sections for IBPA 180° comparing with that for IBPA 90°.

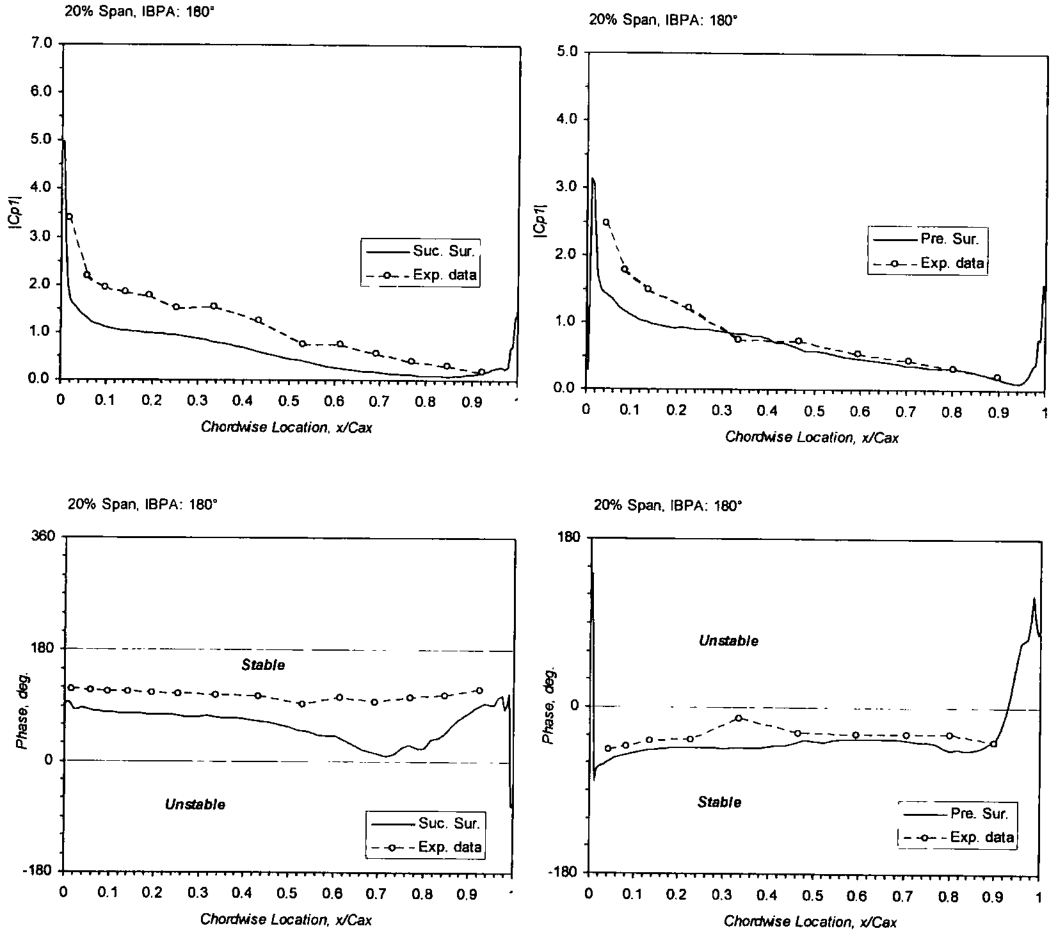

Figure 8.15: Predicted and measured amplitude and phase of the first harmonic pressure coefficient at 20% span for IBPA 180°

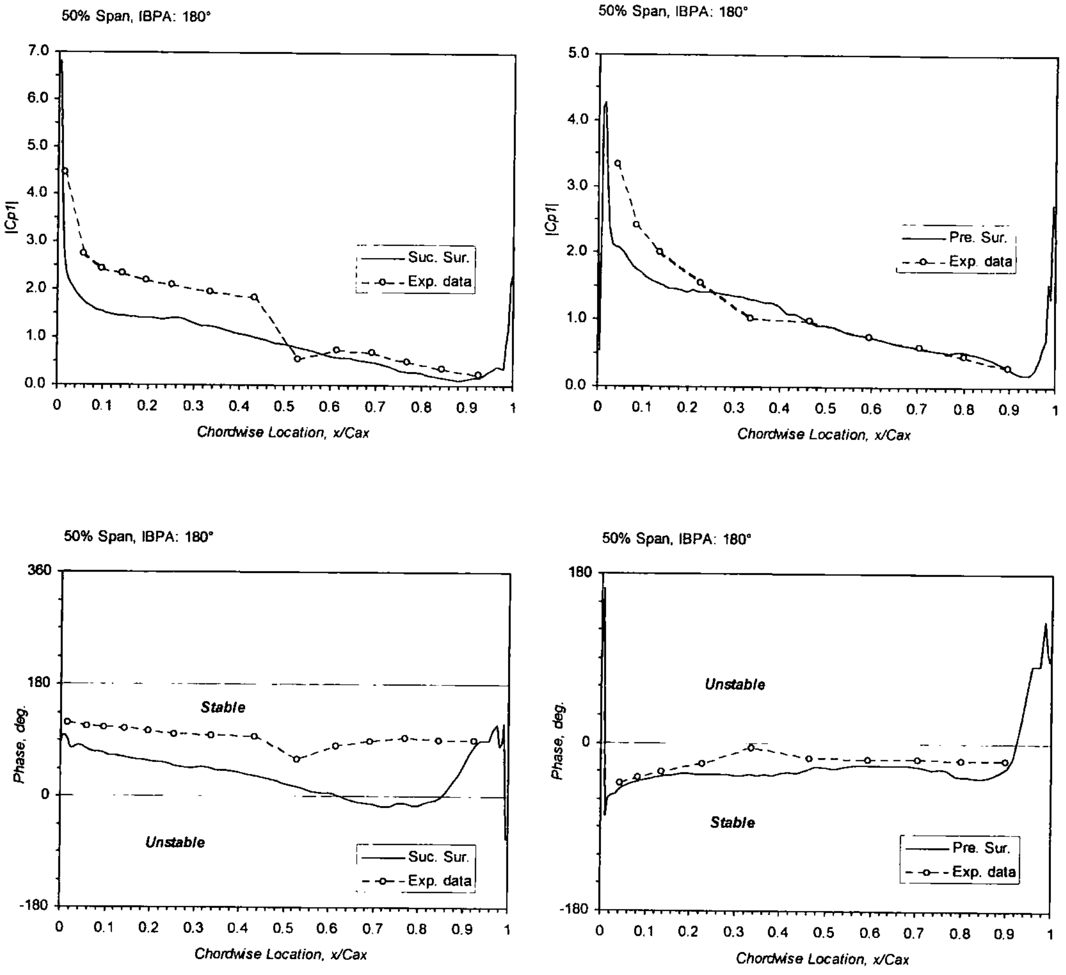

Figure 8.16: Predicted and measured amplitude and phase of the first harmonic pressure coefficient at 50% span for IBPA 180°

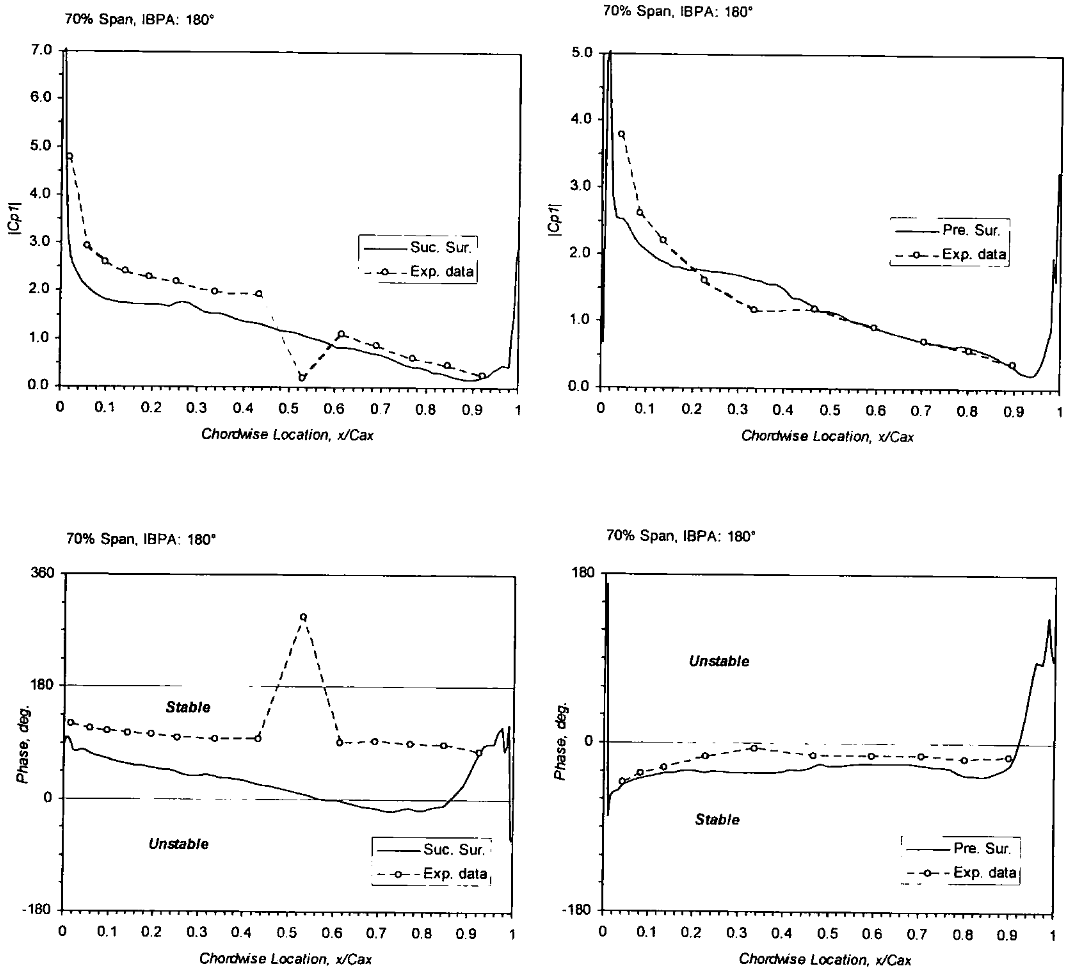

Figure 8.17: Predicted and measured amplitude and phase of the first harmonic pressure coefficient at 70% span for IBPA 180°

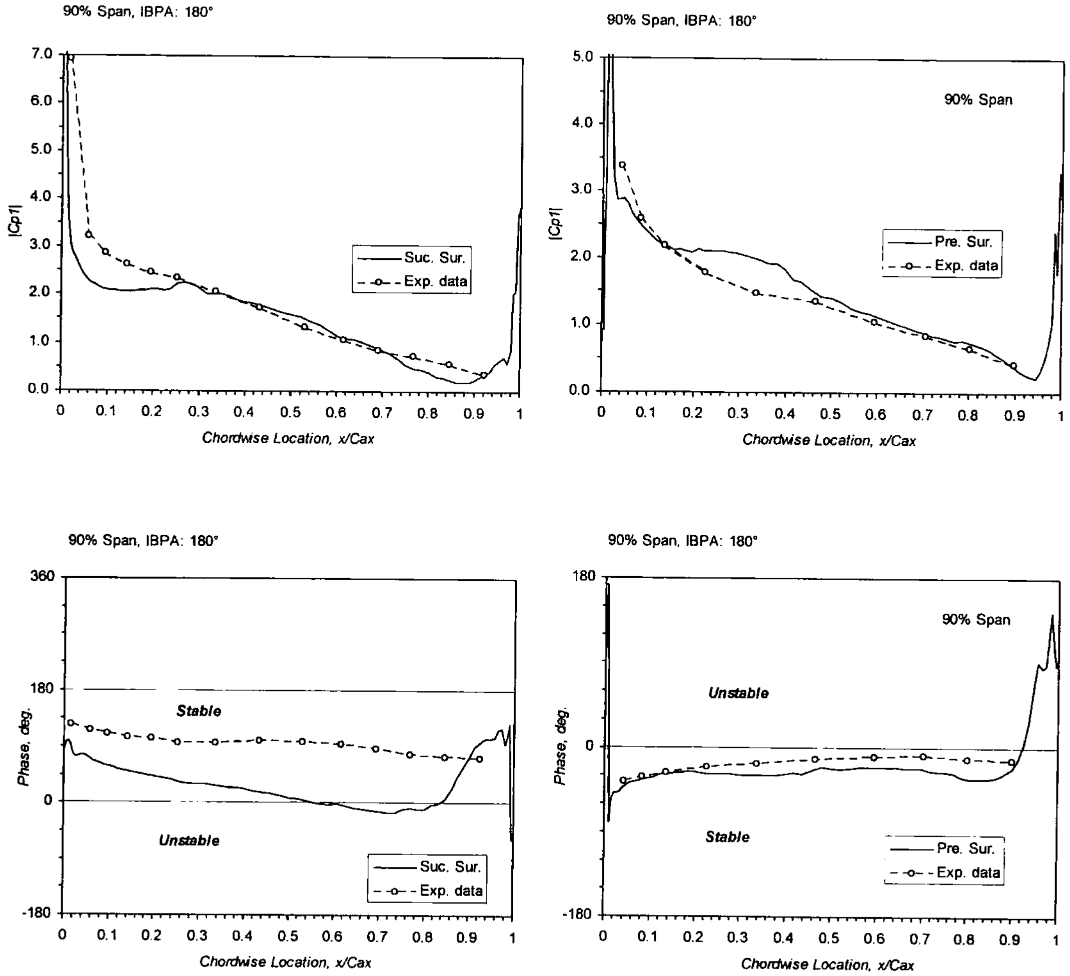

Figure 8.18: Predicted and measured amplitude and phase of the first harmonic pressure coefficient at 90% span for IBPA 180°

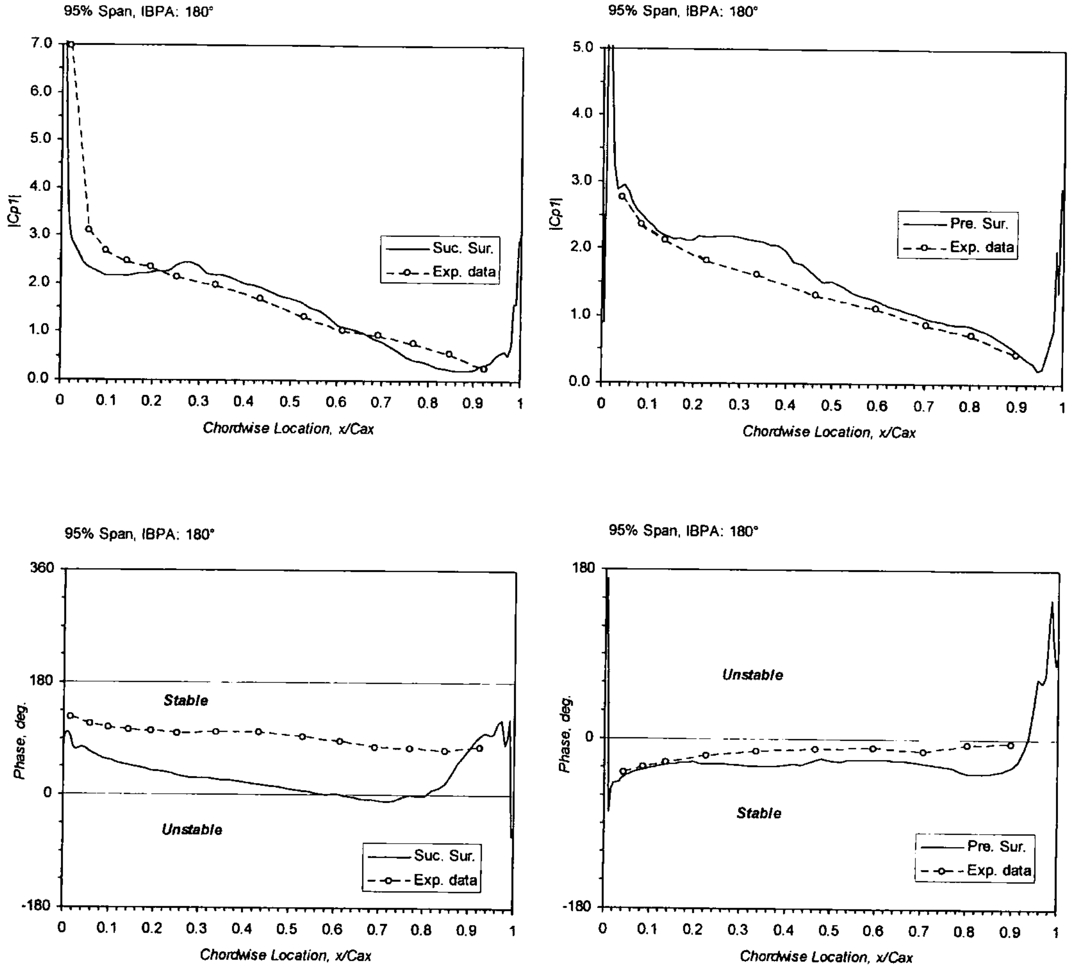

Figure 8.19: Predicted and measured amplitude and phase of the first harmonic pressure coefficient at 95% span for IBPA 180°

In general, the analyses tend to predict slightly smaller amplitudes than the experimental results in the leading edge regions. The phase predictions tend to lag the experimental results by a small amount. Overall, the comparisons between the computations and the experimental data are reasonably satisfactory in terms of the amplitude and phase angle of the first harmonic pressure response, and discrepancies are mainly in the regions of the leading edge and the flow separation.

The spanwise distribution of the predicted local aerodynamic damping is also compared with the experimental result shown in **Figure 8.20** for IBPA 90° and in

Figure 8.21 for IBPA 180°, which demonstrate the stable aeroelastic conditions at all spanwise locations for the two IBPAs.

The predicted local aerodynamic damping along the spanwise location captures the linear trend very well. However, the predicted spanwise amplitude shows disagreement with the experimental data. At 20% span, the local aerodynamic damping is in good agreement with the prediction for the two IBPAs. The predicted values are lower comparing with the experimental data from 20% span for the two IBPAs. The difference is increased toward the blade tip for IBPA 90°, while it is more constant for IBPA 180°. The under-predicted local aerodynamic damping for the two IBPAs mainly results from the low calculated values in amplitude and phase angle over the whole suction surface. The better correlation near the blade tip sections for IBPA 180° can be attributed only to the fact that the predicted amplitude agrees the experimental data well towards the blade tip and the higher amplitude there makes the favourable effect of the well predicted phase angle on the pressure surface more obvious. The difference between the predicted overall aerodynamic damping and the experimental value shown in **Figure 8.8** is a result of the under-predicted local aerodynamic damping over the most blade span.

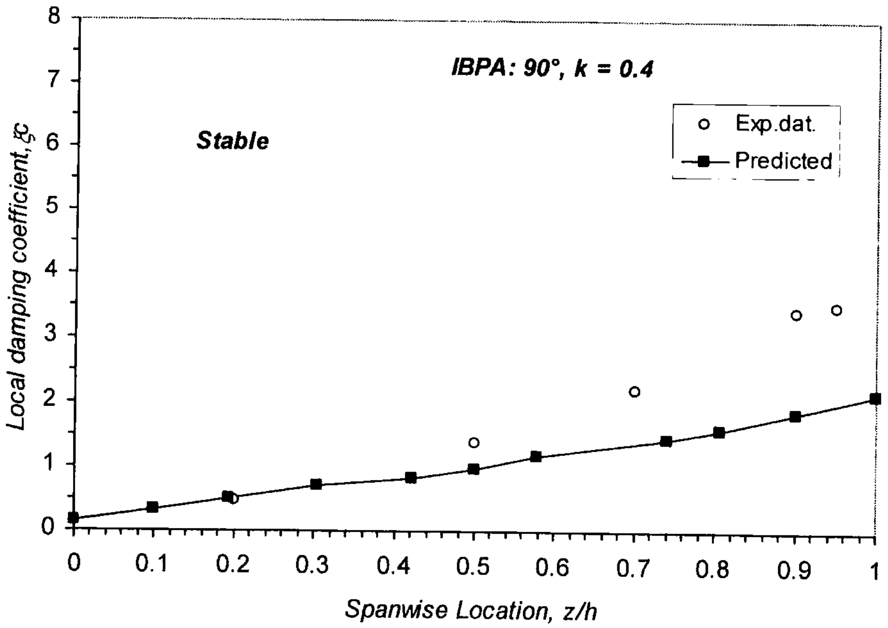

Figure 8.20: Local aerodynamic damping along span section for IBPA 90°

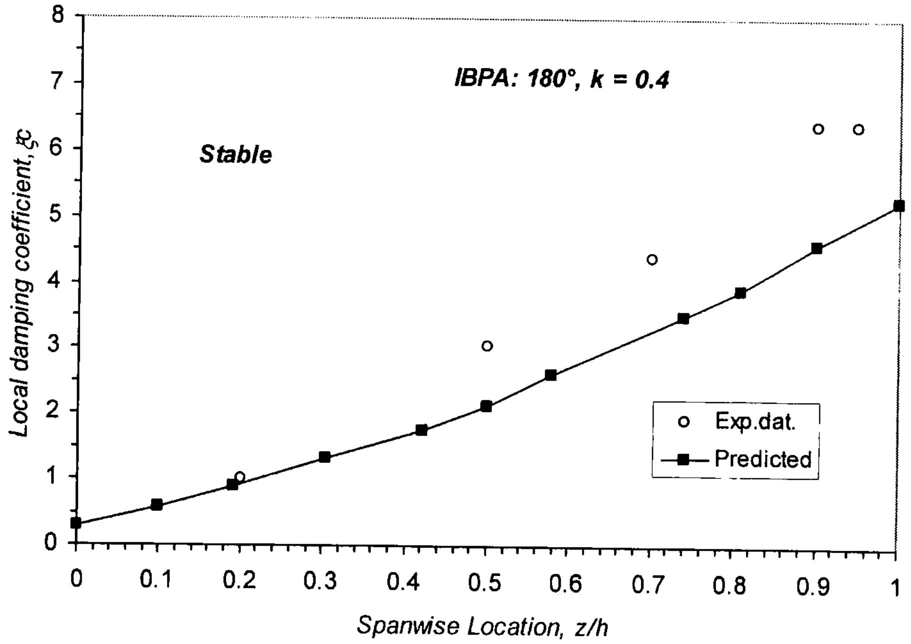

Figure 8.21: Local aerodynamic damping along span section for IBPA 180°

8.4. Conclusion

A 3D prediction of the steady and unsteady viscous flows through a linear compressor cascade with 3D bending oscillation was conducted. The computational steady flow results are in good agreement with the experimental data. The amplitude and phase angle of the first harmonic pressure response at the reduced frequency of 0.4 for IBPA 90° and 180°, and the aerodynamic damping for six IBPAs (0°, 30°, 60°, 90°, 180° and 270°) were predicted for the correlation with the measured results. The reasonably satisfactory comparison shows that the unsteady flow calculations in the frequency domain are able to predict the dominant unsteady effects of the 3D oscillating cascade reasonably well in general. The computational study of the test case was carried out on the linear oscillating compressor cascade, which is of the linear nature evaluated experimentally as documented in Chapter 5. Thus, the present research has not considered any nonlinear behaviour of blade flutter, such as the influence of shock waves and their motions in transonic unsteady flows.

This is the first 3D unsteady aerodynamic calculation comparing with 3D oscillating cascade test data in detail and any other has not seen to be published to the author's knowledge.

Chapter 9

Concluding Remarks

A detailed experimental and computational study into the behaviour of the unsteady flow around an oscillating cascade in a 3D bending mode has been documented, which was motivated by the urgent need to improve current understanding and to provide 3D oscillating cascade test data for the validation of advanced computational methods. A low speed experimental compressor flutter facility was developed. The steady and unsteady experimental data, which constitute the first-known 3D oscillating cascade test cases, are presented and analysed with the validation of the experimental model - Influence Coefficient Method. The prediction of the unsteady flow around the oscillating cascade using a 3D time-linearised Navier-Stokes method was compared with the experimental data. The influence of tip leakage flow on the unsteady aerodynamics of oscillating compressor cascade in a 3D bending mode was for the first time investigated experimentally.

The following sections summarise the conclusions reached and observations made from the present work and offer some suggestions for the future work.

9.1. Conclusions

The Development of a Low Speed Compressor Flutter Facility

A low speed compressor cascade facility described in Chapter 3 was built for the purpose of the present work, which allows the investigation of the detailed unsteady pressure response of the oscillating cascade with and without tip-clearance. The facility employs a linear compressor cascade, in which one blade is driven in a 3D bending mode based on the experimental model of the Influence Coefficient Method.

The experimental methods and techniques used for the steady and unsteady flow measurements were presented in Chapter 4 with the accuracy of the experimental techniques assessed. In terms of the low operational speed and the large scale of the test facility, the detailed measurement of the unsteady pressure response of the oscillating cascade is enabled using the off-board pressure transducers. The Tubing Transfer Function was used to correct the distortion in amplitude and phase of unsteady pressure caused by the tubing system, which separates the blade surface tappings and the off-board pressure transducers. An evaluation of the experimental repeatability and errors indicated an excellent level of repeatability and a good level of accuracy to be achieved in the measurements of unsteady pressures.

The validity of the experimental model for the unsteady pressure measurements has been verified in detail as described in Chapter 5. The blade static surface pressure distribution for the five spanwise sections (between 20% and 95% span) exhibited a reasonably good blade-to-blade periodicity on the middle three blades, which is important for the unsteady pressure measurements using the Influence Coefficient Method. The Influence Coefficient Method was validated by the linear unsteady flow behaviour and the quick convergence of the unsteady aerodynamic influence coefficient. The static pressure distribution at 50% and 70% span indicated a largely 2D laminar separation bubble positioned at 54% axial chord on the suction surface, which was demonstrated to have only a local effect on the unsteady flow. The unsteady aerodynamic response of the oscillating compressor cascade was experimentally assessed to be largely linear. The unsteady aerodynamic influence coefficient was shown to converge rapidly, with only the reference blade and its two immediate neighbouring blades having a significant contribution to the unsteady pressure response.

The Experimental Results

The unsteady aerodynamics of a linear 3D oscillating compressor cascade was documented in Chapter 6. The blade surface unsteady pressure response generated on the oscillating blade as well as that in a tuned cascade superimposed by the Influence Coefficient Method revealed a consistent 3D behaviour of the unsteady flow due to the blade vibration. This is especially evident in the fact that the amplitude of the first harmonic pressure response is largely insensitive to the local bending amplitude, which indicates the unsteady pressure wave has instantaneous radial interaction. This fully 3D feature of the unsteady flow certainly challenges the validity of the conventional quasi-3D strip theory and fully 3D methods will have to be used for aeroelastic problems of real blade systems. The overall aerodynamic damping for all inter-blade phase angles indicated the significant influence of the adjacent blades on the aeroelastic stability of the cascade. The first 3D oscillating cascade test case can be directly used for the validation of numerical codes for aeroelastic problems in turbomachines.

The Influence of Tip Leakage flow on the Oscillating Compressor Cascade Flow

An additional experimental investigation was performed in order to make a preliminary assessment of the previously unknown influence of tip leakage flow on the unsteady aerodynamic response of oscillating compressor cascade, which was described in Chapter 7. This was achieved through a detailed set of steady and unsteady pressure measurements at three different settings of tip-clearance. The steady flow measurements provided the aerodynamic background of the tip leakage flow throughout the range of tip-clearance considered for the unsteady pressure measurements. The tip-gap was shown to have a destabilising effect on the aeroelastic stability of the oscillating cascade for all inter-blade phase angles. The overall aerodynamic damping at the least stable inter-blade phase angle has been reduced by 27%, when the tip-gap was increased from nearly zero to 2.3% span. The detailed unsteady pressure data, obtained from tappings between 20% and 98% span, showed that the unsteady aerodynamics was largely affected in two regions. One is around the leading edge, which coincides with the localized unloading region in the steady flow field. The other is the following high unsteady amplitude region, which is believed to coincide with the core of the tip leakage vortex although its impact on the steady flow loading was not obvious. The influence of tip-gap on the unsteady aerodynamics was shown to reach the most part of the blade span with the pronounced effect near the blade tip due to the 3D unsteady behaviour. The present investigation provides the first hand information on the influence of tip leakage flow on the aeroelastic stability of the oscillating cascade in a 3D bending mode.

The Computational Results

A 3D time-linearised unsteady Navier-Stokes analysis was used to predict the unsteady flow around oscillating compressor cascade. The results were presented in Chapter 8. The computational predictions exhibited a consistently high level of qualitative agreement with the experimental results for the range inter-blade phase angles at the reduced frequency of 0.4. The numerical results clearly showed that time-linearised approaches with an appropriate viscous flow modelling are able to produce reasonably accurate predictions of unsteady flow with bubble-type separation and further indicated the unsteady aerodynamic response to be largely governed by linear mechanism. Some discrepancies are, however, apparent in the prediction of phase angle in the 2D separation bubble region. The unstable effect of this region was demonstrated to be local and subsequently did not significantly influence the overall level of aerodynamic damping prediction.

9.2. Recommendation for Further Work

General Recommendation

It is recognized that the experimental data generated in the present work are at a very low flow speed, which is not typically encountered in turbomachinery. Nevertheless, the ability of these data to verify the state-of-the-art prediction theory is firmly established. An efficient and reliable computational method for predicting blade flutter must be validated over a wide range of aerodynamic operational conditions. It is clear that a significant effort should be to establish a 3D test database on the flutter problems at the aerodynamic conditions of practicable interest, for instance the transonic regimes, and with the different combinations of inlet flow conditions, cascade geometry and adjacent blade rows.

Further Experimental Work

Future experimental work directed at 3D unsteady flow phenomena should allow an assessment of the influence of parameters such as incidence angle on the 3D nature of unsteady flows due to blade vibration. The present work and discussions suppose a perfect tuning (i.e. a tuned cascade with all blade oscillating at the same frequency and a constant inter-blade phase angle) when blade flutter occurs. A further idealisation is that the vibration amplitude changes linearly along span. Additional work is also required to improve understanding of flutter under a realistic mode shape of blade vibration, which now can only be investigated through testing in actual instrumented turbomachines

The Influence of Tip Leakage Flow on the Unsteady Aerodynamic Response of the Oscillating Compressor Cascade

Although the experimental investigation into the influence of tip leakage flow on the unsteady aerodynamic response of the oscillating compressor cascade showed that there was a significant destabilising effect on the unsteady pressure response near the blade tip, it remains difficult to relate this influence to the detailed steady flow feature near the blade tip endwall due to rather limited experimental information. Further CFD analysis would be useful. It would be investigated further how the viscous effects near the endwall (such as wall boundary layer, blade boundary layer and the passage vortex) combined with the tip leakage flow affects the unsteady pressure response of the oscillating cascade.

Computational Work

Recommendations are made for the additional work to improve the prediction model used. It was notable that the time-linearised method is unable to adequately capture the steady and unsteady pressure response of the separation bubble. This suggests that more accurate transition models should be adopted to predict the steady and unsteady behaviour of the separation bubble.

Reference

Abhari, R.S. & Giles, M. (1997), "A Navier-Stokes Analysis of Airfoils in Oscillating Transonic Cascades for the Prediction of Aerodynamic Damping," Journal of Turbomachinery Vol. 119: pp. 77-84.

Ayer, T.C. & Verdon, J.M. (1998), "Validation of a Nonlinear Unsteady Aerodynamic Simulator for Vibrating Blade Rows," Journal of Turbomachinery Vol. 120: pp. 112-121.

Bell, D.L. (1999), "Three Dimensional Unsteady Flow for an Oscillating Turbine Blade," PhD Thesis, School of Engineering, University of Durham, Durham, UK.

Bell, D.L. & He, L. (2000), "Three-Dimensional Unsteady Flow for an Oscillating Turbine Blade and the Influence of Tip Leakage," Journal of Turbomachinery Vol. 122: pp. 93-101.

Bendiksen, O.O. (1990), "Aeroelastic Problems in Turbomachines," *AIAA Paper* 90-1157-CP.

Bölcs, A. & Fransson, T.H. (1986), "Aeroelasticity in Turbomachines Comparison of Theoretical and Experimental Cascade Results," *Communication du Laboratoire de Thermique Appliquée et de Turbomachines, No. 13, Lausanne, EPFL.*

Bryer, D.W. & Pankhurst, R.C. (1971), "Pressure-probe Methods for Determining Wind Speed and Flow Direction," National Physical Laboratory, Her Majesty's Stationary Office.

Buffum, D.H., *et al.* (1998), "Oscillating Cascade Aerodynamics at Large Mean Incidence," Journal of Turbomachinery Vol. 120: pp. 122-130.

Buffum, D.H. & Fleeter, S. (1988), "Investigation of Oscillating Cascade Aerodynamics by an Experimental Influence Coefficient Technique," *AIAA Paper* 88-2815.

Buffum, D.H. & Fleeter, S. (1990), "The Aerodynamics of an Oscillating Cascade in a Compressible Flow Field," Journal of Turbomachinery Vol. 112: pp. 759-767.

Buffum, D.H. & Fleeter, S. (1993), "Wind Tunnel Wall Effects in a Linear Oscillating Cascade," Journal of Turbomachinery Vol. 115: pp. 147-156.

Buffum, D.H. & Fleeter, S. (1994), "Effect of Wind Tunnel Acoustic Modes on Linear Oscillating Cascade Aerodynamics," Journal of Turbomachinery Vol. 116: pp. 513- 524.

Carta, F.O. (1967), "Coupled Blade-Disk-Shroud Flutter Instabilities in Turbojet Engine Rotors," Journal of Engineering for Power Vol. 89: pp. 419-426.

Carta, F.O. (1983), "Unsteady Aerodynamics and Gapwise Periodicity of Oscillating Cascaded Airfoils," Journal of Engineering for Power Vol. 105: pp. 565-574.

Carta, F.O. & St. Hilaire, A.O. (1978), "Experimentally Determined Stability Parameters of a Subsonic Cascade Oscillating Near Stall," Journal of Engineering for Power Vol. 100: pp. 111-120.

Carta, F.O. & St. Hilaire, A.O. (1980), "Effect of Interblade Phase Angle and Incidence Angle on Cascade Pitching Stability," Journal of Engineering for Power Vol. 102: pp. 391-396.

Chassaing, J.C. & Gerolymos, G.A. (2000), "Compressor Flutter Analysis Using Time-Nonlinear and Time-Linearized 3-D Navier-Stokes Methods," *Proceedings of the 9th ISUAAAT*, Lyon, France.

Chuang, H.A. & Verdon, J.M. (1999), "A Nonlinear Numerical Simulator for Three-Dimensional Flows Through Vibrating Blade Rows," Journal of Turbomachinery Vol. 121: pp. 348-357.

Clark, W.S. & Hall, K.C. (2000), "A Time-linearized Navier-Stokes Analysis of Stall Flutter," Journal of Turbomachinery Vol. 122: pp. 467-476.

Collar, A.R. (1946), "The Expanding Domain of Aeroelasticity," Journal of the Royal Aeronautical Society Vol. L: pp.613-636.

Daoud, M. & Naguib, A. (2003), "A Doppler Sensor for High Spatial Resolution Measurements of Unsteady Surface Pressure," Measurement Science and Technology Vol. 14: pp. 13-23.

Denton, J.D. (1983), "An Improved Time-Marching Method for Turbomachinery Flow Calculation," Journal of Engineering for Power Vol. 105: pp. 514-524.

Ehrlich, D.A. & Fleeter, S. (1994), "Chordwise Bending Cascade Unsteady Aerodynamics by an Experimental Influence Coefficient Technique," *AIAA Paper* 94-2972.

Ehrlich, D.A. & Fleeter, S. (2000), "Incidence Effects on Chordwise Bending Cascade Unsteady Aerodynamics," AIAA Journal Vol. 38(No. 2): pp. 284-291.

Elazar, Y. & Shreeve, R.P. (1990), "Viscous Flow in a Controlled Diffusion Compressor Cascade With Increasing Incidence," Journal of Turbomachinery Vol. 112: pp. 256-266.

Erdos, J.I. & Alzner, E. (1977), "Numerical Solution of Periodic Transonic Flow through a Fan Stage," AIAA Journal Vol. 15(No. 11): pp. 1559-1568.

Fleeter, S. & Jay, R.L. (1987), "Unsteady Aerodynamic Measurements in Flutter Research," *AGARD Manual on Aeroelasticity in Axial-Flow Turbomachines*, Volume 1 – Unsteady Turbomachinery Aerodynamics, AGARD-AG-298.

Fleeter, S., ***et al.*** (1977), "An Experimental Determination of the Unsteady Aerodynamics in a Controlled Oscillating Cascade," Journal of Engineering for Power Vol. 99: pp. 88-96.

Fransson, T.H. (1990), "Analysis of Experimental Time-Dependent Blade Surface Pressures from an Oscillating Turbine Cascade with the Influence-Coefficient Technique," *ASME Paper* 90-GT-225.

Fransson, T.H. (1999a), "Important Parameters," *VKI Lecture Series on 'Aeroelasticity in Axial-Flow Turbomachines,'* 1999-05.

Fransson, T.H. (1999b), "Aeroelastic Facilities/Aerodynamic Measurements," *VKI Lecture Series on 'Aeroelasticity in Axial-Flow Turbomachines,'* 1999-05.

Fransson, T.H. (1999c), "Basic Nomenclature of Time-Dependent Internal Aerodynamics," *VKI Lecture Series on 'Aeroelasticity in Axial-Flow Turbomachines,'* 1999-05.

Fransson, T.H. & Borg, R. (1992), "Summary of Aerodynamic Test Methodologies used in Linear and Annular Windtunnel Cascades and Single and Multistage Cold Flow Rotating Turbine Experiments," *Internal Report, LTT-EPT-Lausanne, Switzerland.*

Frey, K.K. & Fleeter, S. (2001), "Oscillating Airfoil Aerodynamics of a Rotating Compressor BLade Row," Journal of Propulsion and Power Vol. 17: pp. 232-239.

Gallus, H.E. (1987), "Unsteady Aerodynamic Measurements on Rotors," *AGARD Manual on Aeroelasticity in Axial-Flow Turbomachines*, Volume 1 – Unsteady Turbomachinery Aerodynamics, AGARD-AG-298.

Gerolymos, G.A. (1988), "Numerical Integration of the Blade-to-Blade Surface Euler Equations in Vibrating Cascades," AIAA Journal Vol. 26(No. 12): pp1483-1492.

Gerolymos, G.A. (1993), "Advances in the Numerical Integration of the Three-Dimensional Euler Equations in Vibrating Cascades," Journal of Turbomachinery Vol. 115: pp. 781-790.

Gerolymos, G.A. & Vallet, I. (1996), "Validation of Three-Dimensional Euler Methods for Vibrating Cascade Aerodynamics," Journal of Turbomachinery Vol. 118: pp. 771-782.

Giles, M.B. (1988), "Calculation of Unsteady Wake Rotor Interaction," Journal of Propulsion and Power Vol. 4(No. 4): pp. 356-362.

Gorlin, S.M. & Slezinger, I.I. (1964), "Wind Tunnels and their Instrumentation," Translated from Russian by the Israel Program for Scientific Translations.

Gregory, J.W., ***et al.*** (2002), "Unsteady Pressure Measurements in Turbomachinery using Porous Pressure Sensitive Paint," *AIAA Paper* 2002-0084.

Grüber, B. & Carstens, V. (1998), "Computation of the Unsteady Transonic Flow in Harmonically Oscillating Turbine Cascades Taking into Account Viscous Effects," Journal of Turbomachinery Vol. 120: pp. 104-111.

Hall, K.C., ***et al.*** (1994), "A Linearized Euler Analysis of Unsteady Transonic Flows in Turbomachinery," Journal of Turbomachinery Vol. 116: pp. 477-488.

Hall, K.C. & Crawley, E.F. (1989), "Calculation of Unsteady Flows in Turbomachinery Using the Linearized Euler Equations," AIAA Journal Vol. 27(No. 6): pp. 777-787.

Hall, K.C. & Lorence, C.B. (1993), "Calculation of Three-Dimensional Unsteady Flows in Turbomachinery Using the Linearized Harmonic Euler Equations," Journal of Turbomachinery Vol. 115: pp. 800-809.

Halliwell, D.G., ***et al.*** (1984), "A Study of Unsteady Pressures Near the Tip of a Transonic Fan in Unstalled Supersonic Flutter," Journal of Vibration, Acoustics, Stress, and Reliability in Design Vol. 106: pp. 198-203.

Hanamura, Y., ***et al.*** (1980), "A Simplified Method to Measure Unsteady Forces Acting on the Vibrating Blades in Cascade," Bulletin of the JSME Vol. 23(No. 180): pp. 880-887.

Hardin, L.W., ***et al.*** (1987), "Unsteady Aerodynamic Measurements on a Rotating Compressor Blade Row at Low Mach Number," Journal of Turbomachinery Vol. 109: pp. 499-507.

He, L. (1990), "An Euler Solution for Unsteady Flows Around Oscillating Blades," Journal of Turbomachinery Vol. 112: pp. 714-722.

He, L. (1992), "Method of Simulating Unsteady Turbomachinery Flows with Multiple Perturbations," AIAA Journal Vol. 30(No. 11): pp. 2730-2735.

He, L. (1998), "Unsteady Flow in Oscillating Turbine Cascades: Part1- Linear Cascade Experiment," Journal of Turbomachinery Vol. 120: pp. 262-268.

He, L. (2003), "Unsteady Flow and Aeroelasticity," Handbook of Turbomachinery, Marcel Dekker, INC., pp. 257-307, Second Edition.

He, L. & Denton, J.D. (1991), "An Experiment on Unsteady Flow Over an Oscillating Airfoil," *ASME Paper* 91-GT-181.

He, L. & Denton, J.D. (1993), "Inviscid-Viscous Coupled Solution for Unsteady Flows Through Vibrating Blades: Part1- Description of the Method & Part2 - Computational Results," Journal of Turbomachinery Vol. 115: pp. 94-109.

He, L. & Denton, J.D. (1994), "Three-Dimensional Time-Marching Inviscid and Viscous Solutions for Unsteady Flows Around Vibrating Blades," Journal of Turbomachinery Vol. 116: pp. 469-476.

He, L. & Ning, W. (1998), "Efficient Approach for Analysis of Unsteady Viscous Flows in Turbomachines," AIAA Journal Vol. 36(No. 11): pp. 2005-2012.

Holmes, D.G. & Lorence, C.B. (1997), "Three Dimensional Linearized Navier-Stokes Calculations for Flutter and Forced Response," *Proceedings of the 8th ISUAAT*, Stockholm, Sweden.

Hoying, D.A., ***et al.*** (1999), "Role of Blade Passage Flow Structures in Axial Compressor Rotating Stall Inception," Journal of Turbomachinery Vol. 121: pp. 735-742.

Irwin, H.P.A.H., ***et al.*** (1979), "Correction of Distortion Effects Caused by Tubing Systems in Measurements of Fluctuating Pressures," Journal of Industrial Aerodynamics Vol. 5: pp. 93-107.

Kang, S. & Hirsch, C. (1993), "Experimental Study on the Three-Dimensional Flow Within a Compressor Cascade With Tip Clearance: Part I- Velocity and Pressure Fields," Journal of Turbomachinery Vol. 115: pp. 435-443.

Kielb, R.E. (1999a), "Flutter Design Analysis," *VKI Lecture Series on 'Aeroelasticity in Axial Flow Turbomachines'*, 1999-05.

Kielb, R.E. (1999b), "Full Scale Engine Testing," *VKI Lecture Series on 'Aeroelasticity in Axial Flow Turbomachines'*, 1999-05.

Kobayashi, H. (1984), "Unsteady Aerodynamic Force Acting on Controlled-Oscillating Transonic Annular Cascade," Conference on Unsteady Aerodynamics of Turbomachines and Propellors, Cambridge, UK.

Kobayashi, H. (1989), "Effects of Shock Waves on Aerodynamic Instability of Annular Cascade Oscillating in a Transonic Flow," Journal of Turbomachinery Vol. 111: pp. 222-230.

Kobayashi, H. (1990), "Annular Cascade Study of Low Back-Pressure Supersonic Fan Blade Flutter," Journal of Turbomachinery Vol. 112: pp. 768-777.

Körbächer, H. & Bölcs, A. (1994), "Experimental Investigation of the Unsteady Behavior of a Compressor Cascade in an Annular Ring Channel," *Proceedings of the 7th ISUAAT*, Fukuoka, Japan.

Lane, F. (1956), "System Mode Shapes in the Flutter of Compressor Blade Rows," Journal of the Aeronautical Science Vol. 23: pp. 54-66.

Lepicovsky, J., ***et al.*** (2001), "On Flowfield Periodicity in the NASA Transonic Flutter Cascade," Journal of Turbomachinery Vol. 123: pp. 501-509.

Lepicovsky, J., ***et al.*** (2002), "Unsteady Pressures in a Transonic Fan Cascade Due to a Single Oscillating Airfoil," NASA/TM- 2002-211723

Lindquist, D.R. & Giles, M.B. (1994), "Validity of Linearized Unsteady Euler Equations with Shock Capturing," AIAA Journal Vol. 32(No. 1): pp. 46-53.

Lynn, P.A. & Fuerst, W. (1989), "Introductory Digital Signal Processing with Computer Applications," *John Wiley & Sons.*

Mailach, R., ***et al.*** (2001), "Rotating Instabilities in an Axial Compressor Originating From the Fluctuating Blade Tip Vortex," Journal of Turbomachinery Vol. 123: pp. 453-463.

Manwaring, S.R., ***et al.*** (1997), "Inlet Distortion Generated Forced Response of a Low-Aspect-Ratio Transonic Fan," Journal of Turbomachinery Vol. 119: pp. 665-676.

Manwaring, S.R. & Wisler, D.C. (1993), "Unsteady Aerodynamics and Gust Response in Compressors and Turbines," Journal of Turbomachinery Vol. 115: pp. 724-740.

Marshall, J.G. (1997), "Prediction of Turbomachinery Aeroelasticity Effects using a 3D Non-linear Integrated Method," PhD thesis, Imperial College of Science, Technology & Medicine, University of London, London, UK.

Mikolajczak, A.A. (1976), "Technology Status for Blade Flutter in Axial Turbomachinery," Journal of Fluids Engineering Vol. 098: pp. 337-339.

Mikolajczak, A.A., *et al.* (1975), "Advances in Fan and Compressor Blade Flutter Analysis and Predictions," Journal of Aircraft Vol. 12(No. 4): pp. 325-332.

Miller, M.F., *et al.* (2000), "Design and Testing of Micromachined Fabry-Perot Pressure Sensors for Aerodynamic Applications," *AIAA Paper* 2000-0253.

Ni, R.H. & Sisto, F. (1976), "Numerical Computation of Nonstationary Aerodynamics of Flat Plate Cascades in Compressible Flow," Journal of Engineering for Power Vol. 98: pp. 165-170.

Ning, W. & He, L. (1998), "Computation of Unsteady Flows Around Oscillating Blades Using Linear and Nonlinear Harmonic Euler Methods," Journal of Turbomachinery Vol. 120: pp. 508-514.

Nowinski, M. & Panovsky, J. (1998), "Flutter Mechanisms in Low Pressure Turbine Blades," *ASME Paper* 98-GT-573.

Ott, P., *et al.* (1998), "The Influence of Tailboards on Unsteady Measurements in a Linear Cascade," *ASME Paper* 98-GT-572.

Pandya, A. & Lakshminarayana, B. (1983), "Investigation of the Tip Clearance Flow Inside and at the Exit of a Compressor Rotor Passage - Part I: Mean Velocity Field," Journal of Engineering for Power Vol. 105: pp. 1-12.

Queune, O.J.R. & He, L. (2001), "Experimental Study of 3D Unsteady Flow Around Oscillating Blade With Part-Span Separation," Journal of Turbomachinery Vol. 123: pp. 519-525.

Sanders, A.J., *et al.* (2003), "Experimental and Numerical Study of Stall Flutter in a Transonic Low-Aspect Ratio Fan Blisk," Proceedings of ASME Turbomachinery Exposition, Atlanta, Georgia, USA, Paper No. GT2003-38353.

Sanger, N.L. (1983), "The Use of Optimization Techniques to Design-Controlled Diffusion Compressor Blading," Journal of Engineering for Power Vol. 105: pp. 256-264.

Sanger, N.L. & Shreeve, R.P. (1986), "Comparison of Calculated and Experimental Cascade Performance for Controlled-Diffusion Compressor Stator Blading," Journal of Turbomachinery Vol. 108: pp. 42-50.

Sasaki, T. & Breugelmans, F. (1998), "Comparison of Sweep and Dihedral Effects on Compressor Cascade Performance," Journal of Turbomachinery Vol. 120: pp. 454-464.

Shannon, J.F. (1945), "Vibration Problems in Gas Turbines, Centrifugal and Axial Flow Compressors," *A. R. C., R & M* 2226

Sims-Williams, D.B. (2001), "Self-Excited Aerodynamic Unsteadiness Associated with Passenger Cars," PhD thesis, School of Engineering, University of Durham, Durham, UK.

Sisto, F. (1987), "Introduction and Overview," *AGARD Manual on Aeroelasticity in Axial-Flow Turbomachines*, Volume 1 – Unsteady Turbomachinery Aerodynamics, AGARD-AG-298.

Snyder, L.E. & Commerford, G.L. (1974), "Supersonic Unstalled Flutter in Fan Rotors; Analytical and Experimental Results," Journal of Engineering for Power Vol. 96: pp. 379-386.

Srinivasan, A.V. (1997), "Flutter and Resonant Vibration Charateristics of Engine Blades," *ASME Paper* 97-GT-533.

Stargardter, H. (1977), "Optical Determination of Rotating Fan Blade Deflections," Journal of Engineering for Power Vol. 99: pp. 204-209.

Storer, J.A. & Cumpsty, N.A. (1991), "Tip Leakage Flow in Axial Compressors," Journal of Turbomachinery Vol. 113: pp. 252-259.

Szechenyi, E. (1987), "Understanding Fan Blade Flutter through Linear Cascade Aeroelastic Testing," *AGARD Manual on Aeroelasticity in Axial-Flow Turbomachines*, Volume 1 – Unsteady Turbomachinery Aerodynamics, AGARD-AG-298.

Vasanthakumar, P., *et al.* (2000), "Three-Dimensional Viscous Computation of Blade Flutter and Forced Response Using Nonlinear Harmonic Approach," *Proceedings of the 9th of ISUAAAT*, Lyon, France.

Vasanthakumar, P. (2003), "Three Dimensional Frequency-Domain Solution Method for Unsteady Turbomachinery Flows," PhD Thesis, School of Engineering, University of Durham, Durham, UK.

Verdon, J.M. (1973), "The Unsteady Aerodynamics of a Finite Supersonic Cascade with Subsonic Axial Flow," Journal of Applied Mechanics Vol. 40: pp. 667-671.

Verdon, J.M. (1977), "Further Developments in the Aerodynamic Analysis of Unsteady Supersonic Cascades: Part1 & Part2," Journal of Engineering for Power Vol. 99: pp. 509-525.

Verdon, J.M. (1993), "Review of Unsteady Aerodynamic Methods for Turbomachinery Aeroelastic and Aeroacoustic Applications," AIAA Journal Vol. 31(No. 2): pp. 235-250.

Verdon, J.M. & Caspar, J.R. (1980), "Subsonic Flow Past an Oscillating Cascade with Finite Mean Flow Deflection," AIAA Journal Vol. 18(No. 5): pp. 540-548.

Verdon, J.M. & Caspar, J.R. (1982), "Development of a Linear Unsteady Aerodynamic Analysis for Finite-Deflection Subsonic Cascades," AIAA Journal Vol. 20(No. 9): pp. 1259-1267.

Verdon, J.M. & Caspar, J.R. (1984), "A Linearized Unsteady Aerodynamic Analysis for Transonic Cascades," Journal of Fluid Mechanics Vol. 149: pp. 403-429.

Watanabe, T. & Kaji, S. (1988), "Experimental Study on Unsteady Aerodynamic Characteristics of an Oscillating Cascade with Tip Clearance," JSME international Journal Vol. 31(No. 4): pp. 660-667.

Yang, H., *et al.* (2003), "Unsteady Pressure Measurement with Correction on Tubing Distortion," *Proceedings of the10th ISUAAA*, Duke University, Durham, U.S.A.

Appendix: Blade Profile Specification

x(*mm*)	y(*mm*)	x(*mm*)	y(*mm*)	x(*mm*)	y(*mm*)	x(*mm*)	y(*mm*)	x(*mm*)	y(*mm*)
0.100	1.797	74.474	20.801	131.230	8.543	128.069	5.351	50.022	10.242
0.297	2.197	76.624	20.639	132.890	8.080	126.663	5.624	48.204	10.070
0.640	2.500	78.772	20.443	134.548	7.615	125.255	5.884	46.387	9.874
1.712	3.130	80.915	20.214	136.205	7.150	123.844	6.130	44.573	9.656
2.784	3.760	83.055	19.952	137.863	6.685	122.431	6.362	42.762	9.415
4.929	4.971	85.191	19.656	139.520	6.220	121.015	6.581	40.954	9.151
7.096	6.144	87.322	19.326	141.183	5.750	119.600	6.800	39.150	8.864
9.284	7.278	89.447	18.964	142.845	5.280	116.955	7.138	37.349	8.554
11.492	8.372	90.394	18.743	144.508	4.810	114.309	7.460	35.552	8.221
13.719	9.426	91.733	18.495	146.170	4.340	111.660	7.769	33.760	7.866
15.964	10.440	93.071	18.241	147.370	3.995	109.010	8.062	31.973	7.488
18.228	11.414	94.407	17.979	148.310	3.732	106.359	8.341	30.190	7.088
20.508	12.347	95.743	17.710	148.846	3.480	103.706	8.605	27.628	6.476
22.805	13.239	97.076	17.433	149.275	3.072	101.051	8.854	25.065	5.864
25.118	14.089	98.408	17.150	149.554	2.549	98.395	9.088	22.503	5.252
27.445	14.898	99.739	16.859	149.653	1.965	95.738	9.308	19.940	4.640
29.787	15.665	101.068	16.561	149.564	1.380	93.080	9.513	18.278	4.238
32.142	16.389	102.395	16.256	149.294	0.853	90.421	9.703	16.615	3.835
34.510	17.071	103.720	15.944	148.871	0.437	87.760	9.879	14.953	3.433
36.889	17.711	105.044	15.625	148.339	0.177	85.099	10.040	13.290	3.030
39.280	18.308	106.367	15.299	147.752	0.097	82.437	10.186	11.630	2.603
41.681	18.861	107.687	14.965	147.410	0.120	79.774	10.317	9.970	2.175
44.091	19.372	109.006	14.624	146.732	0.350	77.110	10.433	8.310	1.748
46.511	19.79	110.322	14.277	146.054	0.580	74.446	10.535	6.650	1.320
48.648	20.116	111.637	13.922	144.693	1.026	71.781	10.621	5.415	1.005
50.791	20.358	112.950	13.560	143.328	1.460	69.116	10.693	4.180	0.690
52.937	20.566	114.613	13.110	141.959	1.880	66.450	10.750	2.945	0.375
55.086	20.741	116.275	12.660	140.586	2.287	66.449	10.754	2.456	0.261
57.237	20.883	117.938	12.210	139.209	2.681	64.623	10.790	1.966	0.117
59.391	20.990	119.600	11.760	137.828	3.062	62.796	10.802	1.530	0.010
61.545	21.065	121.263	11.303	136.444	3.429	60.969	10.791	1.072	0.027
63.701	21.105	122.925	10.845	135.056	3.783	59.142	10.757	0.647	0.196
65.857	21.111	124.588	10.388	133.665	4.123	57.316	10.701	0.302	0.497
68.013	21.084	126.250	9.930	132.270	4.450	55.490	10.620	0.077	0.895
70.168	21.023	127.910	9.468	130.873	4.764	53.666	10.517	-0.002	1.346
72.322	20.929	129.570	9.005	129.473	5.064	51.843	10.391		